The possible use of applied potential tomography for imaging action potentials in the brain

Kevin Graham Boone
PhD thesis

University College London
August 1995

Abstract

There are already excellent techniques for imaging the anatomy of the human brain, and changes in its functional state over seconds. Furthermore, the function of the individual neuron has been studied at time resolutions of less than a millisecond. There is, at present, no technique which combines this fine time resolution with tomographic imaging, although this may be essential if we are ever to understand the processing of information by the brain. The work described in this thesis used mathematical models and *in-vivo* measurement to investigate whether applied potential tomography (APT), a recently-developed imaging technique, may be used for imaging neuronal depolarisation in the brain.

Two factors suggest that APT may be suitable: first, it can acquire data sets at the required rate; second, there is known to be a decrease in the resistance of neuronal membranes, perhaps by up to a factor of 40, when they depolarise. The practicality of APT depends on whether there is corresponding measurable change in the macroscopic impedance of brain tissue. A mathematical model was used to estimate the magnitude and frequency-dependence of brain impedance changes in two tissues: crustacean peripheral nerve and mammalian cortex. The model predicted that at 30 kHz, a typical working frequency for APT, the resistivity change would be 600 times smaller than at DC, for which the predictions were 3.7% for nerve and 0.01% for cortex. Measurements of DC resistivity change during depolarisation of crab nerve (0.2% ~ 2.5%), and afferent stimulation of rabbit cortex (0.01%), were in good agreement with the predicted resistivity changes. Finite element modeling of the head suggested that, with a cosine excitation pattern, the scalp voltage changes would be about 0.001%. Suggestions are given for improving the data collection process to make measurements of these small DC voltage changes more tractable.

Contents

List of contents

Part A: Introduction and review

Part C: experimental investigation

List of figures

List of tables

Acknowledgments

I would like to express my sincere gratitude to the following people: Dr David Holder for his enthusiastic supervision and indomitable optimism; Dr Richard Bayford, of Middlesex University, who collaborated in the design and construction of the instrument described in appendix B and verified the algebra in appendix A; Mr Yi Hanquan and Mr Graham F Crowther, for their assistance in the construction of the electronic equipment described in appendix C; Dr Anling Rao, for assistance with some of the experimental procedures described in chapter 8, and Dr Hugh Bostock, of the Institute of Neurology, for his constructive comments on chapter 7.

This work was financially supported by the Engineering and Physical Sciences Research Council and by the Royal Society.

Previous publication and presentation of the work described in this thesis

The following parts of this thesis have been presented or published previously by the author.

Chapter	Presented	Published
Chapter 2		Boone and Holder, (1996a)
Chapter 5,7	4th EEC concerted action on impedance tomograpy, Heidelberg, September 1995	Boone and Holder (1995d)
Chapter 8	Physiology Society, London, June 1993 International Union of Physiological Sciences, Glasgow, August 1993 2nd Concerted Action on Impedance Tomography, Barcelona, September 1993	Boone *et al.*, (1994)
Appendix B	3rd Concerted Action on Impedance Tomography, Ankara, September 1994	Boone and Holder, (1995c)
Appendix D	COMAC-BME conference on impedance tomography, Jordanstown, May 1994 Concerted action workshop on impedance tomograhy, Keele, May 1995	Boone and Holder, (1995a, b) Boone and Holder (1996b)

Glossary of abbreviations, symbols and terms

Abbreviations

aCSF	Artificial cerebro-spinal fluid
ADC	Analogue-to-digital converter
APT	Applied potential tomography
CBF	Cerebral blood flow
CPU	Central processor unit
CSD	Cortical spreading depression
CSF	Cerebro-spinal fluid
CM	Common-mode (voltage)
CMRR	Common-mode rejection ratio
CAT, CT	Computed (axial) tomography (X-ray)
DAC	Digital-to-analogue converter
DC	Direct current
DLL	Dynamic-link library
DSP	Digital signal processing
ECG	Electrocardiograph, electrocardiogram, electrocardiography
EEG	Electroencephalograph, electroencephalography
EIT	Electrical impedance tomography, normally used synonymously with APT (*qv*)
FET	Field-effect transistor
FEM	Finite-element method; finite-element model
FWHM	Full-width at half-maximum
HF	High frequency
HMPAO	Hexamethyl-propyleneamine-oxim
HPF	High-pass filter
LF	Low frequency
LPF	Low-pass filter
MRI	Magnetic resonance imaging, synonymous with NMR
NMR	Nuclear magnetic resonance; synonymous with MRI
PC	Personal computer
PET	Positron emission tomography
p-p	Peak-to-peak
rCBF	Regional cerebral blood flow
rOER	Regional oxygen extraction rate
RF	Radio-frequency; typically 50 kHz - 1000 MHz
RMS	Root-mean-square
S.D.	Standard deviation

SEP	Somatosensory evoked potential
SNR	Signal-to-noise ratio
SPECT	Single-photon emission computed tomography
SPICE	'Simulation program for instrumentation and circuit emulation'; a computer algorithm for simulation of electronic circuits and components

Symbols

Quantities

§	Denotes a section number in this thesis
α	The proportion which extracellular space makes of a volume of nerve tissue
$\delta\sigma$	Any small change in conductivity
$\delta\phi$	Any small change in potential
ϕ	Electrical potential field (in two or three dimensions)
$\phi(\theta)$	Electrical potential on the boundary of a circular region, at an angle θ from the horizontal axis
ϕ_n	Normalised potential field, i.e. $\delta\phi/\phi$
λ	Length constant (also known as the space constant or characteristic length) of a nerve fibre. The length constant describes the rate at which membrane voltage varies along the length of the fibre.
ρ	Resistivity field (in two or three dimensions)
ρ_e	Resistivity of extracellular fluid, in Ω.cm
ρ_i	Resistivity of axoplasm, in Ω.cm
ρ_m	Specific resistance of cell membrane, in $\Omega.cm^2$
σ_n	Normalised resistivity field, i.e. $\delta\sigma/\sigma$
σ	Conductivity field (in two or three dimensions)
A_c	The function relating boundary voltage to conductivity
$\mathbf{c}$	Vector (piecewise) representation of conductivity, σ
C_m	Specific capacitance of cell membrane, in $\mu F.cm^{-2}$
$\mathbf{c_n}$	Vector (piecewise) representation of σ_n
g	A measurement of voltage, usually on a boundary
$\mathbf{g}$	A vector of boundary voltage measurements; piecewise equivalent of $\phi(\theta)$
$\mathbf{g_n}$	A vector of normalised boundary voltage changes; piecewise equivalent of $\delta\phi/\phi$
I_i	Intracellular current, in amps
i_i	Intracellular current density, in $amps.cm^{-2}$
I_m	Membrane current, in amps
i_m	Membrane current density, in $amps.cm^{-2}$
r	Radius, in cm unless otherwise stated
S	An arbitrary body
∂S	The surface of body 'S'

$\mathbf{S}_c$	Sensitivity or 'Jacobian' matrix: a matrix of values $\partial \mathbf{A}_c / \partial \mathbf{c}$
n	Actual value of noise in a measurement
n'	An estimate of n from measurements of $\mathbf{g}$
s	The systematic error in a measurement of $\mathbf{g}$
V_e	The voltage in the extracellular space near a cell membrane, expressed with reference to a 'distant' electrode
V_i	The voltage in the intracellular space, expressed with reference to a 'distant' electrode
V_m	Cell membrane potential: the voltage across a cell membrane. By convention this is expressed as inside with respect to outside. The membrane potential is normally about -70 mV.
y_n	The admittivity of a neuron

Operators

x'	Unless otherwise stated, represents the Fourier transform of x
∇x	The Poisson operator ($=\mathbf{i}\partial/\partial x + \mathbf{j}\partial/\partial y + \mathbf{k}\partial/\partial z$ where **i**, **j**, and **k** are unit vectors) applied to x
E (x)	The expected value (mean) of x
ln (x)	The natural logarithm of x
Var (x)	Variance of x
SD (x)	Standard deviation of x
x|y	The impedance which would be obtained by connecting impedances x and y in parallel ($= [x^{-1}+y^{-1}]^{-1}$)

Terms

Action potential	The sudden depolarisation (*qv*) of a neuronal membrane, followed by a slower repolarisation. The action potential is accompanied by well-defined membrane impedance changes. *cf* compound action potential.
Admittance	The reciprocal of *impedance* (*qv*). The greater the admittance of a substance, the more current will flow in it for a given applied potential.
Admittivity	The reciprocal of *impedivity* (*qv*).
Algorithm	See *reconstruction algorithm*.
Axon	A 'classical' neuron has a cell body, an arbitrary number of dendrites (small processes) and a single long process, called the *axon* (*qv*). The axon transmits information from the neuron to other cells. It is now known that axons can conduct action potentials (*qv*) both toward and away from the cell. The axons of most neurons are 1-20 μm in diameter, and a few millimetres to a few metres long.
Cable theory	A branch of physics which deals with the electrical properties of long cables in conductive media. Cable theory has been widely applied to modeling the electrical properties of axons (*qv*).

Common-mode rejection.	Of a differential amplifier, its ability to deal with common-mode voltages (*qv*). Common-mode rejection is defined as common-mode gain divided by differential gain.
Common-mode voltage	The component of voltage which is the same at both inputs of a differential amplifier. An 'ideal' differential amplifier would not be affected by such voltages, but in practice a small error is always produced.
Compound action potential	The voltage recorded during depolarisation of a nerve containing a large number of fibres of different sizes. The magnitude of the compound action potential depends on the strength of the stimulus which caused it, and varies with distance between the stimulating and recording electrodes.
Axoplasm	The intracellular fluid (*qv*) contained in an axon.
Cortex	The outer, gray matter, part of the brain. Cortex consists of densely-packed neurons connected by unmyelinated axons (*qv*).
Depolarisation	A change in the magnitude of the voltage across a cell membrane. If the depolarisation is to *threshold* (*qv*), an *action potential* (*qv*) results. In this event, depolarisation continues spontaneously.
Drive (current)	An expression commonly used in place of excitation (*qv*).
Evoked response	Normally, the response seen in the EEG to a stimulus to some part of the nervous system. Evoked EEG responses are normally sufficiently small (microvolts) that the stimulus must be repeated and the responses averaged. In chapters 7 and 8 the term will be used to describe an evoked change in resistance of nervous tissue.
Excitation (current)	The current applied to an object to enable its impedance to be determined.
Fibre (nerve)	The smallest unit into which a sample of nerve tissue can be divided. A fibre is a single nerve cell axon, possibly associated with a myelin (*qv*) sheath. See also *fibril* (*qv*).
Fibril (nerve)	A bundle of nerve *fibres* (*qv*) bound with connective tissue. A peripheral nerve consists of a number of such fibrils. The fibrils themselves are often loosely bound in invertebrates.
Gastric	Related to the stomach
Glia	Cells in the nervous system which are not neurons. There are various types of glia with different roles. Schwann cells and oligodendrocytes secrete myelin (*qv*). Astrocytes are associated with the immune system. So far as is known, all glia have a membrane resistance about one hundred times smaller than neurons, so they are often ignored in modeling studies.
Focal epilepsy	Epilepsy which arises from a well-defined region of brain tissue
Image reconstruction	see *reconstruction.*
Impedance	A property a substance has which results in its (i) restricting the flow of electrical current, and (ii) altering the phase between voltage and current in the steady state. Impedance is the reciprocal of *admittance* (*qv*). The term 'impedance' is used

	almost as a synonym for *resistance* (*qv*) or *resistivity* (*qv*) in applied potential tomography.
Impedivity	Specific *impedance* (*qv*), *i.e.* the impedance which a homogenous unit cube of material would have.
Interstitium	The extracellular space, *i.e.* the part of tissue not contained within cells.
Intracellular fluid	The material inside all cells, consisting principally of ionic solutes in an organic matrix.
Invertebrate	Not possessing a spine.
Myelin	A fatty, insulating material which surrounds certain axons (*qv*) and increases the speed at which an action potential (*qv*) is conducted. Mammalian peripheral nerve fibres and cortical white matter is myelinated, when the axon diameters are greater than about 2 μm. Myelination is unusual in invertebrates, whatever the size of the axon.
Node (of Ranvier)	The small regions of a *myelinated* (*qv*) *axon* (*qv*) where the myelin is depleted and current can cross the membrane.
Noise	Any random feature appearing in a measurement or image
Phantom	A regular and stable object used to test the performance of an imaging system. In APT research, saline-filled tanks are typically used as phantoms.
Polarisation (electrode)	The process by which a layer of charge builds up on a metal-electrolyte interface. This gives rise to a measurable voltage.
R-wave	That part of the electrocardiogram which corresponds to the depolarisation (*qv*) of the ventricles of the heart.
Reconstruction (image)	The process of determining the distribution of resistivity or impedivity in the body, given a set of boundary voltage measurements.
Reconstruction algorithm	In applied potential tomography, this term is often used for any process used to carry out image *reconstruction* (*qv*).
Reciprocity	The theorem which dictates that a voltage measurement at point 'A' due to a current applied to point 'B' is identical to the voltage measurement at 'B' due to the same current applied to 'A'.
Resistance	The tendency for a material to restrict the flow of electric current when a voltage is applied across it.
Resistivity	Specific *resistance* (*qv*), *i.e.* the resistance which a homogenous unit cube of a material would have.
Resolution	The ability to discriminate between features which are close together in time (temporal resolution) or position (spatial resolution). Good resolution is a desirable quality in an imaging system, but often has to a traded off against *noise* (*qv*).
Sheffield Mark 1	An APT system described by Brown and Seagar (1987), now available commercially.
Supine	Lying face-upwards

Threshold (stimulation)	The size of stimulus which must be applied to a nerve to cause a propagating *action potential* (*qv*), or to the brain to cause an *evoked response* (qv).
Vertebrate	Possessing a spine.

Part A: introduction and review

1. Introduction

"Thus there are profound intellectual and technical difficulties with all the methods of investigating the brain currently in use. It is as if we tried to find out how our pocket calculator works by sticking pins in it and measuring the voltages on them, by passing large currents through it, or by noting its reaction to having bits knocked off with a hammer. It is really astonishing that we know anything about the brain at all"

-RHS Carpenter, on neurophysiology (Carpenter, 1992)

1.1 Imaging brain function

1.1.1 The problem

There are already excellent techniques for imaging the structure and anatomy of the human brain, and for imaging changes in its functional state over seconds. Furthermore, the function of the individual neuron has been well studied. We now have a reasonable understanding, for example, of how the neuronal membrane behaves, how information crosses synapses and how neuronal signals are 'integrated' on the projections of the cell. With modern techniques, studying the neuron is comparatively straightforward and rewarding. For example, a cell can be probed with microelectrodes, stained to delineate its anatomical pathways and stimulated with electricity or chemicals. There is, at present, no technique which combines the sub-millisecond time resolution available to single-cell neuronal recording, with tomographic imaging, although this may be essential if we are ever to understand the processing of information by the brain. Carpenter (1992) likened an attempt to understand the brain by reference only to the single cell to understanding the whole human race by studying a single human being. The number of neurons in the brain is certainly of the same order as the number of human beings on Earth. While detailed knowledge of the individual neuron is undoubtedly essential, something else is needed: an understanding of the means by which neurons interact. To obtain this understanding, we require a neurophysiological imaging technique that shows the state of activity of the whole brain at sub-millisecond time intervals. In other words, we need a system for imaging neuronal depolarisation. Clearly, we cannot hope to assimilate all the information from the $\sim 10^{11}$ neurons which comprise the brain, even if an instrument with sufficient sensitivity and resolution could be constructed. We assume therefore that the aggregate properties of groups of neurons will provide the information we need.

1.1.2 Existing techniques for functional imaging of the brain

At least five techniques are already in use for functional imaging of the brain: tracer-enhanced computerised X-ray tomography, single photon emission computerised tomography, positron emission tomography, functional magnetic resonance imaging and inverse EEG (electroencephalograph) modeling. The last of these is not yet an imaging technique in the same sense as the others, since it is normally used to determine the properties of discrete electrical sources in the brain.

Tracer-enhanced computed X-ray tomography. The imaging apparatus measures the absorption of an X-ray beam by the tissues of the patient's head, as in anatomical X-ray computed tomography (CT). Stable xenon modifies the X-ray absorption characteristics of the tissues in which it accumulates, and enables imaging of regional cerebral blood flow (rCBF) (Winkler *et al.*, 1977; Drayer *et al.*, 1972). Clinical applications include the investigation of cerebral trauma and acute stroke (see Johnson *et al.*, 1991 for review). This technique has the disadvantage of a low temporal resolution (minutes). Furthermore, to achieve adequate contrast the patient must inhale a large proportion of xenon (35%). This has an anaesthetic effect, and causes vasodilatation in the brain. However, the high spatial resolution allows measurement of blood flow in a well-defined small area of the brain, for example the thalamus.

Single photon emission computerised tomography (SPECT). This technique is based on the measurement of gamma (photon) emission from a radioisotope such as xenon-133. The subject inhales, or is injected with, a small amount of the radioisotope. The distribution of the radioisotope tracer in a given tissue volume depends on some physiological factor, for example the state of perfusion. The first practical description for a SPECT apparatus for regional cerebral blood flow (rCBF) was by Lassen *et al.*, (1978). More modern tracers include technetium-labelled hexamethyl-propyleneamine-oxim (HMPAO) (See Anderson, 1989 for review). This has a prolonged retention in the brain and a more stable relationship to rCBF (Ell *et al.*, 1985). The retention time influences the spatial resolution. For example, with xenon-133 the gamma detector circles the head approximately once every ten seconds for about 15 minutes; the spatial resolution is 1-2 cm. For HMPAO, the longer retention time allows a slower scan rate, giving a higher spatial resolution of about 1 cm. At best, the temporal resolution of SPECT techniques is about a second; even this can only be achieved at the expense of a reduced spatial resolution.

Positron emission tomography (PET). A PET apparatus detects the annihilation products of a positron and an electron (Ter-Pogossian, 1977). Positrons are administered to the patient as positron-emitting isotopes of biologically active substances, *e.g.*, oxygen-15. Positrons travel 2-3 mm in the tissue, then annihilate with electrons to form pairs of photons which are emitted at almost exactly 180° to each other. The electrons are detected by paired sensors; the resolution of the technique is therefore approximately constant across the imaging field, unlike SPECT and CT, where resolution depends on the distance from the detector. Depending on the type of tracer used, PET can produce images of various physiological parameters, for example rCBF (using carbon dioxide labelled with oxygen-15) and regional oxygen extraction rate (with molecular oxygen-15). Resolution of PET with the best equipment is about 6 mm; the theoretical limit of resolution is determined by the average distance travelled by a positron before annihilation: 2-3 mm.

Functional Magnetic Resonance Imaging (Functional MRI). MRI is based on the behaviour of hydrogen nuclei (protons) when the body is surrounded by an intense magnetic field. To record from a particular small region of the tissue, its protons are set into resonance with an electromagnetic pulse whose frequency is appropriate to the magnetic field strength in that region of tissue. *Gradient coils* produce a variation in magnetic field strength across the body; this allows a particular tissue region to be selected. The resonance decays at a rate dependent on the physical properties of the tissue constituents,

producing a radio-frequency signal. MRI has very good resolution (millimetres) and requires about one minute to record an image with modern equipment. MRI can form images of flow, diffusion and perfusion (Petersen, 1987). In addition, it is becoming possible to study metabolic activity, since haemoglobin, for example, has different magnetic properties in its oxygenated and deoxygenated states.

Inverse EEG Modelling. Electroencephalography has been used for studying certain aspects of brain function for many years. Electrodes on the scalp record the potentials resulting from electrical activity in the brain. The idea that images of instantaneous activity in the brain may be derived from such recordings is attractive, but such a process is unrealisable for mathematical reasons (Van Oosterom, 1991). It is possible, however, to obtain information about a limited number of electrical sources in the brain. If we assume that brain function can be adequately represented by a number of dominant regions, then this may be viable. At present there is no firm evidence that such an assumption is justified.

1.1.3 Are existing techniques adequate for imaging neuronal depolarisation?

PET, SPECT, functional CT and, to a lesser extent, MRI produce images of regional metabolic activity, with time resolutions of seconds to minutes. Neuronal depolarisation simply does not bring about a measurable metabolic change sufficiently quickly for any of these techniques to be practicable. For this application the choice seems to be between APT and inverse EEG modeling; no other applications have even been proposed. This comparison is discussed in §1.4.

1.2 Applied potential tomography

1.2.1 Physical principle

Applied potential tomography (APT) produces images of the distribution of impedivity (or, more commonly, resistivity), or its variation with time or frequency, within the tissue[1]. There is a large resistivity contrast (up to about 200:1) between a wide range of tissue types in the body (Geddes and Baker, 1967). It ought therefore to be possible to use resitivity to form anatomical images.

---

[1]A note on terminology: *Impedance* and *Impedivity* are properties of a material that result in its (i) restricting the flow of electrical current for a given voltage, and (ii) altering the phase angle between voltage and current in the steady state. 'Impedivity' is the 'specific' form of 'impedance', *i.e.*, the impedance which a unit cube of the material would exhibit. The effect on phase makes impedivity a different parameter from *resistivity*, which simply describes the ratio of the in-phase components of voltage and current. The impedance of a metal is constant over a wide range of frequencies. Biological materials, however, being for the most part poor conductors of electricity and having thin membranes, exhibit appreciable capacitance as well as resistance. Thus they need to be considered in terms of impedivity rather than resitivity. In practice however, it is easier to measure resistivity, since the capacitance of the measuring circuit can be eliminated. Most APT research has therefore concentrated on measuring resistivity, and the terms 'resistance', 'resistivity', 'impedance' and 'impedivity' are used almost interchangeably in this field

In recent years, APT has become more commonly known as *electrical impedance tomography* (EIT). The older term is retained in this thesis since it describes a technique for direct current excitation. In this case, impedance cannot be measured, and 'impedance tomography' is an inappropriate term.

Furthermore, there is often a significant contrast between normal and pathological tissue. For example, Grant (1923) found that, at 1 kHz, cerebral gliomas had a resistivity about half that of normal tissue.

To measure resistivity or impedivity, a current must flow in the tissue and the resulting voltages be measured[2]. This applied current will be referred to as the *excitation* current. In practice almost all APT systems use constant current sources, and measure voltage differences between adjacent pairs of electrodes. To obtain an image with good spatial resolution, a number of such measurements is required. This can be achieved by applying different current distributions to the body, and repeating the voltage measurements.

From the set of measurements, an *image reconstruction* technique generates the tomographic image. Mathematically, the 'known' quantities are the voltages and currents at certain points on the body; the 'unknown' is the impedivity or resistivity within the body. At low frequencies, these quantities are related by Poisson's equation:

$$\nabla.\sigma\nabla\phi = 0$$

where σ is the conductivity (admittivity may be represented by a complex σ), ϕ is the potential and ∇ is the Poisson operator. σ and ϕ are spatial fields whose magnitudes are functions of position. ϕ is also a non-linear function of σ. Chapter 3 provides a more detailed description of the various image reconstruction techniques which have been employed. In practice, the solution of Poisson's equation is very sensitive to noise in the measurements, and normalisation techniques must be used. Most *in-vivo* images have been produced using linearised, approximating techniques. These attempt to find a solution for a small change in resistivity from a known starting value. Until recently, the change in resistivity was measured over time, and APT images were inherently of physiological function. It is now possible to produce anatomical images using the same reconstruction technique, by imaging changes with frequency.

1.2.2 A practical APT system: the 'Sheffield Mark 1'

A number of practical data acquisition schemes have been reported (see chapter 2). For illustration this section describes the 'Sheffield Mark 1' system (Brown and Seagar, 1987), whose operation is relatively straightforward. It requires that 16 electrodes be distributed evenly in the same plane around the body. The APT system applies a constant current of 1-5 mA at 50 kHz to an adjacent pair of electrodes. Voltages are measured between the other adjacent pairs (figure 1.1). It then switches the current to another pair of electrodes, and measures a second set of voltages. It is unusual to make voltage measurements from electrodes that are carrying current, since the voltage drop across the electrode-skin resistance is unknown. The 'Mark 1' system can therefore make 13*16 = 208 measurements, of which half are independent (the other half being related to the first by reciprocity).

---

[2]Theoretically there is no difference between applying a known voltage and measuring the resulting current, and applying a known current and measuring voltage. In practice, the former technique is very rarely used, owing to the difficulty of compensating for skin impedance.

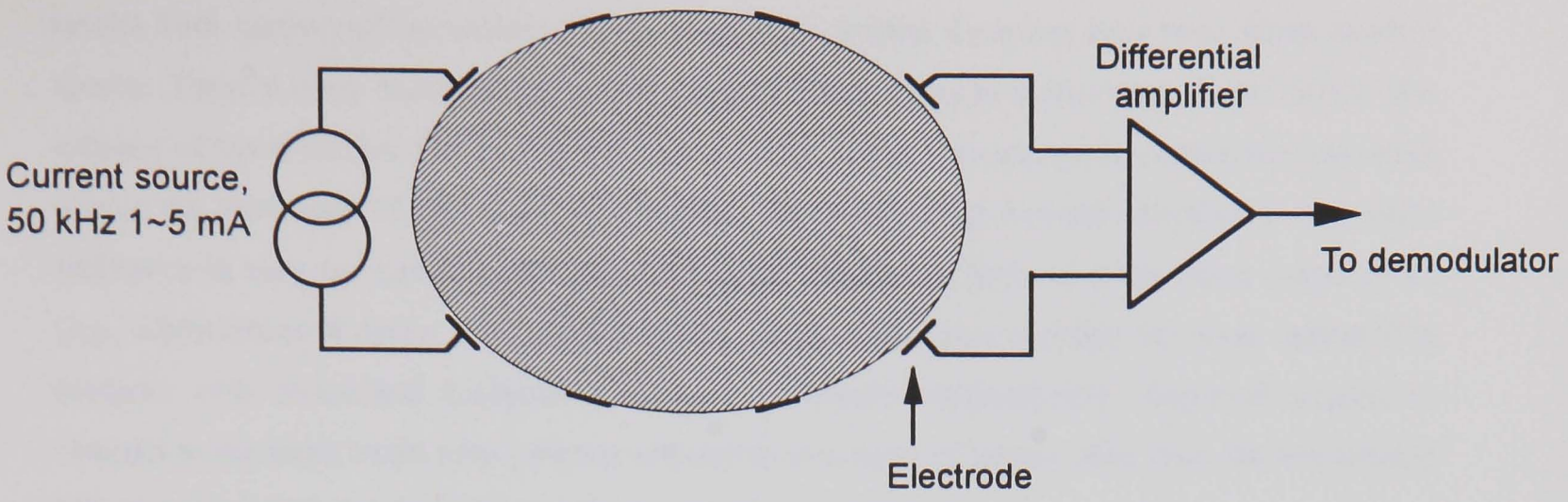

Figure 1.1: a diagrammatic representation of the 'Sheffield Mark 1' data acquisition system

1.3 Could APT be used to study brain function?

1.3.1 Resistivity changes in the brain

It is well known that certain neurophysiological events are associated with resistivity changes in the brain (see Holder, 1993 for review), and if they are measurable from outside the head imaging should be possible. These resistivity changes can be loosely categorised by the physiological mechanism by which they are produced, and will, for brevity, be referred to below as 'large', 'medium' and 'small'.

i. 'Large' resistivity increases occur during anoxia or injury. These last from a few seconds to minutes or hours. Hoffman *et al.*, (1973) measured intracortical resistivity increases of up to 100% during cortical spreading depression (see chapter 3) in animal brains. Focal epilepsy and stroke also produce resistivity increases by anoxia, of about 3% and 20-100% respectively (Holder *et al.*, 1993). The resistivity change may be due to *cell swelling*. Hansen and Olsen (1980) proposed that the metabolic demands placed on neurons is such that their ability to maintain a normal ionic concentration gradient is disrupted. Water can enter the cell, reducing the size of the extracellular space. This theory will be discussed further in chapter 5.

ii. 'Medium' resistivity changes result from redistribution of blood flow during normal brain activity. Increased activity in a cerebral region causes an increase in perfusion; the effect may persist from a few seconds to a few minutes. Blood is about ten times more conductive than brain tissue, and about 10% of current flow might be expected to be intravascular (Van Harreveld *et al.*, 1961; Ranck, 1963). Porter *et al.*, (1964) found resistance changes of about 1.5% during bilateral carotid compression in humans; Adey *et al.*, (1962) found changes of 2% in the cat limbic system due to physiological stimuli.

iii. 'Small' resistivity changes result directly from neuronal action potential activity. This is the phenomenon that underlies all cerebral function. It allows communication between neurons and leads ultimately to cognitive processes and consciousness. The development of a technique that can directly image neuronal depolarisation would be of immense benefit to neuroscience research. At present no equipment has sufficient temporal resolution or sensitivity for this purpose. Nearly sixty years ago, Cole and Curtis (1939) found that a forty-fold decrease in membrane resistance accompanied depolarisation in the unmyelinated giant axon of a squid. This resistance decrease

results from opening of ion channels in the membrane. Similar decreases have been found in other species. There is every reason to expect that a similar effect occurs in human grey matter, which also consists of unmyelinated fibres. It is not clear to what extent this change in membrane resistance affects the resistance of the tissue as a whole. The relationship between membrane and tissue resistance in complex tissues is not well understood. Studies on isolated nerve tissue preparations (*e.g.*, Chailakhian & Iur'ev, 1957; Holder 1989), which might have clarified the issue, appeared to disagree with theoretical predictions, or were technically unsatisfactory. Reported impedance changes in the intact brain were probably affected by a number of factors other than the relationship between membrane depolarisation and resistance change, including:

- the type of stimulation,
- the distribution of electrical current in the measured tissue volume,
- the position of the measured volume within the brain, and
- the measuring frequency.

As a result, the reported figures varied widely: from 0.005% (Klivington and Galambos, 1968) to over 3% (Freygang and Landau, 1955). The two studies cited were both performed on cat cerebral cortex, but the former used a physiological (auditory) stimulus, while the latter used electrical stimulation. The nature of these studies makes it extremely difficult to predict the optimal strategy for imaging neuronal depolarisation.

Physiological events which produce the 'large' and 'medium' sized resistivity changes are mostly amenable to imaging using the techniques described in §1.1.2. APT might have the potential to supplement or replace these techniques, since it uses equipment that is more portable, safer and cheaper by a factor of about one thousand. Moreover, for practical reasons, some neurological applications might be better served by APT than other methods (see §1.5). The work described in this thesis addresses secondarily some of the issues relevant to clinical use of APT, but is primarily concerned with the 'small' resistivity changes which result from neuronal depolarisation.

1.3.2 The problem of the skull

For surgical patients we can consider making APT recordings with *subdural* electrodes, *i.e.*, electrodes inserted into the subdural space by way of a craniotomy. For normal volunteers, only scalp electrodes would be permissible. The skull has a resistivity about thirty times higher than the surrounding tissues. This presents three particular problems.

i. The current density in the brain will be reduced with respect to that in the scalp, so the voltage changes to be measured will be smaller than would be the case with subdural electrodes.
ii. Most image reconstruction techniques are based on the assumption that small resistivity changes occur against a uniform-resistivity background.

Resistance changes are found in the scalp and skull, as well as the brain. During cortical spreading depression in the anaesthetised rat, Holder (1991) found a mean decrease in scalp resistance of 0.8%. This probably resulted from changes in scalp blood flow and temperature; by stabilising the temperature of the scalp it could largely be abolished. In similar experimental conditions, Shevelev *et al.*, (1986) measured temperature increases of up to 1 °C in the exposed skull. Assuming the same thermal

coefficient as for blood (0.4 %/°C), this implies that the skull resistance increased by 0.4%. Although these changes are small, they occur close to the electrodes, where sensitivity is highest.

The modelling study described in chapter 6 suggested that the effect of the skull on sensitivity is not as great as we might expect; nevertheless, the effect on image reconstruction remains to be investigated.

1.3.3 The problem of anisotropy

Nervous tissue is inherently anisotropic. At frequencies approaching DC, Choh-Luh *et al.,* (1967) found that white matter was about 11 times more resistive in the transverse direction than the longitudinal. This anisotropy diminishes with increasing frequency, but an increasing frequency will be accompanied by a reduction in the magnitude of the resistivity change to be measured (see chapter 4; Cole, 1968). Anisotropy places a theoretical limitation on the ability to reconstruct APT images. Kohn and Vogelius (1984) reported sets of anisotropic resistivity distributions that produced identical boundary voltages. This implies that such distributions could not be distinguished from one another by boundary measurements, and therefore that it is impossible *in the general case* to reconstruct an image of an anisotropic resistivity distribution. This is a theoretical limitation, which could not be overcome by *any* reconstruction technique, however sophisticated. It is not yet clear, however, whether resistivity distributions which might occur *in practice* may be reconstructed.

1.4 APT or EEG?

Both APT and inverse EEG modeling merit investigation for sub-millisecond brain imaging. EEG has one obvious advantage over APT: there is no doubt that it can detect normal (*i.e.*, non-pathological) brain activity. For APT, the model described in chapter 6 predicts that the boundary voltage changes during normal brain activity will be very difficult to measure accurately. However, APT has two advantages over EEG that make it the more likely to provide satisfactory brain images.

i. At any instant in time, a full set of EEG measurements contains N-1 independent voltage values, where N is the number of electrodes applied. Since it can apply multiple current patterns, APT can obtain N^2 measurements, of which, in principle, N(N-1)/2 are independent (Barber, 1993). The difference between APT and EEG becomes more significant with an increasing number of electrodes (figure 1.2). Although practical reasons may prevent us measuring all the available independent values, APT will always have a significant advantage in this respect. The number of independent measurements determines the number of independent points that may be obtained for the image.

ii. A voltage source in the brain will produce a signal at the scalp that varies with depth approximately according to the inverse-square law. In practice the voltages from a central source and a superficial one may vary by more than a factor of one hundred. The equivalent variation for APT is about a factor of ten (see chapter 5). An APT system therefore needs a much smaller dynamic range than an equivalent EEG system.

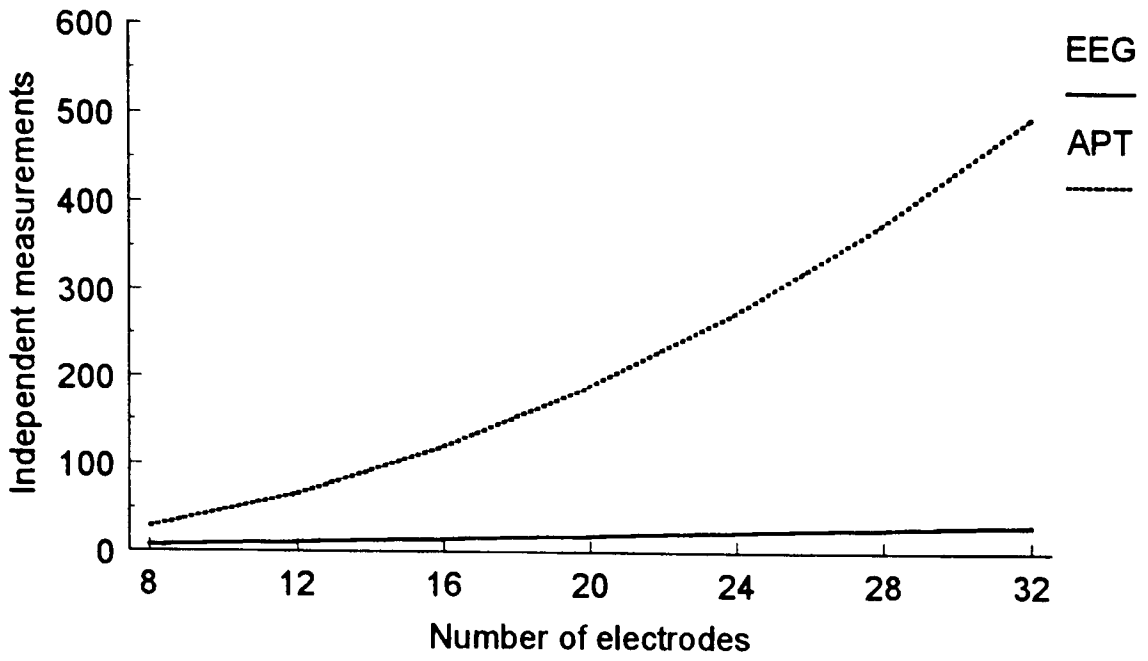

Figure 1.2: the number of independent measurements as a function of number of electrodes

1.5 Possible neurological applications of APT

The use of APT has been investigated for a number of clinical problems (see chapter 4), but proposed applications in neurology are limited. Stroke, cerebral trauma and intraventricular haemorrhage may result in resistivity changes that are large enough for APT imaging. Other imaging techniques also be allow investigation of these conditions, although the size and portability of APT equipment make continuous monitoring more practicable. One application that is not well served by existing technology is that of focal epilepsy.

Epileptic seizures result from intense uncontrolled neuronal discharge, and are normally categorised into *partial* and *generalised* types. A partial seizure is associated with pathology in a localised region of the brain; in a generalised seizure no such pathology can be found. A further classification is into *complex* seizures, where consciousness is disturbed, and *simple* ones where it is preserved. Epileptic disorders cause unpleasant and dangerous symptoms, and patients have a reduced life expectancy for a variety of reasons (Penning *et al.*, 1969). While drug therapy will provide symptomatic relief in many patients, about 20%, particularly those with complex partial seizures, continue to have seizures (Rimmer and Richens, 1988). Of those patients whose symptoms do respond to drugs, some develop adverse reactions. In selected patients, therefore, the surgical removal of that part of the brain containing the epileptic focus is desirable. Of the surgical techniques used in epilepsy, temporal lobectomy is the most common and successful (Polkey, 1988).

For surgical resection to be appropriate, one must be able to locate the focus of epileptic activity with a high degree of confidence. At present this localisation relies on a variety of EEG recordings: from the scalp, in the sub-dural space, and from deep regions of the brain (Binnie, 1988). The EEG recordings are considered along with clinical and radiological findings. This approach has two disadvantages:

i. It may be impossible to detect the focus, or it may be localised incorrectly. Even the most common surgical procedures are not always successful: temporal lobectomy has a failure rate of about 20% (Polkey, 1988). There may also be multiple foci. Spencer *et al.*, (1982) found multiple and non-

localisable foci in 16 out of 32 patients. Resection of the most active of a set of multiple foci is unlikely to give good results (Binnie, 1988).

ii. Intracortical electrodes can cause haemorrhage and infection. In one study, Van Buren (1987) reported permanent neurological damage in 0.8% of patients and other serious complications in 4%. The same author reported another study in which 2 of 140 patients died as a result of surgical complications.

A system that provided accurate localisation, could detect multiple and diffuse foci, and had none of the complications introduced by intracortical electrodes, would clearly be of great clinical benefit. There is good reason to believe that it will be possible to use APT to localise focal epileptic activity in human patients. Since it does not require intracortical electrodes, APT would be safer than existing techniques. Furthermore, APT may show multiple or diffuse foci.

1.6 Overview of the work to be described

The work described in this thesis used mathematical models and *in-vivo* measurement to investigate whether APT may be used for imaging neuronal depolarisation in the brain. It would not be sufficient merely to connect an existing APT instrument to the head of a volunteer and begin recording. If 'positive' results - measurable resistance changes - were detected, it would not be clear whether they were genuine or resulted from some source of artefact. On the other hand, if the results were 'negative', it would be difficult to determine whether the impedance changes were simply too small, or whether the current excitation pattern or frequency was inadequate. Clearly, a more rigorous approach was necessary.

First, it was not obvious what excitation frequency would be optimal for impedance measurement. The capacitive nature of neuronal membranes certainly suggested that the size of the impedance change would increase with decreasing frequency, but the significance of the frequency dependence was unknown. This issue, along with that of the actual magnitude of impedance changes in the brain, was addressed using a mathematical model of nerve tissue (chapter 5). This study had two significant predictions. (i) The decrease in tissue resistivity during depolarisation should diminish very rapidly with frequency, being 600 times greater at DC than at 30 kHz. (ii) In an unmyelinated peripheral nerve, the DC resistance decrease should be large enough to measure accurately: about 3.7%. In the cortex, the predicted change was about 0.01%. It appeared that direct current excitation offered the best opportunity, perhaps the the only opportunity, for measuring the resistance changes due to neuronal depolarisation.

Secondly, given that the resistivity changes in the brain are perhaps large enough to measure, this does not necessarily imply that they would be large enough to image. The practicability of imaging depends on the size of the voltage changes measured with an APT apparatus, which depends in turn on the current excitation pattern. These factors were investigated using a finite-element model of the head (chapter 6). It investigated the effect of the skull and scalp on signal size, as well as the effect of the current excitation pattern. As expected, a 'cosine' distribution of applied current produced the largest boundary voltage changes. A somewhat more surprising finding was that the effect of the skull and scalp on boundary voltage changes was not as large as might be expected: proportional voltage changes were

smaller by about a factor of four; absolute changes by about a factor of two. For pathological conditions (~50% resistance change), the predicted boundary voltage changes were large enough to suggest that imaging would be feasible with any current distribution.

Thirdly, direct current excitation is associated with certain technical difficulties, principally related to the high electrode impedance and to the low acceptable current. These problems had to be overcome before any practical resistance measurement was possible. The development of suitable single-channel and multiple-channel instrumentation is described in appendices B and C. The single-channel instrument was developed in collaboration with Dr Richard Bayford of Middlesex University. This instrument was tested by making measurements of DC resistance change during depolarisation of isolated crustacean nerves (chapter 7). These nerves are unmyelinated, as is mammalian grey matter. These measurements were carried out with the additional collaboration of Dr David Holder. They allowed the predictions of the mathematical model to be confirmed, and significant technical and experimental problems to be detected and eliminated. Thus resistivity changes in the cortex could be measured with some confidence that the results would be valid.

Finally, measurements of resistivity change could be carried out on the cerebral cortices of anaesthetised rabbits (chapter 8). These experiments were performed in collaboration with Dr Holder and Dr Adam Lewis. The impedance change was found to be very small - about 0.01% - during neuronal depolarisation; no imaging was attempted. During the pathological phenomenon of cortical spreading depression, for which a resistance increase of about 16% was predicted, images were successfully recorded with the Sheffield Mark 1 (Brown and Seagar, 1987) system. Spreading depression is a pathological phenomenon with similar characteristics to epilepsy (Marshall, 1955). The implications for the use of APT in clinical conditions like focal epilepsy appear to be favourable. The imaging of neuronal depolarisation represents a considerable engineering challenge, although perhaps not an insurmountable one. Chapter 9 discusses some techniques for improving the data collection process in such a way as to make measurements of these small resistivity changes more practicable.

2. Analogue instrumentation design in applied potential tomography: a review

2.1 Introduction

2.1.1 The need for high-quality measurements

To obtain high-quality images using applied potential tomography (APT), the measurements on which they are based must be of high accuracy and precision. This is particularly true where we expect the resistivity changes to give rise to small signals, as is probably true for imaging the brain. The deceptive simplicity of the measurement process conceals a wealth of technical problems, particularly for multiple-frequency imaging. This chapter describes the origin of some of these technical difficulties, and reviews the design techniques which various workers have used to overcome them. It focusses primarily on the problems of current generation and voltage measurement. The generation of a known current and the measurement of the resulting voltage comprise a measurement of *transconductance*. In its most basic form, such a transconductance measurement can be carried out using only a current source and voltmeter (figure 2.1). The practical measurement situation is much more complicated, as will be described. Until recently, technical problems restricted the application of APT to changes in resistivity over time (*dynamic* imaging), rather than allowing absolute values of resistivity to be obtained (*static* imaging). Mathematical techniques used to reconstruct APT images are often highly sensitive to measurement errors (see Barber (1993) for review). Dynamic imaging tolerates some measurement errors, provided they remain approximately constant over time, but prevents APT being used to reveal details of anatomy.

A recent development is multiple-frequency imaging. Since biological materials exhibit frequency-dependent resistivities, anatomical imaging should be possible provided the measurement errors remain approximately constant with frequency. Despite its limitations, APT offers the advantages of low cost, portability and safety over other imaging techniques.

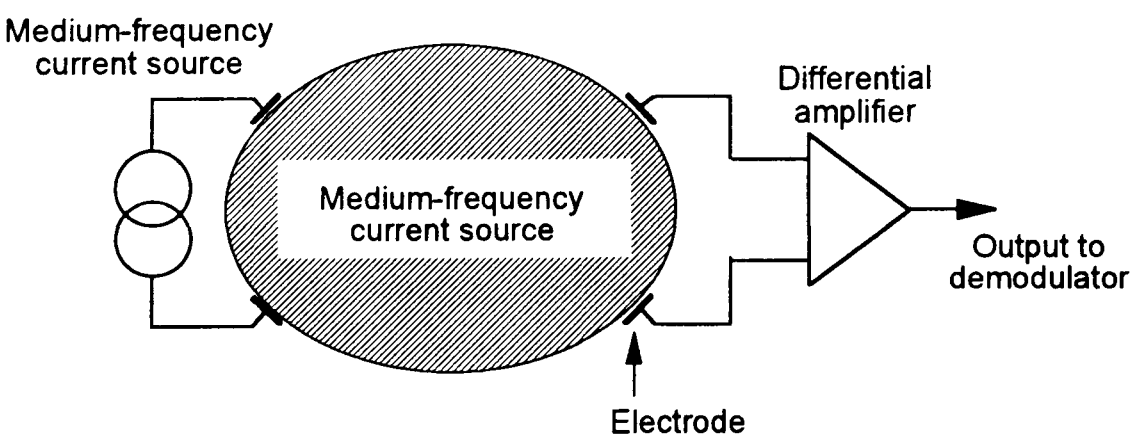

Figure 2.1: an idealised representation of a bioimpedance measurement

2.1.2 System accuracy requirements

The fact that there is no universal agreement on the accuracy required complicates the design of APT instrumentation. This is partly because system designers have had different applications in mind. I have been able to obtain useful dynamic images with the Sheffield Mark 1 (Barber and Seagar, 1987) system with absolute errors as large as 10%-20%. On the other hand, mathematical problems in the reconstruction of static images may impose a maximum error of 0.05% or even 0.02% (Denyer *et al.*, 1994). Many authors report 0.1% as being a desirable maximum error (e.g., Brown and Seagar, 1987; Record *et al.*, 1990). Record and Hargreaves (1994) referred to this figure as the 'holy grail' of APT, an appropriate name for something that is often sought and seldom achieved.

2.1.3 Purpose and scope of this review

This review describes the technical difficulties inherent in making APT measurements, and summarises the electronic techniques which various workers have used to overcome them. It is not intended as a comparison of the various complete APT systems, since there is no agreed mechanism for making such a comparison, and the design objectives of the various systems are not always equivalent. Table 2.1 provides a brief summary of the complete APT systems from which the design examples in the text were taken. This chapter focusses primarily on the problems of current generation and voltage measurement. Other important processes, such as waveform synthesis and signal demodulation, are increasingly performed digitally.

Authors	System name[1]	Electrodes	[2]Type (see §2.5)	Design frequency	[3]Current sources
Brown and Seagar, 1987	Sheffield Mark 1 system	16	SC	50 kHz	Floating
Brown *et al.*, 1990	Sheffield portable system	16	SC	50 kHz	Floating
Smith *et al.*, 1990	Sheffield Mark II system	16	SC	20 kHz	Floating
Jossinet and Trillaud, 1990	Lyon system	16 I + 16 V	PD	32.25 kHz and 250 kHz	Dual
Shi *et al.*, 1990; Rigaud *et al.*, 1990	Toulouse system	16	FD	11.5 kHz - 92 kHz	Single-ended
McLeod *at al.*, 1992	OXPACT-II	32 I +32 V	SC	9.6 kHz	Constant voltage
Riu *et al.*, 1992	Barcelona system	16	SC	8 kHz -1 MHz	Dual
[4]Wang *et al.*, 1992	Manchester system	16	SC	75 kHz - 153.6 kHz	Single-ended

Gisser *et al.*, 1991; Newell *et al.*, 1992 Cook *et al*, 1994	ACT-III	32	SC	30 kHz	Multiple single-ended
Blad, 1994	Lund system	16	SC	1 kHz -1 MHz	Floating, with current measurement
Cusick *et al.*, 1994	University College system	16	SC, miniature	50 Hz - 50 kHz	Balanced
Record, 1994	Keele system	16	FD	10 kHz - 2.74 MHz	Dual
Osypka and Gersing, 1994	Göttingen system	16	SC		Dual
Brown *et al*, 1994; Lu and Brown, 1994	Sheffield Mark III system	32 I + 32 V	SC	9.6 kHz - 1.2 MHz	Balanced
Zhu *et al.*, 1994	OXBACT-III	32I + 32 V	SC	10 kHz - 160 kHz	Multiple single-ended

Table 2.1: a summary of reported APT systems, in order of publication.

Notes:

1. The name given here is the one which is used to identify the system in the text. I have used the authors' own names for their systems wherever possible.
2. SC = self contained; PD = partially distributed (some analogue circuitry on electrode modules), FD = fully distributed (all analogue circuitry on electrode modules). See §2.5 for discussion
3. See §2.2.1 for definition of these current source configurations
4. This system was not primarily intended for medical applications

2.2 The measurement problem

2.2.1 An equivalent circuit

There are a number of factors that complicate the APT measurement process:

i. A minimum of one measurement is required for each desired image pixel. To generate a coarse, 10-pixel by 10-pixel image, we require at least one hundred independent measurements. Typically the APT instrument makes voltage measurements between from sixteen to sixty-four different electrodes, varying the distribution of the applied current between each set of measurements.

ii. The current source and differential amplifier are non-ideal, and not independent of one another.

iii. Biological electrodes have non-linear I-V characteristics and frequency-dependent resistance and capacitance (see Geddes (1972) for review). These properties are variable from one subject to another, and even between electrodes on the same subject (Boone and Holder, 1995a,b; Lu and Brown, 1994). These factors are a greater problem at lower measuring frequencies.

iv. Safety considerations limit the current that we can apply to the human body. Most workers use currents of about 1mA, at frequencies from about 10 kHz (Zhu *et al.*, 1994) to over 1 Mhz (e.g., Riu

et al., 1992). Safety standards also specify insulation resistances of megohms and leakage currents of microamps between the electrical main and the patient-connected apparatus. Apart from complicating the circuit design, this factor also limits the proximity between grounded shields and signal-carrying components.

v. The voltages to be measured may be as small as 25 μV and as large as 160 mV in the same subject (Brown *et al.*, 1994).

By taking these factors into account, we can derive a more realistic equivalent circuit (figure 2.2).

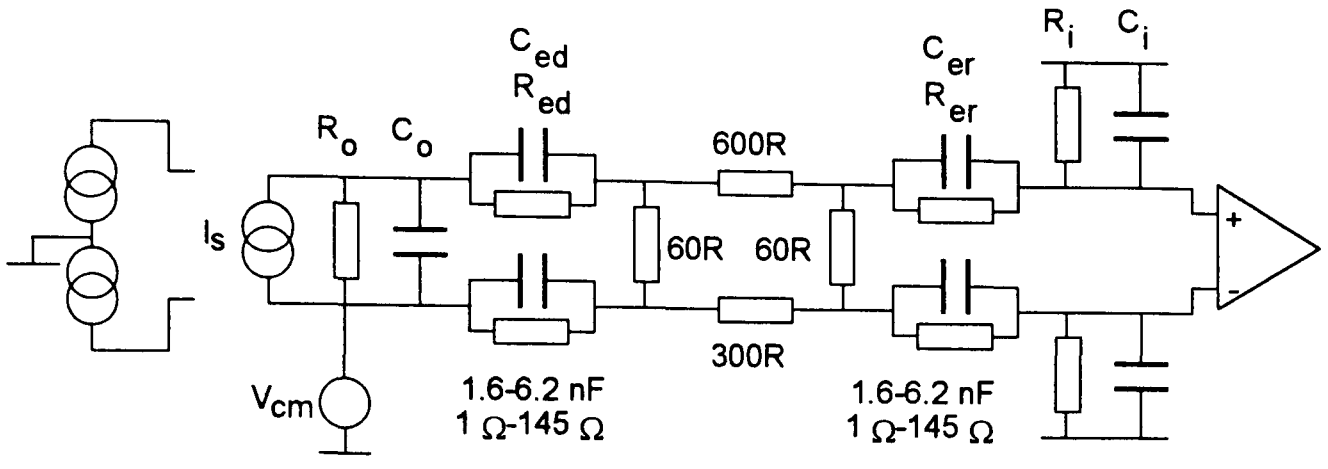

Figure 2.2: a more realistic representation of the measurement scheme of figure 2.1; see text for abbreviations. Where specific component values are given, they were estimated from measurements on a saline phantom or on human skin, as described in the text.

Current source (I_s). An APT system may use a single source (e.g., Sheffield systems), dual sources (e.g., Lyon system) or multiple sources (OXBACT and ACT3 systems). Dual and multiple sources normally have their common terminal at zero volts (as shown to the left of figure 2.2). Single sources may be *single-ended*, where one terminal is at zero volts (Rigaud *et al.*, 1990), or floating (Barber and Seagar, 1987). The current source has a measurable output resistance and capacitance, represented by R_o and C_o. The voltage V_{cm} denotes the undesirable common-mode voltage that develops from the interaction between the source and the rest of the circuit (see §2.2.2).

Electrodes. Electrodes placed on the body surface are used to inject current (R_{ed}, C_{ed}) and to measure voltage (R_{er} and C_{er}). The values in figure 2.2 were obtained by measurement on a human subject at 100 kHz (Boone and Holder, 1995a; appendix D). The lower resistance and higher capacitance correspond to extensively abraded skin; the other figures are for unprepared skin.

Amplifier. The amplifier will have measurable common-mode rejection ratio (CMRR) and input impedance (C_i, R_i).

Multiplexers. Where the system uses fewer sources or measuring circuits than electrodes, multiplexing will be necessary. The capacitance between the multiplexer channels can be modeled as a capacitance in parallel with C_i or C_o.

Leads. Except for 'distributed' designs (see §2.5), the instrument must be connected to the patient by leads. These will have resistance, inductance and core-shield and shield-shield capacitance.

Body tissue. The resistances shown were estimated from measurements at four adjacent electrodes in a saline phantom of 10 cm diameter.

2.2.2 Specific factors leading to measurement error

Voltage and current dividers. R_o and C_o will divide the current output of I_s by an amount that depends on the ratio of $R_o|C_o$ to the impedance of the electrodes $R_{ed}|C_{ed}$ ('|' denotes a parallel RC combination). The voltage divider formed by $R_{er}|C_{er}$ with $R_i|C_i$ has a similar effect. The significance of these effects is small at frequencies less than about 100 kHz: assume typical values of $R_i = R_o = 1$ MΩ, and $C_i = C_o = 10$ pF. At 10 kHz, R_o or R_i will dominate the parallel RC combination, and even if the electrode resistances were as large as 1 kΩ, the error would only be about 0.1%. At frequencies approaching 1 Mhz, The same values of C_o and C_i may have impedances of a few kilohms; in this case the errors would over 10%. A high-frequency system should therefore reduce or compensate for these capacitances.

Common-mode current and voltage. A number of factors can give rise to common-mode signals at the amplifier input:

i. If a single-ended source is used, the common-mode voltage will be at least as large as the differential voltage, and larger if the electrode-skin impedance is not negligible.

ii. An ideal floating source (powered by a separate battery, for example) will introduce no common-mode voltage. In practice the common-mode voltage will depend on the degree of capacitive coupling from source to ground and the relative impedances of the current electrodes. The common-mode voltage at the amplifier inputs may be as large as 2 Volts (Riu *et al.*, 1990).

iii. A 'balanced' dual source design eliminates this problem, but substitutes that of common-mode current injection (Rosell *et al.*, 1988). If no low-impedance current return path is provided for this current (*e.g.*, a zero-volt electrode placed on the body) the effect may be disastrous. The imbalance current will develop a voltage across the input impedance of the amplifiers, producing a very large error signal. If a 1% imbalance is present in 1 mA dual sources, and the input resistance of the amplifiers is 1 MΩ, the common-mode voltage may be as large as 5 *Volts* (10^5 times the differential voltage). In any event, the imbalance current will develop a common-mode voltage across the electrode-skin impedance.

iv. If all the above factors could be eliminated, the difference in effective path length between the current and voltage electrodes would dictate the theoretical minimum common-mode voltage. Murphy and Rolfe (1988) calculated that with 16 electrodes the common-mode voltage would be between 1.3 and 2.0 times as large as the differential signal. Therefore if all other circuit elements were ideal, the voltage amplifier would still need a CMRR of about 60 dB at the working frequency to achieve an accuracy of 0.1%.

Limited common-mode rejection. The common-mode voltage described above may exceed the differential voltage by 60-70 dB (Rigaud *et al.*, 1990; Nowicki, 1990), and will be at the measurement frequency. Mains-frequency common-mode voltages are less of a problem: filtering will eliminate them, at the expense of a reduction in acquisition rate (Murphy and Rolfe, 1988). Even in ideal conditions (e.g., zero source impedance) the intrinsic CMRR of a differential amplifier will tend to decrease with frequency due to internal stray capacitance. A standard integrated instrumentation amplifier will have a CMRR of about 60-70 dB above 50 kHz (e.g., Record and Hargreaves, 1994). In a practical design, non-idealities in other parts of the measuring circuit may prevent even this figure from being achieved. Particularly important are inequalities between the attenuation of the signal in the

inverting and non-inverting inputs to the amplifier. For example, Murphy and Rolfe (1988) showed that 50% variation in multiplexer 'on' resistance and stray capacitance limited the achievable CMRR to 58 dB at 100 kHz. Brown and Seagar (1987) found that typical lead capacitance values gave rise to an input error of 15 mV, even with bootstrapped cable screens (see §2.4.6). The SPICE model of Rosell *et al.*, (1988) produced similar results. Fortunately, a large part of the error signal will be in quadrature with the applied current (Record *et al.*, 1990). If the design is to measure only the resistive component of impedance, synchronous demodulation will eliminate most of the quadrature error. For example, Record *et al.*, (1990) found a quadrature error signal of 50 mV when the in-phase error was 0.2 mV. Riu *et al.*, (1990) showed that variation in electrode resistance produced an error that was mostly in quadrature, but variations in electrode capacitance produced an error in both in-phase and quadrature components.

2.2.3 Summary of error-producing factors

Different authors cited a variety of error-producing factors as being the most significant (table 2.2), but some authors were concerned with *dynamic* imaging applications, and some with *static* (anatomical) imaging. Some factors (e.g., unequal electrode impedance and inadequate CMRR) are related.

Authors	Reported most significant factor
Brown and Seagar 1987	Input stray capacitance, unless driven screens are used
Sakamoto *et al* 1987	Amplifier noise
Jossinet & Trillaud, 1990; Trillaud & Jossinet 1992	Mismatches between amplifiers, inadequate CMRR
Record *et al* 1990	Multiplexer capacitance
Rigaud *et al* 1990	common-mode current injection
McLeod *et al* 1990	Multiplexer capacitance
Riu *et al* 1992	common-mode current injection
Sansen *et al* 1992	Inter-channel stray capacitance
Record and Hargreaves, 1994	Unequal electrode impedance

Table 2.2: various authors' reports of most significant source of error

Appendix D describes a practical implemention of a SPICE model of figure 2.2 (see also Boone and Holder, 1995b). Analysis suggested that, regardless of the configuration of the current source, unequal impedances in the measuring electrodes produced large errors. The effect of mismatch in the current injection electrodes was less significant. An increase in the common-mode rejection of the differential

amplifier contributed to a reduction in error that was greater for a single-ended current source than was the case for balanced sources.

2.3 Current source requirements and techniques

2.3.1 Design objectives

Deciding on a general specification for current sources is difficult, since different types of imaging have different accuracy requirements. A designer should consider the following factors:

i. Current amplitude should be as large as possible without compromising safety. Reported currents are 1-5 mA rms.
ii. The specified output impedance (denoted below by Z_o) is almost always greater than 1 MW.
iii. The relationship between control voltage and output current (transconductance) should be suitably linear.
iv. The source should introduce minimal common-mode voltage into the measuring circuit (see below).
v. For multiple-frequency imaging, the design should meet the specification of the above factors over the design frequency range.

Most authors (*e.g.*, Nowicki, 1990) were concerned primarily with output impedance requirements. For static imaging, which requires a high absolute accuracy, this is certainly important. Lidgey *et al.*, (1990) concluded that their source required a Z_o of 12 MΩ to give the desired 12-bit accuracy. However, for dynamic imaging at medium frequencies, the introduction of minimal common-mode voltage is probably a more important parameter. With load impedance variation between a few ohms and 1 kΩ, to achieve 0.1% accuracy requires an output impedance of about 1 MΩ (see §2.2). However, to achieve this accuracy where the differential amplifier has a CMRR of approximately 60 dB, the common-mode voltage introduced must be at least as small as the expected differential voltage. This differential voltage may be in the order of 100 μV. Output resistance is straightforward to measure, and is usually reported; common-mode voltage depends on the overall system, and is rarely reported.

2.3.2 Single op-amp circuits

A single operational amplifier (op-amp) makes a simple and effective current source (figure 2.3a). With a good quality op-amp, such a circuit will exhibit load regulation errors of less than 0.01% at a given frequency (Nowicki, 1990). Such a circuit always introduces a common-mode voltage, since one end of the load is at a virtual ground. Transformer coupling can reduce this effect; and also partially satisfy medical safety requirements (figure 2.3b). This technique is used in the Sheffield Mark 1 system. The inter-winding capacitance of the transformer determines the common-mode voltage applied by this circuit. If the transformer provides electrical isolation to medical safety standards, the primary and secondary will be loosely coupled, and this capacitance low. This loose coupling has the disadvantage of reducing the output impedance.

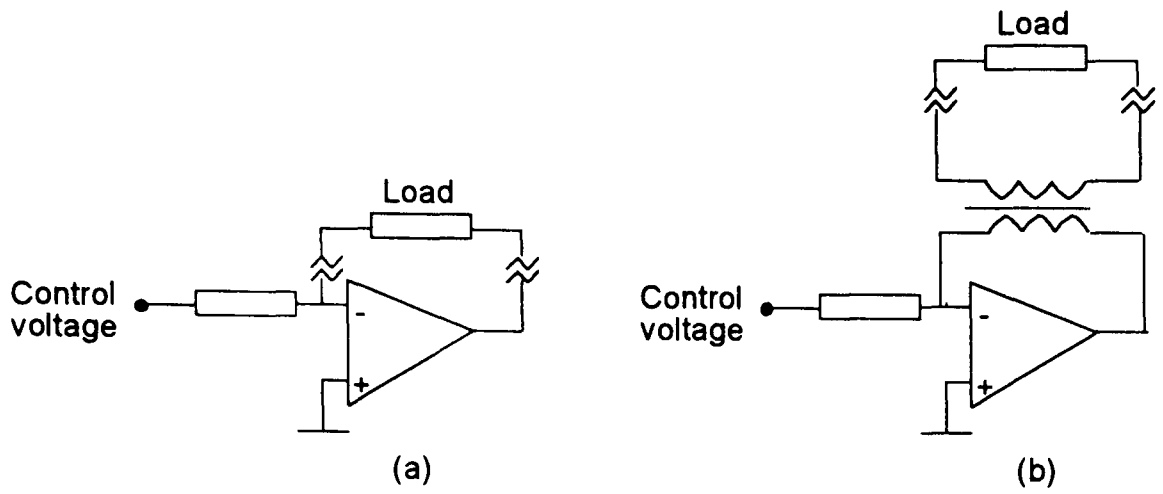

Figure 2.3: single op-amp current sources, non-isolated (a) and isolated (b).

2.3.3 Developments of the single op-amp circuit

A weakness of the circuit of figure 2.3b is its restricted frequency response. Li *et al.*, (1994) replaced the 'load' in figure 2.3a with a second, isolated, current source (figure 2.4a). They reported an output impedance greater than 8 MΩ and errors less than 0.05% over a frequency range 10-400 kHz. An alternative is to isolate the entire current source and waveform generator (fig 2.4b) from the voltage measurement circuit. Although this complicates the design considerably, it is no longer necessary to pass any variable-frequency signal across a transformer.

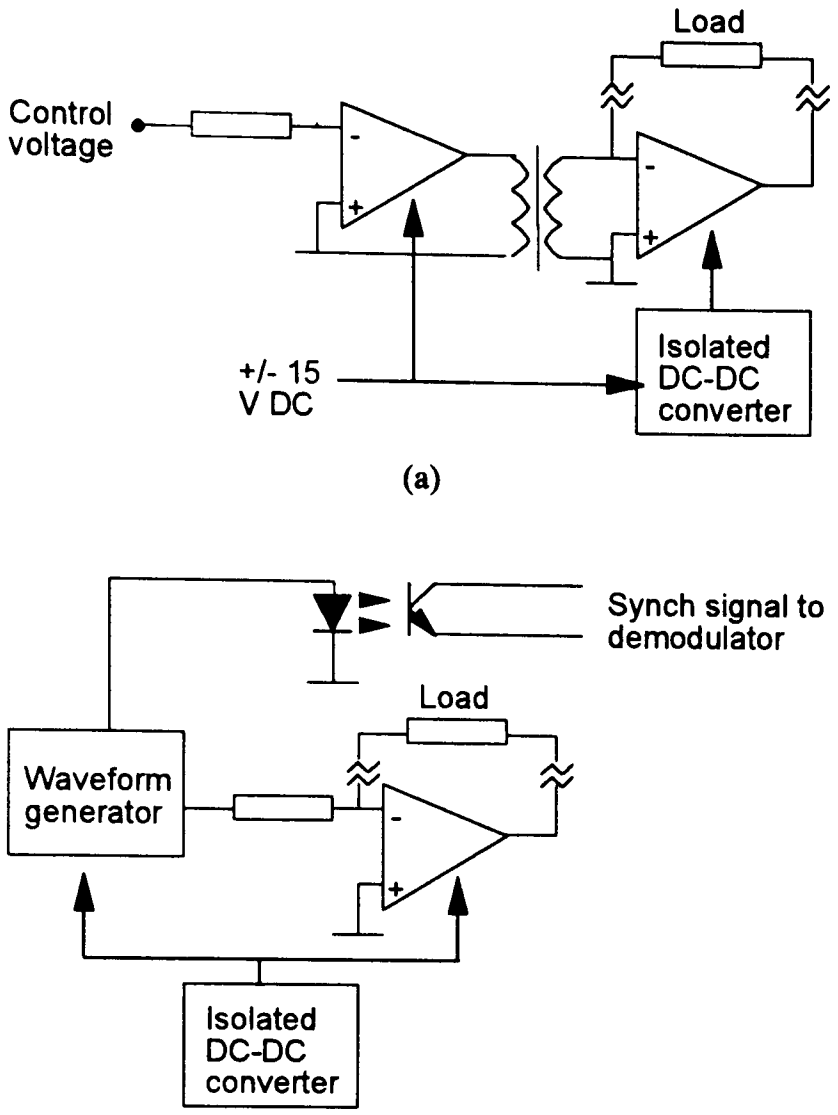

Figure 2.4: isolated developments of the single op-amp current source: (a) schematic representation of the isolated source design of Li et al., *(1994) (b) proposed source design for the 'University College' APT system*

2.3.4 Multiple op-amp circuits

The 3 op-amp design reported by Newell *et al.*, (1988) had an output impedance of about 670 kΩ and 12-bit transconductance linearity at frequencies up to 15 kHz. Wang *et al.*, (1992) reported a dual op-amp design using positive and negative feedback; its measured output impedance was 2.5 MΩ at 76.8 kHz.

2.3.5 Supply-sensing current source

This technique (figure 2.5) was first reported by Wilson (1981). m_1 and m_2 are current mirrors. The circuit relies on the fact that an ideal op-amp allows current to flow only in the supply and output terminals. Thus $I_{p2} = I_{load} + I_{m2}$ and $V/R_c + I_{p1} = I_{m1}$ where 'V' is the control voltage. If the current mirrors are ideal, $I_{p1} = I_{p2}$ and $I_{m1} = I_{m2}$. Therefore $I_{load} = V/R_c$, and is independent of the load impedance. The ability of m_1 and m_2 to mirror current exactly is the limiting factor in the performance of these circuits. A number of workers have investigated this technique in the context of APT (table 2.3).

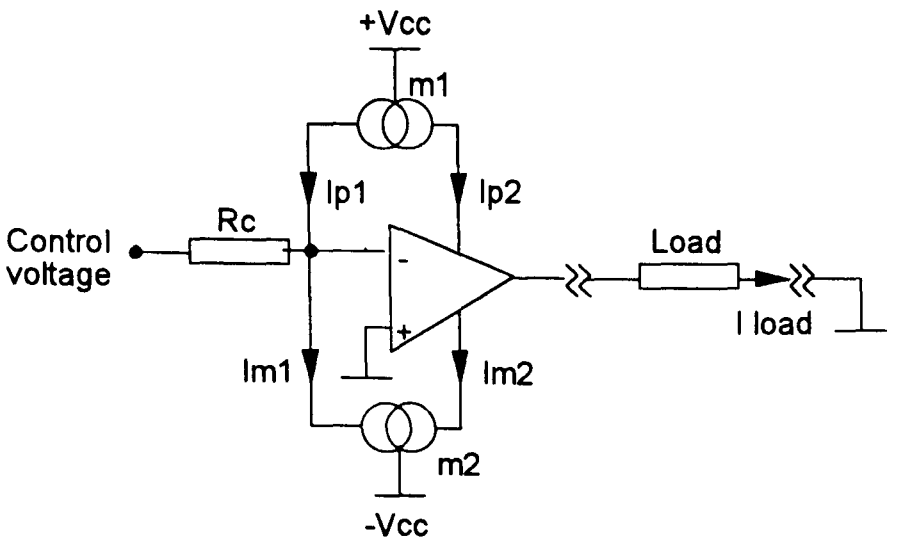

Figure 2.5: the supply-sensing current source used by Denyer et al., *(1994)*

Authors	Magnitude of Z_o	Frequency	Linearity	Notes
Record *et al.*, (1990)	Approx. 2 MΩ	100 kHz		
Leung *et al.*, (1990)	2 MΩ	10 kHz	0.05%	Simulated results
	300 kΩ	100 kHz		
Denyer *et al.*, (1994)	600 kΩ - 8 M	100 kHz		Based on OP-42 op-amp
	approx. 200 kΩ	500 kHz		
Bragós *et al.*, (1994)	1 MΩ resistive,	500 kHz	0.1%	Based on AD-844 IC
	300 kΩ reactive			

Table 2.3: Various authors' reports of the performance of a supply-sensing current source.

2.3.6 Howland circuit

Variations on the basic Howland circuit (figure 2.6) have been reported by a number of workers (table 2.4), especially to obtain balanced dual sources. A critical feature of a multiple source design is that the current imbalance is kept low.

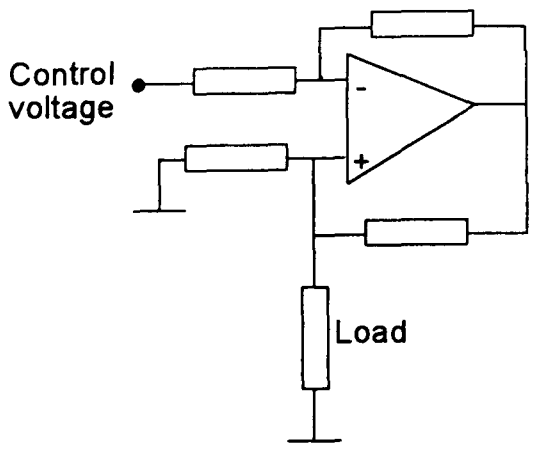

Figure 2.6: 'Howland' circuit, variations of which were used by Cusick et al., *(1994), Jossinet* et al., *(1994) and Osypka and Gersing (1994).*

Authors	Magnitude of Z_o	Configuration	Imbalance	Notes
Cusick *et al.*, (1994)		Balanced dual	Reported as 'unacceptable'	0.1% tolerance components were used
Jossinet *et al.*, (1994)	1 MΩ @ 2 MHz	"	Common-mode voltage 8% of differential	Used a resistor selection procedure; see text
Osypka and Gersing (1994)		"	Current imbalance 0.05%	
Rigaud *et al.*, (1990)	5 MΩ @ 50 kHz	Single ended	Not applicable	

Table 2.4: various authors' reports of the performance of 'Howland' derivatives

To reduce imbalance, component values must be well matched between the two sources. Cusick *et al.*, (1994) found that even 0.1% component tolerance was inadequate, and additional trimming was required. Jossinet *et al.*, (1994) overcame this problem in a pragmatic fashion sorting a large number of 0.1% resistors by measured value. The sorting procedure improved the common-mode current from 42% of differential to 8%.

2.3.7 Current measuring and correcting circuits

Most designers attempted to implement a current source whose properties are as close to the ideal as possible. An alternative is to accept the inevitable non-idealities and attempt to correct for them. Three different schemes have been reported.

i. *Application of a constant voltage, with current measuring* (Sansen *et al.*, 1992; Lidgey *et al.*, 1992). This technique should produce equivalent results to 'ideal' constant current excitation, provided measurement of current is sufficiently fast and accurate. Lidgey *et al.*, (1992) reported an overall accuracy of 0.1% (at 9.6 kHz) with such a technique. Nevertheless, these authors chose not to pursue the method in future: they concluded that the sampling of voltages was too demanding of computer time, and that the voltage could change between sampling points.

ii. *Non-ideal current sources whose outputs are adjusted according to measured current.* Blad *et al.*, (1994) analysed the effect of stray capacitances on the current measurement problem. They concluded that, while accuracy would probably be better than for a current source alone, the circuit was still sensitive to stray capacitance and an unknown electrode-skin impedance. The errors increased with frequency.

iii. *Feedback adjustment of component values so that the current source is close to ideal.* Cook *et al.*, (1994) used a 'negative capacitance' circuit in parallel with the output of the current source to increase its output impedance. A computer-controlled procedure trimmed the amount of 'negative'

capacitance and the transconductance of the current source. Immediately after trimming, output impedances were of the order of 60 MΩ. This trimming process would need to be repeated regularly: 24 hours after trimming the impedances had fallen by about 50%.

2.3.8 Discussion

It is not difficult to produce a current source whose output impedance is over 2 MΩ at 100 kHz, and whose absolute accuracy is 0.1%. For an adaptive current system whose working frequency does not exceed about 100 kHz, the supply-sensing designs (e.g., Denyer *et al.*, 1994) appear to offer the best compromise between accuracy and complexity. For a bipolar drive system, the isolated single source design of Li *et al.*, (1994) may be more appropriate. At higher frequencies it becomes increasingly difficult to obtain high output impedances. At 1 MHz, 1 MΩ output impedance implies an effective output capacitance of 0.08 pF. The negative capacitance circuit of Cook *et al.*, (1994) provides a capacitance of this order, albeit at a lower frequency, at the cost of a very complex system. To achieve good accuracy at higher frequencies almost certainly requires a current measuring circuit.

2.4 Differential voltage measurement requirements and techniques

2.4.1 Design objectives

As was the case for the current sources, it is difficult to provide a general specification for a voltage measurement circuit. The following factors need to be considered:

i. The common-mode rejection ratio (CMRR) should be sufficiently high that the amplifier attenuates the expected common-mode voltage to a level commensurate with the desired accuracy.
ii. The differential voltage at the input terminals will be between about 100 μV and 10 mV. This implies that the voltage gain should be about 100-10000.
iii. With some applied current patterns, the dynamic range of the voltages measured around the boundary may exceed 100:1.
iv. For multiple-frequency imaging, the design should meet the specification over the design frequency range.

Of these factors, the CMRR requirement is probably the hardest to meet, especially at increasing frequency (§2.2). Table 2.5 summarises various authors' estimates of the effective CMRR necessary to achieve a 0.1% measurement accuracy. These were generally based on a measurement of common-mode voltage.

Authors	CMRR to achieve 0.1% accuracy
Rigaud *et al*, 1990	120-130 dB*
Nowicki, 1990	132 dB
Rosell and Riu, 1992	135 dB
Record and Hargreaves 1994	140 dB

*Table 2.5: reported estimates of the CMRR necessary to achieve 0.1% accuracy. *calculated from the authors' CM voltage estimate.*

No medium-frequency amplifier can achieve these CMRR values alone. Normally the amplifier would be used in conjunction with a technique for reducing the common-mode voltage. The use of common-mode compensation for this purpose is discussed at the end of this section. Table 2.6 summarises some of the high-CMRR designs which have been reported. Different authors' measurements of CMRR need to be interpreted in light of the differing input configurations that will be in effect.

Authors	CMRR	Frequency	Design	See section:
Trillaud and Jossinet, 1992	95	3.6 kHz	Transformer-coupled	2.4.2
Zhu *et al.*, 1992	80	10 kHz	Current-mode	2.4.3
	73	50 kHz		
Pallás-Areny and Casas, 1994	103	10 kHz	Floating capacitor	2.4.4
Kourkoulis *et al.*, 1992a, b	67-76	10 kHz	Differential demodulator	2.4.4
Lu and Brown, 1994	80 (simulated)	77 kHz	3 op-amp with FET	2.4.5
	60 (simulated)	1 MHz	buffers	

Table 2.6: a summary of high-CMRR amplifier designs. See text for details.

2.4.2 Transformer-coupled instrumentation amplifier

The CMRR of the 'classic' 3 op-amp instrumentation amplifier circuit (Horowitz and Hill, 1989, p. 425) can be improved by replacing one op-amp by a transformer (figure 2.7). Trillaud and Jossinet (1992) obtained a CMRR of 95 dB at 3.6 kHz using this technique. The use of the transformer limits this circuit to a relatively narrow frequency band.

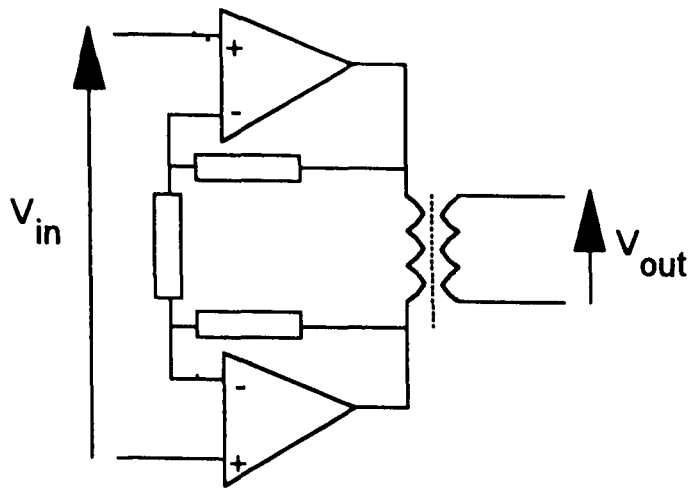

Figure 2.7: a transformer-coupled instrumentation amplifier

2.4.3 Current-mode instrumentation amplifier.

Figure 2.8 shows in outline the current-mode amplifier design of Toumazou and Lidgey (1989). The output of the circuit is proportional to the current in resistor R2. If the current mirrors m_1 and m_2 are ideal, this current is equal to the difference in the supply currents drawn by the op-amp to which m_1 and m_2 are connected. If the op-amps are also ideal, this current will equal I_o, which in turn equals $(V_1 - V_2)$ / R1. The circuit therefore operates as a differential amplifier, but inadequacies in the current mirrors limit the overall performance. Zhu *et al.*, (1992) replaced the transistor current mirrors with op-amp circuits and obtained CMRRs of about 80 dB at 10 kHz, and 73 dB at 50 kHz.

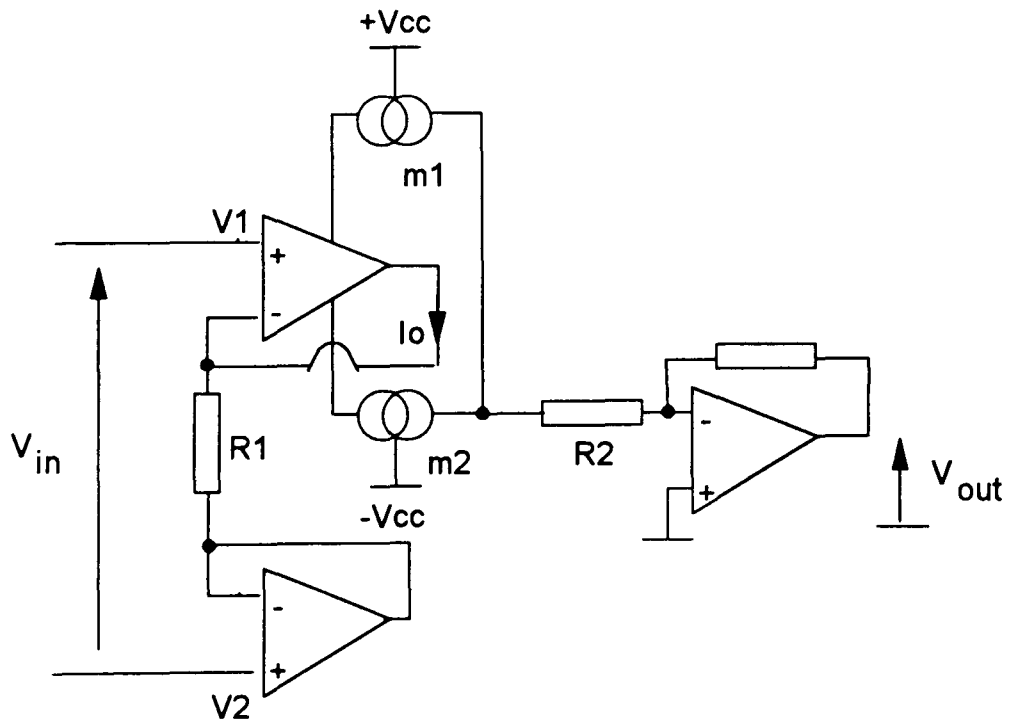

Figure 2.8: outline of the current mode amplifier of Toumazou and Lidgey (1989)

2.4.4 Differential demodulation

A standard integrated differential amplifier can achieve a CMRR above 120 dB at DC. Kourkoulis *et al.*, (1992a, b) described a design that demodulated the voltages at the electrodes *before* differential amplification, which was thus carried out at DC. A sample-and-hold circuit stored the peak voltage at each measuring electrode on a capacitor. The stored (DC) voltages were then subtracted by the

differential amplifier. Errors would be introduced if the voltage storage circuits had different characteristics. The authors therefore multiplexed a single sample-and-hold circuit between the inputs. The CMRR at 10 kHz was between 67 dB and 76 dB, varying with the size of the common mode voltage. At best, the CMRR of this circuit was slightly lower than that of Zhu *et al.*, (1992) but this design does offer the possibility of DC common-mode feedback, as will be discussed in §2.4.8. Pallás-Areny and Casas (1994) used a related technique, the 'floating capacitor' differential amplifier. By switching both terminals of a capacitor between the (buffered) electrodes and the differential amplifier, the amplifier measured a sampled, floating DC potential. Provided stray capacitances are small compared to the 'floating' capacitance, this largely eliminates common-mode voltages. This design achieved a CMRR of 103 dB at 10 kHz, with an input resistance imbalance of 1 KΩ. Both these designs will be subject to higher noise levels than an integrating demodulator, since they only use a small sample of the available signal.

2.4.5 Electrode buffers

Designers typically place buffers between the voltage electrodes and the differential amplifier to increase the input impedance. By placing dual FET buffers in the input circuit of a 3 op-amp instrumentation amplifier, Lu and Brown (1994) were able to achieve a high input impedance without the problems normally associated with input bias current. Circuit simulation showed a CMRR of 80 dB at 77 kHz, and 60 dB at 1 MHz. The authors determined the variable input resistances from skin impedance measurements on 5 volunteers. Buffers must be well matched; several authors (Rigaud *et al.*, 1990; Riu *et al.*, 1992) reported that buffer mismatch determined the overall measurement error. This is particularly important with multiple frequency systems.

2.4.6 Screening

Typical screened cable has a core-shield capacitance of about 30 pF/m. The advantages of an amplifier circuit with a high input impedance would be largely negated if it were connected to the electrodes via two metres of this cable. The input impedance of this arrangement would be about 30 kΩ at 100 kHz. The use of cable screens may, however, be necessary to limit capacitive crosstalk between channels, particularly at higher frequencies. The usual technique for limiting lead-screen capacitance is to 'bootstrap' the screens from a low impedance source. This 'driven screen' technique may reduce effective lead capacitance to about 1 pF (Sakamoto *et al.*, 1987; Brown and Seagar, 1987). While this technique is appropriate at frequencies below about 100 kHz, stray capacitances between screens may introduce problems at higher frequencies. Lu and Brown (1994) used triaxial screens, the inner screen being bootstrapped and the outer grounded. This scheme was prone to instability until its frequency response was modified to remove a gain peak at 20 MHz.

2.4.7 Effect of current excitation pattern on common-mode voltage

The boundary distribution of the applied current influences the size of the common-mode voltage with respect to the differential voltage. Record and Hargreaves (1994) found that measurement errors were 4-

10 times smaller when a pair of current electrodes were diametrically opposite, compared to the case where they were adjacent.

2.4.8 Common-mode compensation.

The principle of common-mode compensation is to 'feed back' a signal whose polarity opposes the prevailing common-mode voltage. Configurations which have been reported for APT applications are:

i. Feedback to the body via a separate electrode(figure 2.9a) (e.g., Brown and Seagar, 1987)

ii. Feedback to some point in the current source circuit (figure 2.9b) (e.g., Rosell *et al.*, 1988, Riu *et al.*, 1992).

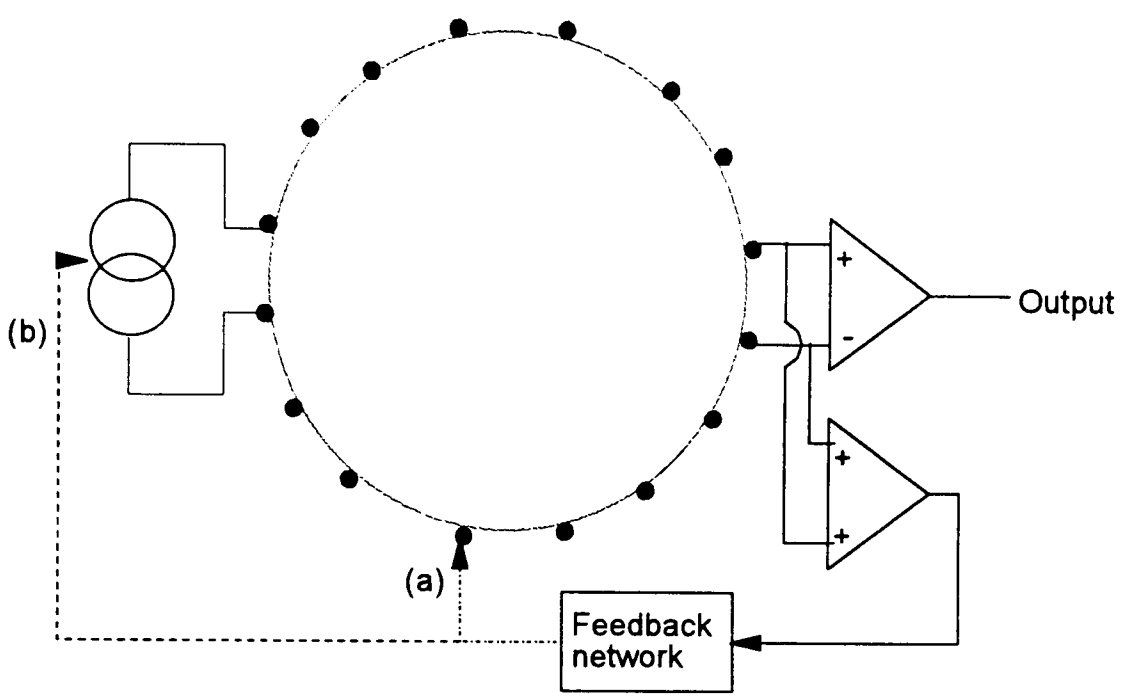

Figure 2.9: common-mode feedback: (a) to an electrode, (b) to the current source(s)

Common-mode compensation is widely used in APT (e.g., Brown and Seagar, 1987; Gisser *et al.*, 1988, 1991; Brown *et al.*, 1990; Rosell *et al.*, 1988, 1989; Riu *et al.*, 1990, 1992; Smith *et al.*, 1990). Rosell and Riu, (1992) found that common-mode feedback provided 40 dB improvement in effective CMRR. With measurements on the human torso these authors measured errors of 10-20% with common-mode compensation, compared to 65% without. Common-mode compensation is most successful for serial, rather than parallel, voltage measurements (Rosell *et al.*, 1988). In the latter case the compensation signal will at best be a compromise between the requirements of the various amplifiers. The technique has not found universal favour, even where it might be applicable, for example:

i. Murphy and Rolfe (1988) argued that common-mode compensation might principally remove error signals which are in quadrature with the applied current. Since they used synchronous demodulation to reject quadrature voltages, these authors concluded that common-mode compensation would offer little extra benefit.

ii. Several workers (e.g., Trillaud and Jossinet, 1992) found that common-mode feedback led to instability. The stability issues were analysed by Rosell and Riu (1992) who concluded that, while a stable feedback network could be set up in theory, it required that the electrode and body

capacitances be known *a priori*. Where these parameters were unknown, a feedback circuit with could be designed which was stable for most practical applications *at a given frequency*.

We might expect it to be more difficult to devise stable common-mode compensation schemes for mutiple-frequency systems. Two 'frequency independent' designs have been reported:

i. *Delayed common-mode feedback.* Record and Hargreaves (1994) used a system of time delays to stabilise their system (figure 2.10a). 15 μsec after any change in the multiplexer settings, the common-mode voltage was sampled. After a further 5 μsec this voltage was passed to a transconductance adjustment terminal in the current source circuit. This adjusted the transconductances relative to one another, so as to reduce the common-mode voltage. Since this is not a closed-loop process, it should always be stable. However, that the system must be carefully calibrated so that the correct amount of common-mode voltage generates the correct level of compensation. It is not obvious how this would be achieved if the relationship between these two factors were not linear. Although the authors reported a reduction in common-mode voltage, there was no significant improvement in reciprocity error.

ii. *DC common-mode feedback.* This scheme is appropriate for a system that uses 'differential demodulation' (see §2.4.4). Since the voltage detector in this scheme is sensitive to DC potentials, it should be feasible to feed back a compensatory DC voltage to one of the electrodes. The system of Koukourlis *et al.*, (1994) (Figure 2.10b) sums the DC potentials at the two measuring electrodes, and feeds an inverted representation to the current electrodes. No quantitative results have yet been published for the CMRR of this system. A potential problem is that it passes a continuous direct current through the electrodes, which might lead to polarisation and perhaps tissue damage. The authors do not give any quantitative information about the magnitude of this current. A more subtle problem is that it precludes DC-blocking capacitors between the instrumentation and the electrodes: A fault condition could exist where it applies the full DC supply voltage to the patient.

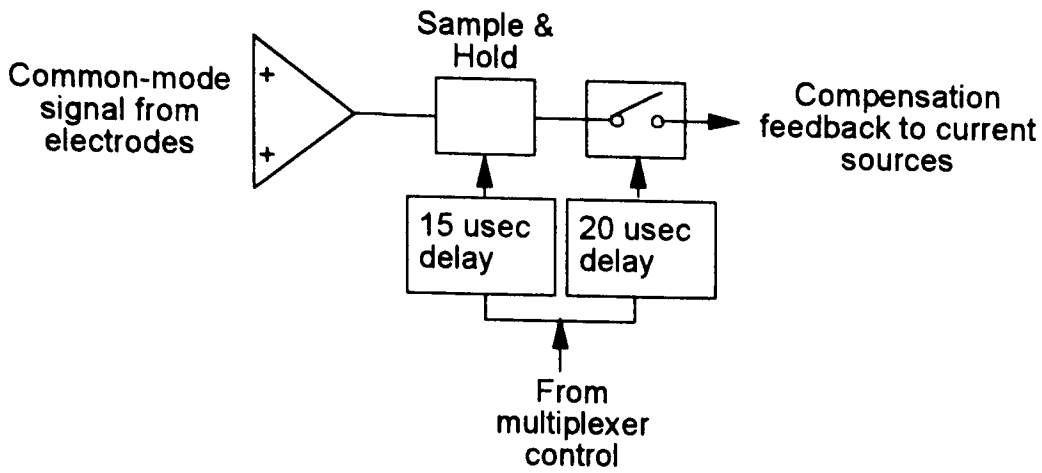

(a)

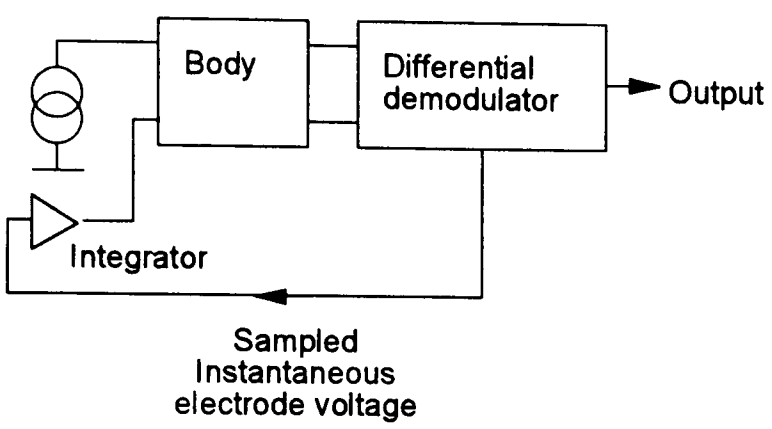

(b)

Figure 2.10: 'frequency-independent' common-mode compensation schemes: (a) delayed feedback scheme, simplified from Record and Hargreaves (1994); (b) DC feedback scheme simplified from Koukourlis et al., *(1994)*

2.4.9 Discussion

None of the amplifier designs reported, if used in isolation, have CMRR values that even approach the level which most authors think necessary to achieve 0.1% error. Of the systems for which practical (rather than simulated) measurements are available, the 'floating capacitor' system seems to offer the best CMRR, at the expense of reduced noise immunity. We therefore have to choose between accepting a reduced accuracy, compensating for common-mode voltage, or implementing a current source with an intrinsically low common-mode voltage. Single-frequency designs can use transformer-coupled sources to reduce the common-mode voltage. With multiple frequencies, considerable development is still needed to achieve comparable accuracies.

2.5 Distributed vs. self-contained systems

There is increasing interest in the use of 'distributed' APT systems, in which all or part of the electronic instrumentation is mounted on (or close to) the electrodes. In principle this should solve many of the problems discussed above, by eliminating stray capacitances. There are various levels of 'distribution,' between the fully self-contained (e.g., 'Sheffield') systems, and fully distributed systems (Rigaud *et al.*, 1990; Record *et al.*, 1994) where all the analogue electronic components are assembled on modules close to the electrodes. The size of such modules can probably be reduced to a few square centimetres. Bragós

et al., (1994) simulated the effects of distributing various parts of the APT system. Errors below 0.1% could be achieved when only the voltage buffer and screen driver were distributed, and no further advantage was obtained by further distribution. These authors did not simulate the effect of source non-idealities. I expect that with higher measurement frequencies the advantages of distributed architecture will become more apparent.

2.6 Conclusion

The measurement of bioimpedance is a complex and subtle issue; formidable technical problems have to be overcome. The fact that useful APT images have been obtained suggests that these problems are not insurmountable. The widely specified target accuracy of 0.1% can be achieved with low-frequency designs (e.g., Brown *et al.*, 1994), at least in a phantom. The current trend is towards more complex and versatile systems: multiple, higher, frequencies, and variable current patterns. While these innovations should in principle produce better images, to the best of my knowledge none of these systems have achieved 0.1% accuracy. Some of the issues that have yet to be fully resolved include:

i. The frequency response of the instrumentation must be sufficiently broad to cover the measurement range, and be well matched between measurement channels.
ii. At the time of writing, there is no obvious way to ensure stability of common-mode compensation over a wide frequency range.
iii. Stray capacitances become increasingly important at high frequencies. More experience with distributed systems is required before it is possible to say whether these might solve the problems of stray capacitance.

At the present time it seems that less sophisticated equipment (single frequency, fixed current pattern) can produce images as useful as more complex systems. These simpler systems also seem more robust with respect to *in-vivo* measurements.

3. An overview of APT image reconstruction

3.1 Introduction

In APT we normally apply a set of known current patterns to electrodes on the body surface, and measure the voltages that these currents develop. Image reconstruction is the process of generating an image from this set of voltage measurements. While tissue impedance may have a substantial reactive component, technical problems have confined almost all measurements to date to the component of voltage that is in phase with the applied current. From this information we can attempt to reconstruct an image of approximate resistivity or conductivity, but not impedivity or admittivity. Expressing the reconstruction problem in terms of conductivity, rather than resistivity, leads to a slightly more concise mathematical description. Conversion of the one to the other is, of course, straightforward. This chapter provides a brief review of some published APT reconstruction techniques.

At low frequencies, conductivity and potential are related by Poisson's equation:

$$\nabla.\sigma\nabla\phi = f \qquad [3.1]$$

where $\phi = \phi(x,y,z,\sigma)$ is the potential and $\sigma = \sigma(x,y,z)$ the conductivity. 'f' denotes the current applied to the object. Since current is only applied to the boundary, it is typical in APT image reconstruction to set $f = 0$, and state the applied current as boundary conditions for equation [3.1].

$$\nabla.\sigma\nabla\phi = 0 \text{ in } S \qquad [3.2a]$$

$$\phi = g \text{ on } \partial S \qquad [3.2b]$$

$$\mathbf{J} = \sigma\frac{\partial\phi}{\partial\mathbf{n}} \text{ on } \partial S \qquad [3.2c]$$

where

g	is the measured boundary voltage on the surface ∂S of the body S,
J	is the current density at the surface ∂S, and
n	is a unit vector, whose direction is normal to surface ∂S.

In equation 3.2a, σ is the quantity that has to be determined. σ is a function of all three spatial co-ordinates. ϕ is also unknown, except at the boundary (boundary condition 3.2b). The current density **J** is known at the positions of the electrodes, and is zero elsewhere. Because the potential ϕ is a non-linear function of the conductivity σ, the reconstruction problem is non-linear. In practice, while ϕ is a continuous function of x, y and z, it can only be measured at discrete locations on the boundary, since there are only a finite number of electrodes. These measured voltage values will be represented as a vector **g**, where $\mathbf{g} = [g_1, g_2, \ldots g_N]^T$ and N is the total number of boundary voltage measurements. ^{T} denotes a vector transpose. Each element of **g** represents a single boundary voltage. The fact that we

have discrete values of **g** suggests that we should only seek values of σ at discrete positions within the image. These discrete values of σ are the image pixels, represented by vector $\mathbf{c} = [c_1, c_2, \ldots c_N]^T$. In a very general sense, the relationship between the boundary voltage **g** and conductivity **c** can be written:

$$\mathbf{g} = \mathbf{A}_c(\mathbf{c}) \qquad [3.3]$$

where $\mathbf{A}_c$ is itself a function of **c**.

We can divide reconstruction techniques into two classes: those that attempt to determine absolute values for the conductivity ('static' imaging), and those which produce images of small conductivity change[1] ('dynamic' imaging). These two reconstruction problems can therefore be stated mathematically as follows.

The 'static' reconstruction problem: given **g**, solve equation [3.3] to find **c**

The 'dynamic' reconstruction problem: given $\delta\mathbf{g}$, approximate equation [3.3] in terms $\delta\mathbf{c}$ and $\delta\mathbf{g}$, and solve for $\delta\mathbf{c}$.

The dynamic imaging problem is by far the simpler to solve, since we can use a linearised approximation to equation [3.3]. Solution for the absolute conductivity **c** invariably requires a non-linear technique. These techniques are normally iterative; however, the linearisation of the reconstruction problem does not preclude the use of iterative methods.

To simplify the mathematical problem, it is usual to make a number of simplifications.

i. The object to be imaged is cylindrical

ii. The conductivity and potential do not change along the length of the cylinder, *i.e.*, the problem is 'two-dimensional'.

iii. The electrodes are uniformly spaced around the body

iv. The electrodes make zero-resistance contact with the body

3.2 Does a unique solution exist ?

3.2.1 A uniqueness theorem for the 'ideal' case

Given the complexity of the reconstruction problem, it is not unreasonable to ask whether it can actually be solved, even in theory, and if so, under what conditions. A precondition for this is the 'uniqueness' of the system: given a particular set of boundary voltages, can we be sure that there is one, and only one, solution to equation 3.3? This is equivalent to asking whether there is more than one resistivity that can produce the same boundary voltages. There is certainly only one distribution of tissue resistivities in the body at a given time.

Given an ideal 'two-dimensional' cylindrical body, Kohn and Vogelius (1984a,b) showed that the relationship between boundary current and voltage is uniquely determined by the conductivity, subject to certain conditions. One of these conditions is that the resistivity be isotropic. In principle, at least, we can determine the conductivity from boundary voltage measurements.

---

[1]We can attempt to find *normalised* conductivity changes, *i.e.*, $\delta\mathbf{c}/\mathbf{c}$ from $\delta\mathbf{v}/\mathbf{v}$, which reduces certain measurement errors, as described below

3.2.2 'Piecewise' uiqueness.

The argument of Kohn and Vogelius (1984) relates to measurements of $\phi(x,y)$ and **J** on the boundary. These quantities were continuous, *i.e.*, known at every point on the boundary. In practice we can only measure the voltage and current at electrodes. The question whether a similar uniqueness theorem exists for such 'piecewise' measurements is more complicated. The 'uniqueness' question becomes: is there a unique vector of conductivities **c** that can produce a given vector of voltages **v**?. We now have to consider the limited set of data; at which points within the body should we attempt to determine the conductivity? Isakov (1988) investigated this problem; it appears that a unique solution may exist only in certain conditions.

3.2.3 Anisotropy

If the resistivity distribution is anisotropic, it cannot be uniquely determined from boundary measurements, even in the ideal case. Kohn and Vogelius, 1984a,b showed that there were certain distributions of resistivity that gave identical boundary voltages. It is still not known whether practical resistivity distributions will be indistinguishable in the same way.

3.2.4 Practical issues

The theoretical existence of a solution to Poisson's equation is no guarantee that an image can be produced in practice; there are two additional problems.

i. Determination of a solution may not be computationally feasible: the best available computers may have insufficient storage, or be too slow, to be able to solve the problem in a practicable time. This is likely to become a particular problem for three-dimensional imaging, where the computational requirements can be overwhelming. This issue is discussed further in §3.4.5.

ii. The solution may be very sensitive to the level of noise and systematic error in the measured voltages. Large changes in resistivity may produce only small changes of boundary voltage, especially when they are towards the centre of the body.

3.3 Linearised methods

3.3.1 Mathematical principle

Linearised methods attempt to find a small change in conductivity given a small change in voltage. Regardless of the form of the function relating conductivity to voltage ($\mathbf{A}_c$), provided it is differentiable it may be expanded as a Taylor series:

$$\mathbf{g}(\mathbf{c}+\delta\mathbf{c}) = \mathbf{g}(\mathbf{c}) + \frac{d\mathbf{A}_c}{d\mathbf{c}}\delta\mathbf{c} + (\ldots) \qquad [3.4]$$

f higher order terms (...) are ignored, which is possible if $\delta\mathbf{c} << \mathbf{c}$, or $\mathbf{A}_c$ is approximately linear in :, [3.4] can be expressed as a single matrix operation:

$$\delta \mathbf{g} = \mathbf{S}_c \delta \mathbf{c} \qquad [3.5]$$

where $\mathbf{S}_c$ is the differential of $\mathbf{A}_c$ at $\mathbf{c}$, and is normally called the 'sensitivity' matrix:

$$\mathbf{S}_c = \frac{d\mathbf{A}_c}{d\mathbf{c}}$$

The image reconstruction process can then be expressed as taking the inverse of $\mathbf{S}_c$, *i.e.*, of finding pixel values $\delta\mathbf{c}$ from measurement $\delta\mathbf{g}$ as follows:

$$\delta \mathbf{c} = \mathbf{S}_c^{-1} \delta \mathbf{g} \qquad [3.6]$$

The elements of $\mathbf{S}_c$ may be found analytically in simple cases; a numerical technique such as the finite element method may be used for more complex geometries. In any case, there are two complications to this approach:

i. The sensitivity matrix must accurately model the physical system under study. This means that it must correctly represent, among other factors, the body geometry, electrode shape and electrode positioning.

ii. Even if the sensitivity matrix is accurate, it is likely to be ill-conditioned and difficult to invert.

A partial solution to the problem (i), used by Barber and Seagar (1987), is to express equation [3.6] in terms of 'normalised' perturbations:

$$\mathbf{c}_n = \mathbf{F}^{-1} \mathbf{g}_n \qquad [3.7]$$

where $\mathbf{c}_n$ is the normalised conductivity change

$$\mathbf{c}_n = \frac{\delta \mathbf{c}}{\mathbf{c}}$$

and $\mathbf{g}_n$ is the normalised boundary voltage change

$$\mathbf{g}_n = \frac{\delta \mathbf{g}}{\mathbf{c}}$$

In [3.7], $\mathbf{F}$ is a variant of $\mathbf{S}_c$ that has been weighted for normalised perturbations by division by a normalising matrix $\mathbf{G}$ (Barber, 1993):

$$\mathbf{F} = \mathbf{G}^{-1} \mathbf{S}_c$$

Although **F** is not necessarily easier to invert than $\mathbf{S}_c$, the value $(\delta\mathbf{g})/\mathbf{g}$ contains a reduced error contribution from inaccurate electrode placement, reducing the dependence of the solution on data collection errors.

The ill-conditioning of the sensitivity matrix has led to the application of a number of approximate inversion techniques. The success of these technique relies, in part, on the finding that, with appropriate ordering of the data in vectors $\mathbf{c}_n$ and $\mathbf{g}_n$, the sensitivity matrix is dominated by the elements on its main diagonal. An approximate inverse in this case is simply the matrix whose diagonal elements are the reciprocals of the diagonal elements in $\mathbf{S}_c$, and all other elements zero.

3.3.2 Inversion of the sensitivity matrix by singular value decomposition (SVD)

The technique of SVD for inverting ill-conditioned matrices has been widely used in other mathematical problems (Press *et al.*, 1992). Zahdehkoochak *et al.*, (1991) presented an implementation of the SVD technique for APT images. The result of their procedure was a set of independent 'basis' images, which could be weighted with the measurements and summed to produce the final image. A useful feature of this technique is that it was possible to use the relative sizes of their eigenvalues to identify the signal-to-noise ratio of each of these basis images. Basis images could be suppressed when they had no components greater than noise. They applied this technique to the sensitivity matrix for the adjacent electrode excitation geometry; it was clear that the basis images with the greatest spatial frequencies had the smallest eigenvalues. Basis images with strong central features also tended to correspond to smaller eigenvalues. This demonstrates quite clearly the compromise between spatial resolution and noise tolerance that is inherent in APT.

3.3.3 Backprojection

Backprojection is the basis for most CT image reconstruction techniques. In APT, boundary voltages are projected from the measuring electrodes back to the current electrodes. The path of the backprojection is normally taken to be an idealised isopotential line. Each pixel under the backprojection path has its value increased by an amount dependent on the corresponding boundary voltage. This procedure is repeated for each current pattern. Backprojection produces a 'blurred' image, because the concentration of backprojection lines is greater in some parts of the image than others.

The most widely used backprojection technique is that first described by Barber and Brown (1984). These authors transformed the normal curved isopotential lines into a conformal space where backprojection was along parallel lines. This process allowed the calculation of coefficients for the backprojection operator. Each image pixel then had to be 'weighted' to compensate for the non-uniform angular distribution of backprojection lines through that point. These authors now formulate the reconstruction algorithm slightly differently, expressing it as follows (Barber, 1993):

$$\mathbf{c}_n = \mathbf{B}(\mathbf{FB})^{-1}\mathbf{g}_n \qquad [3.8]$$

In this expression **B** is the backprojection operator. **F** is the normalised sensitivity matrix as in [3.7], to which this expression reduces if **B** is square. There are two slightly different ways to interpret this expression.

i. Although a straightforward backprojection, *i.e.*, $\mathbf{c}_n = \mathbf{B}\mathbf{g}_n$, gives a blurred image, there is *something* that can be backprojected to give the true image. This quantity can be obtained by 'filtering' the boundary voltages prior to backprojection. In this case the filter function is $(\mathbf{FB})^{-1}$. The concept of filtering an image before backprojection is familiar from CT techniques.

ii. Although **F** has no 'true' inverse, the quantity $\mathbf{B}(\mathbf{FB})^{-1}$ is a pseudo-inverse of F.

Bayford (1994) described a different method of filtering the boundary voltages before backprojection. His filter function was based on consideration of the reconstruction as a constrained optimisation problem. In practice, his filter function derived from measurement of the area enclosed by adjacent sets of isopotential lines. Figure 3.1 shows a comparison of images produced by Bayford's technique with and without filtering. The improvement introduced by the filter is obvious.

It has been argued that (unfiltered) backprojection is equivalent to inversion of the main diagonal of the sensitivity matrix (*e.g.* Kotre, 1994). A more accurate reconstruction might therefore be obtained by consideration of other elements in the sensitivity matrix, without attempting a full inversion.

3.3.4 Sensitivity coefficient methods

The intensity of each image pixel is determined, in principle, by each of the available boundary voltage measurements. The effect on pixel intensity of a change in the boundary voltage is usually referred to as a 'sensitivity coefficient' (*e.g.*, Gadd *et al.*, 1992) or a 'direct sensitivity coefficient' (*e.g.*, Morucci *et al.*, 1994). In APT, sensitivity coefficient methods work by summing, for each pixel, the product of the boundary voltages and the appropriate sensitivity coefficient. The 'sensitivity region' described by Gadd *et al.*, (1992) used a two-dimensional finite-element model to determine the sensitivity coefficients. Each pixel intensity was determined only by the largest sensitivity coefficient to which it was related. Kotre (1994) described a technique that employed all the sensitivity coefficients for each pixel. The sensitivity coefficients were determined by applying the Geselowitz (1971) sensitivity equation to potential fields derived from a three-dimensional finite difference procedure. The method of Morucci *et al.*, (1994) uses a limited number of sensitivity coeffecients, typically 16, to produce the image.

Sensitivity coefficients may be derived from a sensitivity matrix of the form of equation [3.5]. However, even when all sensitivity coefficients are used in the reconstruction, sensitivity coefficient methods are not equivalent to an inversion of the sensitivity matrix, and have more in common with filtered backprojection.

3.3.5 Newton one-step reconstruction

Cheney *et al.*, (1993) presented an algorithm called 'NOSER' (Newton one-step reconstructor) which makes the first iteration of a Newton-Raphson solution to Poisson's equation. Despite using the

Newton-Raphson approach, this is a linear technique. Discussion of this technique will be reserved until §3.4.2, along with other Newton-Raphson variants.

3.3.6 Discussion

All the published linear reconstruction techniques have a number of features in common, which are probably a factor of the linearisation itself, rather than of inadequacies in the methods.

i. Images of small objects are wider than the objects themselves, and this width varies with position. Centrally-placed objects appear wider than peripheral ones of the same size.

ii. If the reconstruction is scaled to represent correctly an overall change in resistivity, then it will underestimate the resistivity change due to a small object. The underestimation is normally greatest for centrally-placed objects.

Furthermore, the spatial resolution, sensitivity and accuracy of these methods are broadly similar, although it is recognised that any these factors can be improved at the expense of the others (Barber and Seagar, 1987; Bayford, 1994). Perhaps a more useful way to compare these algorithms is by how readily they may be adapted to deal with non-uniform initial resistivity, or unequal electrode spacing.

Unfiltered

Filtered by the method of Bayford, 1994

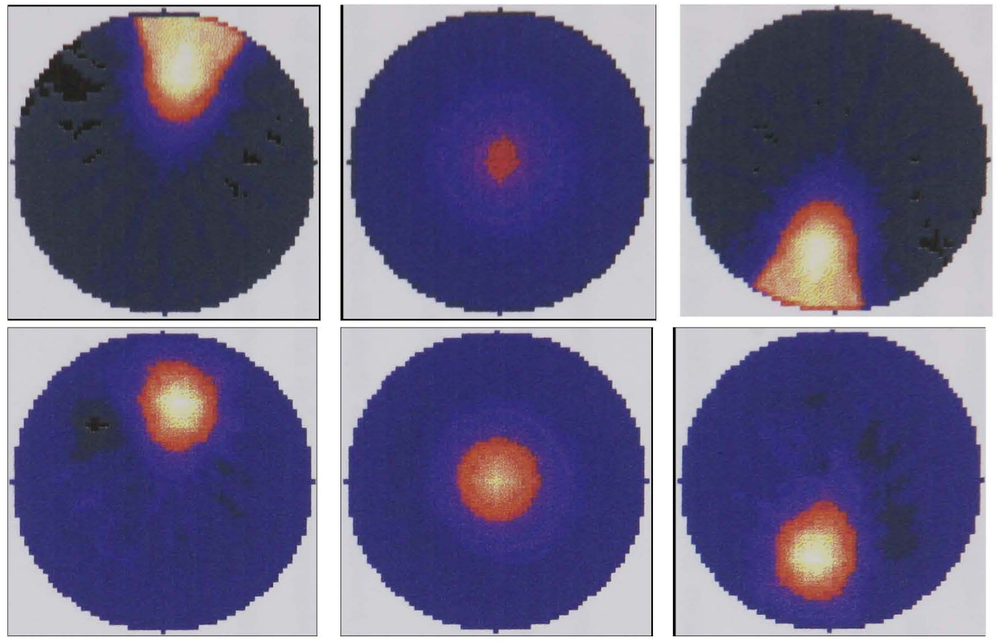

Figure 3.1: a comparison of filtered and unfiltered backprojection. The images are of a glass rod in a saline phantom. The diameter of the glass rod was 10% that of the phantom. Note the 'blurring' of the the unfiltered images, and distortion at the edge. The unfiltered images also show a marked contrast between the amplitudes of a central and a peripheral feature.

3.4 Non-linear methods

3.4.1 Mathematical principle

The following procedure broadly represents all methods that attempt to find an exact solution to equation [3.2].

1. Choose an initial value of σ
2. Solve the 'forward' problem to calculate the boundary voltages **g** from σ. A numerical technique such as the finite element method is normally used for the forward problem.
3. Use the results of the forward solution to determine how close the guessed σ is to the real conductivity
4. Adjust σ as appropriate
5. Repeat from step 2 until the difference between measured and predicted boundary voltages is suitably small.

It is primarily step 3, the determination of the accuracy of the guess at conductivity, which distinguishes one iterative reconstruction technique from another.

3.4.2 Newton-Raphson and variants

The Newton-Raphson technique attempts to find a solution of a set of non-linear equations. It uses the derivatives of the function to move the independent variable from a first estimate of a solution towards a better estimate. This process can be repeated until a suitably accurate solution is obtained. Given an initial estimate of conductivity $\sigma[1]$, it can be shown (Press *et al.*, 1992) that a better estimate $\sigma[2]$ is given by:

$$\sigma[2] = \sigma[1] + \delta\sigma \qquad [3.9]$$

where

$$\mathbf{S}_c.\delta\sigma = -(\mathbf{A}_c - \mathbf{g}_{meas}) \qquad [3.10]$$

$\mathbf{g}_{meas}$ is the measured boundary voltages. To find $\delta\sigma$ at each stage requires the solution of the set of equations [3.10] by, for example, LU decomposition. Like many iterative procedures the Newton-Raphson technique can converge to a strikingly poor solution if the initial estimate is very inaccurate, or even diverge.

A variant of the Newton-Raphson method was applied to APT by Yorkey (1986) and subsequently developed by Woo *et al.*, (1993). Initially they stated the problem as a least-squares minimisation procedure, which attempted to minimise the function[2] P:

$$P = \sum_{i=1}^{m} (\mathbf{g}_i - \mathbf{g}_{meas,i})^2 \qquad [3.11]$$

---

[2] The symbol ϕ was used by the original authors; 'P' is used here to avoid confusion with the symbol for potential.

where m is the number of boundary voltage measurements in vector $\mathbf{g}$, g_i is the i^{th} boundary voltage derived from the solution of the forward problem and $g_{meas,i}$ is the i^{th} measured boundary voltage. In essence, minimising P is equivalent to choosing a conductivity value that generates modelled boundary voltages as close as possible to the real voltages. To find a minimum in P, we determine its derivative and equate it to zero. This produces (Hua and Woo, 1990) an expression for the conductivity update $\delta\sigma$:

$$\delta\sigma = -(\mathbf{S}_c^T\mathbf{S}_c)^{-1}(\mathbf{S}_c)^T(\mathbf{A}_c - \mathbf{g}_{meas}) \qquad [3.12]$$

The difficult stage in the evaluation of [3.12] is the inversion of $(\mathbf{S}_c^T\mathbf{S}_c)$, which can be very ill-posed. Improvements to the technique (Woo *et al.*, 1993) include:

i. introduction of a regularisation factor in the function P which biases the solution towards smooth distributions of resistivity, and
ii. indirect methods of evaluating [3.12] which do not require an explicit calculation and evaluation of $(\mathbf{S}_c^T\mathbf{S}_c)$.

With these improvements, these authors were able to produce images of absolute resistivity whose spatial resolution was 5% at the edge of the image and 7% at the centre. These images were produced in ten iterations, taking about one to five hours. This long computation derives, at least in part, from the necessity to recompute the sensitivity matrix at each step. As yet, no *in-vivo* images have been published, only phantom images.

The 'NOSER' algorithm of Cheney *et al.*, (1993) has produced a small number of 'quasi-static' images of resistivity distribution in the human torso. The algorithm takes only the first step of a Newton-Raphson iteration. The algorithm attempts to minimise, by a least squares technique, the difference between the measured boundary voltages and a set of model-generated boundary voltages corresponding to uniform resistivity. In so doing, it produces an approximate image of absolute resistivity. Because it requires only one step of the iterative procedure, the sensitivity matrix can be pre-calculated, which makes the overall computation much faster than a true iterative technique.

3.4.3 Wexler's double constraint method

This iterative method attempts to minimise the difference, not only between the measured and calculated boundary voltages, but between the measured and calculated boundary current densities. Current and voltage error minimisation steps are applied alternately.

3.4.4 Layer-stripping methods

Layer-stripping methods (Dai *et al.*, 1984; Isaacson and Cheney, 1992) are based on the following procedure.

i. Measure boundary voltages
ii. Estimate the conductivity in the outermost 'layer' of the body

iii. Estimate the voltages on inner surface of this layer

iv. 'Strip away' the outermost layer. Let the predicted voltages on the inner surface of the 'stripped' layer become the new boundary voltages

v. Repeat from step 2, until reaching the centre.

The difference between the various methods is primarily in step (iii). Layer-stripping methods have the advantage over other iterative techniques in that they cannot converge to false 'local minima'., At present, however, published images have only been of computer-generated test data.

3.4.5 Forward problem

So far the emphasis has been on the 'inverse' solution, *i.e.*, the determination of conductivity from boundary voltages. The inverse problem will, however, require evaluation of the 'forward' solution, perhaps many times. The forward solution predicts boundary voltages from a particular estimate of conductivity. In APT, the forward solution is typically provided by a finite-element model. For the reconstruction technique to finish in a practicable time, it is important that the forward solution be computationally efficient. For Newton-Raphson methods, we may need to calculate, not only the relationship between the conductivity and the boundary voltages, but also its derivative, the sensitivity matrix. Fortunately, techniques such as the compensation method (Murai and Kagawa, 1985) can efficiently estimate the sensitivity matrix from the forward solution. Hua and Woo (1990) provided a detailed analysis of computational efficiency.

Efficiency issues are particularly significant for three-dimensional imaging, since the sizes (in elements) of the matrices $\mathbf{A}_c$ and $\mathbf{S}_c$ increase with the square of the number of pixels. For example, for a spatial resolution of 5% of the image radius, we need about 2000 nodes per three-dimensional cross-section (see chapter 6). Without storage-reduction techniques, these matrices would require 3200 Megabytes ($= (2{,}000 * 10)^2 * 8$ bytes) of storage. Fortunately, these matrices are 'sparse', *i.e.*, most of the elements are zeros. Sahalos *et al.*, (1994) described a sparse matrix technique for solving the three-dimensional forward problem that reduced the memory requirement by a factor of 40. A three-dimensional model of the chest with 79 layers could be processed in one megabyte of memory.

3.4.6 Discussion

At present, the Newton-Raphson method appears to provide the best accuracy and spatial resolution, particularly after inclusion of the enhancements described in §3.4.2. However, no reconstruction of *in-vivo* images appear to have been published. There seem to be two particular limitations to the iterative approach:

i. the reconstruction algorithm must include an accurate model of the physical system to be imaged. The required accuracy is not well known: figures suggested include 1% (Barber, 1993) and 0.05% (Denyer *et al.*, 1994). For medical imaging, the model must include the exact positions and shapes of the skin electrodes, and the electrode-skin impedance. A discussion of the measurement errors introduced by skin impedance may be found in appendix D.

ii. The iterative process is particularly sensitive to noise and measurement error. This is because, for any particular part of the body, there will be boundary voltages that change only slightly with a large change in resistivity. This implies that a small error in boundary voltage could produce a large change in the image.

Until these problems are overcome, it is unlikely that useful images of absolute resistivity will be obtained *in-vivo*. Furthermore, images that discriminate between different tissue types (*i.e.*, anatomical images) may be better produced by multi-frequency measurement and a dynamic reconstruction process.

3.4 Three-dimensional imaging

In theory, a three-dimensional resistivity distribution can be determined if the voltage is known over the complete surface of the body. Since an infinite number of three-dimensional resistivity distributions can produce the same two-dimensional boundary data, there is no way to determine uniquely a three-dimensional distribution from measurements in one two-dimensional plane. This is unfortunate since it is, in a sense, what all practical APT experiments attempt to do. A typical APT measurement is carried out with a ring of electrodes arranged in a plane around the body. Current will not be confined to that plane, but will spread out into the tissues above and below the electrodes. Any attempt to use a 'two-dimensional' reconstruction technique will give an 'incorrect' image or no image at all. While linear reconstruction techniques will merely give a 'wrong' answer, iterative techniques may fail to produce an image at all. There is no evidence that a solution to Poisson's equation, even an incorrect one, exists for a two-dimensional model supplied with three-dimensional data. However, it might be that the reconstruction problem is less ill-posed (*i.e.*, easier to solve accurately) in three dimensions; further works needs to be carried out to determine whether this is indeed the case. If so, three-dimensional reconstruction may ultimately be more straightward than two-dimensional, rather than more difficult.

3.4 Dealing with non-uniform starting resistivity

A linear reconstruction technique estimates the small perturbation of conductivity which produced a small change in the boundary voltages. This does not circumvent the need to know how the resistivity was distributed before these changes occurred. Sensitivity or backprojection coefficients derive from some model of the physical system, which includes the initial resistivity. So far, all linear reconstruction techniques have assumed that the resistivity is initially uniform. Although this is never true *in-vivo*, in practice we can usually produce useful images, unless the initial resistivity is very non-uniform (Barber 1993). Unfortunately, one of the parts of the body which has a very wide distribution of resistivity is the head. It was originally thought that this problem could be overcome by a backprojection algorithm that backprojected along 'true' isopotential lines, *i.e.*, those which more accurately reflect the starting resistivity. This was shown not to be the case by Avis *et al.*, (1992). It ought to be possible to use a 'sensitivity' method whose coefficients are derived from an appropriate model of the initial resistivity (Gadd *et al.*, 1993).

3.5 Discussion

With very high-quality data, and in a physical system which can be accuractely modelled, it appears that Newton-Raphson techniques provide images with the best spatial resistivity and accuracy. However, there is no firm evidence that *in-vivo* imaging will be amenable to this technique; so far it has not been possible to deal with electrode position errors or skin impedance. Before we can obtain accurate dynamic images of the brain, we need a scheme to deal with anisotropy and the non-uniform initial resistivity.

4. An overview of APT applications

4.1 Introduction

Despite its obvious advantages of low cost and portability compared to other imaging techniques, and its obviating the need for ionising radiation, no branch of medicine has yet adopted APT as a routine diagnostic tool. This is partly because the performance and versatility of APT hardware are continuously improving, and many researchers seem understandably reluctant to invest considerable time and expense on clinical validation of technology that is in a state of flux. In particular, multiple-frequency systems, which have only been available for a short time, may considerably extend the range of clinical applications that will benefit from APT imaging. Further problems include those of inter-subject variability (see §4.11) and poor spatial resolution. As a result, only about one fifth of all published work in the APT field is concerned with medical applications. This chapter provides a brief summary of this work; an extensive and detailed review of clinical applications was presented by Holder and Brown (1993).

4.2 Gastric function

Measurement of the rate of emptying of the stomach after eating is an important test in the management of certain gastric disorders, *e.g.*, pyloric stenosis. The most widely-used method for assessment of gastric stenosis is gamma scintigraphy: the patient consumes a radio-labeled test substance, and the rate of gamma emission is measured in the region of the stomach. In infants, and in adults who require investigation more often than about twice a year, the radiation dose is potentially dangerous. One may, in these cases, resort to the rather unpleasant 'intubation' methods. For example, in dye dilution studies, the patient swallows a naso-gastric tube, through which small amounts of a substance with intense colouring can be delivered. The naso-gastric tube is then used to withdraw samples of stomach contents. The volume of the stomach at any given time may be found from the ratio of the amount of dye delivered to its concentration in the gastric sample. Many patients find the intubation uncomfortable, and there is a small risk of aspiration of the stomach contents. Clearly, some alternative to these techniques is required.

The assessment of gastric emptying is one of the best validated applications of APT. For example, Mangnall *et al.*, (1987) obtained significant correlations between APT and gamma scintigraphy. A number of groups compared the volume of fluid introduced into the stomach with the corresponding APT images (*e.g.*, Devane, 1993; Nour 1992). A further validation technique is to investigate whether APT can distinguish between healthy individuals, and those with known gastric disease. Lamont *et al.*, (1988) measured the times for the stomach volume to decrease by half in eighteen infants, after a conductive drink. Infants with pyloric stenosis showed significantly longer emptying times (mean 46 minutes) than those without (mean 12 minutes).

Overall, these validation studies showed good agreement between APT and the reference technique, in those images that can be interpreted at all. Unfortunately, some subjects simply do not

produce useful images of gastric function. For example, Wright *et al.*, (1993) carried out six studies on seventeen volunteers. Two subjects, and a further four recordings from other subjects, were uninterpretable. These failures constitute 16% of the recordings. The authors found no conclusive reasons for these failures.

Part of the reason for certain results being uninterpretable may be the poor spatial resolution of APT. This makes it difficult to distinguish between changes in the stomach's conductivity, position and volume. These factors will all contribute, to varying degrees, to the intensity of the image in a given region. An increase in the gastric conductivity, due perhaps to the secretion of acid into the stomach after eating, may be interpreted as an increase in the gastric volume. Most workers suggest that suppression of acid secretion is important in APT studies, although this may not be appropriate in children.

4.3 Pulmonary ventilation

Owing to the large resistivity contrast between inflated and deflated lung tissue, and to the large proportion of the thorax that is occupied by the lungs, pulmonary ventilation should be amenable to APT imaging. A number of authors have shown a strong correlation between inspired air volume and the resistance change in *some* part of the APT image (*e.g.*, Harris *et al.*, 1987; Holder and Temple, 1993) for individual subjects. Similarly, the aspiration of a pleural effusion (Campbell *et al.*, 1994) and the infusion of one litre of normal saline (Campbell *et al.*, 1993) both produced marked and significant changes in some region of the image. Newell *et al.*, (1994) showed resistivity changes in the 'lung' region during oedema induced by oleic acid. We might therefore reasonably expect that certain lung disorders, *e.g.*, pneumothorax or pleural effusion, which compromise ventilation, might be detected and localised using APT. If this were the case, APT might represent a useful alternative to X-ray investigation. Unfortunately, the studies mentioned above have taken as the 'lung', that part of the image that shows the greatest change during respiration. While this allows a good test of the effect of ventilation on APT images in a single individual, it ignores the rather large inter-subject variability in APT images. For example, in images of ventilation presented by Holder and Temple (1993), only about eight out of thirty normal volunteers showed resistivity decreases in regions that correspond, even approximately, to the anatomical positions of the lungs. This being the case, it is hardly surprising that only a patient with a profound pathology (only one lung) showed any statistically significant difference from the normal group. These authors, and others, have concluded that APT is only practical at present for imaging difference in ventilation over time in the same patient. It is likely that multiple-frequency imaging will make diagnostic use practicable soon; a small amount of preliminary work has been published (*e.g.*, Hampshire *et al.*, 1994).

4.4 Perfusion changes during the cardiac cycle

Changes in resistivity take place in the thorax during the cardiac cycle; these are due to the redistribution of blood between the heart, great vessels, and lungs. Such changes are small compared to those due to ventilation. Cardiac gating, *i.e.*, synchronisation of the data acquisition to the cardiac cycle, is normally used to separate the cardiac and ventilation information in the APT recording..

Cardiac gating was first used in APT by Eyüboglu *et al.*, (1987) for imaging the thorax. In this technique, the R-wave of the ECG starts the acquisition of APT data, typically at about 20 frames per second. Each set of frames is averaged to produce an image of resistivity during the cardiac cycle. The authors tentatively suggested that there were separate features in the images corresponding to the descending aorta, right atrium, left and right ventricles, and left and right lungs. McArdle *et al.*, (1993) compared APT images of perfusion in the thorax with M-mode Electrocardiography. They also reduced ventricular stroke volume using glyceryl trinitrate. In contrast to earlier studies, they concluded that APT could only resolve one atrial and one ventricular component in the region of the heart, and that even these might overlap. If this were the case, the true resistivity changes in the region of the heart would be underestimated, since a decreasing resistivity in the atria might 'cancel' an increasing resistivity in the aorta. Furthermore, the heart moves in the chest during the respiratory cycle, and this would further blur the distinction between different parts of the heart. The relative sizes of the cardiac and ventilation components makes it necessary to acquire a large number of data acquisition cycles.

Zadehkoochak *et al.*, (1992) showed that, by separation of the measurements into high and low frequency bands before averaging, perfusion and ventilation effects could be separated using a shorter data acquisition time. The optimal frequency for this separation was 47-55 Hz. Killingback *et al.*, (1993) applied this technique to 20 normal subjects. They took as the 'heart' that area of the image that showed a resistivity change that was at least a fraction $1/e$ of the largest cardio-synchronous resistivity change in the image. They concluded that the area of the heart was significantly different between subjects, compared to inter-subject variability. The was also a significant difference between this area when the subjects adopted a range of postures.

McArdle *et al.*, (1993) used cardiac gating for imaging perfusion in the head. They found a peak resistivity decrease at about 280 msec after the R-wave in 24 subjects. In all measurements, they found that resistivity changes only occupied the central region of the image. This is what we would expect from a reconstruction technique that assumed an initial uniform resistivity. This finding supports the conclusion that the resistivity changes are due to perfusion in the brain, rather than the scalp.

4.5 Perfusion changes unrelated to the cardiac cycle

Leathard *et al.*, (1993) proposed that APT could be used to monitor blood flow rate in the heart and lungs using concentrated (1.8%) saline as a tracer, rather than by averaging. This technique, if successful, would avoid the ventricular and atrial signals 'canceling', as was thought to take place in cardio-synchronous imaging. In one subject, a resistivity decrease of about 4% was observed in the chest after injection of 20 ml of saline into the arm.

4.6 Pelvic venous congestion

Pelvic venous congestion, characterised by dilation of pelvic veins, is a common cause of pain in women. Thomas *et al.*, (1991) made APT images of the change in pelvic resistivity that occurred when twelve patients changed from a supine to a standing posture. The distribution of conductivity between the posterior and anterior pelvis was significantly from that in a control group of fifteen subjects. The authors suggested that the resistivity changes were due to redistribution of blood in the pelvis.

4.7 Monitoring hyperthermia

Hyperthermia, to about 43°C, may be used to reduce tumour size in certain malignancies. There is a need for a technique that can make accurate, non-invasive measurements of temperature, to allow the heating to be concentrated in the tumour without damaging surrounding tissue. Since body tissues increase their resistivity by about 2% per °C, APT might be useful in this application. Conway *et al.*, (1992) imaged temperature variations in a saline phantom, and in the abdomens of human volunteers whose stomachs were rapidly emptied and filled with warm solutions. They found a good correlation between temperature and APT image change. However, we must overcome two problems before this becomes clinically useful. First, the resistivity of tissue during hyperthermia may be affected by other factors than temperature. Möller *et al.*, (1993) compared resistivity measurements with temperature measured by thermocouples during laser hyperthermia. They found that the resistance of tissue continued to decrease even after the temperature had stabilised, and did not return to pre-therapy values after the end of the treatment. Second, it may be necessary to measure small changes in resistivity over as long as an hour. During this time the temperature will increase by up to about 6°C. 'Baseline drift' artefacts in the APT images must therefore be less than about 3% over this time. This degree of stability is difficult to achieve in practice, perhaps due to varying skin impedance (see appendix D).

4.8 Breast cancer screening

Carcinoma of the breast is a significant cause of death; prospects for the sufferer are much better if the disease is detected at an early stage. While X-ray mammography is a useful technique for detecting the condition, it is too expensive to use routinely (by general practitioners, for example), and can itself cause the disease if over-used. APT may be a much more practicable way to apply routine screening for breast cancer. There is known to be a significant difference in impedance between normal breast tissues and tumours (*e.g.*, Jossinet and Risacher, 1994). This application absolutely demands a procedure for producing images of absolute resistivity: we cannot image during the development of a tumour. Holder *et al.*, (1994) attempted to make 'pseudo-static' images of the breast using synthesised reference data, but with limited success. Multiple-frequency imaging may be more successful in the future.

4.9 Swallowing disorders

Difficulties in swallowing accompany a number of common neurological disorders, *e.g.*, stroke, Parkinson's disease. APT might be used to determine the time taken for a bolus of fluid to enter the oesophagus, and therefore assess the severity of the disease. Hughes *et al.*, (1994) compared APT images of the neck and X-ray videoflouroscopy during swallowing. They found that all images showed a decrease in impedance, regardless of the conductivity of the fluid being swallowed. The peak in the APT image corresponded most closely to the point at which the anterior and posterior walls of the pharynx were most closely apposed. The authors proposed that the feature in the APT images was due to the expulsion of air from the pharynx rather than directly to the bolus of fluid.

4.10 Stroke

During cerebral ischaemia, the impedance of brain tissue increases by up to 100% (Holder, 1992). This might allow for a non-invasive method for assessing the severity of stroke. Holder obtained images of cerebral ischaemia in anaesthetised rats, with both intracranial and extracranial electrodes. Other possible applications of APT to neurology were discussed in chapter 1.

4.11 Discussion

Most experiments that evaluated APT in a clinical setting showed clearly that greater success was achieved with measurements of changes in the clinical state of a given patient, than with comparison between subjects. A number of possible reasons have been advanced for this inter-subject variability in APT, including:

i. differences in posture and body shape between patients;
ii. 'off-plane' features, *e.g.*, contributions from the lung appearing in images of the stomach;
iii. skin impedance, particularly when it varies over time (see appendix D);
iv. non-circular geometry, and uneven positioning of the electrodes.

Of the work that has been carried out with APT in clinical medicine, most has been directed towards realising its practical benefits in a diagnostic application. Even though these practical benefits are considerable, its diagnostic power does not even approach that of techniques such as CT and MRI. It is likely that multiple-frequency imaging will improve the range of applications available, since it will be able to distinguish between different tissue types in the same subject. However, little use has yet been found for the unique features of APT, for example its ability to produce hundreds or even thousands of images per second.

Part B: analysis and modeling

5. A model of impedance in unmyelinated nervous tissue

5.1 Introduction

This chapter presents a mathematical model of the impedance of unmyelinated nervous tissue. The model was used to predict the impedance changes that might occur during normal action potentials, and pathological events. Unmyelinated nervous tissue comprises the grey matter of the brain and spinal cord, and the peripheral nerves of invertebrates. In mammals, the white matter of the brain, and most of the peripheral nervous system, is myelinated. The aims of this modeling were as follows:

i. to determine the optimal frequency and electrode positions at which to make measurements of impedance change during action potential activity;
ii. to estimate the maximum impedance changes that might be expected during action potential activity in invertebrate nerves (chapter 7), and during the pathological phenomenon of 'cortical spreading depression' (chapter 8). Clearly, experiments would only be worthwhile if it appeared that the resistance change would be large enough to measure;
iii. to add support to the validity of the measurements made in mammalian brain and invertebrate nerve tissue that are described in chapters 7 and 8.

This chapter assumes familiarity with the anatomy and physiology of nervous tissue, and with the procedures of linear cable theory; descriptions of these may be found in Kandel *et al.*, (1991) and Jack *et al.*, (1975) respectively.

Qualitatively, we might expect the impedance of nervous tissue to decrease when the neuronal membranes depolarise: the opening of ion channels in the membranes allows more current to reach the conductive axoplasm than when the cell is in the resting state. The proportional impedance change will not be as great as the membrane resistance change, for two reasons. (i) The membrane has a capacitive component which will allow AC currents into the axoplasm, even at modest frequencies. (ii) The neurons are surrounded by a conductive interstitial space; this will carry a large proportion of the current, even when the membranes are depolarised. The impedance change caused by a given neuronal process will also depend on the orientation of that process with respect to the applied electric field. When a process is transverse to the field, it presents a small surface to the current. In this case, only a small amount of current will enter the axoplasm, even when the membrane is depolarised. This effect is a familiar one in APT imaging; it is the same effect which makes it difficult to distinguish a small object with a 10% resistivity contrast from one of 100% (*e.g.*, Holder and Khan, 1994). When the field is longitudinal to the neuronal processes, a greater surface area of membrane is available for conduction, and current readily enters the axon. Indeed, in a distance of about 1 mm, all the current which can enter the axon will do so; membrane current will be close to zero at distances greater than this from the point of current application. When the tissue sample consists of a large number of neurons, we have also to consider the effect of incomplete depolarisation. In peripheral nerve, depolarisation will be incomplete because the axons have markedly different conduction velocities. If the measuring electrodes are some distance from the point at which an action potential originates, the membranes under the electrodes will depolarise at different times. Thus the 'active' axons are always surrounded by some 'inactive' tissue

that also appears as a short circuit. This effect further reduces the measured resistivity change. This effect will also be present in the brain, as will synaptic inhibition and summation of nervous activity, which will further reduce amount of tissue which depolarises simultaneously.

The analysis starts with the simplest case: steady-state impedance change in an invertebrate peripheral nerve, with uniformly oriented, identical fibres (§5.2.2). §5.2.3 considers the effect of a low-frequency measurement, in which the impedance will not reach a steady state during the measurement. The model is next extended to include incomplete depolarisation, particularly as a result of a distribution of fibre sizes (§5.2.4). The effect of varying fibre orientation, as in the brain, is treated semi-quantitatively (§5.2.5 and §5.2.6). The cortical resistivity change is evaluated both for action potential activity, and for 'cortical spreading depression' (see §8.1.2). In this latter condition, an impedance change results primarily from a change in the ratio of extracellular to intracellular space.

5.2 Method

5.2.1 Assumptions

To make the analysis tractable, we need to make some fundamental assumptions.

i. For longitudinal measurements, the linear cable theory (Jack *et al.,* 1975) is adequate to model the current and voltage in axons. This requires a linear current-voltage relationship, and a uniform current density over a cross-section through the axoplasm. We assume also that the measurement of impedance is derived from measurment of the voltage developed across a sample of tissue in a uniform electric field. In practice, current will be applied by electrodes. The assumption of a uniform field is reasonable when voltage measurements are made at distances greater than a few millimetres from the electrodes (*e.g.,* Ranck, 1963).

ii. The figures available for parameters such as the intracellular and membrane resistivities are appropriate. I have used published reports of measured values, rather than those derived from othermodels, wherever possible.

iii. In the brain, we need consider only neurons, interstitial space and glial cells. The effects of blood vessels and connective tissue are assumed to be negligible. The resistance of glial membrane (Hild and Tasaki, 1962) is sufficiently low (1 Ωcm^2 - 10 Ωcm^2) that glia are considered identical to intercellular fluid when longitudinal to the current flow, and insulators when they are transverse. This point is discussed further in §5.2.6. In peripheral nerve, only neurons and extracellular space are modeled.

5.2.2 Effective longitudinal impedance of a uniform nerve

For the purposes of modeling the longitudinal impedance, the nerve was assumed to consist of two 'compartments': identical unmyelinated axons oriented parallel to the applied electric field, and interstitial space. Using the procedures of linear cable theory (Jack *et al.,* 1975) we represent the nerve axon itself as a uniform cylinder which consists of axoplasm (resistivity ρ_i Ω.cm) surrounded by a membrane of specific resistance ρ_m $\Omega.cm^2$ and capacitance C_m $\mu F/cm^2$ (figure 5.1). The axon is 'closed-ended' since in practice no current can enter the axon except through the membrane. The axons are

surrounded by interstitial fluid of resistivity ρ_e Ω.cm which occupies a fraction α of the overall tissue volume. Measuring electrodes are placed some distance 2L apart along the length of the nerve, so that the electric field in the interstitial space is parallel to the fibre.

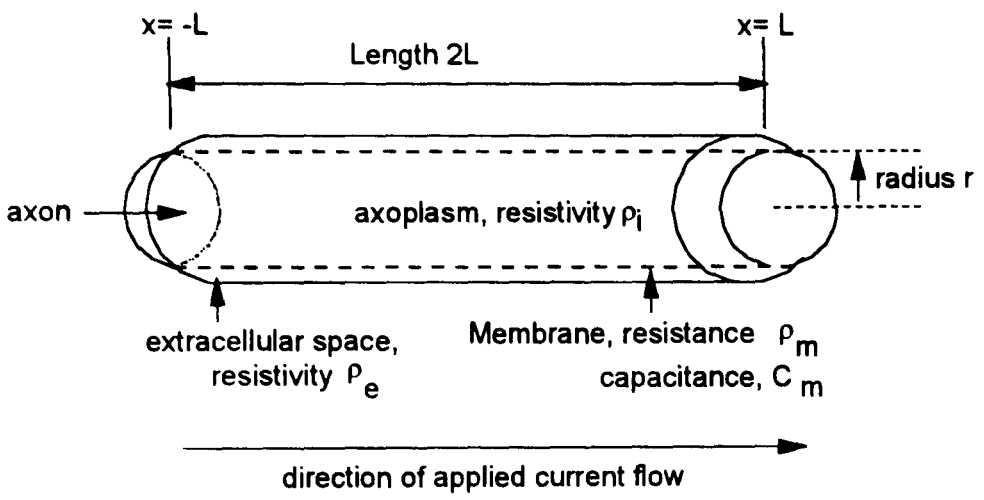

Figure 5.1: the geometry of the longitudinal model. See text for explanation of symbols

It can be shown (Appendix A1) that the longitudinal admittivity y_{total} of this model nerve is given by

$$y_{total} = p_n y_n + p_e y_e \qquad [5.1]$$

where p_n is the proportion of neurons in the nerve, y_e is the admittivity of the extracellular fluid, and p_e is the proportion of extracellular space, which is equal to (1 - p_n). The admittivity y_n of the neuronal compartment, is given by

$$y_n = \frac{1}{\rho_i}\left(1 - \frac{1}{D}\sinh(FL)\right) \qquad [5.2]$$

where

$$D = (1 - K_s)\sinh(FL) + K_s FL\cosh FL$$

and

$$F = \sqrt{(1+j\omega\tau)}/\lambda$$

τ and λ are known as the time constant and length constant respectively, and are given by

$$\tau = \rho_m C_m$$

and

$$\lambda^2 = \frac{r\rho_m}{2(\rho_i + \rho_e(1-\alpha)/\alpha)}$$

K_s is a dimensionless constant that describes the effect of the extracellular space on the membrane potential developed by the applied current:

$$K_s = \frac{1}{1 + \frac{\rho_e \alpha}{\rho_i(1-\alpha)}}$$

The parameter α is the proportion of tissue which does not depolarise. Note that α is equal to p_e only if the nerve consists entirely of identical neurons and extracellular space. The possible contribution of inactive tissue to the parameter α in the cortex will be discussed below.

To obtain the peak resistivity change during depolarisation, equation [5.1] was evaluated with membrane resistivities appropriate for both depolarised and resting states. Percentage resistivity change ($\rho^{\%}$) was expressed as follows:

$$\rho^{\%} = \frac{\text{resistivity at rest} - \text{resistivity when depolarised}}{\text{resistivity at rest}} \qquad [5.3]$$

This assumes that the impedance reaches a steady state in the time during which the tissue under the measuring electrodes is depolarised. This will not be the case for low ($\ll 1/\tau$) measuring frequencies; the implications for low-frequency measurement will be discussed in §5.2.3. I evaluated equations [5.1] - [5.3] using MATLAB (The Mathworks, Inc.) at various frequencies and electrode spacings. The model parameters were chosen to be appropriate for crab peripheral nerves (table 5.1), to allow comparison with the experimental results of chapter 7.

Parameter	Value	Source
Neuronal cytoplasm resistivity ρ_i	90 Ωcm	Hodgkin and Rushton, 1946
Neuronal membrane resistivity ρ_m	8000 Ωcm^2	Hodgkin and Rushton, 1946
Neuronal membrane capacitance C_m	1.0 $\mu F/cm^2$	Hodgkin and Rushton, 1946
Neuronal fraction p_n	0.75	see text[1]
Interstitial resistivity ρ_e	20 Ωcm	Hodgkin and Rushton, 1946
Interstitial fraction p_e	0.25	= 1- p_n
α	0.25	= 1- p_n
axon radius	4 μm	see text[2]
Membrane resistivity during depolarisation	1/40 * ρ_m	Cole and Curtis, 1939

Table 5.1: Model parameters for crab nerve

Notes:

[1]From measurements of potassium concentration, Keynes and Lewis (1951) calculated that the proportion of extracellular space (p_e) could not be greater than 25% in the crab carcinus maenus.

[2]Crab peripheral nerves have diameters from < 1μm to 30 μm. The figure of 4 μm was taken as representative of the nerve; it corresponds to the estimated mean radius of the fibres which are active at the peak of depolarisation (§5.2.4)

5.2.3 The effect of membrane time constant on low-frequency measurements

The analysis above assumed that the percentage resistance decrease during depolarisation can be adequately determined from the difference between the steady-state resistivities in the resting and depolarised states. This implies that the measurement must be able to reach a steady state in the time during which the tissue under the measuring electrodes is depolarised. The time constant of the crustacean cell membrane is about 10 msec at rest (Hodgkin, 1948) while the membrane action potential lasts about 1 msec (Hodgkin, 1938). Clearly a measurement at very low frequency will not reach a steady state during the action potential. The charge stored in the membrane capacitance will tend to oppose decreases in the membrane voltage, and give a false impression of the resistance decrease during depolarisation. In practice the membrane resistance, and therefore the time constant, will be decreased during depolarisation. This effect is analysed, for direct current excitation, in appendix A2. The resistance change which would be measured in a nerve with a certain membrane time constant τ is given by multiplying the change in the steady-state resistances by a constant k_τ, where

$$k_\tau = \frac{\delta V_m(L)_\tau}{\delta V_m(L)_0}$$

In this expression, $\delta Vm(L)_\tau$ is the change in membrane voltage during depolarisation when the membrane has a time constant τ. $\delta Vm(L)_0$ is the change which would be observed for a membrane with a time constant of zero.

To estimate k_τ, we will assume that the membrane voltage is proportional to that which would be obtained with a constant current applied across a parallel RC network (figure 5.2). The values of 'R' and 'C' are not known; however, since we are deriving a voltage ratio, the actual values are irrelevant; the product RC is the important factor.

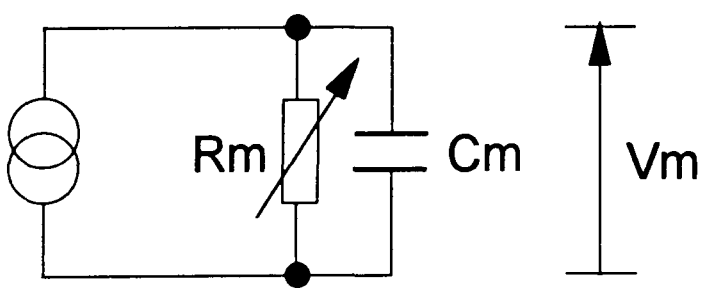

Figure 5.2: a model of the neuronal membrane under constant-current excitation. The actual values of current, Rm and Cm are unknown; the product R_mC_m is specified.

To predict the membrane potential we need an estimate of the shape and magnitude of the membrane resistance decrease of a single fibre during depolarisation. The duration of the action potential, about 1 msec, taken from Hodgkin's (1948) single fibre study on *carcinus maenas*, was assumed to represent also the duration of the membrane depolarisation. The size of the membrane resistance decrease was taken from the results of Cole and Curtis (1939) for the giant axon of the Atlantic squid *loligo pealii*. It

was assumed the shape of the resistance decrease could be adequately represented by a descending half-cycle of a sine function; this is a reasonable approximation to the latter author's results.

5.2.4 The effects of mixed fibre size and incomplete depolarisation

Until now, we have assumed that all nerve fibres are of the same diameter. This is unlikely to be the case in reality, especially in peripheral nerve. This section describes a model of the effect of mixed fibre size on the compound action potential, and draws some inferences about the effect on impedance decrease. The effect on the compound action potential is important: as will be discussed in chapter 7, the experimental technique for impedance measurement relies on the compound action potential decreasing very rapidly with distance from the stimulating electrode.

The effects of fibre size on the action potential include:

i. Larger fibres generate a larger extracellular action potential. The monophasic measurement of action potential invariably falls short of the membrane potential change, which might be over 100 mV in crab nerve fibres. This attenuation is due to the potential divider formed by the intracellular and extracellular resistances (*e.g.*, Hodgkin, 1938) between the active part of the membrane and the indifferent electrode. If the extracellular resistivity were very large, the action potential would approach the membrane potential. For a larger fibre, the ratio of extracellular to intracellular resistance is larger. This ratio depends in turn on the ratio of the axonal volume to the interstitial volume.

ii. Larger fibres conduct the action potential more quickly. There is theoretical (*e.g.* Noble, 1979) and experimental (*e.g.*, Hodgkin, 1954) evidence that unmyelinated fibres conduct at a rate proportional to the square root of their diameters. Since the conduction velocity in crab nerve fibres of 30 μm diameter is about 5 $m.sec^{-1}$ (Hodgkin, 1939), a general expression for conduction velocity in such fibres is $u_c = 0.913\sqrt{d}$ where u_c is the conduction velocity in $m.sec^{-1}$ and d is the fibre diameter in micrometres. This relationship fits a wide range of fibre sizes; for example, it correctly predicts the velocity of conduction of squid giant axon (d = 500 μm) as 20 $m.sec^{-1}$. This implies that, as the recording electrode is moved further from the stimulus, the time at which different fibres depolarise will be more dispersed. For example, when depolarisation of the fast fibres reaches the electrode, other, smaller fibres will be in the resting state, and may be considered to be 'in parallel' with the extracellular space. By the time the slow fibres depolarise, the faster fibres will have repolarised, and these in turn may be considered to be in parallel with the extracellular space. This means that the compound action potential will last longer, and exhibit a smaller amplitude.

Keynes and Lewis (1951) reported a typical distribution of fibre diameters from a single crab walking-leg nerve (figure 5.3).

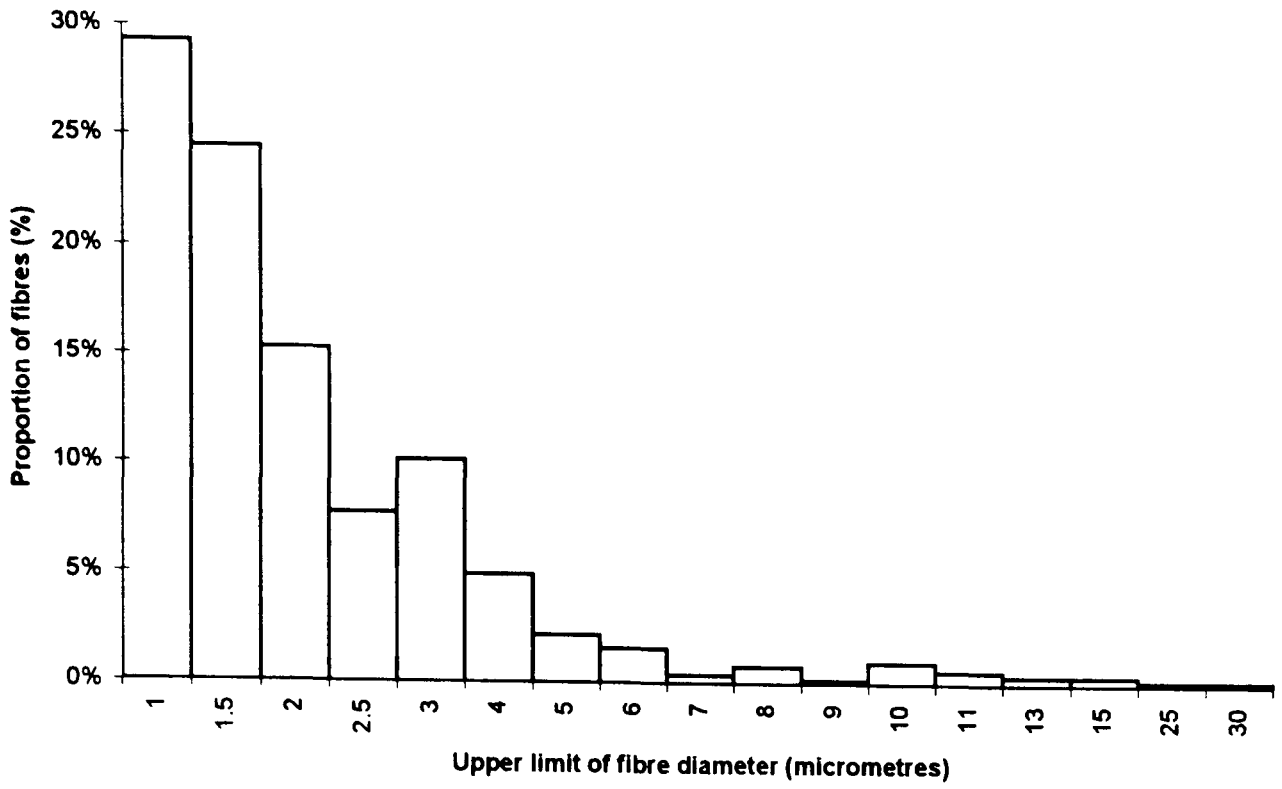

Figure 5.3 the distribution of nerve fibre diameters in a crab walking-leg nerve, from Keynes and Lewis (1951). Note that, although small fibres are more prevalent than large ones, the large fibres account for a greater proportion of the tissue volume. In this example, fibres of diameter > 8 μm occupy just over half the total volume. In other nerves, these fibres occupied less than 12% of the volume.

We will assume for simplicity that each 'class' of fibres produces an action potential which is a rectangular voltage pulse. The compound action potential will be taken to be the sum of the action potentials from each fibre class. There are a number of models of varying complexity which attempt to relate single-fibre to compound action potentials (see Schoonhaven *et al.*, 1986b for review). A simple model is justified here, since the greatest inaccuracy is likely to be due to inadequate knowledge of the nerve geometry and composition. We assume that, at any given instant in time during depolarisation, the voltage developed by a class of fibres will be proportional to (i) the radius of fibres in that class, and (ii) the proportion these fibres occupy of the overall nerve area. From this definition,

$$V_n(t) = K.S_n(u_{cn}, t).p_{depol}(n, t).r_n$$

In this expression:

$V_n(t)$ is the contribution made to the action potential by fibres of class *n* at time *t*,

$S_n(u_{cn},t)$ is a step function taking the value '1' when the fibre is depolarised and '0' when it is quiescent,

$p_{area}(n)$ is the proportion of the nerve area occupied by fibres of class *n*,

r_n is the radius of fibres in class *n*, and

K is a constant determined by the geometry and composition of the nerve.

S_n is a function both of time and the conduction velocity of fibres in class *n*. The constant *K* is related to the intracellular and extracellular resistivities, and was determined by experiment (§7.4.3). The compound action potential is therefore given by summing the contributions of each class:

$$V(t) = \sum_{n=1}^{k} N_n V_n(t) \qquad [5.4]$$

where *k* is the total number of size classes and N_n the number of fibres in class *n*. Equation [5.4] was evaluated using a MATLAB program for action potentials of duration 1 msec. The value of K was determined by comparison of the calculated compound action potential with the experiment which is described in chapter 7. As shown in figure 5.8, the compound action potential decreases in magnitude with increasing distance from its origin.

In a nerve, to a first approximation, both the impedance change during depolarisation and the size of the action potential will be dominated by the same factor: the ratio of the extracellular resistance to the intracellular resistance. I have therefore assumed that both will be smaller by the same proportion than the figure predicted for complete depolarisation. The same consideration will be assumed to apply to the cortex, although in this case the justification is somewhat weaker. While membrane resistance only *decreases* during depolarisation, action potentials can propagate in various directions, leading to their 'cancellation' from a voltage recording. The comparison of cortical action potential to membrane action potential may therefore overestimate the reduction in impedance change. Nevertheless, some brain regions are subject to a largely uniform aligment of fibres, and a better model would require detailed information about the three-dimensional structure of the brain that is not available.

5.2.5 Effective impedance of 'transverse' fibres

Many workers have considered the case of 'transverse' current flow in nerve and muscle fibres (*e.g.*, Bozler and Cole, 1935). It is typical to model these fibres as long cylinders in a uniform transverse field. Such an analysis is complicated by two factors:

i. These analyses are typically based on the 'Maxwellian' technique that assumes that the field strength within the cylinder is uniform and parallel to the external field. This neglects the 'cable' properties of the cells.
ii. The cells are assumed to form a 'dilute suspension', *i.e.*, the intracellular compartment comprises only a small part of the total tissue volume. Ranck (1963), for example, was reluctant to use the 'Maxwell' approach because of this complication. More recently, Cole (1975) showed empirically that Maxwell's technique may be valid for a much greater neuronal proportion than was previously thought.

Bozler and Cole (1935) presented a full derivation of the mathematical relationship between neuronal parameters and effective impedance ρ_{trans} for the 'transverse' case; only the result will be quoted here:

$$\rho_{trans} = \rho_e \frac{(1-p_n)\rho_e + (1+p_n)(\rho_i + Z_3)}{(1+p_n)\rho_e + (1-p_n)(\rho_i + Z_3)} \qquad [5.5]$$

where

$$Z_3 = \frac{\rho_m}{r_n(1+j\omega\tau)}$$

(symbols as in §5.2.2). This equation was evaluated for the tissue parameters given in table 5.1 (figures 5.9 and 5.10).

5.2.6 Mixed fibre orientation: resistivity of the cortex

§5.2.2 - §5.2.5 considered the impedance of nerve fibres oriented exclusively in the transverse or longitudinal direction relative to the applied field. To estimate the impedance, and therefore the impedance change, in the cortex, we need to consider the effect of variable fibre orientation. When the fibres are uniformly oriented at some angle other than 0° (longitudinal) or 90° (transverse), their impedance will be a complicated function of the cable and 'Maxwellian' properties of the fibres and of the angle θ. In practice, however, a considerable simplification can be made by noting that longitudinal and transverse currents dominate at widely separated frequencies, as described below.

Low frequencies. At low frequencies no current is carried by axons with θ=90°, irrespective of depolarisation (§5.3.5), although there may be a small current flow across cell bodies (Ranck, 1964). At a small angle from transverse, some current would be carried longitudinally. This longitudinal current is lower than the case when the axon is at 0°, because the component of the external field longitudinal to the axon is reduced. The resistivity change during depolarisation at frequencies less than a few hundred kilohertz therefore depends only on the longitudinal resistivity change and the angle θ.

High frequencies. When the cells are longitudinal to the field, the current carried in the axoplasm increases with frequency up to about 5 kHz (§5.3.1). Above this frequency there will be little change in longitudinal resistivity, and the axon can be considered as a region of uniform resistivity ρ_i. This resistivity appears in parallel with the transverse resistivity. Even at frequencies at which transverse current might be significant (> 100 kHz), the current will flow predominantly in the lower resistivity of the longitudinal path and the extracellular space. Only when all fibres are entirely transverse will the transverse current be affected by the membrane resistance.

In summary, at practical frequencies (< 1 Mhz), the resistivity change in the tissue depends only on the longitudinal resistivity change and the angle θ. At higher frequencies, negligible resistivity change will be observed at any orientation except $\theta \approx 90°$. Clearly, the structure of the brain is too complex to allow for a detailed mathematical analysis, but some general conclusions may be drawn.

'Random' fibre orientation. Ranck (1963) suggested that axons in the grey matter of the cortex could be modeled as 'randomly' oriented. If no transverse current crosses the axon, the effective neuronal resistivity in this configuration increases by a factor of 3.0, and the extracellular resistivity by 1.42. The former factor results from the 'open circuit' transverse fibre component, the latter from the increased path length.

Neuroglia. Neuroglia may occupy a tissue volume comparable to that of neurons. A glial cell's length is normally many times greater than its length constant (a few microns), so the longitudinal resistivity of the glial component may be considered to be equivalent to that of intracellular fluid. However, the glial transverse resistivity will still be much higher than its intracellular fluid. I have

assumed that the overall resistivity of glial tissue will be three times the longitudinal value, as for neurons. The effect of neuroglia will therefore to be to carry about half of the applied current, regardless of whether the neurons are depolarised or not.

Extracellular space. The figure of α = 25% for crab peripheral nerve is probably too large for grey matter. Electron microscopy suggests that 10% is probably a better estimate (Ranck, 1963). In any case, evaluation of equation 5.1 for extracellular spaces between 10% and 25% produce only a 25% variation in the overall resistivity change. This is partly because an increase in extracellular space increases the proportion of extracellular current, but also increases the length constants of neurons. These two factors are complementary.

Length constant and fibre length. In the analysis of resistivity change during depolarisation of peripheral nerve, the electrode spacing (2L in equation [5.2]) was an important factor. This was because the fibres were continuous. In grey matter, there is a high resistance between neurons, so the average length of neuronal projections is more important than the electrode placement. This average length is short compared to the length constant, leading to an increased resistivity change. The factor 'L' must therefore be considered to represent the average length of the neuron between cell bodies.

By taking these factors into account, a cortical resistivity change may be predicted using the same model as described above, with equation [5.1] expanded to give

$$y_{total} = p_n y_n + p_e y_e + p_g y_g \qquad [5.6]$$

where p_g is the proportion of the tissue occupied by glia, and y_g is the effective glial admittivity, which was set equal to one third the conductivity of the cytoplasm.

Parameter	Value	Source
Neuronal cytoplasm resistivity ρ_i	100 Ωcm	Ranck, 1963
Neuronal membrane resistivity ρ_m	3000 Ωcm	Ranck, 1963
Neuronal membrane capacitance C_m	3.2 μF/cm^2	Ranck, 1963
Neuronal fraction p_n	0.45	see above
Glial fraction	0.45	see above
Glial cytoplasm resistivity	100 Ωcm	assumed equal to ρ_i
Interstitial resistivity ρ_e	60 Ωcm	Ranck, 1963
Interstitial fraction p_e	0.1	see above
α	0.25	$=p_e+p_g/3$; See text[1]
mean axon length	400 μm	Ranck, 1963
axon radius	0.4 μm	Ranck, 1963
Membrane resistivity during depolarisation	1/7 * ρ_m	Araki and Terzuolo (1962); see text[2]

Table 5.2: Model parameters for human cortex.

Notes:

[1] *'α' is the size of the extracellular space as 'seen' by neurons. This factor includes one third the size of the glial compartment, since it appears as intracellular space to neurons.*

[2] *This value is the 'best' case of the range 1/1.8~1/7 reported by the authors for cat motoneurons*

The analysis above assumed that all neuronal membranes in the volume of tissue being measured depolarise at the same time. The true resistivity change is likely to be much smaller than this, because

i. the effect of membrane time constant will be to reduce the resistance change, as in §5.2.3;

ii. action potentials will probably not be conducted to all the processes of a given neuron (Freygang and Landau, 1955);

iii. there is no reason to assume that a physiological stimulus activates all the neurons in a particular volume. The proportion of neurons which do depolarise is unknown, but is likely to be small.

Spreading depression. During cortical spreading depression, the neurons depolarise intensely, and the extracellular space decreases in volume by about 50% (Hansen and Olsen, 1980). This may produce a large impedance increase, even at high frequencies. Reported values for measurement on rabbit or cat cortex cover the range 10% (Freygang and Landau (1955), measured with 0.1 msec pulses) to 100% (Hoffman *et al*, (1973), at 1600 Hz). At 50 kHz, Ranck (1964) reported a resistivity increase of 40%. The effect of reducing extracellular space was modeled by evaluating equation [5.6] with values of p_e, the proportion of extracellular space, between 0% and 10%. To maintain the same overall tissue volume, the proportions of glia and neurons were reduced in proportion.

5.3 Results

5.3.1 Longitudinal impedance change in nerve during complete depolarisation

Figure 5.4 shows the predicted decrease in the resistive component of the nerve impedance during complete depolarisation, evaluated from equation [5.1]. The resistivity decrease diminished rapidly above 10-100 Hz, as the resistivity of the tissue became dominated by the axoplasm rather than the membrane (figure 5.5). The decrease in the reactive component during depolarisation was even larger than for the resistive, but the initial magnitude of the reactive component is much smaller (figure 5.6). This would make it very difficult to measure.

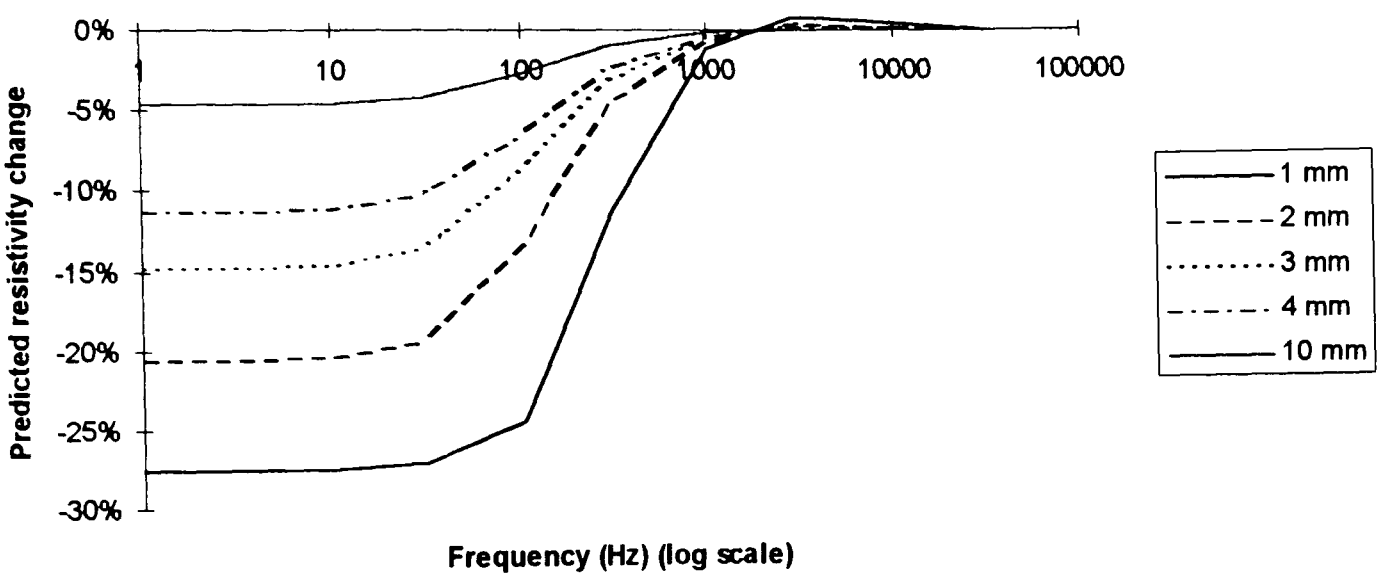

Figure 5.4: the predicted decrease in resistivity of a uniform nerve (4 μm fibre diameter) sample at various frequencies and electrode spacings, from eq. [5.1]

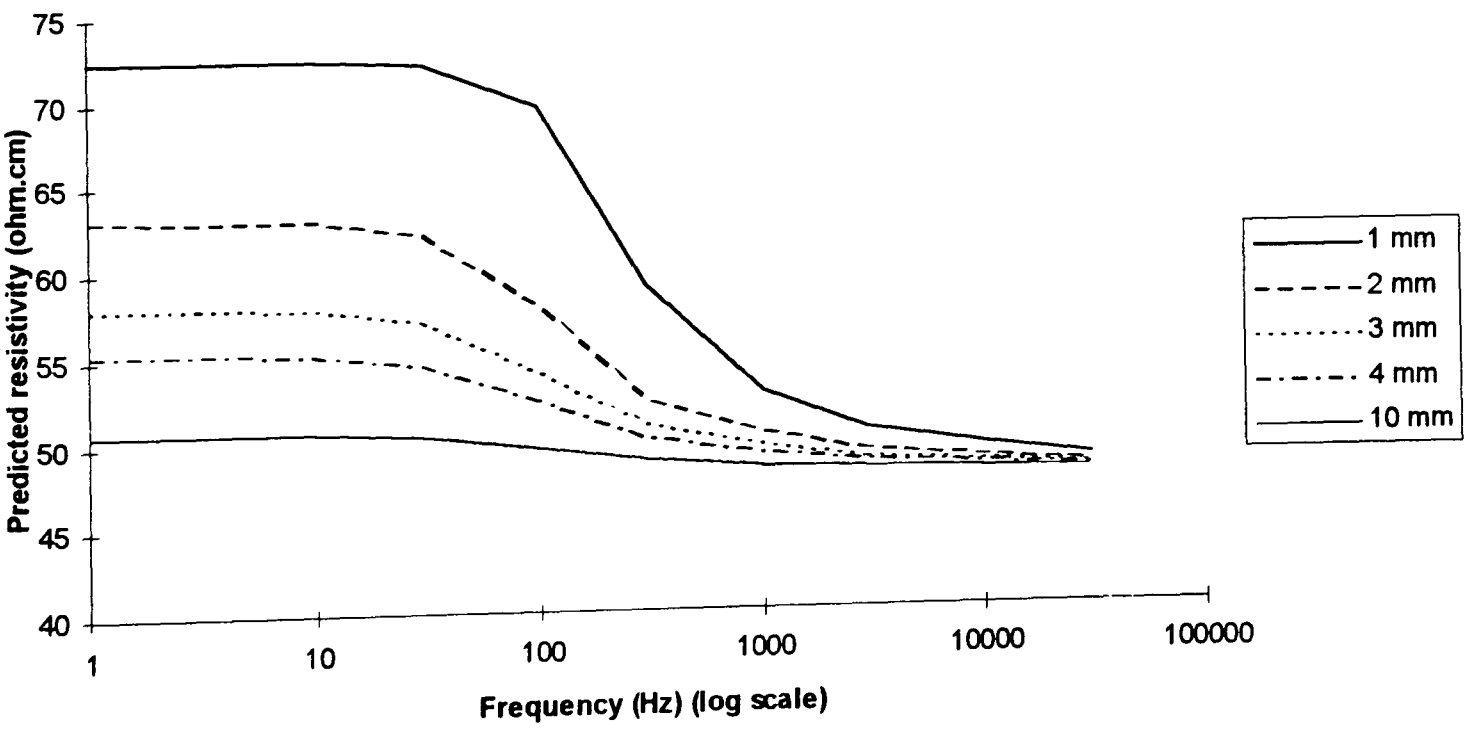

Figure 5.5: the predicted absolute resistivity of a nerve sample at various frequencies and electrode spacings, from eq. [5.1]

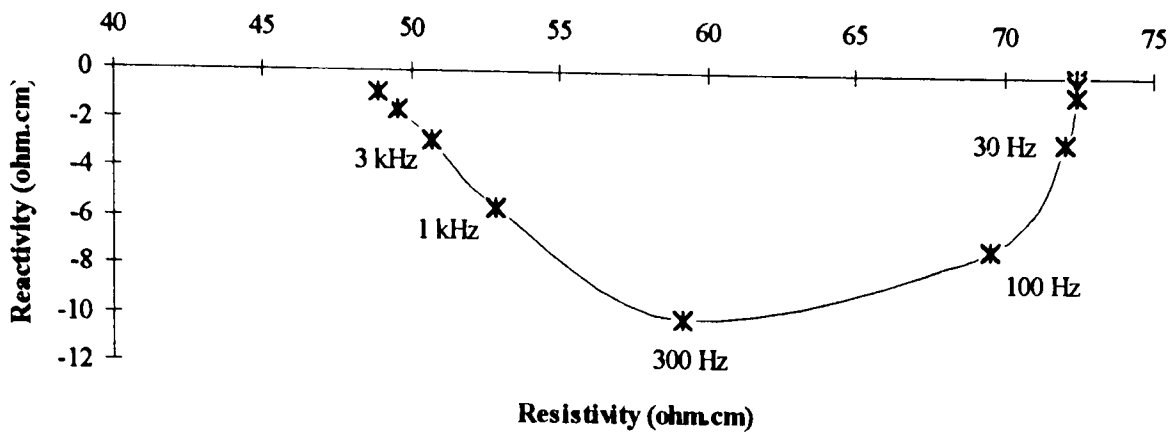

figure 5.6: the predicted resistivity-reactivity ('Cole-Cole') plot for a longitudinal nerve sample with 1 mm electrode spacing, from eq. [5.1]

As can be seen from figure 5.5, the longitudinal DC resistivity with 1 mm electrode spacing approximates to that of the extracellular compartment alone (about 80 Ωcm, or 20 Ωcm/α): only a small current enters the axon. At frequencies above a few hundred Hertz, the cell membrane is insignificant, and the intracellular compartment appears in parallel with the extracellular. The overall resistivity is then 48 Ωcm.

5.3.2 The effect of membrane time constant on low-frequency measurements

During depolarisation, the effective DC resistance change underestimated the steady-state resistance change, and lasted longer (figure 5.7). At peak depolarisation, $\delta V_m(L)_\tau$ / $\delta V_m(L)_0$ is (1-0.34)/(1-0.025) = 0.68. The apparent resistance change of the neuronal compartment will therefore be 0.68 times the value which would be obtained if the membrane depolarised indefinitely. Since most of the current is carried in the neuronal compartment, the overall effect of membrane capacitance on tissue resistance will be only slightly less than that on the neuronal compartment. For example, at DC and with 1 mm electrode spacing, the factor $k_\tau = 0.68$ which applies to the neuronal resistance corresponds to a factor of 0.70 for the whole tissue.

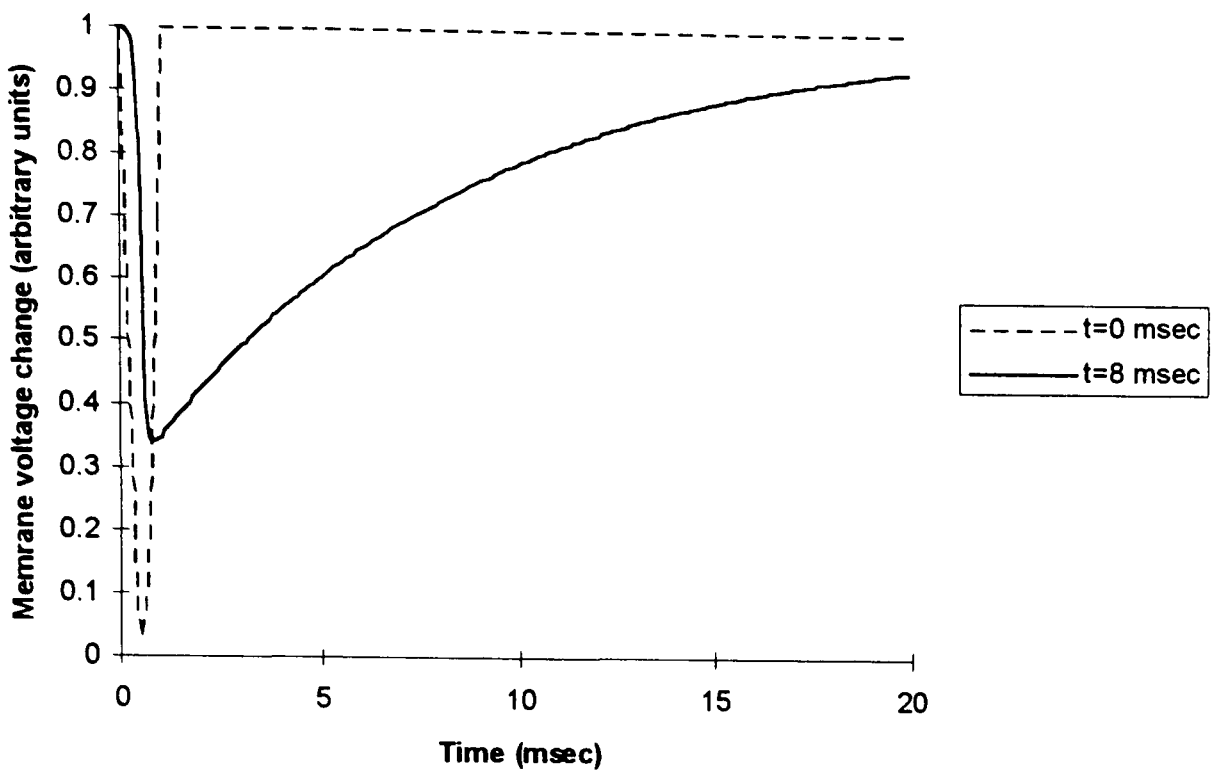

Figure 5.7: membrane voltage against time for membranes with time constants of 0 and 8 msec.

5.3.3 The effect of mixed fibre size and incomplete depolarisation

Figure 5.8 shows the compound action potential from (a) calculation from equation [5.4], and (b) measurement on crab nerves (see chapter 7).

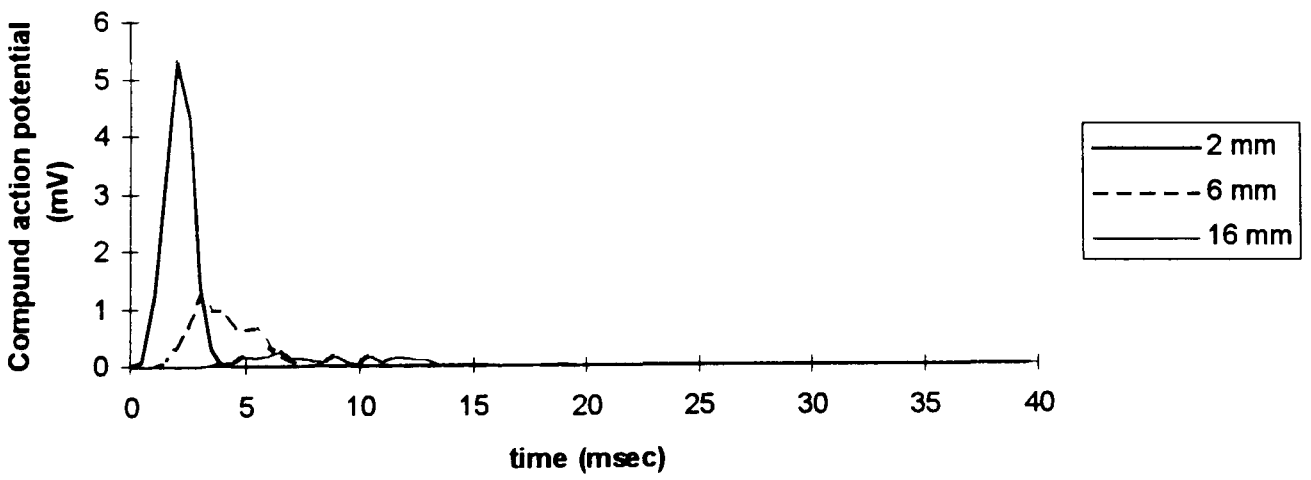

(a)

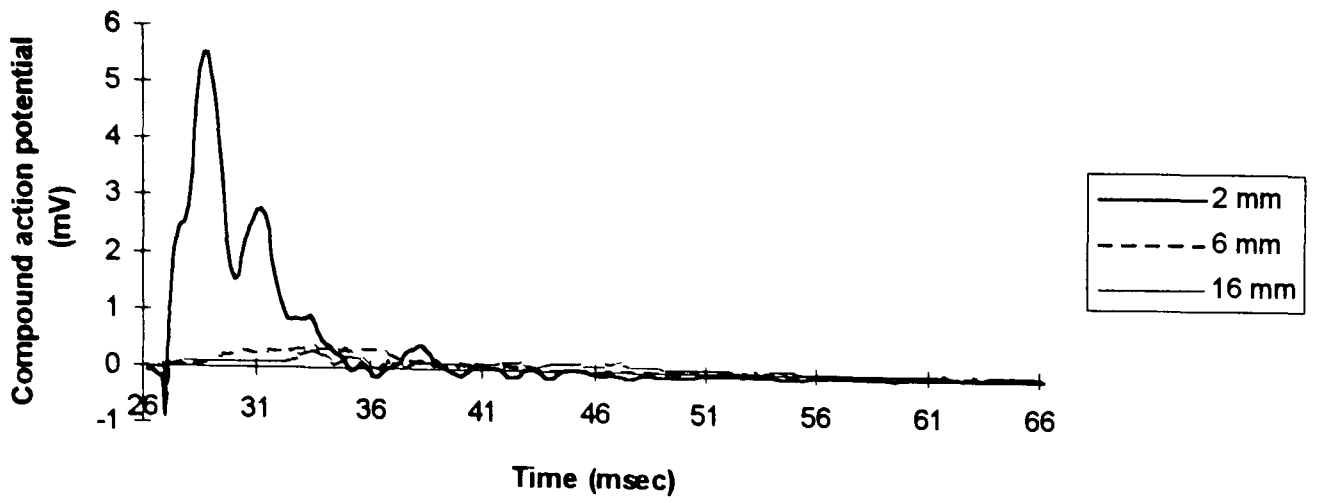

(b)

Figure 5.8 predicted (a) and measured (b) compound action potentials from crab walking-leg nerve. The legend shows the distance of the measuring electrode from the stimulating electrode.

Agreement to within a factor of 2~3 is obtained between calculation and measurement for the reduction in amplitude and increase in duration with increased electrode spacing.

The analysis described in §5.2.2 allowed for only one axon radius. For greatest accuracy, the value chosen for this radius had to be in some way representative of the nerve, which contains many fibres. From figure 5.3 it was possible to determine the mean diameter of the active fibres at the point of peak depolarisation (table 5.3).

Distance from stimulus	Mean fibre diameter at peak depolarisation
2 mm	2.9 μm
6 mm	8.6 μm
16 mm	10 μm

Table 5.3 Characteristics of the compound action potential at different recording positions

It can be seen that, as the distance from the stimulus increases, the mean fibre size at the point of maximum depolarisation increases. At 6 mm separation, the mean fibre radius which will be in effect at maximum depolarisation will be about 4 μm (≈ 8 μm / 2); this figure was taken for the axon radius in generating the results shown in figures 5.4-5.6.

Most of the experimental measurements on crab nerves (chapter 7) were carried out with a spacing between the stimulus and closest measurement electrodes of 5 mm, and a further 1 mm between measurement electrodes. The simulated compound action potential at 'zero distance' from the stimulating electrode is greater than that at 6 mm by a factor of five. If the argument put forward in §5.2.4 is valid, the resistance change during depolarisation will be reduced by the same factor.

5.3.4 Summary of results for unmyelinated nerve

Longitudinal measurement. Table 5.4 summarises the predicted resistivity decreases during depolarisation.

Frequency	Maximum decrease in 'ideal' conditions	... allowing for a fibre-size dispersion	... allowing also for membrane capacitance
DC	27%	5.4%	3.7%
30 kHz	0.045%	0.009%	0.009%

Table 5.4: predicted resistance decreases during depolarisation. The 'ideal' figures in column 2 are from figure 5.4, and assume a mean fibre diameter of 8 μm. Column 3 shows figures after adjustment for fibre size dispersion, assuming the measurement electrodes are 6 mm from the stimulus. Column 3 shows the further adjustment for charge storage in the membrane capacitance, which is only applicable to low frequencies.

5.3.5 Effective impedance of 'transverse' fibres

Figure 5.4 shows the predicted absolute resistivity of the 'ideal' nerve (*i.e.* identical fibres of diameter 4 μm) as a function of frequency.

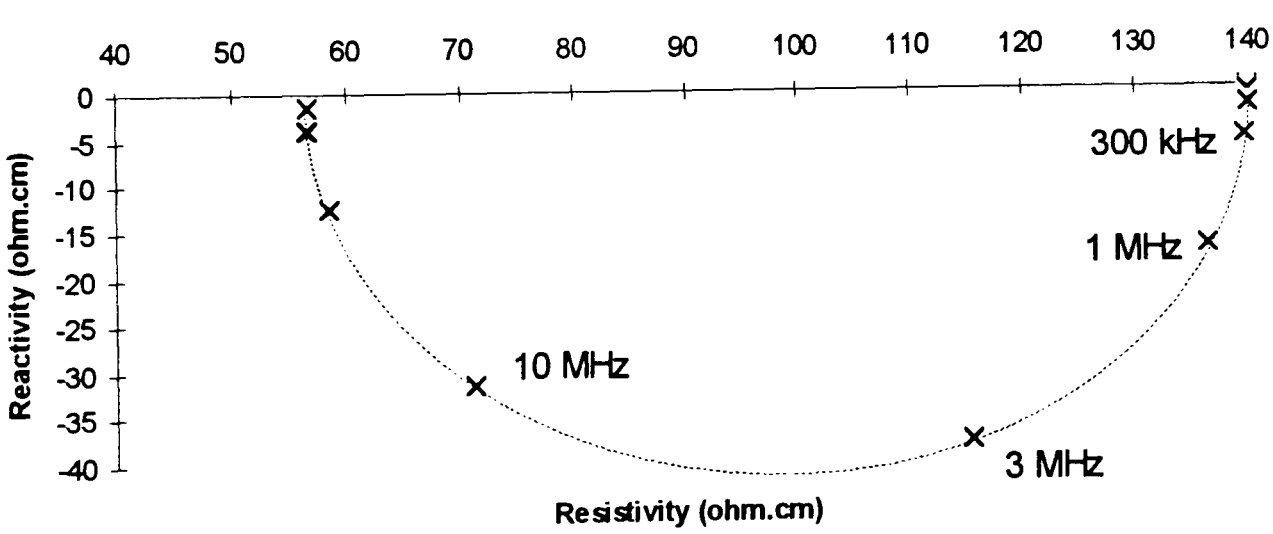

Figure 5.9: predicted resistivity-reactivity ('Cole-Cole') plot for a sample of nerve fibres transverse to the electric field (proportion of fibres = 75%). The dotted line is the best-fit semicircle.

The resistivity at DC is simply the resistivity of the extracellular space (20 Ωcm divided by α), increased by a factor which accounts for the increased average path length for current. For circular cells, this factor is approximately half the circumference divided by the diameter, or π/2.

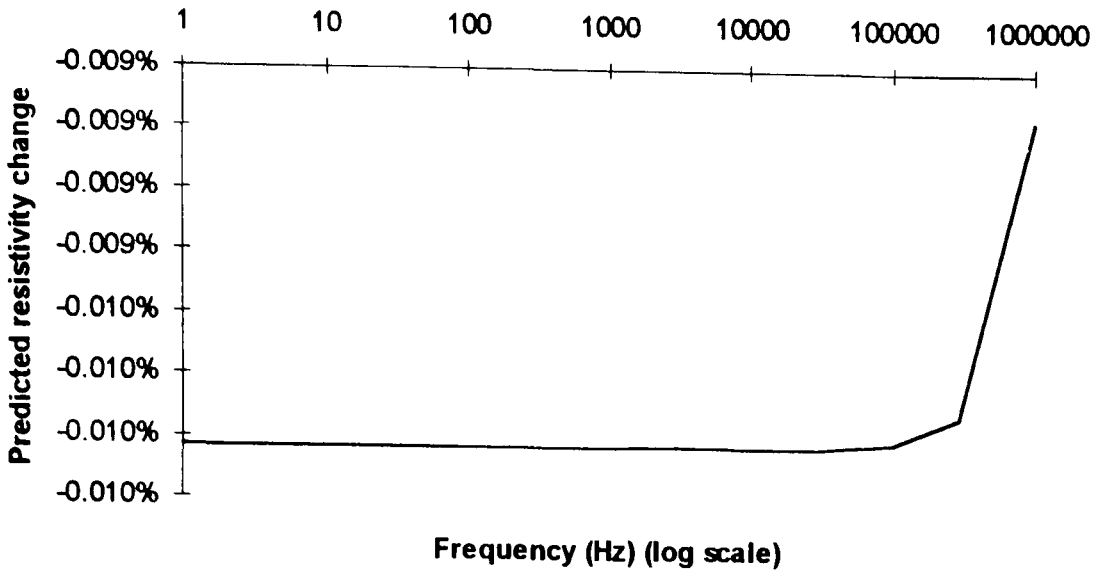

Figure 5.10: predicted change in transverse resistivity during depolarisation

This increased path length makes the transverse low-frequency resistivity somewhat higher than the longitudinal. The predicted resistivity change during depolarisation (figure 5.10) is much smaller than the transverse case.

5.3.6 Resistivity change in the cortex

During the action potential. With tissue parameters chosen to be appropriate for human cortex (table 5.2), the predicted cortical resistance decreased by 12.2% at DC, and 0.03% at 10 kHz.

During spreading depression. At 50 kHz, Ranck (1964) reported a resistivity increase of 40%. For this current model to predict such a large resistance change, based only on a change in extracellular volume, requires that the extracellular volume reduce to 0%. This is somewhat greater that the measured volume decrease of 50% reported by Hansen and Olsen (1981). Applying this latter figure to the model gives a predicted resistance increase of 16% at 50 kHz. It is possible other factors contribute to the impedance increase, including an *increase* in the membrane resistance of glia (Ranck, 1964). However, measured values of resistance change of 5%-20% at 50 kHz (chapter 8) are in good agreement with the model, even allowing for inaccuracies in the APT process.

5.4 Discussion

5.4.1 Optimum measurement frequency.

When the measuring electrodes are placed along the length of a nerve, the predicted resistivity change during depolarisation decreases rapidly at frequencies above 10 Hz -100 Hz. Since it is a change in *voltage* that must be measured when the nerve depolarises, both resistivity and its proportional change contribute to the decrease in signal size as the excitation frequency increases. For example, the resistivity decrease is about 600 times greater at DC than at 30 kHz. The absolute resistivity is about 30% higher. The overall signal size will therefore be about 800 times larger. There is little difference in the resistivity decreases between DC and about 10Hz. Neglecting technical problems, the optimum excitation frequency would be as near DC as possible.

For spreading depression, the choice of measuring frequency is not critical: large resistance increases are predicted even for frequencies of 50 kHz.

5.4.2 Optimum measurement configuration for peripheral nerve

For the experimental determination of resistivity change in nerve, the measuring conditions should maximise the measurability of the small resistance decreases. The excitation electrodes should be as close together as possible (see figure 5.4). The smallest practicable spacing is probably about 1 mm. The excitation electrodes need to be close to the stimulus, to reduce the effect of dispersion of fibre sizes. If they are too close, however, the distal voltage electrode will record a very large stimulus artefact. A reasonable compromise would be about 5 mm - 6 mm.

5.4.3 Measurability of the resistance decreases during depolarisation

Action potentials in crab nerve. With measuring conditions as above (§5.4.2), the predicted resistivity decrease during depolarisation is 3.7% with direct current excitation. The decrease in this figure is marked at frequencies over 10-100 Hz: at 30 kHz the model predicts a 0.009% resistivity change. The decrease with electrode spacing is less dramatic: at 4 mm the resistance decrease should be reduced to 40% of the value at 1 mm. The transverse resistivity in the resting condition is predicted to be about 2.6 times as high as the longitudinal, and to decrease by only about 0.01% during depolarisation.

Action potentials in cortex. The predicted resistivity decrease during depolarisation in the cortex was 12.2%, assuming complete depolarisation. The proportion of tissue which actually depolarises is not well known. Some idea may, however, be obtained by considering the size of the cortical EEG response to a stimulus, compared with a single-fibre action potential. The former is unlikely to be greater that about 40 μV - 100 μV, the latter of the order 40 mV - 100 mV. If there is the same ratio of resistivity change between full depolarisation and a realistic response, we might expect the latter to give a resistance change of about 0.01%.

Spreading depression in cortex. The predicted resistivity increase was 16%.

5.4.4 Possible criticisms of the model

This analysis has attempted to represent a tissue of very complex structure as a rather simple model. We should therefore not expect perfect quantitative results. A full analysis probably requires a calculation of the resistivity of a set of mixed-size fibres in three dimensions, rather than a 'mean' figure for fibres of representative radius. As well as being mathematically very complex, the accuracy of such an analysis would still depend on the accuracy of the information which could be provided about the detailed structure of the tissue. The results derived above can perhaps be taken as providing a 'semi-quantitative' indication of the sizes of impedance change which we might measure in APT. Other possible limitations of the model are described below.

Other tissue components are not taken into account. After neurons, glia and interstitium, the next largest constituent of grey matter is probably blood. This comprises only about 2% of the volume of the cortex, and has a higher resistivity (130 Ωcm for rabbit) than nervous tissue (Ranck, 1963). It is unlikely that it will have a significant effect on short-term resistance changes in the cortex.

The tissue is complex and irregular. The analysis above assumed that the properties of an individual cell, such as its membrane resistance, do not vary with length. If this is not the case the parameters listed in tables 5.1 and 5.2 may be taken as 'mean' values, and, provided the measurement encompasses a reasonable proportion of each axon, the results should still be applicable.

Cellular parameters are not well known. Factors such as neuronal membrane resistance vary widely between species; this is probably also the case for other factors. No doubt there is also variation between individuals and between cells in the same individual. Clearly, these variations will alter the predictions of the model. In practice, I have found no parameter which influences the results of the analysis out of proportion to its own variation. For example, table 5.5 shows the predicted cortical resistivity changes with various values of membrane resistance, fibre radius and extracellular space. No reasonable variation in these parameters changes the conclusions of the analysis.

Membrane resistance $\rho(\Omega cm^2)$	Fibre radius (μm)	Proportion of extracellular space (%)	DC resistivity change during depolarisation
3000	0.4	0.1	-12.2%
3000	0.4	0.2	-9.55%
3000	0.8	0.1	-12.4%
1000	0.4	0.1	-10.6%

Table 5.5: the effect on predicted cortical resistivity change of some variations in model parameters

The effect of incomplete depolarisation on cortical impedance change is difficult to predict. This issue was discussed above. Regardless of the validity of the arguments given, the principal conclusion of the analysis - that of the optimum frequency - seems unlikely to be changed.

5.4.5 Myelinated fibres

The white matter of the brain and the peripheral nerves of vertebrates are mostly myelinated. Myelin is essentially an insulator: current can cross the axonal membrane only at the nodes of Ranvier, where the myelin is depleted. From the dimensions given by Hodgkin (1938), the ratio of the surfaces areas of the internodal to nodal membrane for the sciatic nerve of the frog is about 500:1. When the axon depolarises, only this part of the membrane will show a resistance change. If the whole membrane has a resistance which is dominated by the myelinated part ($\rho_m \approx 10^5$ Ωcm), then the difference between transverse and longitudinal resistivities will be determined entirely by the difference in the effective path lengths for conduction in the two directions. In practice, the ratio of transverse to longitudinal resistivity is about 10 (Nicholson, 1965): too high for this to be the only factor. Clearly, some other element carries current in the transverse direction. It is more likely that neuroglia are responsible for the additional current, rather than there being significant membrane current in the myelinated fibres.

6. Sensitivity requirements for APT in neurophysiology: a finite element model study

6.1 Introduction

6.1.1 Resistivity changes in the brain

Chapter 1 described possible neurological and neurophysiological applications of APT. These applications were associated with resistivity changes of various magnitudes and durations. This chapter describes a finite element model of the head which was used to determine the boundary voltage changes produced by resistivity change of different sizes. For the purposes of this study, resistivity changes in the brain are loosely divided by their physiological mechanisms into 'large', 'medium' and 'small' categories (table 6.1). The resistivity change which might be associated with the 'small' (action potential) category is taken from the model described in chapter 4. It predicted that the resistivity change would be maximal with DC excitation: about 0.01%. A similar figure was obtained from measurement on rabbit cortex (chapter 8). The boundary voltage change to be measured will depend on technical factors (see sections 6.1.2 and 6.1.3) and the application, as well as on the characteristics of the resistivity change itself.

Category	Approx. size of resistivity change	Approx. time duration	Physiological mechanism
'Large' changes	50%	Minutes	Stroke; anoxia
'Medium' changes	1%	Seconds to minutes	Perfusion variation
'Small' changes	0.01%	Milliseconds	Normal action potential activity

Table 6.1: categories of cerebral resistivity variation. The second column shows the representative resistivity change applied to the model described in the text.

In some applications, for example studies of evoked changes in perfusion, the measurements may be repeated and averaged. This will probably not be practicable in epilepsy, and certainly not in stroke or intraventricular haemorrhage.

6.1.2 Electrode placement

Three electrode placements will be considered, having differing degrees of 'invasiveness'.

Extracranial electrodes. While extracranial recording is desirable for practical and ethical reasons, it is subject to technical difficulties. These are the result of the high resistivity contrast (about 30:1) between the skull, scalp and cerebro-spinal fluid (CSF). Many workers have considered this problem to be insurmountable (*e.g.*, Holder, 1993). They expected the applied current to be mostly confined to the scalp and not to enter the brain. Such pessimism was not universal, however. Nathan *et al.*, (1993) studied the effect of extracranial electrode separation on intracranial current density, from the

standpoint of cortical stimulation. These authors estimated a ratio J_s/J_c, where J_s is the current density in the scalp and J_c that in the cortex. With electrodes 2 cm apart, J_s/J_c was 3.5; it decreased to 2:1 at 13 cm separatation. In the newborn, with 'diametric' (electrodes diametrically opposite one another) excitation, conditions are even more favourable: Gadd *et al.*, (1993) estimated that 81% of the applied current entered the brain in this configuration.

Embedded electrodes: In surgical patients it might be feasible to implant electrodes in the skull, with their surfaces in the subdural space. This is minimally less invasive than intracranial recording, and may overcome the effect of the scalp on current density.

Intracranial electrodes: These are routinely used before surgery in patients undergoing investigation for drug-resistant epilepsy. APT could probably make use of the same electrodes (Holder, 1993).

Only extracranial electrodes would be suitable for use in volunteers; the other electrode configurations might be suitable for surgical patients.

6.1.3 The effect of current pattern

'Current pattern' refers to the distribution of the excitation current between electrodes. Current patterns may be divided into 'bipolar' (two electrodes supplying current) and 'multiple' (more than two electrodes supplying current) techniques. For either of these we have also to consider the spatial frequency of the applied current. For bipolar techniques this amounts to choosing the separation between driven electrodes.

Multiple or bipolar? The 'cosine (θ)' pattern can be shown to give the best sensitivity to a discrete resistance change in any initially-uniform cylindrical object (Seagar *et al.*, 1987). With this pattern, the current amplitude at each electrode varies as the cosine of the angle between the electrode and some arbitrary radial line. Gisser *et al.*, (1987) showed that, for any initial distribution of impedance, there is a 'best' current pattern for maximising sensitivity. Attempts to determine and apply such patterns are referred to as 'adaptive' (Gisser *et al.*, 1988) or 'optimal' (Kyriacou *et al.*, 1993; Paulson *et al.*, 1993) techniques. In practice, the 'best' current pattern often turns out to be 'cosine-like' (Barber, 1993). I have therefore assumed that the 'cosine (θ)' pattern represents the adaptive approach, at least as far as sensitivity is concerned. Despite the increased theoretical sensitivity such techniques provide, multiple-excitation methods have two practical problems:

i. All current sources must be precisely matched, to avoid the problem of common-mode current injection (chapter 2).
ii. The *total* amount of current applied is greater than for bipolar patterns, for a given current from any *single* electrode. For the 'cosine (θ)' case with 16 electrodes, the total current will be

$$I+I\cos(22.5°)+\cos(45°)...$$

where I is the peak current at 0°. The total current will therefore be about 10 times as high as the corresponding bipolar configuration. Medical safety standards limit the total current; for a multiple-

electrode excitation technique to be worthwhile it needs to provide a sensitivity that is not merely better, but ten times better, than a bipolar pattern.

Spatial frequency. The most widely proposed bipolar current patterns are 'adjacent' and 'diametric' (also known as 'polar' and 'opposite'). Diametric excitation has a low spatial frequency and is the closest bipolar approximation to the cosine. We therefore expect it to provide a better sensitivity than the adjacent pattern. §6.5.3 discusses the effect of current pattern on the spatial resolution of the images.

6.1.4 Experimental design

This study was carried out to determine:

i. which of the three current patterns described in §6.1.3 is optimum for sensitivity,
ii. how much extracranial measurement reduces the sensitivity compared to intracranial, and
iii. would we expect measurable boundary voltage changes to accompany the resistivity changes in table 6.1, with any current pattern?

A two-dimensional finite-element model simulated the distribution of current and voltage in the head. The model had layers representing the scalp, skull, CSF and brain. The model was first validated against theory and a physical phantom of similar structure. It then simulated resistivity disturbances of 0.01%, 1% and 50%, occupying 1% of the cranial area, in various positions within the brain.

6.2 Theory

The finite element modelling technique to be described is based closely on that described by Woo (1990), who provides full mathematical details. This chapter presents only a summary of the mathematical analysis.

6.2.1 Overview of the finite-element method

The steady-state potential, current and resistivity in a body are related at low frequencies by Poisson's equation (see chapter 3 for more details):

$$\nabla.\sigma\nabla\phi = 0$$

where σ is the conductivity, ϕ is the potential and ∇ is the Poisson operator. σ and ϕ are spatial fields whose magnitudes are functions of position. ϕ is also a non-linear function of conductivity. Analytical solutions to this equation have been found only for simple resistivity distributions. For arbitrary distributions we normally use a numerical technique. Of these techniques, the finite element method (FEM) is the most widely used in APT research. This method divides the body into a large number of regions (*elements*), each with uniform resistivity. Together these elements form a network (*mesh*). A relationship between resistivity, potential and current is found for any uniform element, and used to specify the potential at the vertices (*nodes*) in terms of the resistivity and current. Since the potentials at interconnecting nodes must be equal, the potentials are related to one another by a set of simultaneous linear equations. This set of equations can be solved to obtain the voltage distribution for any applied current.

In a two-dimensional FEM problem the elements are usually triangular or quadrilateral; triangular elements were used in this study. There are a number of methods for specifying the potential throughout the

element. Greater accuracy may be obtained for a given element size by placing extra nodes within an element and interpolating between them. For APT it seemed reasonable to seek an increased accuracy by increasing the actual *number* of elements and having no 'internal' nodes. This is computationally simpler, and allows a greater spatial resolution of resistivity. The finite element modelling technique therefore comprises three stages:

i. calculation of the *element matrix* which relates currents and voltages within a single element,

ii. construction of the mesh, and

iii. generation of the *master matrix*, which associates the individual elements with the mesh.

6.2.2 Generation of the element matrix

For a triangular element with vertices (x_1, y_1), (x_2, y_2) and (x_3, y_3), the solution of Laplace's equation inside the element can be expressed as follows:

$$\mathbf{I_e} = \mathrm{y}.\mathbf{V_e}$$

where $\mathbf{I_e}$ and $\mathbf{V_e}$ are column vectors representing the currents and voltages at the three vertices. The element admittance matrix y is given by:

$$\mathbf{y} = \frac{\sigma}{4\Delta}\begin{bmatrix} b_1^2 + c_1^2 & b_1b_2 + c_1c_2 & b_1b_3 + c_1c_3 \\ b_1b_2 + c_1c_2 & b_2^2 + c_2^2 & b_2b_3 + c_2c_3 \\ b_1b_3 + c_1c_3 & b_3b_2 + c_3c_2 & b_3^2 + c_3^2 \end{bmatrix}$$

where $\Delta = (x_2y_3 - x_3y_2 + x_3y_1 - x_1y_3 + x_1y_2 - x_2y_1) / 2$, the area of the triangle; σ is the conductivity of the element, and coefficients *a*, *b*, and *c* are given by

$$a_1 = x_2y_3 - x_3y_2$$

$$b_1 = y_2 - y_3$$

$$c_1 = x_3 - x_2$$

The other *a*'s, *b*'s and *c*'s are obtained by cyclic permutation of the subscripts.

6.2.3 Construction of the mesh

The size and shape of the mesh elements affects the numerical stability of the solution. For triangular elements the angles should be as close to equal as is possible. The circular region was divided into 20 concentric rings, with one node at the centre, six in the next ring, eighteen in the next, up to the outermost ring. Triangular elements were made by linking three adjacent nodes, starting from the centre and working outwards. This yielded a mesh with a very regular structure: the triangles are close to equilateral. The final mesh (figure 6.4) had 1141 voltage nodes and 2166 elements. The 'thickness' of the rings was not constant, for reasons discussed below; it decreased by a factor 0.94 at each step from the centre.

6.2.4 Generation of the master matrix

The master matrix **Y** relates the currents at all points in the object, to the potential at corresponding points as follows:

$$\mathbf{I} = \mathbf{Y}.\mathbf{V}$$

where **I** is the vector of nodal currents and **V** is the vector of nodal voltages. The master matrix was constructed by extracting the coefficients for each node from each appropriate element matrix. Each node must be numbered *globally* (*i.e.*, for the whole mesh) as well as *locally* (for the element). The nature of the global numbering is, in principle, irrelevant. In practice the global nodes were numbered from the centre outwards; this reduces the overall computation time by increasing the sparsity of the master matrix (Hua *et al.*, 1990).

Having computed the master matrix, the nodal voltages may be found by solving for **V**. The only currents injected into the system are the applied currents at the boundary; all other elements in the vector **I** are zeros. One node must be set to a known potential to obtain a unique solution; the central node was chosen arbitrarily to be a zero-volt point.

6.3 Validation of the model

Two validation technqiues were applied. First, predicted boundary voltages for a uniform resistivity distribution were compared with theoretical values. This was primarily to detect errors in the software implementation. Second, complete sets of boundary voltage data were generated for various resistivity distributions, and reconstructed into images. These images were compared with corresponding measurements on a physical phantom. The presence of the 'skull' leads to a large resistivity contrast between adjacent elements on the model. This could potentially cause mathematical instability. To test that this was not the case, the physical phantom and finite element model both included a simulated 'skull' in this validation exercise.

6.3.1 Method

Comparison with theory. Boundary voltages produced by the model were compared with the theoretical values for a cylinder with a uniform resistivity of 1.0 Ωm and a 10 cm radius (Chen and Paoloni, 1992). The theoretical model assumed a continuous current distribution of 1 mA * cos (θ). We should expect the finite element model to underestimate the theoretical one, since the current injection is into 'point' electrodes, which reduces the total applied current. The boundary voltage 'profiles' should, however, be similar.

Comparison with physical phantom. The phantom (figure 6.1) consisted of two parts. The base was a shallow dish containing saturated calcium sulphate (resistivity 2.87 ± 0.01 Ωm) to a depth of 8 mm. Into this base was inserted a plaster-of-Paris (hydrated calcium sulphate) ring to represent the 'skull'. The resistivity of the 'skull' was 90 ± 5 Ωm. The use of calcium sulphate rather than saline was expected to reduce any tendency for the outer layer of the plaster ring to dissolve in the fluid and change its dimensions or resistivity. A fortunate coincidence gives the plaster 'skull' a resistivity thirty-one times than that of the fluid, a similar resistivity contrast to that between skull and brain. The 'skull' was allowed to equilibrate in the fluid for at least 24 hours before making measurements.

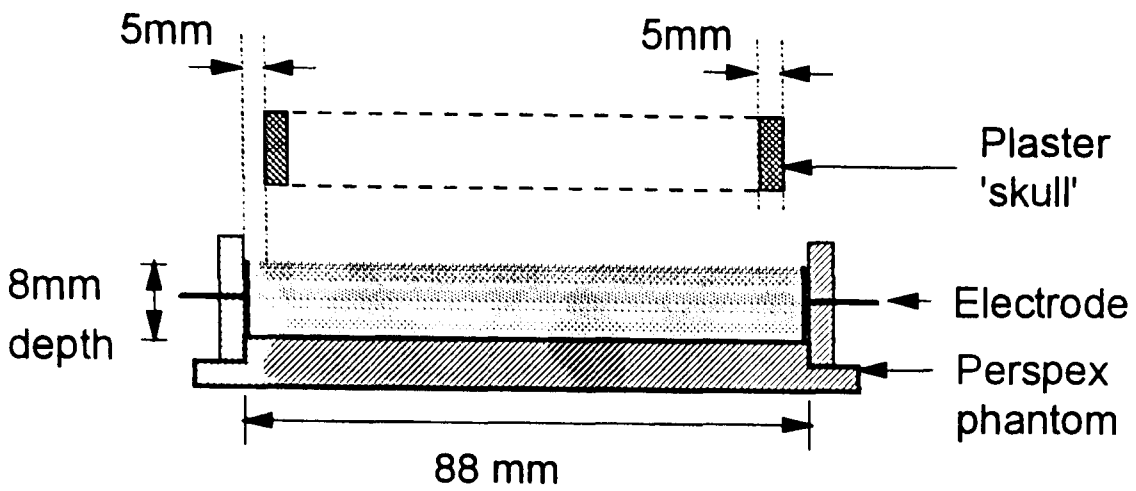

Figure 6.1: construction of the 'two-dimensional' physical phantom, shown in cross-section

Since the fluid level was shallow, and of the same height as the electrodes, the current was confined almost to a 'two-dimensional' distribution. We should therefore expect the boundary voltages to be similar to those from the two-dimensional finite element model, except for measurement error. A perspex rod created a resistivity disturbance at one of seven positions between the centre and edge. These resistivity disturbances occupied 1% of the phantom area. APT data were recorded using the Sheffield Mark 1 (IBEES, Sheffield) data collection system. Finite element simulations were then performed of a 50% resistivity increase against a background containing a model of the plaster 'skull'. The dimensions of the 'skull' in the model matched those of the physical phantom as closely as the mesh allowed. The position of the resistance increase was varied from the centre to the edge of the model in four steps. Images from the phantom and the FEM were reconstructed using the Barber and Seagar (1987) algorithm.

6.3.2 Results

Comparison with theory. The boundary voltage predicted by the FEM has the same form as the theoretical one, but underestimates the magnitude as expected (figure 6.2).

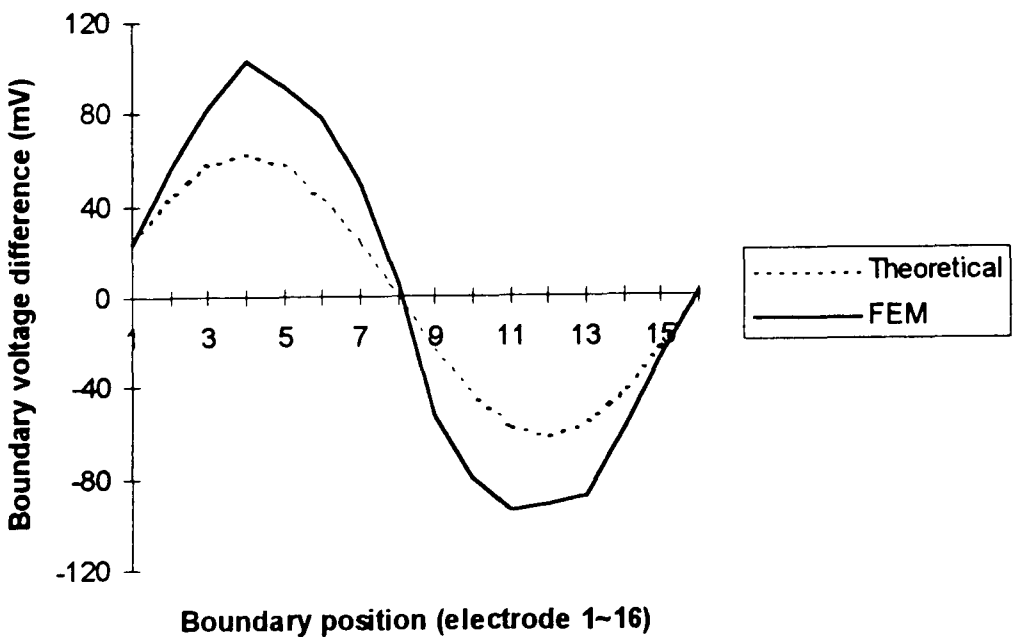

*Figure 6.2: comparison with theoretical values of the boundary voltages from the finite element model. The theoretical model has a continuous current distribution I = 1 mA * cos (θ).*

Comparison with physical phantom. There was good agreement between the position and width of the resistivity change in images from the FEM and the phantom (figure 6.3). Both techniques produce images that underestimate the distance of the features from the centre, as previously described for the head (McArdle, 1988).

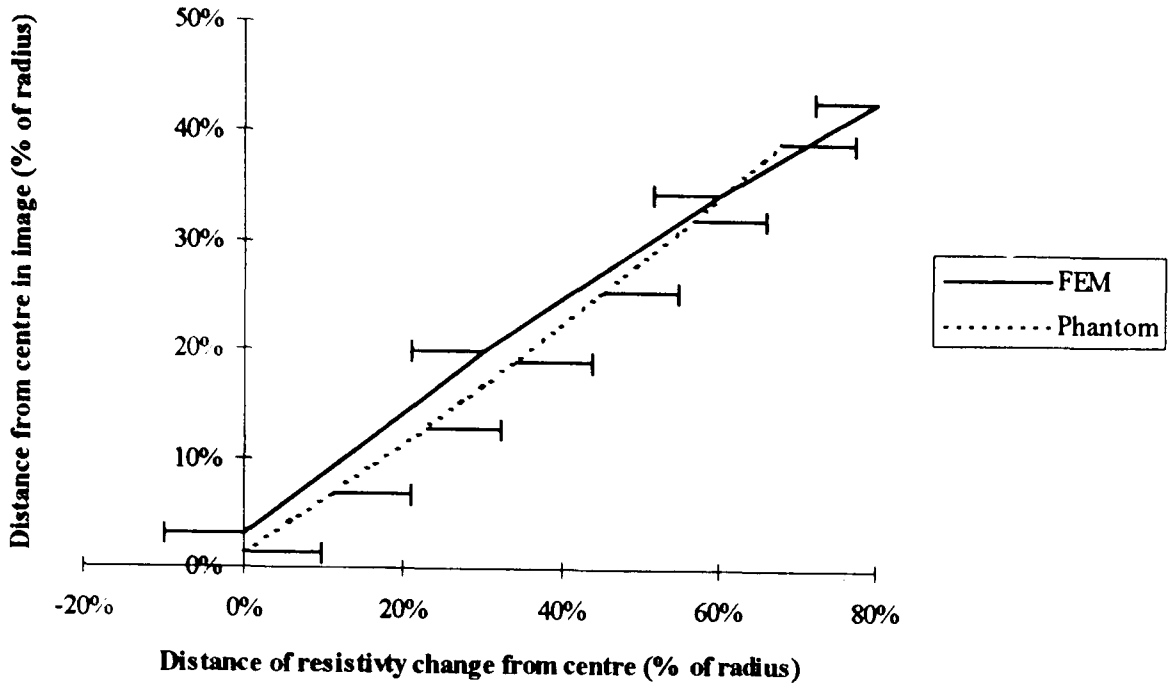

Figure 6.3: comparison of the finite-element model and physical phantom with 'skull' in place. The x-axis shows the position at which the test-object or modeled resistivity change was placed. The y-axis shows the position of the object in the image. Both measurements are expressed as distance from the centre, as a fraction of the radius. The error bars show the half-width at half-maximum, also as a fraction of the radius

6.4 Simulation of resistivity changes in the brain

6.4.1 Method

Configuration of the mesh. Approximate thicknesses of the skull, scalp and CSF spaces were obtained by measurement of MRI images of the normal adult cranium (Elster, 1988) at the level of the temporal lobes. An average was taken of four measurements at the front, back, left and right of the head. An individual thickness could vary by up to 50% of the average value. The 'rings' of the mesh were assigned to skull, scalp, brain or CSF regions, to give the best match to the measured thicknesses (figure 6.4). To avoid the use of mesh elements with very acute angles, the CSF region was made one third the thickness of the skull (one ring) rather than 15% of its thickness. Its resistivity contrast was decreased to compensate. Since there was little marrow in evidence, marrow cavities were not included in the model. Table 6.2 shows the thicknesses and resistivities of the various layers of the mesh.

Component	'Ring' thickness (% of head radius)	Rings in model (1=outermost, 20 = innermost)	Resistivity
Scalp	3%	1	5.8 Ωm
Skull	9%	2,3,4	150 Ωm
CSF	3%	5	1.4 Ωm
Brain	85%	6-20	5.8 Ωm

Table 6.2: configuration of the finite element mesh

The best spatial resistivity of a sixteen-electrode APT system is about 10% of diameter (Sinton *et al.*, 1992). The mesh therefore had a mean spatial resolution much finer than this: 5% of radius. This required approximately 2000 elements. The spatial resolution of the mesh was greater at the boundary than at the centre. This allowed the modelled thicknesses of the scalp and skull to agree more closely with measurement. The use of a gradual change in element size, rather than introducing extra nodes at the boundary, prevented the introduction of unfavourable angles in the elements.

Implementation of the finite-element process. Apart from the solution of the linear system of equations as specified by the master matrix, all stages of the finite-element computation were carried out by a program written in Pascal for Microsoft Windows (Borland Inc.; Pascal V6.0). The linear system was solved using MATLAB (The Math Works Inc.). The master matrix was large (~1.3 million elements) but sparse (only 0.59% of elements were non-zero). The Pascal program therefore produced a list of non-zero nodes to be read by MATLAB, rather than a complete matrix. The longest part of the computation was the construction by MATLAB of a sparse matrix from this list. This took about 10 seconds (on a 50 Mhz i486 PC); the solution took a further 3 seconds for each current pattern.

Simulations. Boundary voltage profiles were generated for resistivity increases of 0.01%, 1% and 50% at five points between the centre of the 'head' and the inner edge of the 'skull'. Adjacent, polar and cosine current patterns were applied, for each of intracranial, extracranial and embedded electrodes. The area of the resistivity change was as close to 1% of the overall area as the mesh allowed. This figure was chosen on the basis of measurements of evoked reponses in the rabbit brain (chapter 8). The area of the cortex which showed a maximal response to median nerve stimulus was about 2 mm in diameter, while the brain itself had a diameter of about 20 mm.

6.4.2 Results

Normalised boundary voltage change. Normalised boundary voltage (g_n) is defined as

$$g_n = \frac{\delta V}{V}$$

where δV is the change in voltage caused by the change in resistivity, and V is the initial voltage. In all

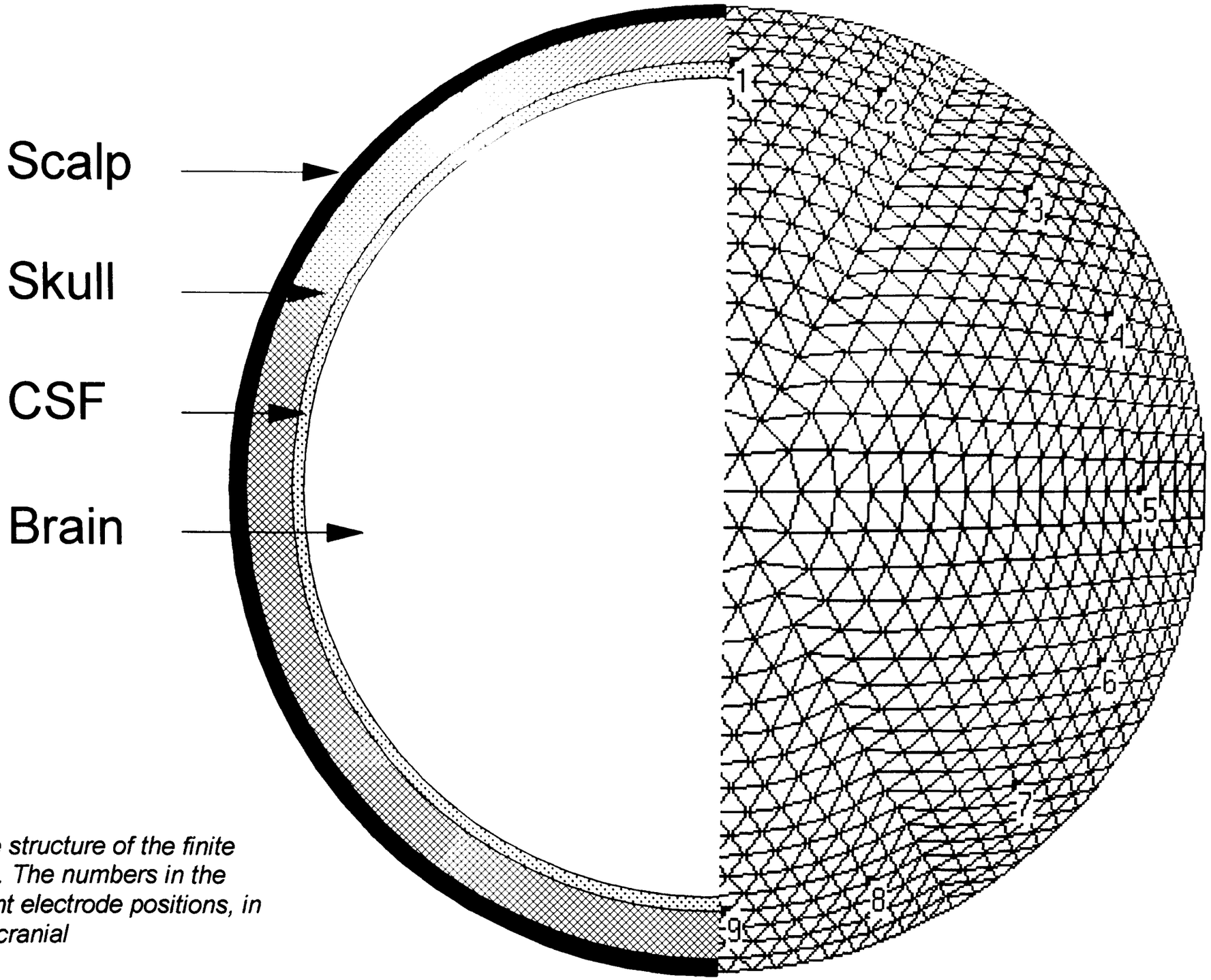

Figure 6.4: the structure of the finite element mesh. The numbers in the mesh represent electrode positions, in this case intracranial

simulations the magnitude of the normalised voltage change for the 'embedded' electrodes was only 15-20% lower than the equivalent value obtained with intracranial electrodes. To reduce the amount of data to be presented, I have taken these configurations to be approximately equivalent. Table 6.3 shows the normalised voltage change predicted for a central resistivity change. These figures are expressed graphically, as a required sensitivity in dB, in figure 6.5.

Resistivity change	Maximum boundary voltage change with intracranial electrodes			Maximum boundary voltage change with extracranial electrodes		
Excitation→	Cosine	Diametric	Adjacent	Cosine	Diametric	Adjacent
50%	18.6%	8.9%	0.65%	3.14%	2.64%	0.48%
1%	0.47%	0.22%	0.02%	0.08%	0.07%	0.01%
0.01%	0.005%	0.002%	0.0002%	0.001%	0.0007%	0.0001%

Table 6.3: Maximum boundary voltage changes with adjacent, diametric and cosine current patterns

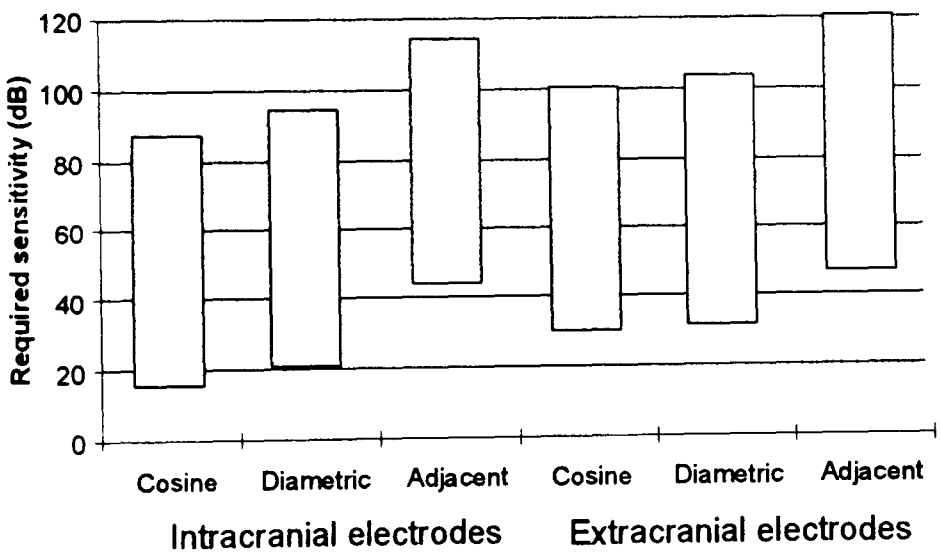

Figure 6.5: the figures of table 6.3 represented as a sensitivity requirement, in dB. The rectangles represent the complete range of resistivity change, from 0.01% to 50%. The larger sensitivities correspond to the smaller changes.

The most peripheral resistivity change studied was 10 mm from the skull. With this change, the largest boundary voltage change was a maximum of 10 times larger than the value in table 6.3 with intracranial electrodes, and about 6 times larger with extracranial electrodes (adjacent excitation).

Absolute boundary voltage. Figure 6.6 shows the absolute voltages at various points on the boundary. The largest values for all three excitations are similar, but that for adjacent excitation falls rapidly with distance from the excitation electrodes. Table 6.4 summarises figure 6.6; it shows the absolute boundary voltage between the electrodes that showed the largest proportional voltage changes.

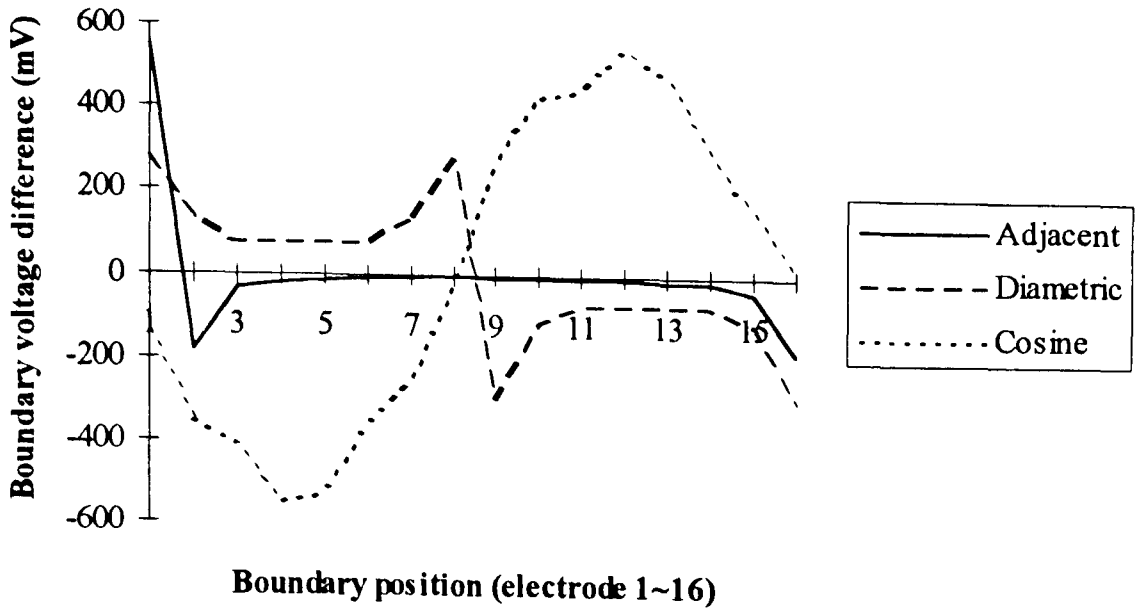

(a)

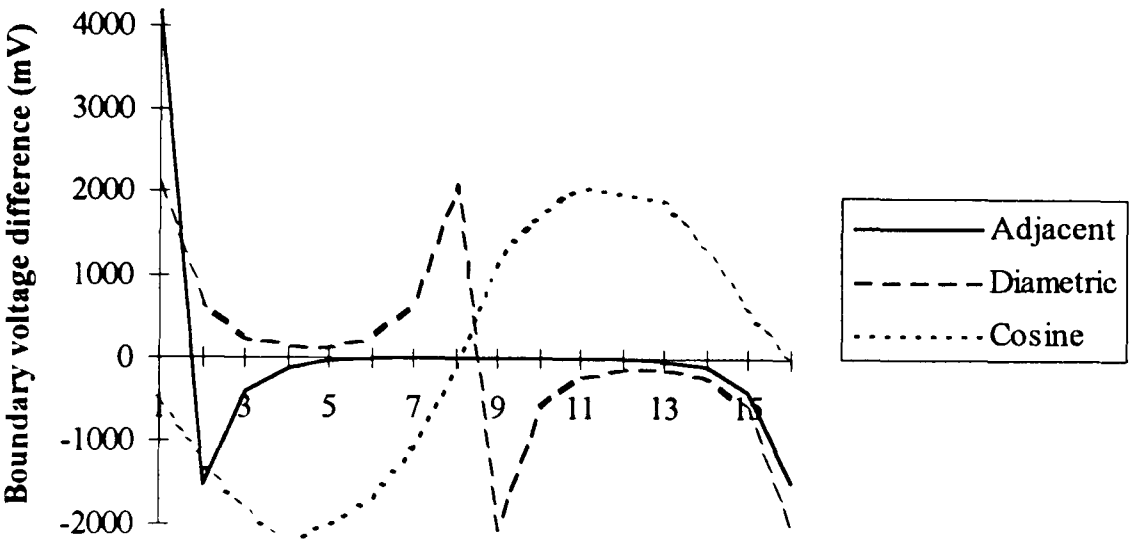

(b)

Figure 6.6: absolute boundary voltages for adjacent, diametric or cosine excitation, with (a) intracranial and (b) extracranial electrodes.

Electrodes	Intracranial			Extracranial		
Excitation→	Cosine	Diametric	Adjacent	Cosine	Diametric	Adjacent
Voltage (mV)	532	76	6.7	2008	226	7.7

Table 6.4: absolute boundary voltage differences at the position which shows the largest voltage change for a central resistivity increase. Excitation current was 1 mA

Absolute boundary voltage change. For particular current amplitude, the figures of tables 6.3 and 6.4 allow us to calculate an absolute boundary voltage change (table 6.5). The current amplitude for 50% and 1% changes was set to 1 mA, except for the cosine drive which was limited to 100 μA (see §6.1.3). I have assumed that the smallest changes, corresponding to neuronal depolarisation, will be recorded using DC excitation. The excitation amplitude in this case was also 100 μA.

Resistivity change	Absolute boundary voltage change with intracranial electrodes			Absolute boundary voltage change with extracranial electrodes		
Excitation→	Cosine	Diametric	Adjacent	Cosine	Diametric	Adjacent
50%	9.8 mV	6.8 mV*	43 μV*	6.3 mV	6 mV*	37 μV*
1%	2.5 mV	160 μV*	1.3 μV*	1.6 mV	160 μV*	0.77 μV*
0.01%	2.6 μV	150 nV	1.3 nV	2.0 μV	150 nV	770 pV

Table 6.5: Absolute boundary voltage changes corresponding to the figures in table 6.3. Excitation current was 100 μA, except where marked '' for 1 mA*

6.5 Discussion

6.5.1 Summary of results

Normalised voltage change. Unsurprisingly, cosine excitation alway produced the greatest normalised voltage changes. Diametric excitation produced voltage changes between 40% and 89% of the cosine, while adjacent excitation showed changes of 4%-15% of the cosine.

Absolute boundary voltage change. All three current patterns produced peak boundary voltages within a factor of two of each other[1]. However, there is a marked difference in how these voltages vary with electrode position. Adjacent excitation produces voltages that fall more rapidly with distance from the excitation electrodes than the cosine. Diametric excitation produces voltages that fall less rapidly, but the voltages are still seven times smaller than for the cosine at the electrodes most distant from the current injection. Where the resistivity change is central, both the bipolar patterns studied suffered from having the smallest boundary voltages at the position that shows the largest proportional change. Taking the proportional change and the absolute voltage into account, the cosine pattern produces absolute voltage changes up to 18 times as large as diametric, even allowing for the smaller allowable current. The adjacent pattern produces absolute voltage changes about 2000 times smaller than the cosine.

Intracranial or extracranial electrodes? The figures in table 6.5 suggest that intracranial electrodes will normally record a voltage about twice that for an extracranial placement.

6.5.2 Can the required sensitivities be achieved?

To determine the required sensitivity, we need to consider both normalised and absolute boundary voltage changes.

'Large' resistivity changes (> 10%). Predicted voltage changes are tens of microvolts, even with adjacent excitation; these should not present a problem, even in this worst case.

---

[1]It is not relevant for this study that, for bipolar current patterns, these peak voltages appear at electrodes which are carrying current. For cosine excitation we must either provide separate current and voltage electrodes, or record from current electrodes; it is only fair to allow similar considerations to apply to the bipolar methods.

Figure 6.7 shows an image obtained from the 'Mark 1' system of a centrally-placed 50% resistivity increase in the 'skull' phantom. The resistivity increase was created by a cylinder of polyacrylamide gel (Holder and Khan, 1994) whose radius was 10% that of the phantom. A corresponding image from the finite element model is shown for comparison. The image quality is good, apart from an artefactual region of resistivity decrease above and to the right of the object. This was probably due to the plaster 'skull' being slightly off-centre; the sensitivity of the system is more than adequate. In focal epilepsy, the resistance changes might be up to 3% (Holder *et al.*, 1993). Interpolating from table 6.5 suggests voltage changes of a few microvolts with adjacent excitation. With typical equipment, averaging of a number of samples would probably allow the measurement of such changes. A system like the 'Mark 1' is probably unable to record data sufficiently fast to allow such averaging, although it may be satisfactory for superficial foci. The predicted voltage changes with diametric or cosine excitation are of the order of millivolts, and readily measurable.

'Medium' (~1%) resistivity changes. These changes are probably too small for adjacent excitation. With diametric or cosine excitation, we might expect voltage changes of tens of microvolts. These should certainly be measurable, but it will almost certainly be necessary to average a number of responses to obtain an adequate signal-to-noise ratio.

'Small' (~0.01%) changes. Neither the adjacent current pattern nor the diametric is likely to be suitable. A cosine current pattern may perhaps produce useful results, with prolonged averaging. The system has to be sensitive to voltage changes of about 2 μV in 200 mV, or 0.001%. This latter figure is about ten to one hundred times as high as the senstivity of instrument which was designed for DC resitivity measurements in nerves (chapter 7; appendix B).

6.5.3 Issues other than sensitivity

So far we have considered the effect of the current pattern only on sensitivity. The current pattern also affects the spatial resolution of the images. This precise nature of this effect is still the subject of some controversy (*e.g.*, Avis and Barber, 1994). The achievement of a high spatial resolution implies current patterns with high spatial frequency (Barber and Seagar, 1987). It is clear however that, lacking *a priori* information about the resistivity distribution, we cannot obtain the resistivities at more points than we have independent voltage measurements. If two voltage measurements are indistinguishable because of noise or systematic error, they cannot be said to be independent. This factor is particularly important for brain imaging, since the effect of the skull will be to limit the number of independent measurements from the brain. In principle, the cosine current pattern has the lowest spatial frequency, but creates the greatest current density in the brain. Therefore we may obtain more independent measurements from the brain than with the adjacent pattern, which has a high spatial frequency but confines more current to the scalp. Nevertheless, it is may be appropriate to use a current pattern with high spatial frequency when the signal-to-noise ratio is good, and a lower spatial frequency when it is poor.

6.6 Conclusion

Best sensitivity is obtained with the cosine current distribution, even after taking into account the lower allowable current. This is true both for normalised and absolute boundary voltage changes. However, the

voltage changes accompanying resistivity changes greater than about 10% (pathological changes) should be measurable with any current pattern. 1% changes (*e.g.*, perfusion variation) are amenable to imaging with diametric or cosine excitation. Resistance changes of less than 0.01% require a cosine or adaptive current pattern; even in this case a system is required that can measure voltage changes of about 0.001%. Obtaining this performance, with direct current excitation, represents a significant engineering challenge.

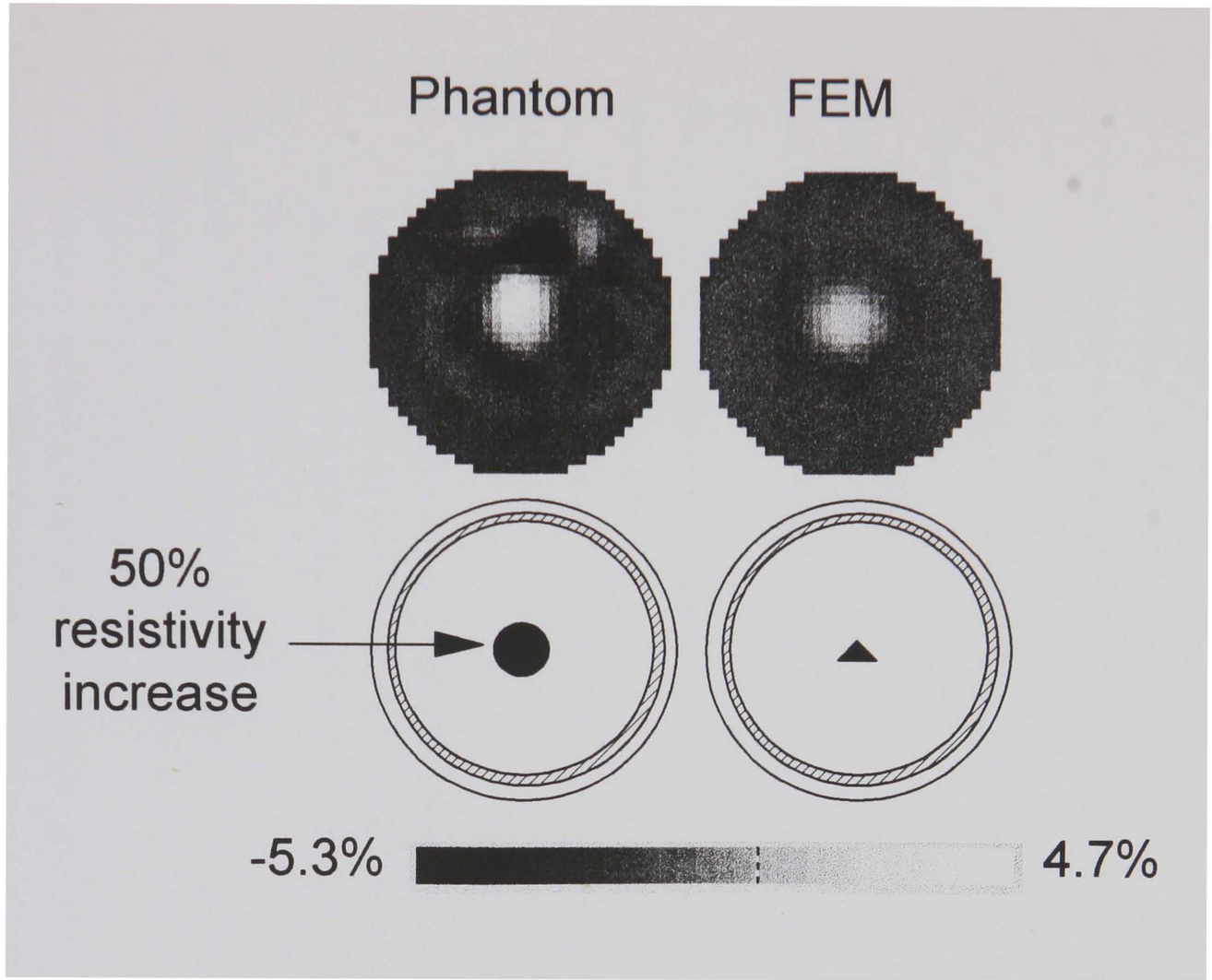

Figure 6.7: images of a 50% resistivity increase in the skull phantom (left) and finite element model (right)

Part C: experimental investigation

7. Measurement of the resistivity decrease in unmyelinated peripheral nerve during depolarisation

7.1 Introduction

The model described in chapter 5 predicts that, when an unmyelinated nerve depolarises, it exhibits a change in impedance. The magnitude of this change is greatest at DC, and decreases rapidly with increasing frequency. Indeed, if the analysis is correct, it will only be practicable to measure neuronal resistance changes at DC. For example, for the electrode configuration described in §7.3.1, the predicted values were 3.7% at DC and 0.009% at 30 kHz. This chapter describes the measurement of DC resistivity changes in the unmyelinated walking-leg nerve of a crab, *Cancer Pagurus*. This study had two main objectives. First, to determine whether there was a measurable DC resistance change, and how closely its magnitude agreed with the model. Second, to detect possible sources of artefact associated with DC excitation, and thereby increase confidence in the validity of subsequent cortical resistance measurements (chapter 8)

Crab nerve was chosen in preference to a cortical preparation or an myelinated nerve for the following reasons.

i. Being unmyelinated, the nerve should exhibit a large enough resistance change to measure accurately.

ii. The physiological and experimental conditions can be better controlled than would be the case for measurement in the brain, for example:
   - the nerve may be stimulated electrically, ensuring depolarisation of much of the tissue;
   - the excitation current can be confined to volume of tissue that is well-defined, compared to a cortical measurement;
   - peripheral nerves may be isolated from the animal, whereas a cortical measurement requires an intact-animal procedure. As well as being technically more difficult, there are more biological variables (*eg.*, blood pressure, level of anaesthesia) to confuse the interpretation of results.

iii. Suitable electrode positioning can reduce the effect of measurement artefacts.

iv. The structure of crab peripheral nerve is relatively simple and uniform; the measurements should be in good agreement with the theoretical model.

DC excitation requires a voltage measurement whose bandwidth extends near to DC. This bandwidth includes the voltage change due to the action potential itself. Some means therefore had to be found to extract the resistance signal from the action potential. The method adopted was to reverse the polarity of the excitation between measurements (see appendix B). The signal due to the resistance change therefore appeared inverted in every second measurement, while the action potential remained constant. The data acquisition process extracted the resistance change by subtracting alternate measurements. For this technique to be successful, it was of critical importance that the excitation did not affect the action potential itself. If this were not the case, the subtraction would reveal the effect of

the excitation on the action potential rather than the resistance change. Some care therefore has to be taken to measure and reduce the effect of this artefact. Other artefact sources were also investigated.

7.2 Nerve preparation and handling

Nerves were extracted from the walking legs of seven recently-killed edible crabs. After cutting the ligaments joining the upper and lower leg, the nerve could be withdrawn in one piece. Although great care was taken, some stretching of the nerve was inevitable. 8 cm - 10 cm of nerve could normally be obtained in one piece. The nerve was placed onto an array of electrodes (figure 7.1) made from lengths of 0.5 mm silver wire. Except during measurements, the nerve and electrodes were lowered into a bath of Ringer's solution (table 7.1) at a temperature of 1°C - 5°C. Nerve 'survival' time decreased if the temperature was higher than this, or if the nerve was exposed to air at ambient temperature for more than about a minute. Nerves usually remained viable for 30-60 minutes. A nerve was discarded when either:

i. the magnitude of the compound action potential fell by more than 50% from the starting value, or
ii. the stimulus (of duration 0.5 msec) necessary to produce a maximal response rose to more than 4.0 V.

In later experiments, oxygen was bubbled into the Ringer's solution; this did not markedly improve the survival time of the nerves. Immersion of the nerve into mineral oil rather than Ringer's solution dramatically reduced the survival time.

Electrolyte	Concentration
NaCl	460 mmol.l^{-1}
$MgCl_2$	27.6 mmol.l^{-1}
$CaCl_2$	5.5 mmol.l^{-1}
KCl	10.4 mmol.l^{-1}

Table 7.1: composition of the Ringer's solution

To make a measurement, the electrodes and nerve were raised from the solution. The spaces between electrodes were immediately dried with blotting paper, to prevent any meniscus of Ringer's solution providing a short-circuit path for the excitation current.

7.3 Measurement of resistivity changes during depolarisation

7.3.1 Method

Longitudinal measurement configuration. The longitudinal electrode array (figure 7.1a) consisted of 15 electrodes spaced over 10 cm. The 'proximal' six electrodes were separated by 1-2 mm, the others by 1 cm. A single measurement required seven electrodes, including a 'zero volt' reference for the amplifier. The unused electrodes were used to support the weight of the nerve, or were pushed aside. A constant-voltage stimulus was applied at the 'proximal' end of the nerve. This initiated a compound action potential that propagated past voltage electrode V1 and the excitation electrodes. Voltage electrode V2 was as far as possible (45 - 90 mm) from the stimulator, as dictated by the available length of nerve.

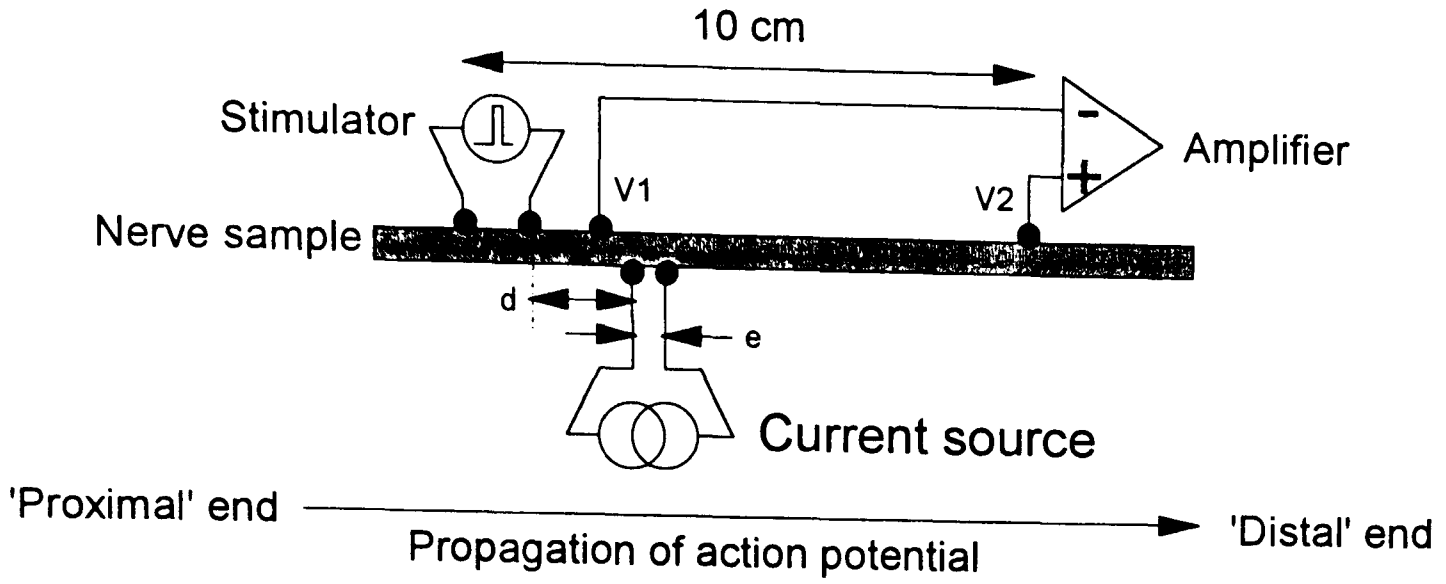

Figure 7.1a: configuration of the longitudinal measurement electrodes. Distance 'd' is the spacing between the distal stimulating electrode and the proximal current electrode: 3.5 mm or 5 mm. Distance 'e' is the separation between current electrodes: 1 mm or 4 mm. The stimulating electrodes were always 2 mm apart. The reference electrode was between the stimulating electrodes and V1.

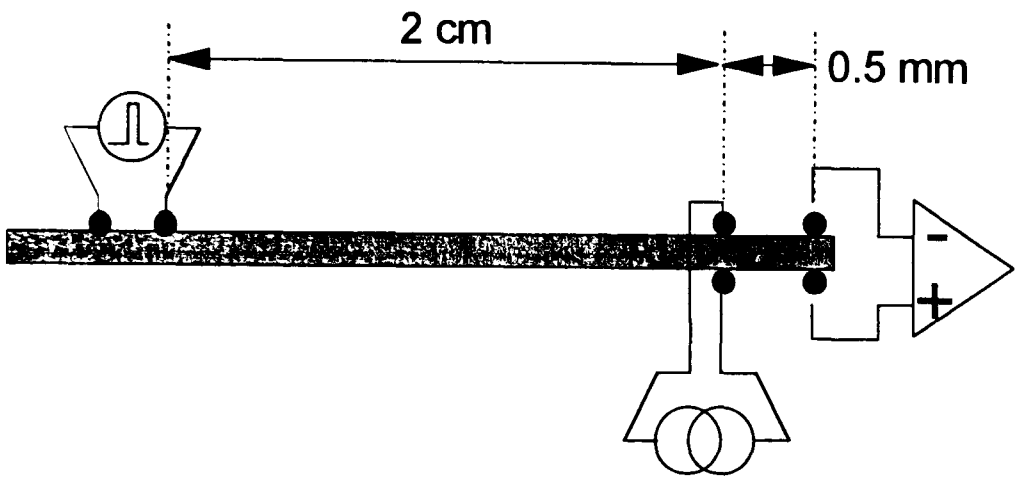

Figure 7.1b: configuration of the transverse measurement electrodes. The symbols have the same meaning as in figure 7.1a. The zero volt reference electrode was mid-way between the stimulation and excitation electrodes.

Although the measurement technique required four electrodes to reduce the effect of electrode contact impedance, the results were considered to be equivalent to measurements of 'two-terminal' resistance between the current electrodes. For this to be the case, the current density must be low except in the region bounded by the current electrodes. The proportion of the applied current which flows outside this region is dictated by the radius of the nerve and its length constant. At distances from the current electrodes that are large compared to these parameters, the current density is small.

On the assertion that most current flows only in the region between the current electrodes depends not only the accuracy of the resistance measurement, but also an important source of measurement artefact. It was important that the applied current did not change the characteristics of the measured compound action potential (see §7.4.3). This could be ensured if both voltage electrodes were a significant distance from the excitation. Electrode V2 was so distant (> 45 mm) from the stimulus that measurement from this electrode, although affected by the excitation, could not contribute significantly

to the overall action potential (see §7.4.3). However, the distance of electrode V1 from the excitation current was limited by the need for the excitation electrodes to be as close to the stimulus as possible (see §5.7). This was to reduce the effect of dispersion of the compound action potential, which would make the resistance change small at distances more than about 16 mm from the stimulus. The distance between V1 and its nearest current electrode was normally 3 mm. The radius of the nerve was about 0.5 mm, and the predicted length constant (see chapter 5) about 0.6 mm. Thus the closest voltage electrode to the excitation was 5 length constants from its nearest current electrode. Although it was felt that the current density at this distance would be insignificant, tests were still carried out for artefacts it might cause (§7.4.3). Longitudinal measurements were made on seven nerves from four crabs

Transverse measurement configuration. The electrode configuration for the transverse measurement (figure 7.1b) was identical with that described by Holder (1989). The excitation current was applied, and the voltage measured, between electrodes on opposite sides of the nerve. The voltage and current electrodes were separated longitudinally by 0.5 mm, which would cause the measurement to underestimate the true resistance. Transverse measurements were made on five nerves from two crabs.

Measurement protocol. The following three 'thresholds' were determined at the start of each experiment.

i. To reduce the effect of the excitation current on the action potential, it was necessary to determine the current that was sufficient to initiate an action potential from the excitation electrodes. The point at which stimulation occurred was taken as the point at which the first sign of an action potential was visible above the background noise level of 10-50 μV. This threshold was 24 μA - 60 μA for a 1 mm electrode spacing. The higher of these figures was found only in one sample; all others had thresholds below 40 μA. During resistance measurements, the excitation current was at most one quarter of this value. The threshold for stimulation was always lower when the excitation electrodes were more widely spaced: at 4 mm, the excitation current normally had to be less than 5 μA.
ii. The threshold was determined for stimulation using a voltage pulse of 0.5 msec duration at the normal stimulating electrodes. This was normally 0.2-1.0 volts. A nerve was discarded if this threshold was initially greater than 1.0V.
iii. The stimulation voltage was increased until there was no further increase in action potential amplitude. The stimulation for resistance measurement was set at three times this level, normally 6-9 V.

The resistance measurement apparatus is described in Appendix B. Normally 200 measurement cycles were acquired and averaged, following the sequence described in §2.5 of appendix B. On occasion the level of 50 Hz interference was sufficiently large that this had to be extended to 500 cycles. This was regarded as the absolute maximum duration for longitudinal measurements, since the nerve was exposed to warm air for about one minute. For transverse measurements, the nerve was enclosed in a sealed chamber, so averaging could be extended to 1000 cycles.

7.3.2 Results

With transverse measurement, four nerves showed no measurable resistance change (« 0.01%), although a compound action potential was detected between electrodes separated longitudinally by 1 cm. One

nerve showed resistance decreases which appeared to be about 0.01% in three subsequent measurements; the signal-to-noise ratio was such that the actual value may have been between 0.005% and 0.02%. Since this effect is too small to be of interest for tomography, no further transverse measurements were made. The following results are derived from 53 longitudinal recordings on 7 nerves from 4 crabs. Resistance decreases in all animals, nerves and experimental conditions were between 0.17% and 2.5%. A representative example of a resistance recording and simultaneous compound action potential is shown in figure 7.2.

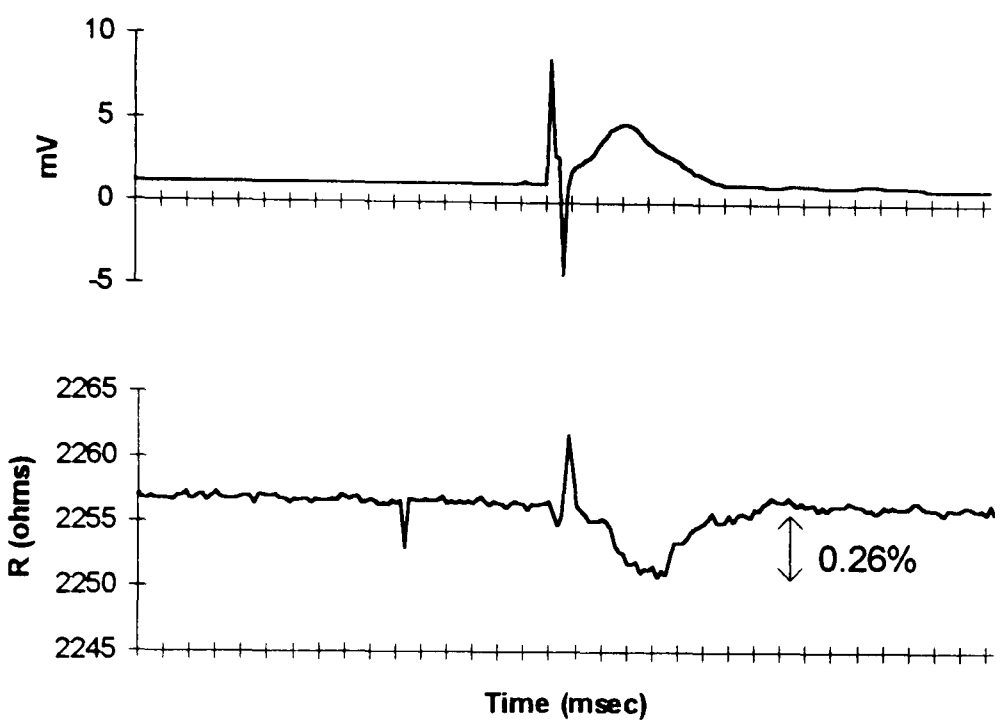

Figure 7.2: an example of the resistivity decrease (lower trace) accompanying the compound action potential (upper trace). Each horizontal division represents 1 msec. There is some breakthrough of the stimulus onto both traces: the short biphasic deflection on the action potential trace and largely monophasic deflection on the resistance trace

Variation of resistance change between measurements, nerves and animals. There was substantial variation between resistivity changes in the same nerve. The variations were often, but not always, accompanied by a noticeable variation in the compound action potential. Three nerves from the same animal were studied in near-identical experimental conditions. The separation between stimulus and excitation electrodes ('d') was 5 mm, and between excitation electrodes ('e') 1 mm. The temperature of the Ringer's solution was 2°C - 3°C (table 7.2). Excitation current was 4 μA - 10 μA.

	Nerve 1	Nerve 2	Nerve 3
Number of recordings	7	3	4
Mean resistance decrease	1.29%	1.20%	1.10%
Standard deviation	0.28%	0.35%	0.14%

Table 7.2: mean and standard deviations from 3 nerves in identical experimental conditions.

One-way analysis of variance revealed no significant variation in mean resistance change between nerves ($p > 0.5$), corresponding to a variance ratio F=0.63. The variation between measurements is greater than that between nerves. This variation showed no obvious trend over time (figure 7.3), except when a nerve was reaching the end of its experimental life.

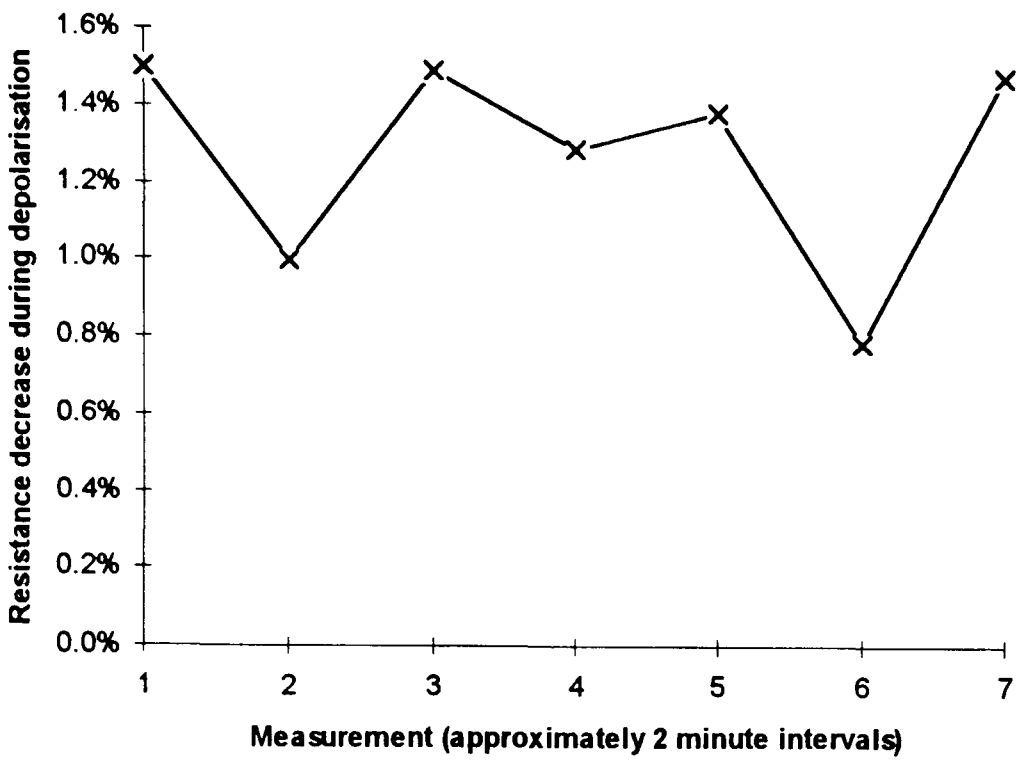

Figure 7.3: typical example of the time variation of resistance change for a single nerve.

Some possible sources of this variation are discussed below. I have assumed that measurements made with identical electrode configuration on different nerves from the same animal may be pooled to improve statistical confidence.

	Crab 1	Crab 2	Crab 3	Crab 4
Number of measurements	6	14	14	4
Mean resistance decrease	0.36%	1.21%	1.55%	0.60%
Standard deviation	0.10%	0.29%	0.70%	0.12%

Table 7.3: mean resistance decreases for different crabs, based on pooled data from 7 nerves.

Despite the large inter-measurement variability, there was a significant difference between crabs (table 7.3). One-way analysis gives F=13.1, $p < 0.001$.

Effect of excitation electrode spacing. Nine measurements were made on a single nerve; the separation of excitation electrodes ('e') alternated between 1 mm and 4 mm. All other electrode positions remained constant. Distance ('d') was 5 mm. The resistivity decreases are summarised in table 7.4.

Excitation spacing ('e'):	1 mm	4 mm
Number of measurements	5	4
Mean resistance decrease	0.38%	0.23%
Standard deviation	0.08%	0.05%

Table 7.4: mean and standard deviations of resistivity change for varying excitation electrode spacing

The mean resistance change at 1 mm was larger by 65% than at 4 mm. The difference between the mean resistivity changes was significant at the 1% level, assessed by t-test, assuming equal variances.

Effect of distance between excitation electrodes and stimulus. The mean resistivity decrease with a 3.5 mm separation between stimulus and excitation electrodes was 40% larger than when the separation was 5 mm (table 7.5), on the same nerve.

Distance between stimulus and excitation	3.5 mm	5 mm
Number of measurements	7	6
Mean resistance decrease	0.52%	0.36%
Standard deviation	0.14%	0.10%

Table 7.5: comparison of the resistivity changes for different distances ('d') between stimulus and excitation

The difference between means was significant at the 5% level, assessed as above.

In summary, the longitudinal resistance change during depolarisation, with measurement electrodes separated by 1 mm, was 1.0% ± 0.6% (mean ± S.D.); these are pooled figures for 48 recordings on 7 nerves from 4 crabs.

7.4 Measurement of possible sources of artefact

The experiments described above may have been subject to a number of potential sources of artefact. This section describes these artefact sources, and the experimental procedures by which their significance was evaluated. Only longitudinal measurement is considered; the transverse resistivity changes were so small that their validity was not investigated.

7.4.1 Effect of excitation on electrode 'polarisation'

Mechanism. The flow of excitation current in the nerve produces two effects in addition to developing a DC voltage between the electrodes. First, the current will charge the membrane capacitance. This is normally regarded as a passive process, whose time constant will not depend on the polarity or magnitude of the applied current (Hodgkin, 1938). Second, the current will 'polarise' the electrode-saline interface. This will cause a disturbance in the normal electrode-electrolyte potential, which in these experiments was 10 mV - 200 mV between any pair of electrodes. There is no reason to assume that the magnitude or time duration of this 'polarisation disturbance' is related linearly to the excitation (Geddes, 1972). In these experiments, the excitation current was biphasic, but it was difficult to ensure

that the two phases were of exactly equal magnitude. Thus the time constant of electrode polarisation would be different for 'odd' and 'even' measuring cycles. In experiments on isolated nerve fibres from *Carcinus Maenas,* Hodgkin (1938) found that the polarisation of current-carrying electrodes produced a voltage about 25% that due to capacitive charging of the membrane. This capacitive voltage was in turn up to 40% that of the propagated action potential. Thus, in the worse case, the polarisation voltage could be of the order 100 μV. Since the recorded voltage due to excitation of the nerve in these experiments was 5 mV -10 mV, this effect could imitate a resistance change of about 1%.

Method. Before making a quantitative measurement of resistance change in any nerve, a number of recordings were made with the stimulator alternately enabled and disabled. Similar measurements were made on a piece of saline-soaked string, and a resistor network.

Results. Even when the stimulator was deactivated, many resistance recordings still showed deviations in the baseline of similar size to the resistance change during depolarisation. The resistance record typically showed a sharp increase at the start of each recording (figure 7.4), then changed more slowly throughout the remainder of the measurement. A similar effect was observed in the recordings made on wet string. By contrast, the artefacts obtained with the resistor network were higher in frequency, and at least ten times smaller. The 'shape' of electrode artefacts varied with the amplitude of the excitation current, and generally worsened over long periods (2-3 hours) of experimentation. Although these artefacts could be large, they normally had a time duration too long to be mistaken for events related to the action potential.

Discussion. These results support the contention that electrode polarisation artefacts can mimic resistance changes. Furthermore, the 'true' resistance decrease of about 1% at the start of the recording of figure 7.4 is difficult to distinguish from artefact. However, by making a resistance recording with the stimulator disabled at the start of each experiment, the stimuli could always be timed to coincide with a relatively 'flat' part of the recording. Surprisingly, no improvement was obtained when the electrodes were chlorided (10 μA for 2 minutes each).

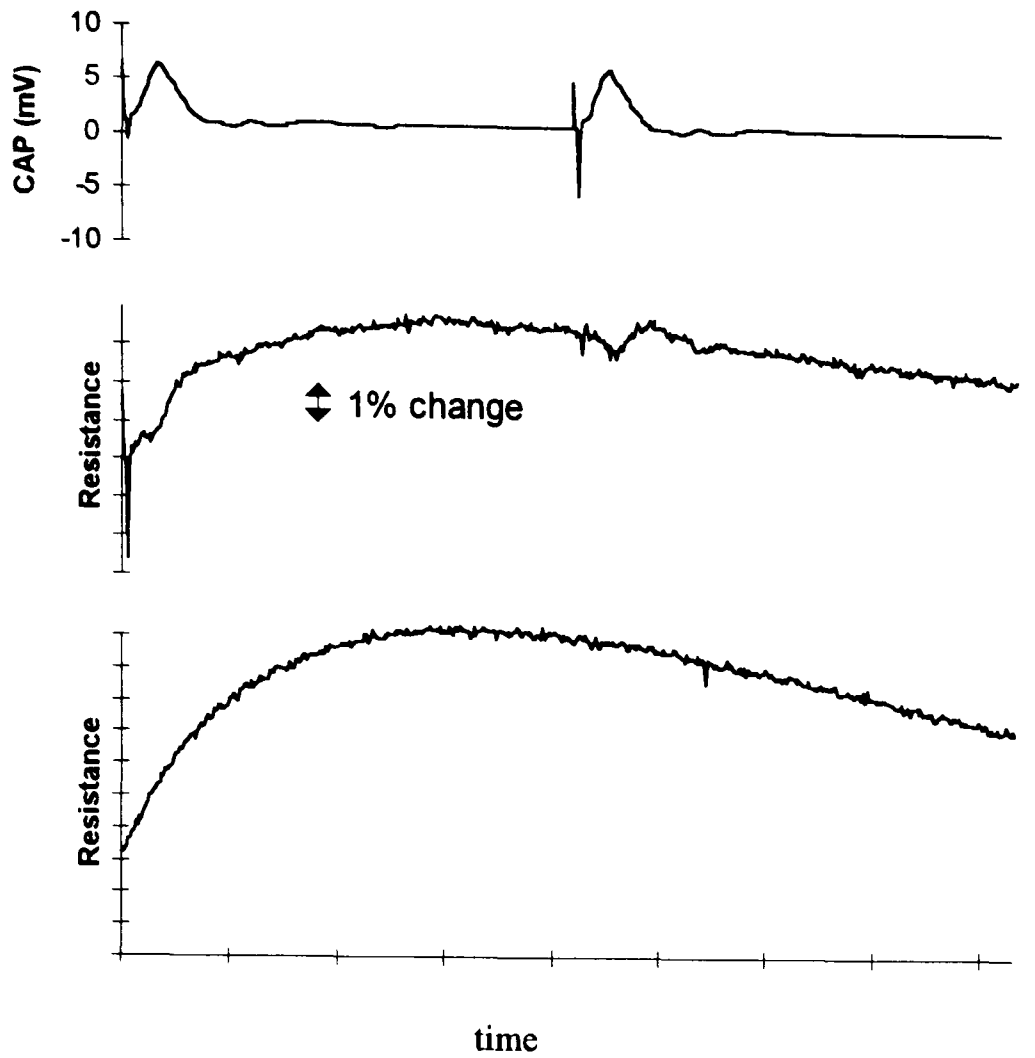

Figure 7.4: comparison of resistance and action potential records obtained with, and without, a stimulus. The top trace shows the compound action potential corresponding to the middle resistance trace. The apparent resistance increase at the start of the recording is primarily artefactual, as can be seen by referring to the lower trace. This shows a resistance recording from the same nerve with the stimulator switched off. The second resistance change is clearly distinguished from the background. Horizontal scale: 1 division = 10 msec. Vertical scale: 1 division = 1% resistance change, from a starting value of 400 Ω

7.4.2 Effect of stimulus on electrode polarisation

Mechanism. An electrode polarisation artefact could be caused by the stimulus, rather than by the excitation current as described in §7.4.1.

Method. Resistance changes were recorded in a nerve as described in §7.3.1, before and after soaking in a 1% lignocaine solution. Lignocaine is a membrane-stabilising agent: it prevents the propagation of an action potential.

Results. After it had been soaked in lignocaine, neither action potential nor resistance change could be elicited from the nerve.

Discussion. Polarisation due to a stimulus does not appear to be an important source of artefact. This is as expected, since the nerve stimulator is powered separately from the rest of the apparatus; there would be no significant flow of current between the stimulator and the more distal electrodes.

7.4.3 Effect of excitation current on the action potential

Mechanism. After initiation, the action potential 'passes through' a region of DC excitation. At the excitation cathode the membrane will be slightly depolarised, while at the anode it will be hyper-polarised. Although the effect on membrane potential might be equal and opposite at the anode and cathode, there is no reason to assume equal and opposite effects on the action potential. The relationship between DC excitation current and membrane permeability is not a linear one (Cole and Baker, 1941). Since the nerve consists of fibres whose diameters range from about 1 μm to 30 μm (Keynes and Lewis, 1951), different fibres will be affected by the excitation current to differing degrees. This means that the shape, size and onset of the recorded action potential could depend on the excitation current. When the successive cycles are subtracted, the action potential signals might not be canceled, leaving a residual artefact.

The recording arrangement was expected to eliminate this source of artefact, since:

i. the proximal voltage electrode was 'upstream' of the excitation current, so it would not be affected by the excitation, and
ii. the distal voltage electrode, although 'downstream', was so far from the stimulus that it would record no significant action potential, owing to dispersion of the action potential.

These assumptions were tested in two ways. First, monophasic action potentials were recorded from electrodes at various distances distal to the stimulus. This procedure was carried out both with, and without, excitation current. Second, the resistivity change during depolarisation was measured at various current excitation settings. If the decrease in the resistance recording was due to a decrease in passive tissue resistance, the proportional resistance change would be independent of the excitation current.

Method. (1) Monophasic action potentials were recorded with the active electrode a distance of 2, 6, 16, 25 or 67 mm from the stimulus without excitation. With excitation (at one quarter of the threshold current), recordings were made at distances 16, 26 and 67 mm; the presence of the excitation electrodes prevented the use of the smaller spacings. This procedure was carried out on two nerves from the same animal. The arrangement of the electrodes is shown in figure 7.5. The records were made monophasic by enthusiastic crushing of the distal end of the nerve (*e.g.*, Erlanger and Gasser, 1938).

(2) The resistance change was measured, as described in §7.3.1, using currents between 1 μA and one quarter of the excitation threshold. The procedure was repeated on three nerves from the same animal, which was different from that used for the experiments in part (1) above. Since the inter-measurement variation was large even at one excitation current, a number of measurements were made at different currents, and subjected to statistical interpretation.

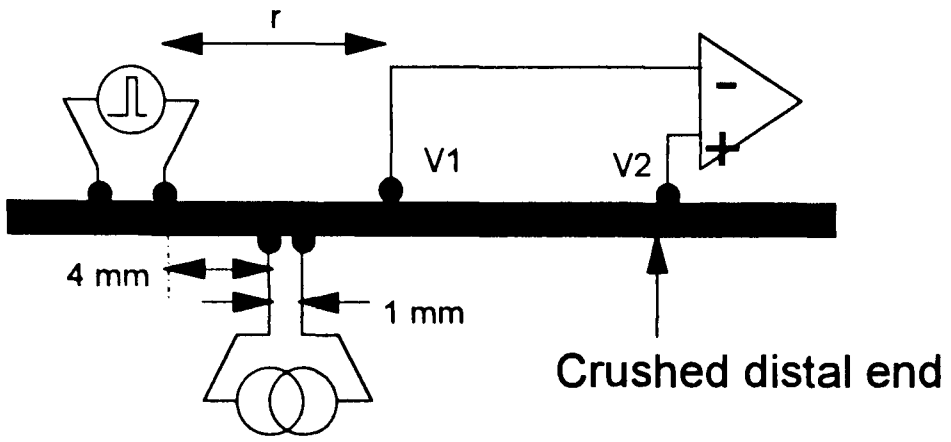

Figure 7.5: the arrangement of the excitation and recording electrodes for determination of action potential artefact. Distance 'r' is the separation between V1 and the distal stimulating electrode. All other symbols and distances are as figure 7.1a. Note that both amplifier inputs were distal to the excitation, so no component of resistance change was measured, even with excitation current switched on

Results. (1) Monophasic compound action potentials without excitation were shown in figure 7.6. Both nerves produced similar results. The subtracted voltage records with excitation showed no deflections greater than noise, at any current, when the recording electrode was more than 25 mm from the stimulus. At 16 mm, the action potential differed slightly according to the excitation polarity, when the excitation current was one-quarter threshold. On two successive measurements, the remaining voltage signals after subtraction were 8 μV and 16 μV, for action potentials of 1.4 and 0.6 mV respectively. Since the voltage due to the excitation current was normally about 5 mV, this artefact would mimic an impedance change of about 0.3%, which is comparable with the smaller of the resistance changes measured.

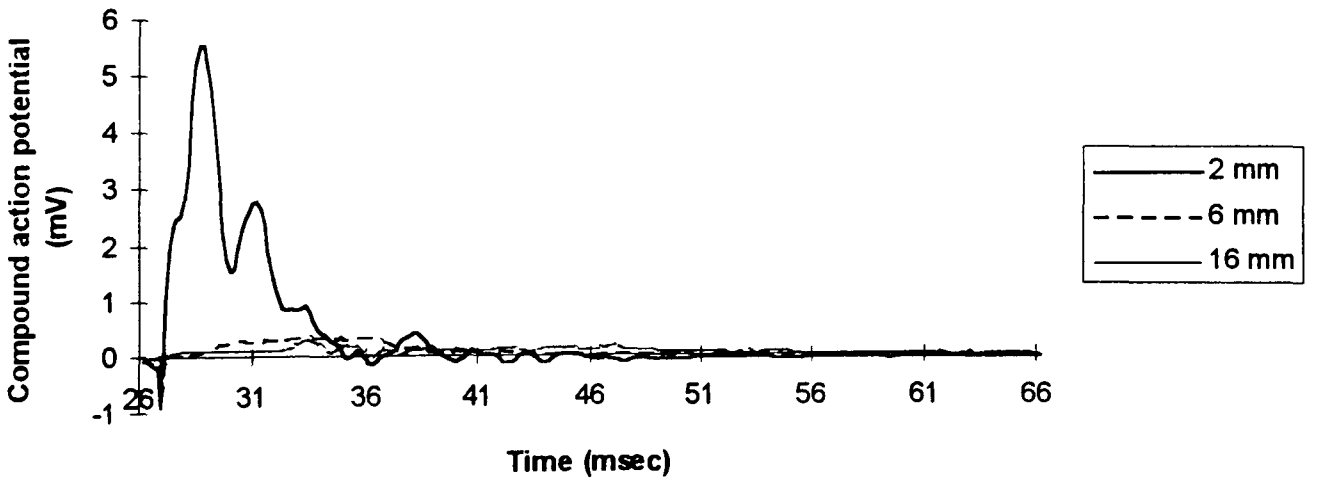

Figure 7.6: monophasic action potentials recorded with the active electrode at various distances from the stimulus. At separations greater than about 25 mm, no action potential was visible above the background noise

Excitation current	1 μA - 2μA	4μA	6 μA	8 μA -10 μA
Number of measurements	2	8	4	6
Mean resistance decrease	1.0%	1.3%	1.8%	1.4%
Standard deviation	0%	0.6%	0.4%	0.9%

Table 7.6: the effect of excitation current on resistance decrease, based on pooled data for three nerves from the same animal

(2) The variation of resistivity change with excitation current in one nerve was no larger than the variation between measurements at the same current (Table 7.6). One-way analysis of variance gave $F = 0.92$, $p > 0.4$.

Discussion. The resistance decreases during depolarisation were constant within the limits of inter-measurement variability over a range of excitation currents. We should expect this to be the case, since the effect of excitation on the action potential would be unmeasurably small at the distal electrode, and the proximal electrode is 'upstream' of the stimulus. For the experiments described in §7.3, the separation between stimulus and distal voltage electrode was always greater than 45 mm. It is highly probable that this type of artefact, although potentially a source of serious error, was not significant in these experiments.

7.4.4 Effect of inadequate common-mode rejection

As described in §7.4.3 above, the excitation current affected the compound action potential. This effect was expected not to cause an artefact, because of the configuration of the measurement electrodes. When a compound action potential had propagated just past the current excitation electrodes, it would be affected by the excitation, but would be too far from voltage electrode V2 to be measured in the differential signal. This reasoning would not be valid, however, if the common-mode rejection of the amplifier was inadequate. The common-mode signal V1+V2 would contain a component which varied with the excitation current. Could this have caused the apparent resistance changes? The smallest resistance change measured in these experiments was 0.17%; the smallest voltage was 5 mV. If these two conditions had occurred in the same measurement, the voltage change would have been 8.5 μV. The common-mode rejection of the amplifier was over 100 dB between 10 Hz and 1 kHz (see appendix B). For a common-mode artefact to imitate even the smallest of the resistance changes, it would have had to be 850 mV: two orders of magnitude greater than the largest compound action potential. Had the common-mode rejection been only 40 dB, it is possible that this artefact would have been significant.

7.5 Discussion

7.5.1 Summary of results

In the experimental conditions described, the longitudinal resistivity change during depolarisation was 1.0% ± 0.6% (mean ± S.D.) with 1 mm spacing of the excitation electrodes. An increase in separation of

the excitation electrodes to 4 mm resulted in a 65% decrease in the mean resistivity change. A decrease in the separation between the stimulating and excitation electrodes from 5 mm to 3.5 mm resulted in the mean resistance change being increased by 40%. The transverse resistivity change was of the order 0.01%, and not repeatable.

7.5.2 Comparison of measurements with the prediction of the models of chapter 5

The predicted transverse resistivity decrease appeared to agree exactly with measurement: both 0.01%. However, this is less of a confirmation of the theory than might be expected, since the resistance change was small, and difficult to measure accurately.

Table 7.7 shows the comparison between measured parameters and the predictions of the model, for longitudinal measurement. The first column shows the decrease in DC resistance during depolarisation; the measured values are somewhat smaller than those predicted. The predicted effect of changing the measurement electrode spacing ('e') is within the limit of experimental error. The model slightly overestimates the effect of changes in the spacing between the stimulus and excitation electrodes ('e').

	DC Resistance decrease during depolarisation at d=5 mm, e= 1 mm	Effect on DC resistance change of increasing 'e' to 4 mm	Effect on DC resistance change of reducing 'd' to 3.5 mm
Measured results	1.0%	-65%	+40%
Model prediction	3.7%	-59%	+61%

Table 7.7: a comparison between measurement and theoretical prediction of the DC resistance change and its variation with electrode spacing.

The deviations from theory are probably somewhat larger than can be accounted for by difference in tissue parameters (*eg.*, Intracellular resistivity) alone. However, we would expect the tissue resistance change to be smaller than predicted if :

i. the tissue is not completely depolarised at the stimulating electrodes, or

ii. the conduction velocity along the nerve is slower than expected.

Two observations support the contention that these factors were the source of variation between the theory and the measurements. First, the variation in action potential amplitude with distance from the stimulating electrodes was greater than predicted by theory. This would suggest a reduced conduction velocity. Second, although the stimulus applied was greater than that needed to produce a response of maximum amplitude, the duration and shape of the compound action potential continued to change with increasing stimulus strength. This suggests that further fibres are depolarised by the larger stimulus. Two further factors have to be taken into account. First, a short-circuit path is formed by a meniscus of Ringer's solution between the electrodes (see §7.5.3). Second, the measuring instrument underestimated resistance changes by up to 15% in calibration studies (appendix B).

7.5.3 Sources of variability in the resistance measurements

While we would expect a variation between measurement on different animals, there was also a considerable variation between measurements made sequentially on the same nerve. A possible explanation is the variable amount of Ringer's solution retained between the current electrodes during each measurement. This solution may have formed a meniscus between the wire electrodes, which were usually only 1 mm apart, or been absorbed between the fascicles of the nerve. Since some trouble was taken to dry the electrodes before measurement, the latter is more likely to be the correct explanation. This effect would cause the apparent absolute resistivity of the nerve to vary between measurements. Such variability was observed; in an extreme case, measurements of absolute resistance on the same nerve varied between 420 Ω and 1570 Ω. There was some indication that the larger resistances were associated with larger resistance changes, but the small number of measurements available for any single nerve did not allow for a statistical analysis.

Another possible explanation is temperature variation. The rate of action potential conduction decreases with decreasing temperature. In crab nerve, the resulting increase in conduction velocity dispersion would result in a reduction in resistance change. I was unable to find any quantitative studies of this effect in unmyelinated nerve. In frog sciatic nerve Burlakova *et al.*, (1959) measured the effect of temperature on the conduction velocity of the main complex of the compound action potential. This increased by about 44% with a change from 5 °C to 10 °C. If a similar figure (approximately 9% increase in conduction velocity per °C) applied to crab nerve, it could account for at least part of the variability. Although the temperature of the Ringer's solution did not vary by more than about 2 °C during sets of measurement, the nerve was exposed to air at room temperature during an individual measurement. Since the ambient temperature was often as high as 25 °C, the nerve would change its temperature rapidly before and during measurement. Furthermore, the effect of high ambient temperature would have been to partially dry the nerve during measurement.

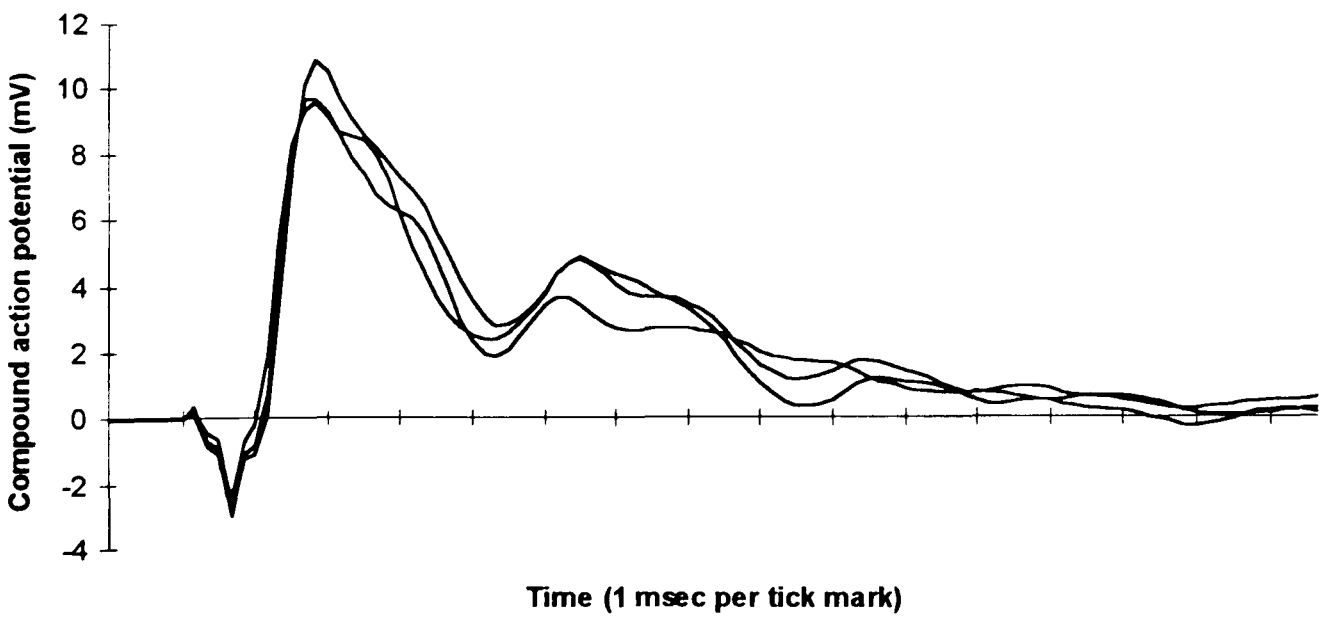

Figure 7.7: three compound action potentials from the same nerve, corresponding to resistance decreases of between 0.4% and 1.0%. The action potentials all differ slightly, but not as much as the resistivity changes seem to suggest.

If variation in the dispersion of conduction velocities was a source of variability, this should be reflected in a variation in the compound action potentials. While there was considerable variability in the action potential, it was often not as large as the variability in resistance change seemed to demand (figure 7.7). It is possible that there were other temperature-related effects which did not manifest themselves in the action potential.

7.5.5 Significance of artefacts

Some considerable trouble was taken to assess, and where possible eliminate, the effect of artefacts which might manifest themselves as resistance changes. The following factors argue against the measured results being due to artefact.

i. The measurements are broadly in agreement with the predictions of the theoretical model.
ii. Electrode 'polarisation' artefacts were significant, but could be separated from 'true' resistance changes by adjustment of the timing of the stimulus.
iii. The recording arrangement would have rejected artefacts caused by the effect of excitation current on the measurement of the 'downstream' compound action potential; this rejection was confirmed by experiment.
iv. The measured resistance change is constant over a range of excitation currents, within the limits of experimental error.
v. The ability of the instrumentation to measure accurately resistance changes of the size and duration described was verified on resistor networks (appendix B).

The effect of excitation current on the 'upstream' recording electrode was difficult to assess. Theoretical considerations, and the fact that the distance between this electrode and the current source was much larger than the radius of the fibre, suggest that it should not have been significant. Furthermore, if this effect was a significant source of artefact, the putative resistance change would be expected to be current-dependent. This was not found to be the case.

7.6.6 Comparison with other nerve studies

There are few studies of resistance changes during depolarisation in isolated nerve tissue. Holder (1989) found transverse resistance decreases of 0.3% in nerves from the same species of crab as used for these experiments. This disagrees strongly with the current results, in which the transverse resistivity change was no more than about 0.01%. A possible explanation is that the common-mode rejection of this author's sense amplifier was inadequate. The common-mode component of the compound action potential would have been affected by the excitation current (see §7.4.4), and may have produced an artefact resembling a resistance change. Holder (1989) also found a decrease in the longitudinal resistance of 0.3%. The spacing between his current electrodes was 24 mm; theory (§5.5) predicts that this spacing should produce a resistance change about one tenth that for 1 mm spacing, *i.e.*, approximately 0.37%. The resistivity change would have been further reduced (to about 0.1%) by the increased spacing (12 mm) between the stimulating and excitation electrodes. The reported figure of 0.3% does not contrast strongly with theory or the results described above. However, the measurement configuration, which placed the measurement electrodes in the excited region of the nerve, was

unsatisfactory for the reason described in §7.4.3. The measurements were composed partly of the 'true' resistance change, and partly of an artefact caused by the effect of the excitation current on the action potential; it is not obvious how much of the resistance change was due to each of these two factors.

Chailakhian & Iur'ev (1957) found resistance changes of about 0.03% in frog sciatic nerves at 35 kHz. Their experimental technique was subsequently used by others (Burlakova *et al.*, 1959; Prudnikova, 1959) to investigate the time relationship between the action potential and the putative impedance change. Although these authors used a small spacing (1.5 mm) between the measurement electrodes, an impedance change this large in a myelinated nerve is in conflict with the assumption that the impedance of the membrane is dominated by the myelinated component (§5.8.3). The impedance change in the sciatic nerve was determined from the 'unbalance' signal of a balanced Wheatstone bridge; this is inherently a 'two-terminal' technique; the apparent impedance change will include a contribution from the electrode contact impedance. The authors demonstrated that the stimulus produced an artefactual impedance change which was sometimes larger than that assumed to be due to depolarisation. It is possible that the passage of the action potential between the measurement electrodes was able to disturb the balance of the bridge by the same mechanism as the stimulator. Alternatively, it may be the case that the impedance change in myelinated tissue is larger than predicted. In any case, it would not be possible to confirm or refute the validity of these measurements using the technique described above. The much greater conduction velocity in myelinated tissue invalidates the assumption that artefacts are eliminated by the wide voltage electrode spacing.

7.6 Conclusion

Measurements of the resistance change during depolarisation were made on crab peripheral nerve. Longitudinal resistivity changes were about 1%; transverse changes were too small to measure accurately: less than 0.02%, and not repeatable. These results, and the effects of electrode spacings, are in reasonable agreement with the predictions of the model described in chapter 5.

8. Measurements of functional resistivity changes in the brains of anaesthetised rabbits

8.1 Introduction

8.1.1 Purpose and scope of these experiments

In chapter 1, resistivity changes during activity in the brain were divided into three broad categories, on the basis of their physiological mechanism. The purpose of the experiments described in this chapter was to determine whether how well APT might be used to image

i. large, pathological changes resulting from cerebral anoxia, and
ii. small resistivity changes during evoked responses to stimuli, resulting from neuronal depolarisation.

The model described in chapter 5 predicted the sizes of these changes to be +16% and -0.01% respectively. 'Medium' (~1%) resistance changes, resulting from slow evoked changes in cerebral perfusion, are under investigation by other workers, and were not included in this study; these changes will be discussed briefly in §8.4.3.

The pathological changes were found to be large enough to image at 50 kHz, using the Sheffield Mark 1 (Brown and Seagar, 1987) APT system. For these pathological events, of particular interest was a quantitative measure of APT's ability to localise the 'focus' of activity; localisation of epileptic foci is potentially an important application for APT (see §1.6).

The resistance changes during evoked EEG activity were not large enough to image; measurements were made only with the current electrodes directly over the active region of the brain.

8.1.2 Large, pathological resistance changes

In these experiments, APT data sets were collected from a ring of electrodes placed on the brain, during the phenomenon of *cortical spreading depression* (CSD) in anaesthetised rabbits. Cortical spreading depression was first reported by Leâo (1944). It may be initiated by various stimuli (Marshall, 1955): chemical, thermal, mechanical and, as in these experiments, electrical. A wavefront of intense electroencephalographic (EEG) activity then spreads outwards at about 3 mm/min. A depression of EEG activity follows this effect, and is accompanied by an increase in cortical resistivity of up to 100% at 1600 Hz (Hoffman *et al.*, 1973) or 40% at 50 kHz (Ranck, 1964) Cortical spreading depression can be elicited in grey matter anywhere in the brains of susceptible animals (Grafstein, 1956); in these experiments, it was only elicited in the cerebral cortex. White matter is not susceptible. The changes due to CSD do not normally cross the midline of the brain, probably because the region of the longitudinal fissure does not contain sufficient grey matter to support it. Figure 8.1 shows diagramatically the spread of CSD after initiation. The initial resistivity increases are probably due to 'cell swelling' (Hansen and Olsen, 1980), while propagation is probably caused by passive diffusion of excitatory substances ahead of the active region (Burês, 1973). For the purposes of APT imaging, cortical spreading depression is an appropriate model of epilepsy since it has similar, focal resistivity

characteristics (Marshall, 1955), although the resistivity increases are somewhat larger. Furthermore, unlike epilepsy, a sequence of well-defined cortical DC potential changes accompanies spreading depression, so EEG monitoring during experiments is unnecessary. This is fortunate because the Sheffield Mark 1 APT system injects signals into the cortex with components in the EEG bandwidth.

In the rabbit the cortex forms a disk-shaped layer 1-2 mm deep, while the rest of the brain is approximately shaped like an inverted hemisphere (Figure 8.2). The 'region of interest' is therefore confined to a thin disc around whose periphery we can place electrodes after surgical exposure. The Barber and Seagar (1987) image reconstruction algorithm assumes that the imaging target has a resistivity distribution which is initially homogenous and is 'two dimensional'. This preparation satisfies these requirements to some extent, so we might expect an accuracy comparable to that achieved in a saline-filled tank.

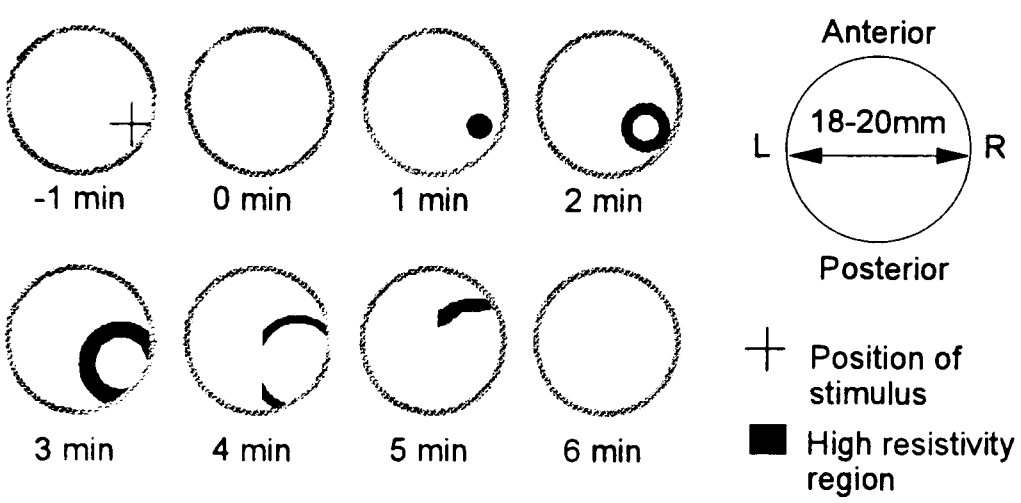

Figure 8.1: a schematic representation of the spread of the high-resistivity region during cortical spreading depression. '0 minutes' represents the time at which the stimulus was applied. Note that the effect does not cross the midline.

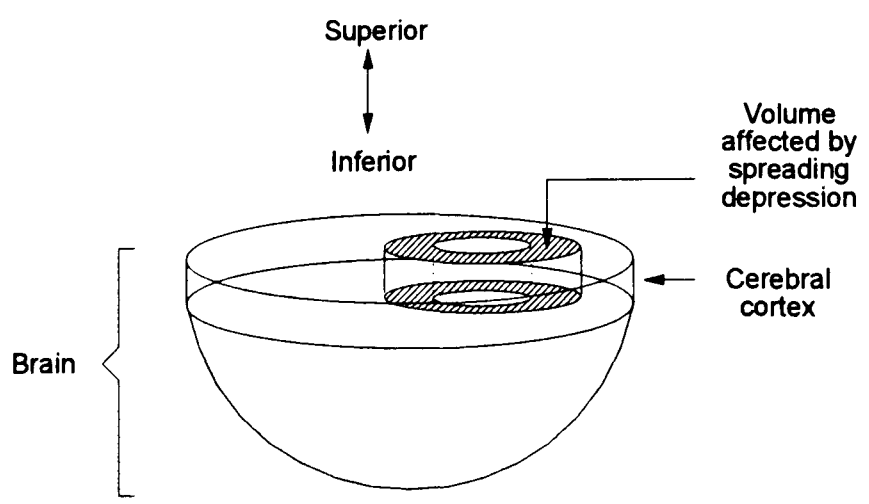

Figure 8.2: the rabbit brain. Cortical spreading depression (hashed region) only affects the grey matter. This region corresponds to time 2 minutes in fig 8.1

8.1.3 Evoked resistance changes during the action potential

To determine the resistivity change which results from the action potential, measurements were made with pulsed DC excitation, using the protocol, technique and equipment described in chapter 7 and appendix B. Resistivity changes were measured during electrical stimulation of the median nerve, which activates the parietal cortex. In one experiment, visual (light flash) stimulation was attempted. However, the duration of the response was sufficiently long (up to 40 msec) that the resistance change could not be accurately distinguished from electrode polarisation artefacts (see §7.4.1) which were of similar duration.

8.2 Methods

8.2.1 Animal preparation

Eight adult New Zealand White rabbits were anaesthetised as follows:

i. Induction by Hypnorm (Janssen Animal Health) 0.3 ml/kg intra-muscular and diazepam 2 mg/kg subcutaneous.
ii. Maintenance by 0.5%-2% halothane in 50%/50% nitrous oxide/oxygen mixture (spreading depression studies) or 0.1%-5% halothane in 70%/30% mixture (evoked response studies).
iii. Neuromuscular blockade with pancuronium bromide 0.05 mg/kg. This was administered at approximately 30 minute intervals, after testing for adequate depth of anaesthesia.

A small animal ventilator (Scientific Research Instruments Ltd) and endotracheal canula maintained respiration. Arterial blood pressure and end-tidal expiratory CO_2 were measured continuously; arterial blood gasses or pH were measured from a femoral cannula several times during an experiment. The brain was exposed by removing a circular section of cranium approximately 25 mm in diameter. While measurement directly from the cortex (*i.e.*, with the *dura mater* removed) might be expected to produce a larger resistance change, it is technically easier to perform experiments with the *dura mater* in place. The exposed cortex dries rapidly, and may be damaged. It was necessary to irrigate the cortex regularly with a solution similar in composition to cerebro-spinal fluid (CSF). This 'artificial CSF' (aCSF) contained Na^+, K^+ and Cl^- ions in similar concentration to biological CSF. Unfortunately, applying a conductive solution to the cortex changed its resistivity dramatically, producing a very variable baseline. Therefore the *dura mater* was only resected in two of the spreading depression experiments. In the evoked response experiments, the *dura mater* was always removed, since a low signal amplitude was expected. The effect of irrigation on the recording baseline was not important in these experiments, since the recording time was very short (250 msec) with respect to the rate of drying.

When the *dura mater* was intact, it was sometimes difficult to elicit cortical spreading depression, possibly because CSF under the *dura* 'shunted' the current and diminished the current density in the cortex. The cerebro-spinal fluid was therefore allowed to drain spontaneously by pricking the *dura mater* with a needle.

8.2.2 Electrodes

After exposing the brain, an array of silver/silver chloride 'ball' electrodes was lowered onto the cortical or dural surface. The electrodes had to be suitable for accurate positioning, but at the same time prevent undue pressure being placed on the delicate cortex. Two designs were tried. Early experiments used a spring-loaded insulator to carry the electrode. The insulator was free to move along the axis of the electrode, but not to move laterally (figure 8.3a). A perspex ring, with sixteen equally spaced holes, held the electrodes in position. While this design allowed the electrodes to be rapidly positioned with reasonable accuracy, it was difficult to produce a spring which was sufficiently compressible to avoid deforming the cortical surface. Later experiments therefore used electrodes in which the ball was mounted on a spring consisting of a few turns of silver wire (figure 8.3b). These electrodes placed negligible pressure on the brain, but were somewhat more difficult to position accurately. In both electrode designs, the 'ball' had a surface area of about 0.8 mm^2.

8.2.2 Spreading depression experiments

The cortical electrodes were connected to the Sheffield Mark 1 (IBEES Ltd, Sheffield, UK) data collection system, and to a DC data acquisition system (Keithley Instruments Inc., Series 500) which sampled at 1 Hz. The 3 dB bandwidth of this system was DC-1 Hz. To use the Sheffield Mark 1 system in this configuration, I modified it so that the applied current could be selected from the front panel. Before each measurement, the current was set at the highest value that did not cause saturation of the input amplifiers. In practice this was 0.5-1.0 mA (peak) since the inter-electrode resistance is higher than normally encountered in APT measurements. The gain and discriminator phase of the APT system were set to give the smallest maximum reciprocity error. Cortical spreading depression was initiated by a DC cathodal stimulus of 0.6 - 1.5 mA for 30 - 60 seconds. The stimulus strength used was the lowest that could induce spreading depression in each case. APT data and DC potentials were recorded for 5 minutes before and 10 minutes after each stimulus. The DC potentials confirmed that cortical spreading depression had taken place, and that it propagated at a speed within the normal range of 2 mm - 5 mm per minute.

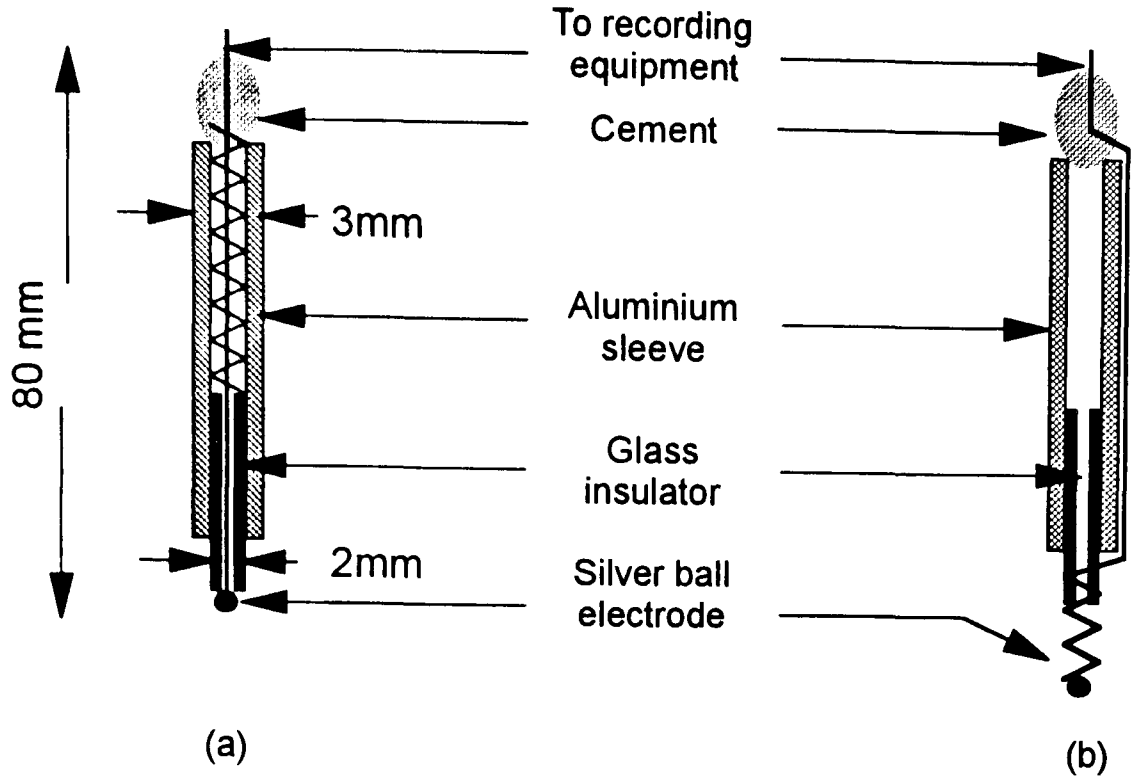

Figure 8.3: construction of the 'rabbit brain' electrodes. (a): first design; the silver ball was mounted on a spring-loaded glass insulator. (b): second design; the silver ball was mounted on a spring of silver wire.

As a comparison for the animal results, a saline-filled perspex beaker of diameter and height 25 mm was used as a phantom. An impedance change was generated by a perspex rod of 1 mm diameter submerged to a depth of 2 mm, the expected depth of the affected region of the brain. The same electrodes and equipment were used as for the animal experiments. A micromanipulator allowed the rod to be centred between the electrodes and then displaced in steps of 1 mm while recording APT data.

In the images obtained from the animal experiments, the 'focus' of activity was taken as the position of the peak resistivity change in the first image which showed focal activity after the stimulus. Correction for 'baseline drift' was sometimes necessary. This was carried out by subtracting a linear function from the instantaneous resistivity value in each image pixel. The coefficients of this function were determined by fitting a straight line to the resistivity values in the first and last minutes of measurement. Localisation accuracy was expressed as the distance between the measured position of the simulating electrode and the position of the image peak, as a percentage of the image diameter.

8.2.3 Evoked response experiments

The stimulus was a 70 V pulse, of duration 0.5 msec, applied to the median nerve. A clinical evoked EEG apparatus ('Sapphire', Medelec Ltd, Woking, UK) was used to determine the region of the cortex which showed the largest EEG response to the stimulus. The EEG was recorded between the cortex and an indifferent electrode in the animal's neck. Responses of about 40 μV - 50 μV were obtained in a well-defined region of parietal cortex with a diameter of about 2 mm. This will be referred to as the 'active region'. Outside the active region, the EEG response decreased rapidly: at a distance of 1 mm the EEG response decreased to about 5 μV.

The measurement of DC resistance changes in the cortex may be subject to the same sources of artefact as measurement on isolated nerves (chapter 7). The most troublesome of these was the effect of

the excitation current on the evoked action potential. If the excitation current caused a change in the timing or amplitude of the evoked EEG, this would manifest itself as a resistance change. To limit this source of artefact, the current electrodes were placed in the active region, while the voltage electrodes were placed at least 3 mm outside it (figure 8.4). This was expected to eliminate this source of artefact for two reasons:

i. In this configuration, the EEG recorded between voltage electrodes V1 and V2 was very small (< 2 μV). If the voltage change which results from the putative resistance change is as large as this, it cannot be entirely due this artefact.

ii. The arrangement of neurons in the cortex generates an electrical field which is predominantly radial to its surface (Kandel *et al.*, 1991, pp. 780ff). Since the rabbit cortex is flat, voltage electrodes V1 and V2 will be close to the zero-voltage isopotential line of an EEG source in the active region. The EEG recorded between V1 and V2 may therefore result, not from volume conduction from the active region, but mostly from separate physiological conduction from the thalamus to V1 and V2. This would not be affected by excitation current flow in the active region.

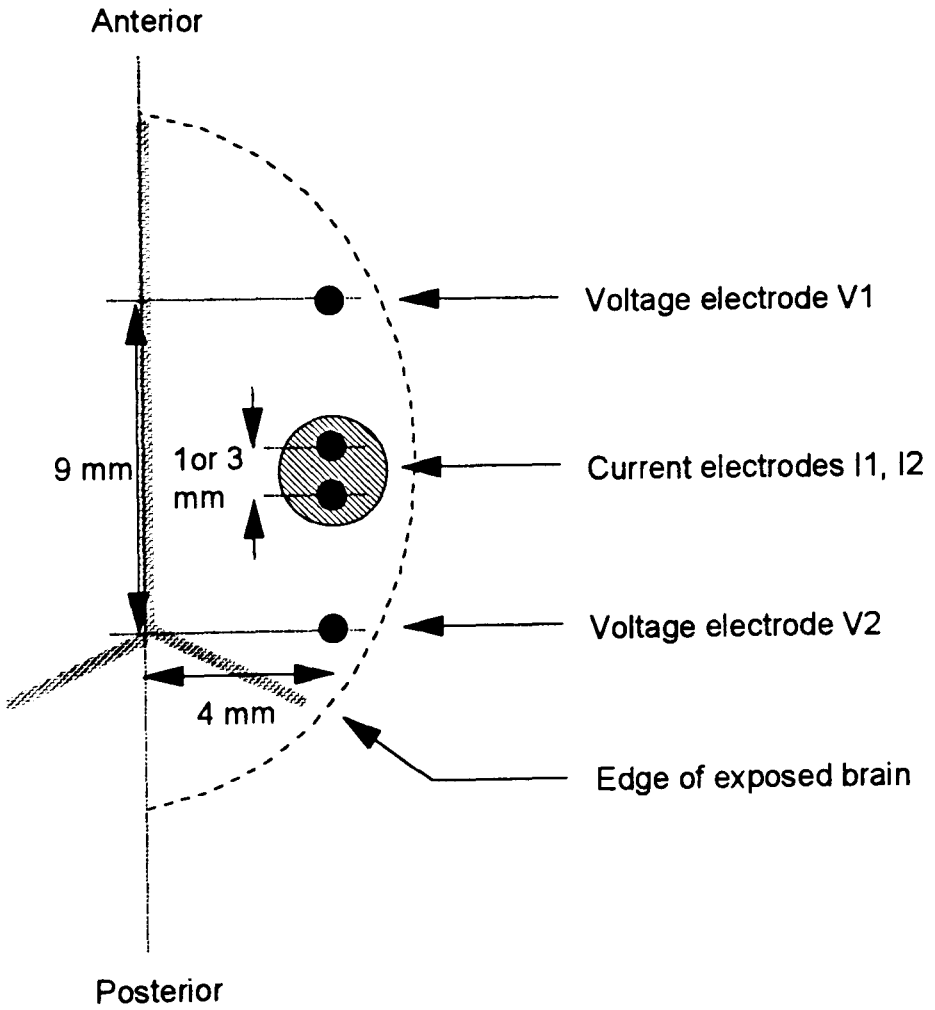

Figure 8.4: typical positions of the electrodes for DC resistance measurement in the rabbit cortex. The electrode positions are shown relative to the midline and the major blood vessels (shown as solid grey lines). The hatched area is the region which showed a large EEG response to stimulation.

The technique for recording evoked resistance changes was the same as described in chapter 7 and appendix A. Briefly:

- the excitation current was set to a given polarity, and a stimulus delivered to the nerve; the voltage between electrodes V1 and V2 was recorded at 6000 samples per second for 250 msec;
- the excitation polarity was reversed, a further stimulus delivered, and another set of voltages recorded;
- the two sets of voltages were added to obtain the evoked EEG signal, and subtracted to obtain the resistance. The subtraction causes a cancellation of the EEG signal, which should be the same regardless of the excitation polarity.

To obtain an adequate signal-to-noise ratio, this cycle was repeated, and the measurements averaged, 800-2000 times in each experiment, which lasted up to about eight minutes. The amplitude of the excitation current was 10 μA - 20 μA. For comparison, recordings were also made with the nerve stimulator or the excitation current disabled.

8.3 Results

8.3.1 Spreading depression experiments

Predominantly linear baseline drifts were evident in most recordings. The baseline drifts in epidural recordings were always smaller than those made on the exposed cortex (figure 8.5). The large negative deflections in the cortical trace (figure 8.5, solid line) correspond to irrigation of the cortex with aCSF; the drift was greater than in the epidural recordings even when the effect of this irrigation had subsided. After correction for baseline drift there was a consistent pattern of resistivity increase. Figure 8.6 shows a set of reconstructed images taken during a measurement with cortical electrodes. Before stimulation the resistivity was relatively constant over the image (frames 0-1 in figure 8.6). Shortly after the stimulus there was an initial discrete resistivity increase that corresponded to the point of initiation (frame 2). The peak resistivity increases in the images was 5% - 20%. This high resistivity area then expanded (frames 3-4). Subsequent spread was variable; it was more pronounced towards the periphery and had a propagation speed of about 3 mm/min (frames 5-6). The resistivity eventually returned to the baseline level (frame 7).

Localisation error was assessed for 17 cortical spreading depression events in five animals, which met the following criteria:

i. The calculated propagation speed of the spreading depression wavefront was 2-5 mm/min.

ii. The mean arterial blood pressure was greater than 9.3 kPa (70 mmHg).

Two further recordings met these criteria but had to be eliminated, owing to the presence of multiple foci. The distance (mean ± S.D., as percentage of diamter) between the peak of this initial resistivity increase and the known site of initiation was 5.9% ± 2.8% (n=5) and 11.5% ± 10% (n=12) for cortical and epidural recordings respectively. These distances are expressed as a fraction of the image diameter. The small size of the data set, and the non-parametric nature of the error distribution, make testing for the differences between these two experimental conditions somewhat problematic. The observed errors were divided into two approximately equal groups ('< 12%' and '> 12%') and subjected to Fisher's exact probability test. This yielded $p > 0.255$ (two-tailed, based on doubling the one-tailed value, as Armitage, 1971; pp137-). This implied that the distribution of localisation errors

between the '< 12%' and '> 12%' groups was not significantly different between cortical and epidural conditions. The cortical and epidural data were therefore pooled to give an overall mean localisation error: 8.7% ± 6.4%. While this analysis showed that it was reasonable to pool the accuracy figures, there was not enough data to show with any certainty that the accuracies in the two experimental conditions were truly equivalent.

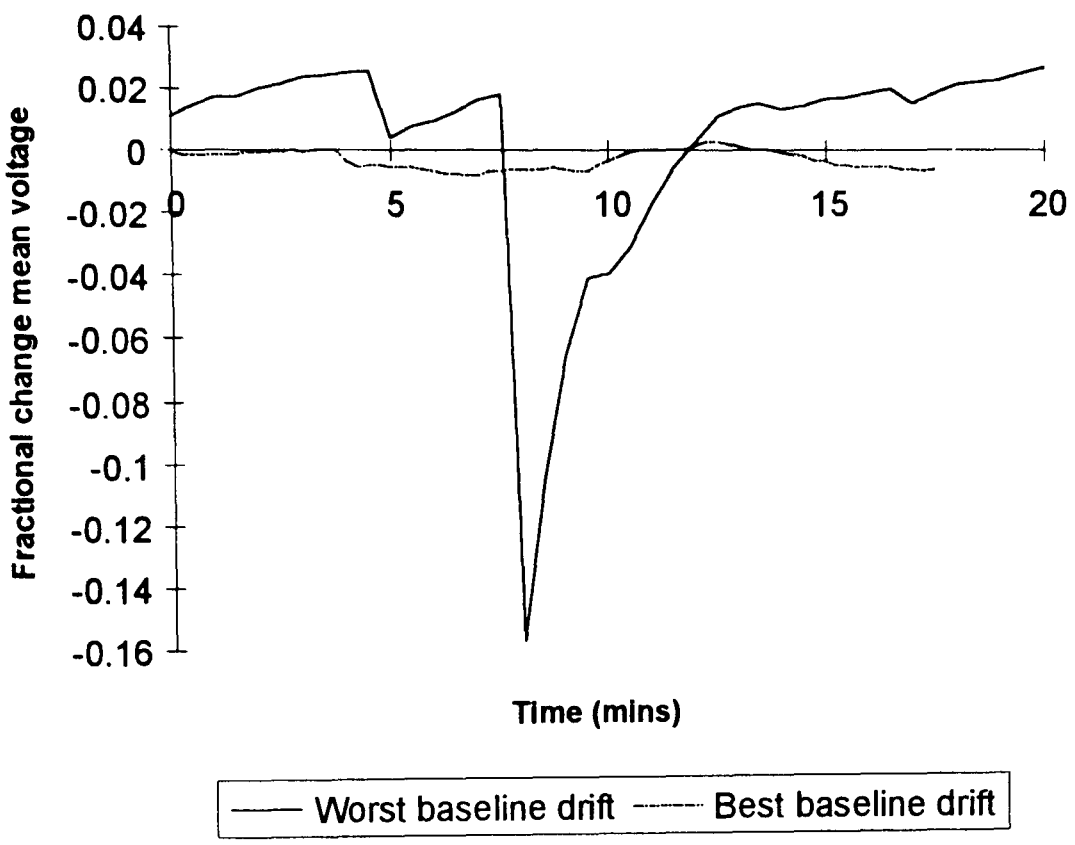

Figure 8.5: baseline drift measurements in the best and worst cases. The best case corresponded to eipdural recording, the worst to epicortical

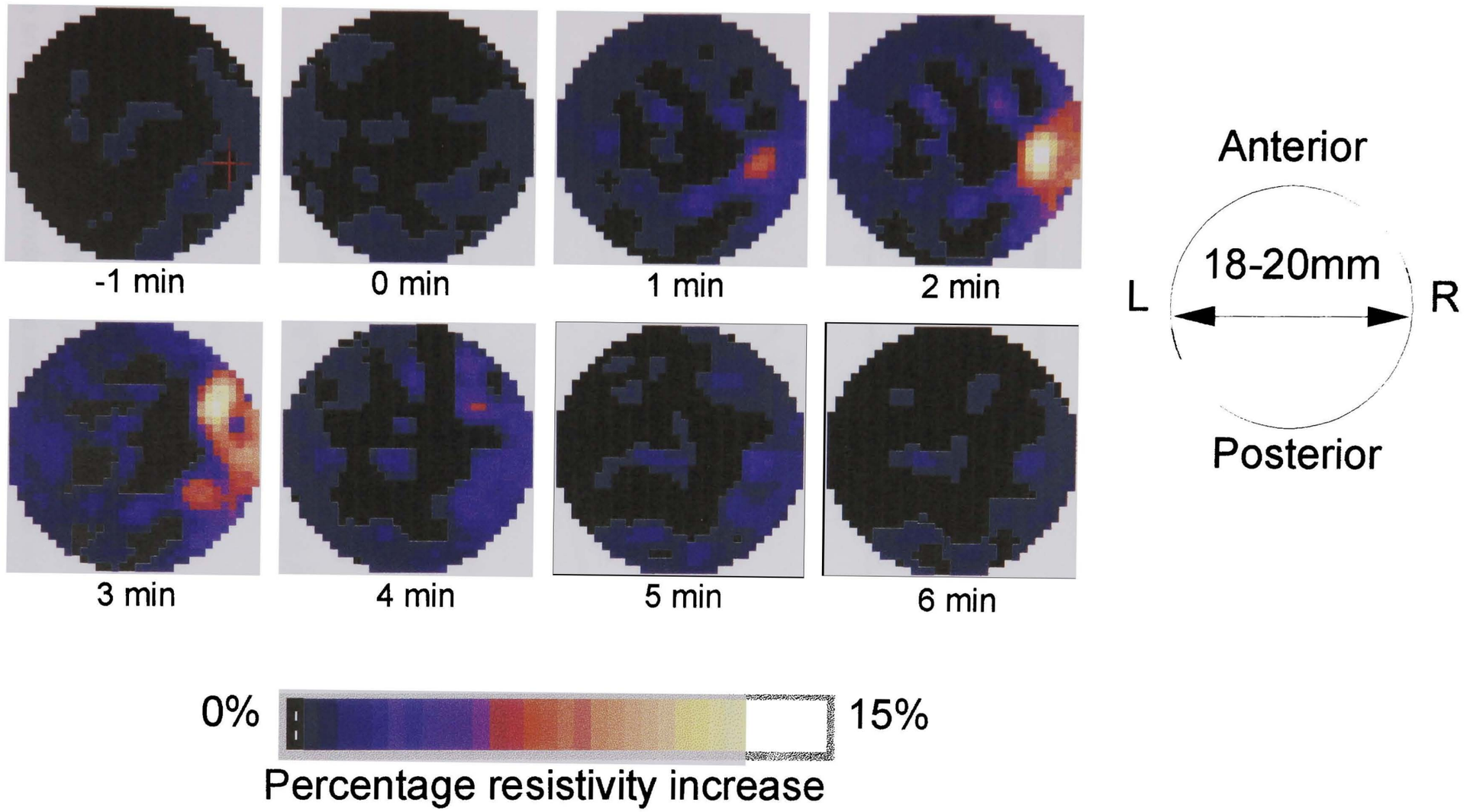

Figure 8.6: An example of a recording of resistivity change during cortical spreading depression. The red cross marks the position of the stimulating electrode. Times shown above the images are relative to the onset of the stimulus

The localisation error for the perspex rod in the saline phantom was 7.6% ± 1.3% (n=10). Part of this error was a systematic decrease in the apparent distance of the rod from the centre. After correction for this effect the mean error was reduced to 5.0%.

8.3.2 Evoked response experiments

Twenty recordings were made on two animals, of which seven were technically satisfactory; there were two main reasons for rejecting a recording as being unsatisfactory:

i. because the resistance changes were so small, they were sometimes partly obscured by electrode polarisation artefacts in the same part of the recording;
ii. the signal-to-noise ratio was too low to allow any small features to be detected. Since the signal-to-noise ratio was never better than about 3 to 1, even when changes were visible, no quantitative analysis of the measurements was attempted.

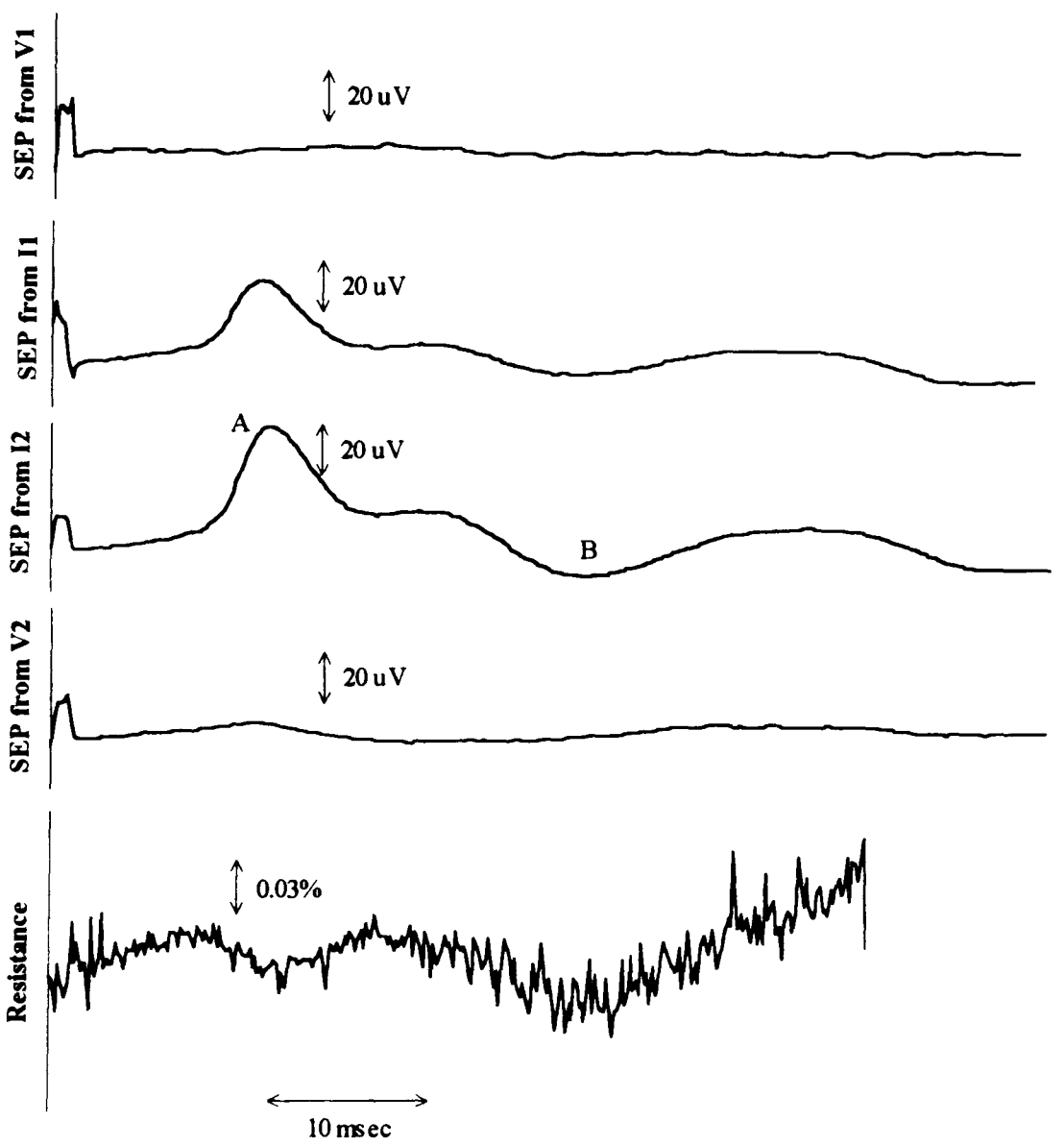

Figure 8.7: a typical recording of resistance change during median nerve stimulation. Upper four traces: somatosensory evoked potentials (SEPs) from electrodes V1, V2, I1 and I2 with respect to an indifferent electrode in the neck. Note that the potentials at I1 and I2 are much larger than at V1 and V2. Lower trace: small resistance decrease following the same stimulus, recorded with current between I1 and I2. In all recordings, the stimulus was delivered at the start of the trace. The maximum response occurred 10-20 msec after the stimulus

In the satisfactory recordings, the measured resistance changes during the initial part of the response (point 'A' in figure 8.7) were between 0.01% and 0.03%. In four recordings, there also appeared to be a longer, later resistance decrease, coincident with the EEG response at point 'B'. Because of slow variation in the baseline of the resistance recordings, it was difficult to quantify this change.

8.4 Discussion

8.4.1 Summary of results

This section summarises the results of the experiments above, and compares them to the predictions of the model described in chapter 4 and to the results of other studies.

Spreading depression. APT localised these large resistivity changes with a mean accuracy of 8.7% of diameter; this accuracy was not quite as good as for a physical phantom of similar geometry. The resistivity increases were 5%-20% in the APT images. The Barber and Seagar (1987) reconstruction process underestimates resistivity changes of this physical size and amplitude by about 25% (Holder and Khan, 1994). The true resistivity change is therefore likely to be 6.3% - 25%. This is somewhat lower than the figure reported by Ranck (1964) of 40%, but in reasonable agreement with the model prediction of 16%.

Evoked responses. DC resistance decreases of 0.01% - 0.03% occurred during median nerve stimulation. These are in good agreement with the model, which predicted decreases of 0.01%. The measurements are in poor agreement with the work of Klivington and Galambos (1968), who reported resistance changes of 0.005% at 10 kHz, during auditory evoked responses in the cat. According to the model, the resistance changes should have been 600 times larger at DC, or 3%. A resistance change of approximately this size was measured by Freygang and Landau (1955), in cat cortex, using direct electrical stimulation of the cortex. These authors' results are in reasonable agreement with the model: it predicts a cortical resistivity decrease of about 10% with electrical stimulation. It is likely, therefore, that the measurements described by Klivington and Galambos overestimated the true resistance change. Moreover, Freygang and Landau were unable to detect any resistance change due to nerve stimulation.

8.4.2 Sources of error in localisation of focal pathology

For APT to be useful in the clinical management of focal epilepsy (see §1.6), it must be able to localise the focus of the epileptic activity accurately. Factors which might be expected to produce systematic localisation errors include:

i. departures from the ideal circular geometry expected by the Barber and Seagar (1987) reconstruction process;
ii. anisotropy in the neural tissue. The fibrous nature of white matter makes anisotropy possible, but the resistivity changes in which we were interested were confined almost entirely to the grey matter (Grafstein *et al*, 1956). This is not thought to be significantly anisotropic (Hoffman *et al.*, 1973);
iii. inhomogeneities in the tissue produced, for example, by surgical injury.

In the phantom experiment, the test object appeared consistently closer to the centre than in reality, and the position of the object in the image could be corrected by increasing its radial position by 30%. This

is consistent with other quantitative studies (Eyüboglu *et al.*, 1991). The *in-vivo* results could not be improved by a correction of this sort. This suggests either that

i. any systematic errors in these experiments were smaller than random ones, or

ii. the rabbit brain is closer to the two-dimensional geometry than the saline phantom.

The latter is likely to be true, since the grey matter is more conductive than the white by about a factor of three. The grey matter layer is thin, and may approximate a two-dimensional geometry.

Possible sources of random error are:

i. baseline drift. This may affect localisation accuracy for at least two reasons. First, it was sometimes difficult to see the feature of interest, although baseline correction generally allowed the focus to be enhanced. Second the large variations in resistivity across the brain may undermine the reconstruction algorithm, which requires a reasonable degree of homogeneity of resistivity. In human patients the skull will be closed during measurement. If the baseline drift in these experiments was due to drying of the brain, which seems likely, baseline drift in patients should be at least as low as the best figures in these experiments;

ii. there were stimulus artefacts in some recordings. Although we used a battery-operated stimulator with its own return lead, it is still possible that the stimulating current developed a potential difference between measuring electrodes. This may have been sufficient to change the thickness of the chloride layer on the electrodes. This would change the electrode contact resistance, and result in a voltage error. This problem could be abolished simply by disconnecting the APT electrodes during stimuli;

iii. it was very difficult to measure the position of the stimulating electrode on the brain; the electrode connections were very dense, and the brain was not perfectly smooth. The uncertainty in these positional measurements is probably in the order of $\pm 5\tilde{}10\%$, and may well have been the largest source of error.

No significant difference was found between the localisation error for eipdural and epicortical measurement. However, baseline drift improved when the *dura* was intact, presumably because the rate of drying of the brain was smaller. This suggests that future experiments of this sort would be technically easier to perform if the *dura mater* were kept intact.

8.4.3 Validity of the measured evoked resistance changes

The measured resistance changes during evoked EEG activity were small (0.01% - 0.03%) and may have been subject to the same artefacts as were discussed in §7.4 concerning measurement on the crab nerve. Where possible, the same precautions were taken against artefacts in this study. Two factors add weight to the argument that the apparent resistivity changes are not due to an artefact related to the EEG.

i. 'Late' resistance decreases were found in some traces, which corresponded to late voltage changes in the unipolar EEG recorded at the site of the current electrodes (point 'B' in figure 8.7). No such late activity was found in the bipolar voltage recorded between the voltage electrodes V1 and V2, from which the resistivity change was derived.

ii. The voltage change which corresponded to the putative resistance change was of the order 1 μV - 3 μV. The EEG recorded between V1 and V2 was no greater than 4 μV. For an EEG artefact to cause an apparent resistance change of this magnitude would require that one polarity of the stimulating current changed the amplitude of the EEG response by 25%. However, there was no evidence that the EEG amplitude was different to that obtained without current excitation, within the limits of measurement error.

8.4.3 What categories of neurophysiological events can be imaged?

'Large' changes. These experiments clearly demonstrate the ability of APT to detect large (> 10%) focal resistivity changes in the brain in ideal conditions (large, slow resistivity changes; intracranial electrodes), as was predicted by the models described in chapters 5 and 6. If the resistance change during focal epilepsy is 3% (Holder *et al.*, 1993), it will probably be on the limit of detectability for the Mark 1 system. Diametric excitation will probably make this application very practicable.

'Medium changes'. The model described in chapter 6 predicted that resistivity changes of about 1% would probably be too small to image using adjacent-electrode excitation. Nevertheless, an ongoing study by DS Holder and A Rao has shown that images related to cerebral perfusion can be obtained using the Sheffield Mark 1 system. An example from their study is shown in figure 8.8; images are of resistivity change in the rabbit cortex (preparation as §8.2) during repetitive stimulation of the left median nerve. During three minutes of stimulation at a rate of five pulses per second, the blood flow in the right sensory cortex, as determined from laser Doppler flowmetry, increased by about 4%. However, the resistivity decrease in the images was up to 8%, and in reality may have been larger. It seems unlikely that the Mark 1 system will be able to image 1% changes, but, again, a different excitation pattern may improve the situation.

'Small changes'. Resistivity changes during action potential activity, where they could be measured, were between 0.01% and 0.03%. Imaging such changes will be very difficult. The feasibility of this imaging application is discussed in more detail in chapter 9 below.

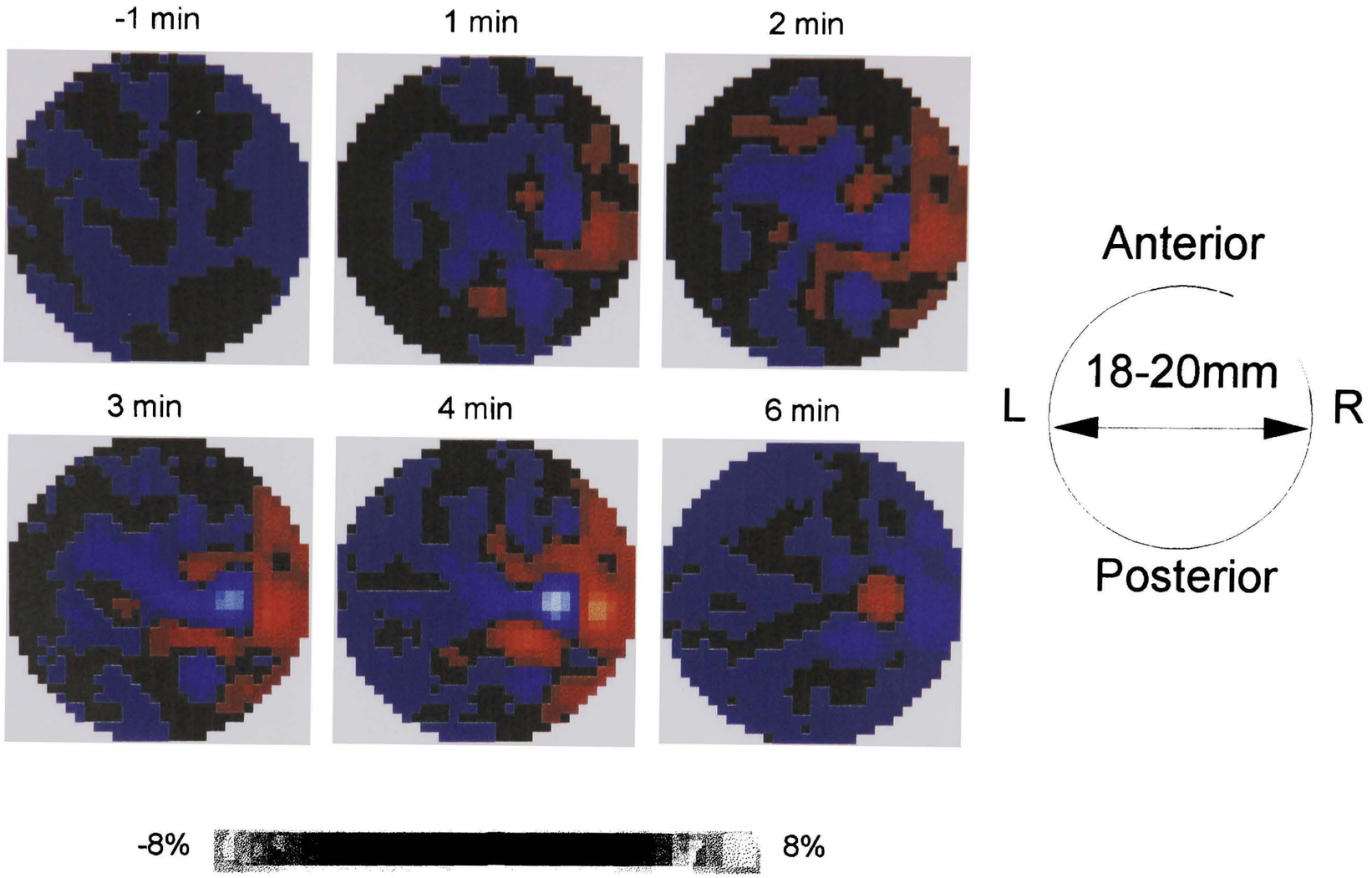

Figure 8.8: An example of a recording of resistivity change during continuous stimulation of the median nerve. The resistivity changes probably resulted from an increase in blood flow in the sensory cortex. The stimulation started at time zero, and continued for three minutes. Times shown above the images are relative to the onset of stimulation. Images kindly provided by DS Holder and A Rao.

Part D: discussion

9. Discussion

The main objective of this theoretical and experimental study was to determine whether APT might be used to image action potential activity in the brain. This section considers the extent to which this question has been answered, and briefly describes some issues which need further investigation.

9.1 Summary of results

Chapter 5. The model described in chapter 4 predicted that functional impedance changes in nervous tissue would depend markedly on frequency. For pathological changes due, for example, to anoxia, the predicted resistivity increase of 16% at 50 kHz (§5.3.6) was sufficiently large that there would be little advantage to using a lower frequency. The same is likely to be true of impedance changes that result from perfusion. For imaging neuronal depolarisation, the situation was somewhat different. Since only a small proportion of the available membrane area actually undergoes depolarisation (§5.4.3), the resistivity decrease was predicted to be small (~0.01%), even at DC. These results suggested that, in so far as neuronal depolarisation was amenable to APT imaging at all, an excitation frequency approaching DC was necessary.

Chapter 6. The finite element simulation described in chapter 5 confirmed the expected improvement in sensitivity from a 'cosine' excitation pattern compared a 'adiametric' one, and a 'diametric' over an 'adjacent' (§6.4.2). The presence of the skull, scalp and CSF did not change this conclusion; indeed, the effect of these tissues on the sensitivity was less than might be expected (§6.5.1). For imaging neuronal depolarisation, if the predictions of chapter 4 were borne out by experiment, we should expect changes of a few microvolts in an absolute boundary voltage approaching a volt. For focal epilepsy, the predicted boundary voltages were small enough that it is doubtful whether an adjacent-excitation APT apparatus would be appropriate. For this application, and for perfusion imaging, a 'diametric' or 'cosine' excitation pattern would probably put the sensitivity requirement within reach of existing APT equipment. For pathological events like stroke, the predicted boundary voltage changes were of tens of microvolts, and readily amenable to imaging, regardless of excitation pattern or frequency.

Chapter 7. When changes in DC resistivity were measured in isolated nerves of crabs (chapter 7), the findings were broadly in agreement with the predictions of the modeling study of chapter 4. The maximum decrease in resistance was 2.5%, the mean 1.0% (§7.3.2). With an equivalent measuring configuration, the model predicted a resistance decrease of 3.7%. The effect of positioning of the measuring electrodes also showed reasonable correspondence with the model.

Chapter 8. Resistivity changes due to cortical spreading depression could be imaged at 50 kHz. The localisation accuracy of the pathological focus was 8.7% of diameter. The evoked change in DC resistance after a median nerve stimulus was 0.01% - 0.03%, where it could be measured.

9.2 Questions remaining to be answered

In the light of these findings further questions have to be answered to decide whether APT will be a practicable technique for imaging action potential activity.

9.2.1 Is it practicable to construct an APT imaging device which can measure changes of a few microvolts in an absolute boundary voltage of about one volt DC?

During measurement of DC resistivity change, the apparatus described in appendix B was able, in calibration experiments, to measure changes equivalent to a few microvolts in a few millivolts. Its accuracy at this signal amplitude was about 4%-15% of reading. In the measurements of resistance change on the rabbit cortex, it measured what appeared to be changes of about 1 μV in a few tens of millivolts, although its accuracy for such signal sizes could not be determined. It is clear that this apparatus could not be used to measure resistance changes one hundred times smaller than this. To determine whether *any* apparatus would be adequate, we need to consider the various possible limitations on the sensitivity.

i. *Resolution of the analogue-to-digital converter.* The converter was a sixteen-bit device; the need to average at least 200 cycles provided a further 7-8 bits of 'effective' (oversampling) resolution. This should easily provide the eighteen-bit resolution required for 0.001% sensitivity.

ii. *Systematic error in the analogue instrumentation and electrode system.* There were systematic artefacts in the resistance recordings which were often of similar size to the evoked resistance changes. In the isolated nerve experiments, these artefacts were normally overcome by varying the timing of the stimulus with respect to the excitation waveform. In addition, the 'true' resistance changes were somewhat shorter than the artefacts. As the resistance changes became smaller, it became more difficult to distinguish between the signal and the artefact. With resistance changes of 0.01%, it is likely that these systematic artefacts were the main limitation on the sensitivity of the system. They have undoubtedly more than one origin. When the resistance measurement instrument was connected only to a resistor network, it recorded artefacts of about 0.1% of the signal amplitude. These were traced to a ripple on the output of the current source; this can almost certainly be improved with a different source design. Larger artefacts, with lower frequencies, appeared in measurements on tissue. These latter are almost certainly the result of variations in electrode potential (§7.4.1). They can probably be reduced by an improvement in the 'balance' of the current source (*i.e.* the ratio of the 'positive' to the 'negative' charge). In measurements on the human brain, the electrodes would have a larger surface area, which would also reduce the artefact. I think it likely that the systematic artefact can be reduced by a about factor of ten. Furthermore, systematic errors, by their very nature, can be measured, and some sort of compensation applied.

iii. *Noise in the instrumentation.* In addition to systematic errors, measurement on a resistor network was subject to a small random noise component; after averaging 200 acquisition cycles its amplitude was about 0.01% of reading. A similar signal-to-noise ratio applied to the measurements on crab nerve. In measurements on the cortex, signal averaging typically continued for 2000 cycles, which should have improved the signal-to-noise figure to about 0.003%. Further improvements in the

instrumentation would almost certainly bring the random noise to a level compatible with measuring a 0.001% change in resistance.

iv. *Noise in the brain.* In practice the noise in the cortical measurements was about 0.03% of reading: about ten times as large as for the crab nerve or the resistor network, for the equivalent number of averaged cycles. Apart from its increased amplitude, another factor argues in favour of this noise having a physiological, rather than a physical, origin. The noise level invariably decreased during the response to a stimulus, and increased afterwards. This can be explained as the action potential activity in the cortex being brought into synchronisation by the stimulus, and reverting to desynchronisation afterwards. This intrinsic EEG activity will set a limit on the signal-to-noise ratio which can be achieved, regardless of the performance of the instrumentation. Since the duration of averaging used in these experiments could not be extended much further, any reduction in this noise component will have to come from a re-arrangement of the electrodes. A reduction of the effect of intrinsic EEG activity is necessary, not only because it constitutes 'noise' in the resistance measurement, but because variations in the evoked EEG response could imitate a resistance change. This is discussed further below.

9.2.2 If adequate sensitivity were achieved, could we be sure that the resistivity changes were not artefactual?

There is no doubt that an excitation current can modify the action potential and cause artefacts which imitate a resistance change (§7.4.3). In both the isolated nerve and cortical experiments, this artefact was eliminated by appropriate placement of the electrodes. Such control of electrode position will not be possible in an imaging system; the electrodes must lie on the scalp or in the subdural space, and be supplied with a particular spatial distribution of current. To prevent artefact, we ideally need an electrode which can record voltages due to the applied excitation current, but is insensitive to intrinsic EEG sources. Such an electrode cannot realistically be constructed. However, the fact that the applied current and the EEG sources produce electric fields with different characteristics means that there may be an arrangement of electrodes that partially fulfill this requirement. The applied current will produce a field which is approximately parallel to plane of the measuring electrodes, while the intrinsic sources, which are assumed to be radial to the cortex[1], produce a radial field pattern. A possible scheme for attenuating the signal due to intrinsic sources is shown in figures 9.1 and 9.2. At least two rings of electrodes are required. One of these rings is supplied with excitation current in the normal way. Figure 9.1 shows a 'diametric' drive configuration; a 'cosine' configuration may also be used, but separate electrodes will be required for excitation and for measurement.

---

[1] The human cortex is convoluted, so a source which is radial to the cortex may not be radial to the electrode ring. However, the sources to which this applies will be further from the electrodes, and their contribution to the intrinsic signal smaller.

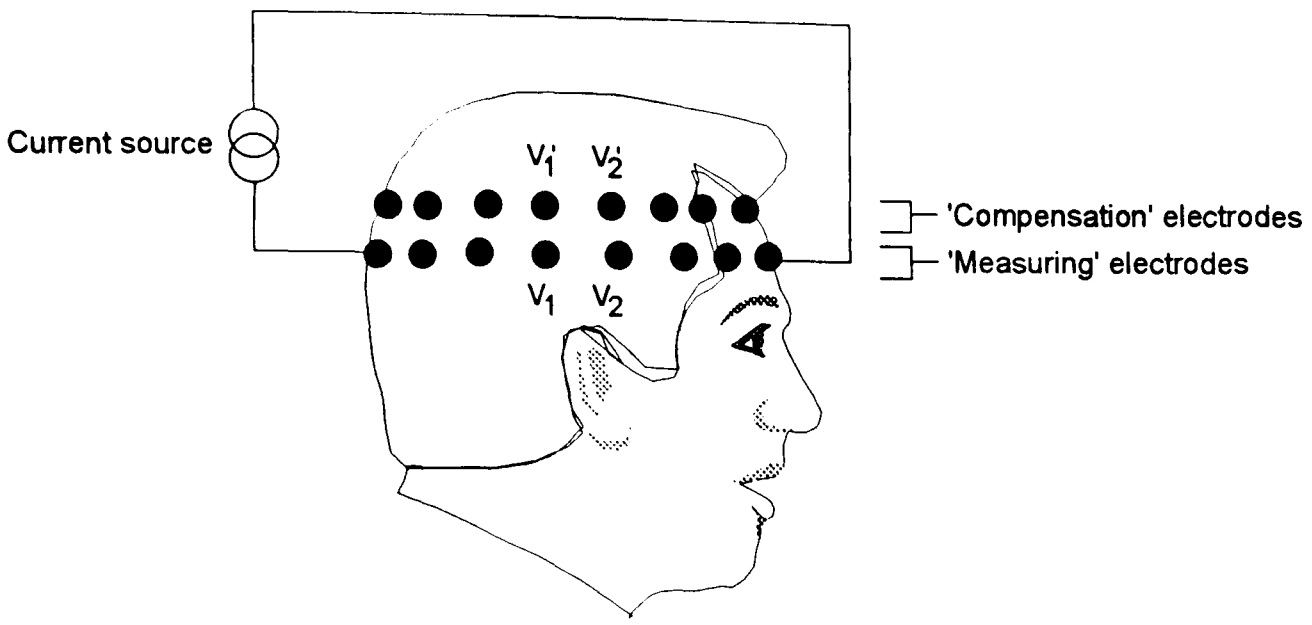

Figure 9.1: a proposed scheme for 'compensating' the measured boundary voltages for the effects of intrinsic EEG activity. The upper row of electrodes is used for compensation, the lower for measurement

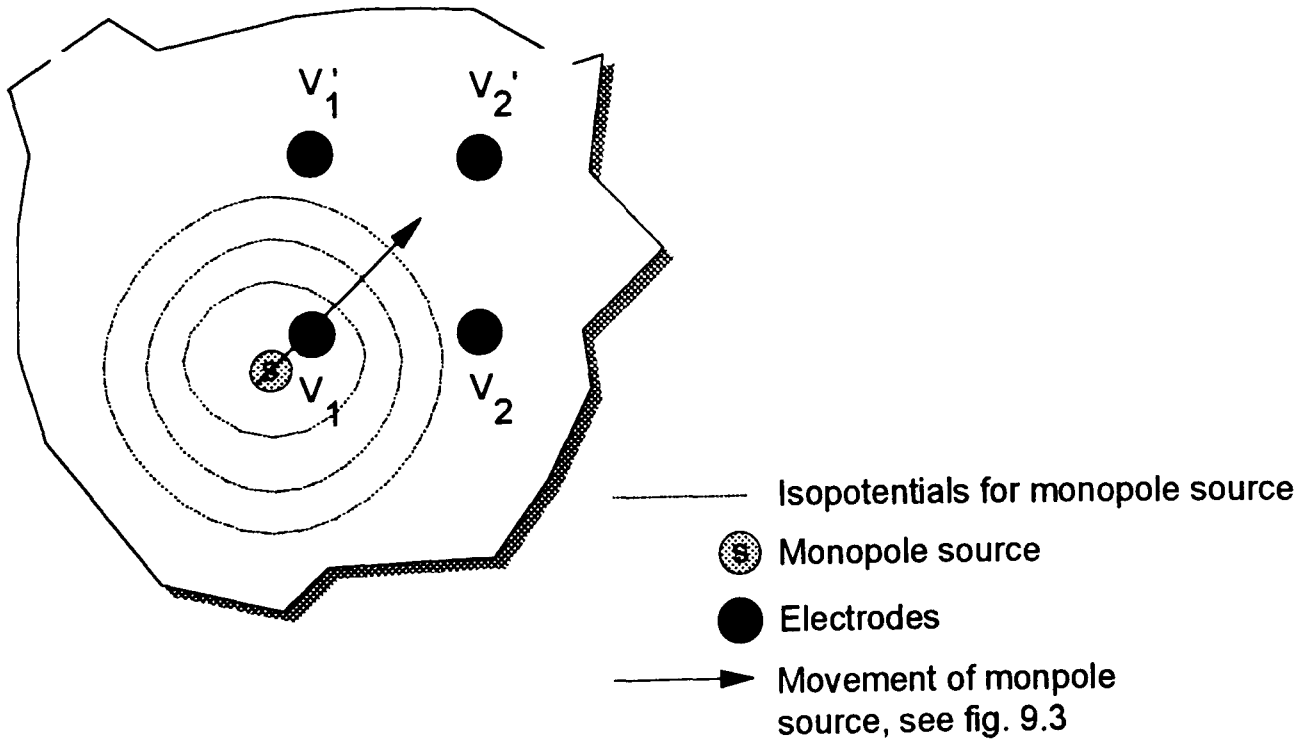

Figure 9.2: expanded detail of the region including electrodes V_1 and V_2 in figure 9.1. A hypothetical monopole source is shown in the region of V_1, along with its isopotentials. The flow of current from the excitation electrodes is from left to right.

Figure 9.2 shows the area around four of the electrodes: V_1 and V_2 in the 'measuring' plane, and V_1' and V_2' in the 'compensating' plane. The boundary voltage would normally be measured as the difference between the voltages at V_1 and V_2. In the proposed scheme, the 'compensated boundary voltage' g_{comp} would be determined from four electrodes rather than two. One possible determination is:

$$g_{comp} = [(v_1 - v_2) + (v_1' - v_2') - (v_1 - v_1') + |v_2 - v_2'|] / 2 \qquad [9.1]$$

where v_1 is the voltage at V_1, *etc.*

Because the field resulting from the applied current is approximately parallel to the plane of the electrodes, the applied current produces voltage such that $v_1 \approx v_1'$ and $v_2 \approx v_2'$. Equation [9.1] therefore reduces to:

$$g_{comp} = v_1 - v_2$$

which is identical to the standard differential boundary voltage. If an intrinsic EEG source is approximated as a monopole or a dipole, its effect on the standard boundary voltage v_1-v_2 will be large when it is below either electrode V1 or V2. Its effect on g_{comp}, as determined from equation [9.1] is considerably smaller. Figure 9.3 shows a comparison between the 'uncompensated' boundary voltage (v_1-v_2) and g_{comp} for a monopole source at various positions between the measuring electrodes. The source was moved on a line between electrodes V_1 and V_2, as shown in figure 9.2. Except for a small range of positions, the EEG voltage in the compensated boundary voltage is considerably smaller than without the compensation. The improvement is by a factor of 6 when the source is beneath the electrodes.

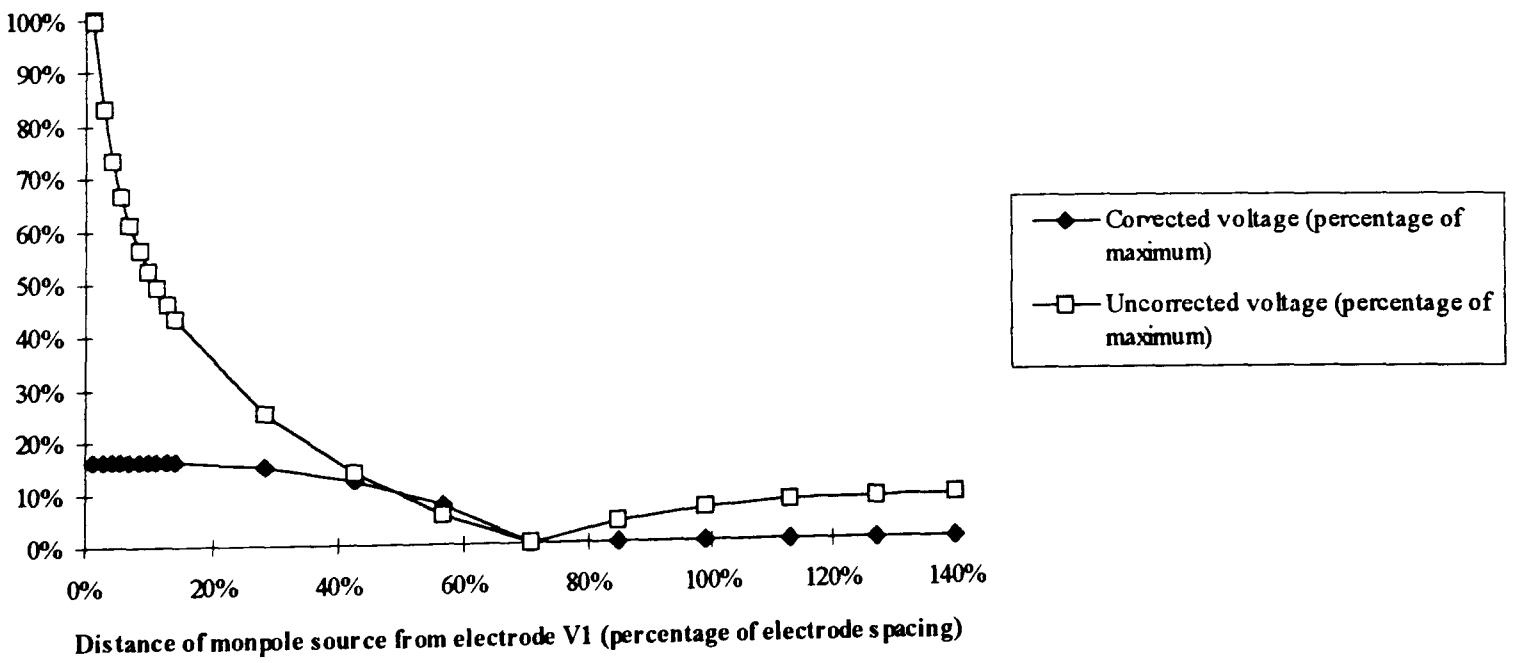

Figure 9.3: comparison of the size of EEG voltage on boundary voltages measured in the normal way, with those obtained by the compensation scheme described in the text

The form of equation [9.1] was determined experimentally, and I make no claim that it represents an optimal technique. It does demonstrate, however, that useful rejection of EEG activity may be obtained with such a method. The optimal compensation will depend on the configuration (dipole, monopole) which best represents the intrinsic sources. Furthermore, better compensation may be obtained by including additional electrodes.

9.2.3 Given the impracticality of the adjacent-electrode excitation scheme for this application, can we achieve an adequate spatial resolution with a cosine current distribution?

The model described in chapter 5 predicted that the boundary voltage change resulting from excitation of adjacent electrodes would be about 1 nV; it is probably impossible to measure such a change accurately. The boundary voltage change with a cosine excitation pattern was about 1000 times larger; even this will be very difficult to measure. There is every reason to think that the spatial resolution will be limited when the excitation is of low spatial frequency. However, as was discussed in §6.5.3, it can be argued that, with diametric or cosine excitation, the spatial resolution will suffer less from the presence of the skull and scalp than would adjacent excitation. Whether this resolution will be adequate for practical applications is unknown. I have performed some preliminary studies comparing the spatial resolution of diametric with adjacent excitations; similar considerations will apply to the cosine case. Boundary voltages were generated using the finite-element model of the head which was described in chapter 5. These boundary voltages corresponded to both diametric and adjacent excitation patterns. A 'point' resistivity change (one mesh element) of a factor of 1000 was positioned at the centre, then displaced 30%, 60% and 80% of radius towards electrode 13. Images were reconstructed using unfiltered backprojection[2]. It is well known that, with adjacent excitation, the presence of the skull causes a distortion of the image, such that features are compressed towards the centre (*e.g.* McArdle *et al.*, 1988). If the skull is uniform, the compression is uniform: the angular position of features remains unchanged. The compression of the image features towards the centre can be taken as a measure of the effect of the skull on the spatial resolution. To return the image features to their correct positions would require a uniform 'stretch' of the centre of the image. This would also increase the widths of the features, and reduce the effective spatial resolution. The full-width at half-maximum of a feature at the centre of the image was increased by the amount necessary to restore the image features to their correct positions. This new full-width was taken to be a measure of the worst-case spatial resolution.

An example of the images produced by the two excitation methods is shown in figure 9.4. The image produced by diametric excitation showed a feature which was obviously wider than that with adjacent excitation, but both images provided useful information about the position of the feature. The compression of feature towards the centre was present in these experiments both with adjacent

---

[2] The software to perform the unfiltered backprojection was kindly supplied by Dr Richard Bayford of Middlesex University. A filtered backprojection algorithm is under development for the diametric configuration, but was not available at the time of writing. To make a fair comparison with the adjacent excitation case, these images also were produced using unfiltered backprojection.

excitation, and, to a lesser extent, with diametric excitation. Figure 9.5 show a comparison between the radial position of the feature in the image, and the known position of the disturbance in the finite element mesh. The upper traces correspond to adjacent excitation. With a uniform initial distribution of resistivity, the images followed the 'ideal' trace quite closely. However, the compression of the image with 'head' resistivity is clear.

'Adjacent'

'Diametric'

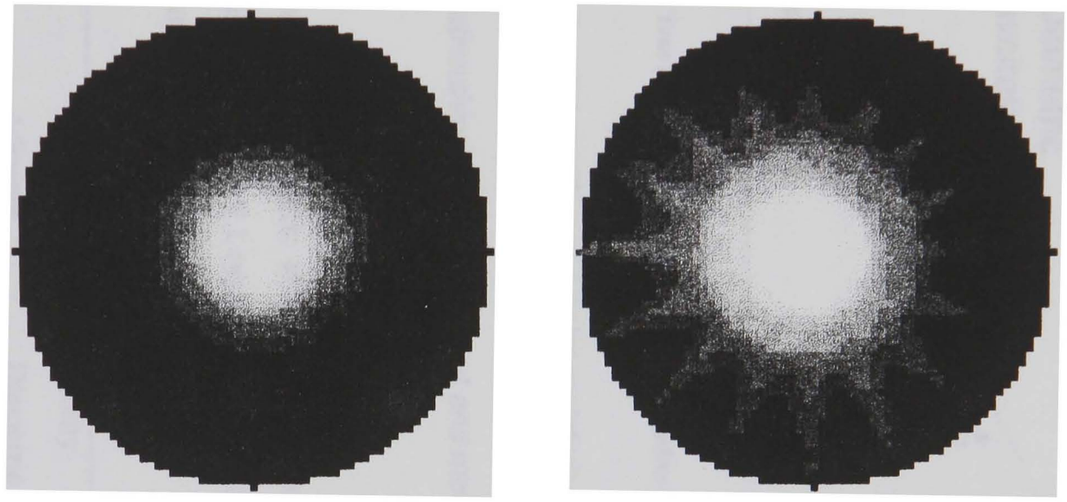

Figure 9.4: images of a central 'point' resistivity increase of a factor of 1000, obtained with 'adjacent' and 'diametric' excitation patterns. The model from which the boundary voltages were calculated included a 'skull', as described in chapter 5. Both images were produced using unfiltered backprojection.

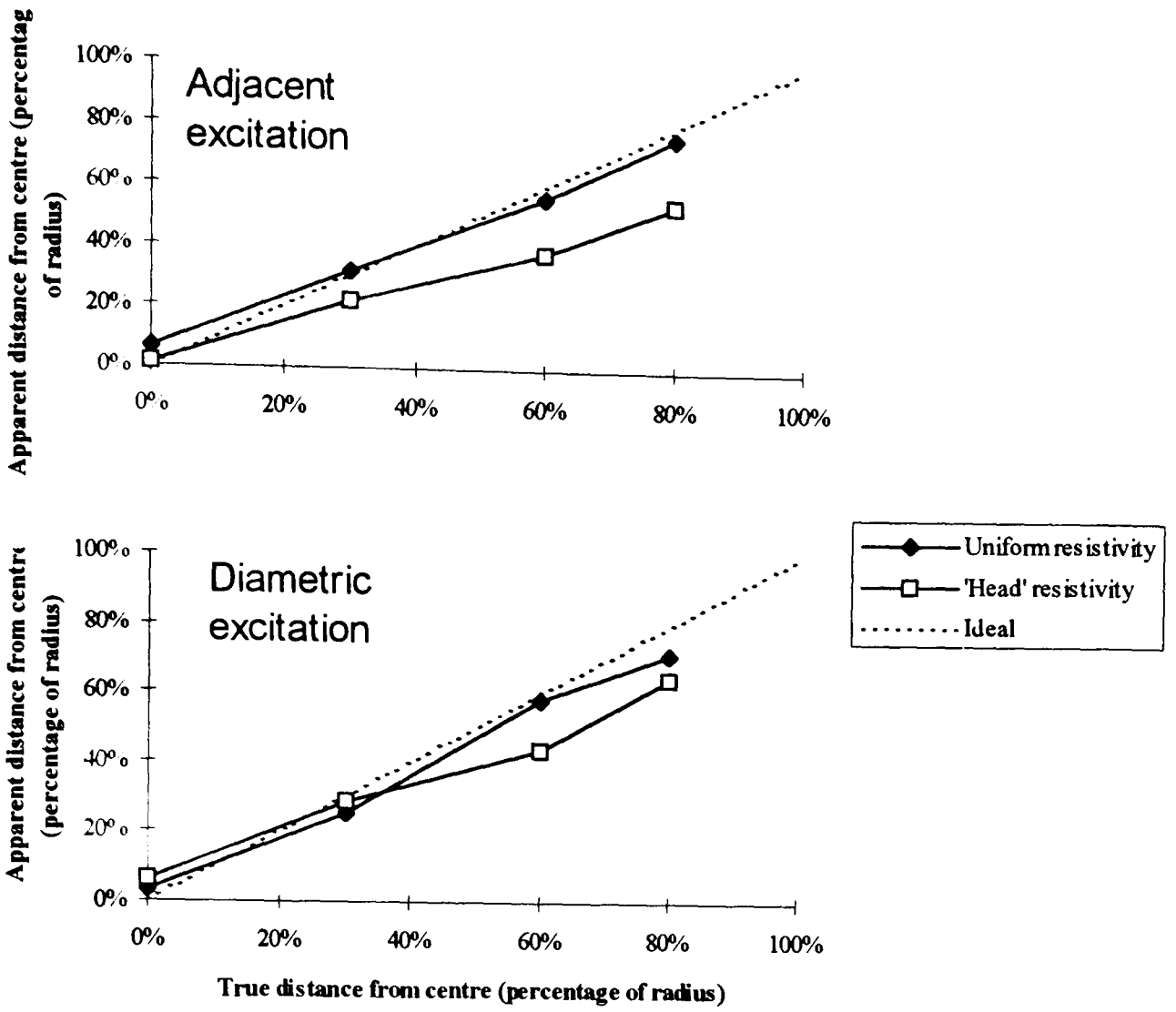

Figure 9.5: apparent radial position of a point resistivity change, for adjacent and diametric excitation, with uniform and 'head' resistivity distributions. The dashed lines are of unity slope, and represent the relationship between apparent and measured position for an 'ideal' imaging system.

The lower traces correspond to diametric excitation; the position of the feature was somewhat less affected by the 'head' resistivity. Table 9.1 summarises the effect of the 'head' resistivity distribution on the image compression and spatial resolution.

	Uniform initial resistivity		'Head' distribution of initial resistivity	
	Adjacent	Diametric	Adjacent	Diametric
Compression of features towards centre.	13%	12%	36%	25%
Full-width at half-maximum (FWHM) at centre of image.	36%	75%	31%	54%
FWHM adjusted for image compression.	42%	86%	48%	71%

Table 9.1: a comparison of the image compression and spatial resolution obtained with diametric and adjacent excitation. The full-widths at half-maximum are expressed as percentages of the image radius.

Row 1 shows the amount by which the image features were compressed towards the centre. This was taken to be

$$\text{compression} = 1 - \text{slope of trace in figure 9.5}$$

Row 2 shows the full-width at half-maximum (FWHM) of the feature in the centre of the image. Row 3 shows the FWHM multiplied by the amount needed to restore features to their correct position, *i.e.*,

$$\text{new FWHM} = \frac{\text{original FWHM}}{\text{slope of trace in figure 9.5}}$$

This was taken as a measure of the achievable spatial resolution.

It can be seen that the spatial resolution is always better with adjacent excitation. However, the effect of the head resistivity was to decrease the spatial resolution, from 42% to 48%. With diametric excitation, the spatial resolution is actually better in the head model (71%) than with uniform resistivity (86%). Furthermore, if the initial distribution of resistivity is unknown, the finding that the diametric pattern is less affected by the initial resistivity means that it will localise features in the image with greater accuracy.

In summary, it seems that useful images can be obtained using diametric excitation, although the spatial resolution is reduced. Further work will be required to determine whether improvements in the reconstruction technique will lead to a better resolution.

9.2.4. What is the effect of anisotropy?

We should only expect to obtain images of resistivity change in the grey matter of the brain (§5.4.5). Nevertheless, most of the excitation current has to cross the myelinated white matter of the brain, which is anisotropic. The effect of anisotropy on image reconstruction is not well understood; at present it is ignored, (Barber, 1993) being of minor importance to most APT applications. For imaging of the brain we cannot take this approach. At best, anisotropy will be a source of error; at worst, it may completely undermine the image reconstruction technique and prevent any useful images being obtained. If the anisotropy were non-uniform, it may be necessary to incorporate information about it into the reconstruction process itself. If this necessitates an iterative, non-linear reconstruction technique, it is very doubtful whether the voltage measurements will ever achieve sufficient accuracy (§21.2). If the anisotropy is relatively uniform, it will probably have a similar effect on images reconstruction as did the skull in §9.2.3. There the error took the form of a uniform compression of image features towards the centre. The effect could be corrected, with some reduction in spatial resolution, by a uniform expansion of the centre of the image. Some work needs to be directed to finding out whether anisotropy can be controlled in the same way.

9.2.5 Can the signals be made larger?

If the applied excitation current were allowed to be larger than the 100 μA assumed in chapter 5, this would bring two advantages. First, the voltage change resulting from the resistance change would be increased. This would not obviate the need for 0.001% sensitivity, but would reduce the influence of noise in the instrumentation. Second, the voltage change would be increased with respect to intrinsic EEG sources. The excitation current must be low enough not to cause damage, but it is likely that stimulation of the brain will occur before damage.

Ranck (1975) analysed the stimulation current thresholds from ten studies of stimulation in the central nervous system. He showed that, when the thresholds were plotted against the distance between the neuron and the stimulating electrode on log-log paper, all the values were close to a line of unity slope. This was true for myelinated axons, unmyelinated axons and grey matter, and did not depend significantly on the size, shape or position of the stimulating electrode, or the species. There was however, a variation of about a factor of ten in measurements made in the same conditions on different animals. This implies that, for a given stimulus duration, the most important factor in the determination of the stimulus threshold is the distance between current source and neuron. All Ranck's results were normalised to a stimulating pulse duration of 200 μsec. The relationship between the strength of the current and the duration necessary for it to cause stimulation was found empirically to be:

$$I_{threshold} = I_{rheobase}(1 + c / t)$$

where $I_{threshold}$ is the stimulation threshold for a pulse of duration t, c is the chronaxie (see below) and $I_{rheobase}$ the largest current which will *not* stimulate, regardless of duration. Chronaxie is the duration needed to cause stimulation with twice the minimum current, and was found to be approximately 0.7 times the membrane time constant. Since DC tomography requires a long current pulse, the applied current must be less than the rheobase current. If the membrane time constant is assumed to be 10 msec (see chapter 4), the chronaxie is 7 msec, and the term (1+c/t) is equal to 36; this is the factor by which the thresholds reported by Ranck must be divided to be approximately equivalent to the maximum excitation current. For example, stimulation of the monkey cortex with surface electrodes required about 2 mA; the corresponding maximum excitation threshold would be 55 μA. With scalp electrodes, the current density may only be reduced by a factor of two, giving a limit to the excitation current of 110 μA. It would seem from this that there is little scope for increasing the signal size by increasing the excitation current. However, Freygang and Landau (1955) were able to apply a current pulse of 3.5 mA to the cortex for up to 700 μsec without causing stimulation. This is a considerably larger stimulus than those reported by Ranck (1975). A possible explanation is that this current was delivered to a pool of saline on the exposed cortex, rather than to an electrode, resulting in a reduced cortical current density. When widely-separated electrodes are used to inject current, the current density will be rather higher at the edges than at the centre (Cheng *et al.*, 1989); dividing the applied current by the surface area of the electrode will give a misleadingly low figure for peak current density. Peak current density may be

reduced by the use of a large array of closely-spaced electrodes, excited with a cosine current pattern, but a more practical method might be to induce a current in the head using magnetic coils.

Magnetic induction of an excitation current been shown to be practicable for impedance imaging (*e.g.*, Gençer and Ider, 1994), at least with 30 kHz - 50 kHz fields. The excitation field is more uniform than that obtained from electrodes, and can, in principle, be concentrated towards the centre of the head. Moreover, magnetic excitation removes one of the main problems of APT: electrode impedance and polarisation. However, it is not yet known whether it is possible in practice to construct a magnetic imaging system which uses low frequency or DC excitation.

In summary, the amount of current which can safely be applied to the scalp is probably greater than 100 μA, but is unlikely to be more than about twice as great. Magnetic excitation may allow greater current densities to be concentrated in the centre of the brain, and has other technical advantages; it needs to be decided whether low-frequency magnetic excitation is practicable.

9.3 Conclusion

This work has demonstrated that APT is a suitable technique for imaging brain pathology; APT provides practical benefits of portability, safety and low cost compared to other techniques. In addition, APT almost certainly has the potential for imaging cerebral perfusion in research and clinical practice, although further development of hardware and software techniques is probably required. It has also been shown that, at least as far as sensitivity is concerned, the tissues of the skull, scalp and CSF do not prevent the use of extracranial electrodes. As regards imaging neuronal depolarisation, the sensitivity required, and the presence of extraneous EEG signals, makes this an extremely demanding application.

From the results of this study, some idea may be obtained of the characteristics which an APT system must have, if it is to be used for imaging action potential activity:

i. it must use a 'cosine' excitation current distribution, or perhaps better still an 'adaptive' one, which can optimise itself for sensitivity;
ii. it must ideally apply a direct current excitation, or at worst a frequency below about 10 Hz.;
iii. it must be able to measure changes of a few microvolts in an absolute boundary voltage of about one volt

I propose that a DC tomograph with these characteristics could be implemented; however, considerable refinement of the electronic instrumentation would undoubtedly be required. The limiting factor on the smallest resistivity changes which can be imaged is probably not the sensitivity of the measuring instrument, but the effect of intrinsic signals from the cortex. Further investigation will show whether these may be controlled.

References

References

Abeyratne UR, Kinouchi Y, Oki H, Okada J, Shichijo F and Matsumoto K 1991 Artificial neural networks for source localisation in the human brain *Brain Top.* **4** 3-19

Adey WR, Kado RT and Didio J 1962 Impedance measurements in brain tissue of animals using microvolt signals *Exp. Neurol.* **5** 47-66

Agnew WF and McCreery DB 1987 Considerations for safety in the use of extracranial stimulation for motor evoked potentials *Neurosurg.* **20** 143-7

Anderson AR 1989 99mTc-D,L-hexamethylene-propyleneamine oxime (99mTc-HMPAO): basic kinetic studies of a tracer of cerebral blood flow *Cerebrovasc. Brain Metab. Rev.* **1** 288-318

Araki and Terzuolo 1962 Membrane currents in spinal motoneurons associated with the action potential and synaptic activity *J. Neurophysiol.* **25** 772-89

Armitage P 1971 *Statistical Methods in Medical Research* (Oxford: Blackwell)

Avis NJ and Barber DC 1993 Image reconstruction using non-adjacent drive configurations *Physiol. Meas.* **15** (Suppl. 2A) 153-60

Avis NJ, Barber DC, Brown BH and Kiber MA 1991 Distortions in applied potential tomographic images due to non-uniform reference distributions *Proc. 13th Ann. Conf. IEE. EBMS.* 20-1 New York: IEEE

Barber DC 1993 An overview of image reconstruction *Clinical and Physiological Applications of Electrical Impedance Tomography* ed Holder DS (London: UCL Press)

Barber DC and Brown BH 1984 Applied potential tomography *J. Phys. E: Sci. Instrum.* **17** 723-33

Barber DC and Brown BH 1986 Recent developments in applied potential tomography *Information processing in medical imaging* ed Bacharach S (Dordrecht: Martinus Nijhoff)

Barber DC and Seagar AD 1987 Fast reconstruction of resistance images *Clin. Phys. Physiol. Meas.* **8** (Suppl. 2A) 47-54

Bayford R 1994 *Ph.D. Thesis* Middlesex University

Bayford R, Hanquan Y, Boone KG and Holder DS 1995 Experimental validation of a novel reconstruction algorithm based on backprojection of Lagrange multipliers *Clin. Phys. Physiol. Meas.* (in press)

Binnie CD 1988 Electroencephalography *A Textbook of Epilepsy* eds Laidlaw J, Richens AN and Oxley J (Edinburgh: Churchill Livingstone)

Blad B 1994 An electrical impedance tomography system for complex impedance imaging *Innov. Tech. Biol. Med.* **15** (Suppl. 1) 80-8

Blad B, Bernstam L, Persson B and Lindstrom K 1992 Improvements in the hardware of the Lund impedance tomography system *Clin. Phys. Physiol. Meas.* **13** (Suppl. A) 15-7

Blad B, Lindström K, Bertenstam L and Persson BRR 1994 A current-injecting device for electrical impedance tomography *Clin. Phys. Physiol. Meas.* **15** (Suppl. 2A) 169-77

Bland JM and Altman DG 1986 Statistical methods for assessing agreement between two methods of clinical measurement *Lancet* **February 8, 1986** 307-10

Boone KG, Lewis AM and Holder DS 1994 Imaging of cortical spreading depression using EIT: implication for localisation of epileptic foci *Physiol. Meas.* **15** (Suppl. 2A) 189-90

Boone KG and Holder DS 1995a Assessment of noise and drift artefacts in electrical impedance tomography measurements using the Sheffield Mark I system *Innov. Tech. Biol. Med.* (in press)

Boone KG and Holder DS 1995b A model of the effect of variations in contact and skin impedance on APT measurement artefacts *Innov. Tech. Biol. Med.* (in press)

Boone KG and Holder DS 1995c A prototype system for imaging action-potential activity using direct current tomography *Physiol. Meas.* (in press)

Boone KG, Bayford R and Holder DS 1995d Modelling and measurement of the DC resistance change in crab peripheral nerve during the action potential *in press: Proceedings of the 4th European Concerted Action on Impedance Tomography* (abs)

Boone KG and Holder DS 1996a Current approaches to analogue instrumentation design in EIT: a review *Physiol. Meas.* (in press)

Boone KG and Holder DS 1996b The effect of skin impedance on measurement error and image quality in electrical impedance tomography *Med. Biol. Engng. Comp.* (in press)

Bozler E and Cole KS 1935 Electrical impedance and phase angle of muscle in rigor *J. Gen. Physiol.* **6** 229-41

Bragós R, Rosell J and Riu P 1994 A wideband AC-coupled current source for electrical impedance tomography *Clin. Phys. Physiol. Meas.* **15** (Suppl. 2A) 91-9

Breckon WR and Pidcock MK 1987 Mathematical aspects of impedance imaging *Clin. Phys. Physiol. Meas.* **8** (Suppl. A) 77-84

Brown BH 1983 Tissue impedance methods *Imaging with Non-Ionizing Radiations* ed Jackson DF (Guildford: Surrey University Press)

Brown BH 1990 Overview of clinical applications *Proceedings of the Copenhagen meeting on electrical impedance tomography (Copenhagen 1990)* ed Hames TJ (Sheffield: University of Sheffield)

Brown BH 1993 A review of systems available for medical use *Clinical and Physiological Applications of EIT* ed Holder DS (London: UCL Press)

Brown BH, Barber DC, Leathad AD, Lu L, Wang W, Smallwood RH and Wilson AJ 1994 High frequency EIT data collection and parametric imaging *Innov. Tech. Biol. Med.* **15** (Suppl. 1) 1-8

Brown BH, Barber DC and Seagar AD 1985 Applied potential tomography: possible clinical applications *Clin. Phys. Physiol. Meas.* **6** 109-21

Brown BH, Lindley E, Knowles R and Wilson AJ 1990 A body-worn APT system for space use *Proceedings of the Copenhagen meeting on electrical impedance tomography (Copenhagen 1990)* ed Hames TJ (Sheffield: University of Sheffield)

Brown DC and Seagar AD 1987 The Sheffield data collection system *Clin. Phys. Physiol. Meas.* **8** (Suppl. A) 91-8

Brown DC and Seagar AD 1987 Limitations in hardware design *Clin. Phys. Physiol. Meas.* **8** (Suppl A) 91-8

Burês J, Buresóva O and Krivanek K 1974 *The Mechanism and Application of Leao's Spreading Depression of Electroencephalographic Activity* (New York: Academic Press)

Burlakova YeV, Veprintsev BN and Rass IT 1959 Lag of the impedance effect behind the action potential in frog nerve *Biofizikia* **4** 617-20

Campbell JH, Harris ND, Zhang F, Brown BH and Morice AH 1994 Clinical applications of electrical impedance tomography in the monitoring of changes in intrathoracic fluid volumes *Physiol. Meas.* **15** (Suppl. 2A) 217-22

Campbell JH, Harris ND, Zhang F, Morice AH and Brown BH 1993 The monitoring of changes in intrathoracic fluid volumes with the Sheffield EIT system *Clinical and physiological applications of electrical impedance tomography* ed Holder DS (London: UCL Press)

Carpenter RHS 1992 *Neurophysiology* (Sevenoaks, UK: Hodder and Stoughton)

Cendes ZJ, Shenton D and Shahnasser H 1983 Magnetic field computation using Delauny triangulation and complementary finite element methods *IEEE. Trans. Magnetics.* **Mag-19** 2551-4

Chailakhian LM and Iur'ev SA 1957 An investigation of the time relations of the action potential and impedance changes on excitation in the frog nerve *Biofizikia* **2** 417-26

Chen ZQ and Paoloni PJ 1992 An error study of some linear reconstruction algorithms for electrical impedance tomography *Clin. Phys. Physiol. Meas.* **13** 389-410

Cheney M and Isaacson D 1991 An overview of inversion alogorithms for impedance imaging *Cont. Math.* **122** 29-39

Cheney M, Isaacson D, Newell JC, Simake S and Goble J 1990 NOSER: An algorithm for solving the inverse conductivity problem *Int. J. Imag. Sys. Technol.* **2** 66-75

Cheney M, Isaacson D, Newell JC, Simske S and Goble J 1990 NOSER: an algorithm for solving the inverse conductivity problem *Int. J. Imag. Sys. Technol.* **2** 66-75

Cheng K, Isaacson D, Newell JC and Gisser DG 1989 Electrode models for electric current computed tomography *IEEE. Trans. Biomed. Eng.* **36** 918-24

Choh-Luh L, bak AF and Parker LO 1967 Secific resistivity of cerebral cortex and white matter *Exp. Neurol.* **20** 544-57

Cole KS 1968 *Membranes, ions and impulses* (Los Angeles: University of California Press)

Cole KS 1975 Analogue solution for electrical capacity of membrane covered square cylinders in square array at high concentration *Proc. Natl. Acad. Sci. USA.* **72** 4936-9

Cole KS and Baker RF 1941 Longitudinal impedance of the squid giant axon *J. Gen. Physiol.* **24** 771-88

Cole KS and Baker RF 1941 Transverse impedance of the squid giant axon during current flow *J. Gen. Physiol.* **24** 535-49

Cole KS and Curtis HJ 1936 Electric impedance of nerve and muscle *Quant. Biol.* **4** 78-89

Cole KS and Curtis HJ 1939 Electric impedance of the squid giant axon during activity *J. Gen. Physiol.* **22** 649-70

Cole KS and Hodgkin AL 1939 Membrane and protoplasm resistance in the squid giant axon *J. Gen. Physiol.* **22** 671-87

Conway J, Hawley M, Mangnall YF, Amasha H and van Roon GC 1992 Experimental assessment of electrical impedance imaging for hyperthermia monitoring *Clin. Phys. Physiol. Meas.* **13** (Suppl. A) 185-90

Cook RD, Saulnier GJ, Gisser DG, Goble J, Newell JC and Isaacson D 1994 ACT3: A high-speed, high-precsion electrical impedance tomograph *IEEE. Trans. Biomed. Eng.* **41** 713-22

Cook RD, Saulnier GJ and Goble JC 1991 A phase sensitive voltmeter for a high-speed high-precision electrical impedance tomograph *Proc. 13th Ann. Conf. IEE. EBMS.* **13** 22-3

Cusick G, Holder DS, Birkett A and Boone KG 1994 A system for impedance imaging of epilepsy in ambulatory human subjects *Innov. Tech. Biol. Med.* **15** (Suppl. 1) 34-9

Dai WW, Marsili PM, Martinez E and Morucci J-P 1994 Using the hilbert uniqueness method in a reconstruction algorithm for electrical impedance tomography *Physiol. Meas.* **15** (Suppl. 2A) 161-8

Davies ER 1993 *Electronics, Noise and Signal Recovery* (London: Academic Press)

Denyer CW, Lidgey FJ, McLeod CN and Zhu QS 1994 Current source calibration simplifies high-accuracy current source measurement *Innov. Tech. Biol. Med.* **15** (Suppl. 1) 48-55

Denyer CW, Lidgey FJ, Zhu QS and McLeod CN 1993 High output impedance current source for electrical impedance tomography *Physiol. Meas.* **15** (Suppl. 2A) 79-82

Devane SP 1993 Application of EIT to gastric emptying in infants: validatioin against residual volume method *Clinical and physiological applications of electrical impedance tomography* ed Holder DS (London: UCL Press)

Dines KA and Lytle RJ 1981 Analysis of electrical conductivity imaging *Geophysics* **46** 1025-36

Drayer BP, Wolfson SK Jr and Reinmuth OM 1972 Xenon-enhanced computed tomography for the analysis of cerebral integrity, perfusion and blood flow *Stroke* **9** 123-30

Durand D 1984 The somatic shunt cable model for neurons *Biophys. J.* **46** 645-53

Ell PJ, Hocknell JML, Jarritt PH, Cullum I, Lui D, Campos-Costa D, Nowotnik DP, Pickett RD, Canning LR and Neirinckx RD 1985 A 99-Tc-m-labelled radiotracer for the investigation of cerebral vascular disease *Nucl. Med. Communic.* **6** 437-41

Elster DE 1988 *Cranial Magnetic Resonance Imaging* (New York: Churchill Livingstone) pp. 31-42

Erlanger J and Gasser HS 1937 *Electrical signs of nervous activity* (Philadelphia: University of Philadelphia Press)

Eyüboglu BM, Brown BH and Barber DC 1989 Limitations to SV determination from APT images *Proc. 11th Ann. Conf. IEEE. EBMS.* 442-3 New York: IEEE

Eyüboglu BM, Brown BH, Barber DC and Seagar AD 1987 Localisation of cardiac-related impedance changes in the thorax *Clin. Phys. Physiol. Meas.* **8** (Suppl. A) 167-73

Flasterstein AH 1966 Voltage fluctuations of metal-electrolyte interfaces in electrophysiology *Med. Biol. Engng.* **4** 583-8

Flasterstein AH 1966 A general analysis of voltage fluctuations of metal-electrolyte interfaces *Med. Biol. Engng.* **4** 589-94

Freygang WH and Landau WM 1955 Some relations between resistance and electrical activity in the cerebral cortex of the cat *J. Cell. Comp. Physiol.* **45** 377-92

Fricke H and Morse S 1925 The electric resistance of blood between 800 and 4.5 million cycles *J. Gen. Physiol.* **9** 153-67

Fuks LF, Cheney M, Isaacson D, Gisser DG and Newell JC 1991 Detection and imaging of electric conductivity and permitivitty and low frequency *IEEE. Trans. Med. Imag.* **38** 1106-10

Gadd R, Record P and Rolfe P 1992 A sensitivity region reconstruction algorithm using adjacent drive current injection strategy *Clin. Phys. Physiol. Meas.* **13** (Suppl. A) 101-5

Gadd R, Record PM, Vinther F and Rolfe P 1993 The Keele approach to EIT in the neonatal head *Clinical and Physiological Applications of Electrical Impedance Tomography* ed Holder DS (London: UCL Press)

Galambos R and Velutti R 1968 Evoked resistance shifts in unanaesthetised cats *Exp. Neurol.* **22** 243-52

Geddes L 1972 *Electrodes and the Measurement of Bioelectric Events* (New York: John Wiley & Sons)

Geddes L and Baker LE 1967 The specific resistance of biological materials: a compendium of data for the biomedical engineer and physiologist *Med. Biol. Engng.* **5** 271-93

Geddes LA, Baker LE, Moore AG and Coulter TW 1969 Hazards in the use of low frequncies for the measurement of physiological events by impedance *Med. Biol. Engng.* **7** 289-96

Gençer NG and Ider YZ 1994 A comparitive study of serveral exciting magnetic fields for induced current EIT *Physiol. Meas.* **15** (Suppl. 2A) 51-7

Gençer NG, Kuzoglu M and Ider YZ 1994 Electrical impedance tomography using induced currents *IEEE. Trans. Med. Imag.* **13** 338-50

Geselowitz DB 1971 An application of electrocardiographic lead theory to impedance plethysmography *IEEE. Trans. Biomed. Eng.* **BME-18** 38-41

Gesteland RC, Howland B, Lettvin JY and Pitts WH 1958 Comments on microelectrodes *Proc. IRE.* **47** 1856-62

Gielen FLH, Walinga-de Jonge W and Boon KL 1984 Electrical conductivity of skeletal muscle tissue: experimental results from different muscles in vivo *Med. Biol. Eng. Comp.* **22** 569-77

Gisser DG, Isaacson D and Newell JC 1987 Current topics in impedance imaging *Clin. Phys. Physiol. Meas.* **8** (Suppl. A) 13-31

Gisser DG, Isaacson D and Newell JC 1988 Theory and performance of an adaptive current tomgraphy system *Clin. Phys. Physiol. Meas.* **9** (Suppl. A) 35-41

Gisser DG, Newell JC, Salunier G, Hochgraf C, Cook RD and Goble JC 1991 Analog electronics for a high-speed high-precision electrical impedance tomograph *Proc. 13th Ann. Conf. IEE. EBMS.* 23-4 New York: IEEE

Godin DT, Parker PA and Scott RN 1991 Noise characteristics of stainless steel surface electrodes *Med. Biol. Eng. Comp.* **29** 585-90

Grafstein B 1956 Locus of propagation of spreading depression *J. Neurophysiol.* **19** 309-16

Grant FC 1923 Localisation of brain tumours by determination of the electrical resistance of the growth *J. Amer. Med. Ass.* **81** 2166-9

Guardo R, Boulay C, Murray B and Bertrand M 1991 An experimental study in electrical impedance tomography using backprojection reconstruction *IEEE. Trans. Biomed. Eng.* **38** 617-27

Hampshire AR, Smallwood RH, Brown BH and Primhak RA 1993 Multi-frequency and parametric images of neonatal lungs *Proceedings of the 3rd meeting of the European Concerted Action on Impedance Tomography, Anakra, Turkey, September 1994*

Hansen JH and Olsen CE 1980 Brain extracellular space during spreading depression and ischaemia *Acta. Physiol. Scand.* **108** 355-65

Harris ND, Suggett AJ, Barber DC and Brown BH 1987 Applied potential tomography: a new technique for monitoring pulmonary function *Clin. Phys. Physiol. Meas.* **9** (Suppl. A) 79-85

Hodgkin AL 1938 The subthreshold potentials in a crustacean nerve fibre *Proc. Roy. Soc. B.* **126** 87-121

Hodgkin AL 1939 The relation between conduction velocity and the electrical resistance outside a nerve fibre *J. Physiol.* **94** 560-70

Hodgkin AL and Rushton WAH 1946 The electrical constants of a crustacean nerve fibre *Proc. Roy. Soc. Lond. B* **133** 444-79

Hoffman CJ, Clarck FJ and Ochs S 1973 Intracortical Impedance Changes during spreading depression *J. Neurobiol.* **4** 471-86

Holder 1992 Impedance changes during the compound action potential: implications for impedance imaging of neuronal depolarisation in the brain *Med. Biol. Eng. Comp.* **30** 140-6

Holder DS 1990 Phyiological constraints to imaging brain function with EIT and scalp electrodes *Clinical and Physiological Applications of Electrical Impedance Tomography* ed Holder DS (London: UCL Press)

Holder DS 1991 *Ph.D. thesis* University College London.

Holder DS 1992 Electrical impedance tomography of global cerebral ischaemia with cortical or scalp electrodes in the anaesthetised rat *Clin. Phys. Physiol. Meas.* **13** 87-98

Holder DS 1993 Physiological constraints to imaging brain function using scalp electrodes *Clinical and Physiological Applications of EIT* ed Holder DS (London: UCL Press)

Holder DS 1993 Opportunities for EIT in the nervous system *Clinical and physiological applications of electrical impedance tomography* ed Holder DS (London: UCL Press)

Holder DS, Anells N and Boone KG 1994 In-vivo images of the female breast obtained with the Sheffield Mark 1 electrical impedance tomography system *Proceedings of the 3rd meeting of the European Concerted Action on Impedance Tomography, Ankara, Turkey, September 1994*

Holder DS, Binnie CD and Polkey CP 1993 The possible application of EIT to imaging epileptic foci *Proceedings of the COMAC meeting on biomagnetism* (in press)

Holder DS and Brown BH 1993 Biomedical application of EIT: a critical review *Clinical and Physiological Applications of EIT* ed Holder DS (London: UCL Press)

Holder DS and Khan A 1994 The use of polyacrilamide gels to determine the linearity of the Sheffield Mark 1 EIT system *Clin. Phys. Physiol. Meas.* **15** (Suppl. 2A) 45-50

Holder DS and Temple AJ 1993 Effectiveness of the Sheffield EIT system in distinuishing patients with pulmonary pathology from a series of normal subjects *Clinical and physiological applications of electrical impedance tomography* ed Holder DS (London: UCL Press)

Horowitz P and Hill P 1990 *The art of electronics* (New York: Cambridge University Press)

Hossman K 1971 Cortical steady potential, impedance and excitability changes during and after total ischaemia of cat brain *Exp. Neurol.* **32** 163-75

Hu MQ, Hua P and Webster JG 1987 Measurement error in an electrical impedance tomography system *Proc. IEEE. EBMS.* **9** 1425-6

Hua P, Webster JG and Tompkins WJ 1988 A regularised electrical impedance tomography reconstruction algorithm *Clin. Phys. Physiol. Meas.* **9** (Suppl. A) 137-41

Hua P and Woo EJ 1991 Reconstruction algorithms *Electrical impedance tomography* ed Webster JG (Bristol: Adam Hilger)

Hua P, Woo EJ and Webster JG 1993 Using compound electrodes in electrical impedance tomography *IEEE. Trans. Biomed. Eng.* **40** 29-34

Hua P, Woo EJ, Webster JG and Tomkins WJ 1993 Finite element modelling of the electrode-skin contact impedance in electrical impedance tomography *IEEE. Trans. Biomed. Eng.* **40** 335-43

Hua P, Woo EJ, Webster JG and Tompkins WJ 1991 Iterative reconstruction methods using regularisation and optimal current patterns in electrical impedance tomography *IEEE. Trans. Med. Imag.* **10** 621-8

Hughes TAT, Liu P, Griffiths H, Lawrie BW and Wiles CM 1994 An analysis of studies comparing electrical impedance tomography with X-ray videoflouroscopy in the assessment of swallowing *Physiol. Meas.* **15** (Suppl. 2A) 199-209

Isaacson D 1986 Distinguishability of conductivities by electric current computed tomography *IEEE. Trans. Med. Imag.* **5** 91-5

Isaacson D and Cheney M 1992 Comments on reconstruction algorithms *Clin. Phys. Physiol. Meas.* **13** (Suppl. A) 83-9

Isakov V 1988 Of uniqueness of recovery of a discontinuous conductivity coefficient *Appl. Maths.* **41** 865-77

Jack JJB, Noble D and Tsien RW 1975 *Electric current flow in excitable cells* (Oxford: Blackwell)

Johnson DW, Stringer WA, Marks MP, Yonas H, Good WF and Gur D 1991 Stable xenon CT cerebral blood flow imaging: rationale for and role in clinical decision making *Am. J. Neuroradiol.* **12** 201-13

Jolles P, Chapman PR and Alavi A 1989 PET, CT and MRI in the evaluation of neuropsychiatric disorders: current applications *J. Nuclear. Med.* **30** 1589-606

Jossinet J and Risacher F 1995 The variability of resistivity in human breast tissue *Proceedings of the European Concerted Action on Impedance Tomography workshop on 'reproducibility in clincal EIT'*

Jossinet J, Tourtel C and Jarry R 1994 Active current electrodes for in-vivo electrical impedance tomography *Clin. Phys. Physiol. Meas.* **15** (Suppl. 2A) 83-90

Jossinet J and Trillaud C 1990 A high contrast dual frequency multi-eelctrode system for electrical impedance tomography *Proceedings of the Copenhagen Meeting on Electrical Impedance Tomography* ed Hames TJ (Sheffield: Sheffield University)

Julian FJ, Moore JW and Goldman DE 1962 Membrane potentials of the lobster giant axon obtained by a sucrose gap technique *J. Gen. Physiol.* **45** 1195-216

Kandel ER, Schwartz SH and Jessel TM 1991 *Principles of neural science* (New York: Elsevier)

Keynes RD and Lewis PR 1951 The resting exchange of radioactive potassium in crab nerve *J. Physiol.* **113** 73-98

Killingback ALT, Zadehkoochak M, Blott BH and Hames TK 1993 Pulmonary ventilation, pulmonary perfusion and ventricular ejection profile studies with EIT *Clinical and physiological applications of electrical impedance tomography* ed Holder DS (London: UCL Press)

Kim Y, Woo HW and Luedtke AE 1989 Impedance tomography and its application in deep venous thrombosis detection *Eng. Med. Biol. Mag.* **March**

Klivington R and Galambos R 1968 Rapid resitance shifts in cat cortex during click-evoked responses *J. Neurophysiol.* **31** 565-73

Koch C and Poggio T 1985 A simple algorithm for solving the cabel equation in dendritic trees of arbitrary geometry *J. Neurosci. Methods* **12** 303-15

Kohn RV and Vogelius M 1984 Identification of an unknwon conductivity by means of measurements at the boundary *Proc. SIAM-AMS.* **14** 113-23

Kohn RV and Vogelius M 1984 Determining conductivity by boundary measurements *Comm. Pure. App. Math.* **37** 289-98

Kotre 1994 EIT image reconstruction using sensitivity-weighted filtered backprojection *Physiol. Meas.* **15** (Suppl. 2A) 125-36

Kotre CJ 1993 EIT image reconstruction using sensitivity coefficient weighted backprojection *Physiol. Meas.* **15** (Suppl. 2A) 125-36

Koukourlis CS, Kyriacou GA and Sahalos JN 1994 An improvement of the common-mode rejection in EIT *Innov. Tech. Biol. Med.* **15** (Suppl. 1) 90-6

Koukourlis CS, Kyriakou GA and Sahalos JN 1992 Differential synchronous demodulation for electrical impedance tomography *Clin. Phys. Physiol. Meas.* **13** (Suppl. A) 31-4

Koukourlis CS, Kyriakou GA and Sahalos JN 1992 Performance of a differential synchronous demodulator for electrical impedance tomography *Clin. Phys. Physiol. Meas.* **13** (Suppl. A) 35-8

Kozuoglu M, Leblebicioglu K and Ider YZ 1994 A fast image reconstruction technique for electrical impedance tomography *Physiol. Meas.* **15** (Suppl. 2A) 115-24

Kyriacou GA, Koukourlis CS and Sahalos JN 1993 A reconstruction algorithm of electrical impedance tomography with optimal configuration of the driven electrodes *IEEE. Trans. Med. Imag.* **12** 430-8

Lassen NA 1985 Cerebral blood flow tomography with xenon-133 *Sem. Nucl. Med.* **15** 347-56

Lassen NA, Sveinsdottir E, Kanno I, Stokely EM and Rommer P 1978 A fast moving single positron emission tomograph for regional cerebral blood flow studies in man *J. Comput. Assist. Tomogr.* **2** 661-2

Lassen NA, Sveinsdottir E, Kanno L, Stokely EM and Rommer P 1978 A fast moving single positron emmision tomograph for regional cerebral blood flow studies in man *J. Comput. Assist. Tomogr.* **2** 661-2

Lauritzen M 1987 Cerebral blood flow in migraine and cortical spreading depression *Acta. Neurol. Scand.* **76** (Suppl. 1) 113

Leao AAP 1944 Spreading depression of activity in cerebral cortex *J. Neurophysiol.* **7** 359-90

Leao AAP and Morrison RS 1945 Propagation of cortical spreading depression *J. Neurophysiol.* **8** 33-45

Leathad AD, Caldicott L, Brown BH, Sinton AM, McArdle FJ, Smith RWM and Barber DC 1993 Cardiovascular imaging of injected saline *Clinical and physiological applications of electrical impedance tomography* ed Holder DS (London: UCL Press)

Leung HTL, Williams RJ and Griffiths H 1990 A wide-band current source for electrical impedance tomoography

Li J, Joppek C and Faust U 1994 An isolated wideband current source used in multifrequency electrical impedance tomography *Innov. Tech. Biol. Med.* **15** (Suppl. 1) 63-8

Lidgey FJ, Vere-Hunt MA and Toumazou C 1990 Developments in current driver circuitry *Proc. Copenhagen meeting on electrical impedance tomography (Copenhagen, 1990)* ed Hames TJ (Sheffield: Sheffield University Press)

Lidgey FJ, Zhu QS, McLeod CN and Breckon W 1992 Electrode current determination from programmable current sources *Clin. Phys. Physiol. Meas.* **13** (Suppl. a) 43-6

Loeb GE, Walker AE, Uematsu S and konigsmark BW 1977 Histological reaction to various conductive and dielectric films chronically implanted in the subdural space *J. Biomed. Mater. Res.* **11** 195-210

Lu L and Brown BH 1994 The electrode and electronic interface in an EIT spectroscopy system *Innov. Tech. Biol. Med.* **15** (Suppl. 1) 97-103

Mangnall YF, Baxter AJ, Avill R, Bird NC, Brown BH, Barber DC, Seagar AD, Johnson AG and Read NW 1987 Applied potential tomography: a new non-invasive technique for assessing gastric function *Clin. Phys. Physiol. Meas.* **8** (Suppl. A) 119-30

Mangnall YF, Baxter AJ, Avill R, Bird NC, Brown BH, Barber DC, Seagar AD, Johnsson AG and Read NW 1987 Applied potential tomography: a new technique for assessing gastric function *Clin. Phys. Physiol. Meas.* **8** (suppl A) 131-40

Marshall WH 1959 Spreading cortical depression of Leao *Physiol. Rev.* **39** 239-79

McAdams EA and Jossinet J 1990 Electrode-skin impedance in electrical impedance tomography *Proc. Copenhagen meeting on electrical impedance tomography* ed Hames TJ (Sheffield: Sheffield Unviersity Press)

McArdle FJ, Brown BH and Angel A 1989 Imaging of resistivity changes in the adult head during the cardiac cycle *Proc. 11th Ann. Conf. IEEE. EBMS.* **11** 480-1

Mcardle FJ, Brown BH and Angel A 1990 Imaging cardiosynchronous impedance changes in the adult head *Clincal and Physiological Applications of Electrical Impedance tomography* ed Holder DS (London: UCL Press)

McArdle FJ, Brown BH, Pearse RG and Barber DC 1988 The effect of the skull of low-birthweight neonates on applied potential tomography imaging of centralised resitivity changes *Clin. Phys. Physiol. Meas.* **9** (Suppl. A) 55-60

McArdle FJ, Turley A, Hussain A, Hawley K and Brown BH 1993 An in-vivo examination of cardiac impedance changes imaged by cardiosynchronous averaging *Clinical and physiological applications of electrical impedance tomography* ed Holder DS (London: UCL press)

McLeod CN, Breckon WR and Murphy D 1990 OXPACT: The development of an adaptive current tomograph *Proceedings of the Copenhagen Meeting on Electrical Impedance Tomography* ed Hames TJ (Sheffield: Sheffield University)

Meijs JW, Weier OW, Peters MJ and Van Oosterom A 1989 On the numerical accuracy of the boundary element method *IEEE. Trans. Biomed. Eng.* **36** 1038-49

Möller PH, Tranberg KG, Blad B, Henriksson PH, Lindberg L, Weber L and Persson BRR 1993 EIT for measurement of temperature distribution in laser thermotherapy *Clinical and physiological applications of electrical impedance tomography* ed Holder DS (London: UCL Press)

Monakhov KK, Fifková E and Burês J 1962 Vertical distribution of the slow potential change of spreading depression in the cerebral cortex of the rat *Physiol. Bohemosolv.* **11** 269-76

Morucci JP, Marsili PM, Granié M, Dai WW and Shi Y 1994 Direct sensitivity matrix approach for fast reconstruction in electrical impedance tomography *Physiol. Meas.* **15** (Suppl. 2A) 107-14

Morucci J-P, Marsili PM, Granié M, Shi Y, Lei M and Dai WW 1994 A direct sensitivity matrix approach for fast reconstruction in electrical impedance tomography *Physiol. Meas.* **15** (Suppl. 2A) 115-24

Murai T and Kagawa Y 1985 Elecical impedance computer tomography based on a finite-element model *IEEE. Trans. Biomed. Eng.* **BME-32** 177-84

Murphy D 1987 Impedance imaging in the newborn *Clin. Phys. Physiol. Meas.* **8** (Suppl. A) 131-40

Murphy D and Rolfe P 1988 Aspects of instrumentation design for impedance imaging *Clin. Phys. Physiol. Meas.* **9** (Suppl. A) 5-14

Nathan SS, Surabh RS, Gordon B, Lesser RP and Thakor NV 1993 Determination of current density distributions generated by electrical stimulation of the human cerebral cortex *Electroenc. Clin. Neurophysiol.* **86** 183-92

Newell JC, Gisser DG and Isaacson D 1988 An electric current tomograph *IEEE. Trans. Biomed. Eng.* **35** 828-33

Newell JC, Isaacson D, Cheney M, Salnier GJ, Gisser DG, Goble JC, Cook RD and Edic PM 1992 An electric current tomograph *Proc. 11th Ann. Conf. IEEE. EBMS.* **14** 1752-3

Newell JC, Isaacson D, Cheney M, Saulnier GJ, Gisser DG, Goble J, Cook RD, Edic PM and Newton AM 1993 In vivo impedance images using sinusoidal current patterns *Clinical and Physiological Applications of Electrical Impedance Tomography* ed Holder DS (London: UCL Press)

Newell JC, Isaacson D, Saulnier GJ, Cheney M and Gisser DG 1994 Qunatitative assessment of pulmonary edema by impedance imaging *Proceedings of the 3rd meeting of the European Concerted Action on Impedance Tomography, Anakra, Turkey, September 1994*

Nicholson PW 1965 Specific impedance of cerebral white matter *Exp. Neurol.* **13** 386-401

Nour S 1992 *Ph.D. Dissertation* Uinversity of Sheffield

Nowicki DJ 1990 Current generators *Electrical Impedance Tomography* ed Webster JG (Bristol: Adam Hilger)

Nowicki DJ and Webster JG 1989 A one op-amp current source for electrical impedance tomography *Proc. 11th Ann. Conf. IEEE. EBMS.* **11** 457-8 New York: IEEE

Ollmar S, Nyrén M, Nicander I and Emtestam L 1994 Electrical impedance compared with other non-invasive bioengineering techniques and visual scoring for detection of irritation in human skin *Br. J. Dermatol.* **130** 29-36

Osypka K and Gersing E 1994 Parallel signal processing and multi-electrode current feeding in a multi-frequency EIT system *Innov. Tech. Biol. Med.* **15** (Suppl. 1) 57-61

Pallas-Areny R and Casas O 1994 Modeling of systematic errors in dual-frequency EIT *Innov. Tech. Biol. Med.* **15** (Suppl. 1) 109-15

Paulson K, Breckon W and Pidcock MK 1990 The importance of electrode modelling in electrical impedance tomography *Proc. Copenhagen meeting on electrical impedance tomography (Copenhagen 1990)* ed Hames TJ (Sheffield: Sheffield University)

Paulson K, Lionheart W and Pidcock M 1993 Optimal experiments in eletrical impedance tomography *IEEE. Trans. Med. Imag.* **12** 681-6

Penning R, Müller C and Ciompi L 1969 Mortalité et cause de décès des épileptiques *Psych. Clin.* **2** 85-94

Persson BRR, Blad B and Weber L 1990 The use of electrical imedance tomography for non-invasive tempereature monitoring in hyperthermia treatment of cancer *Proc. Copenhagen meeting on electrical impedance tomography (Copenhagen, 1990)* ed Hames TJ (Sheffield: Sheffield University)

Peterson SB 1987 Flow, perfusion and diffusion: the potential role of NMR *The impact of functional imaging in neurology and psychiatry* ed Wade J (London: John Libbey)

Polkey CP 1988 Neurosurgery *A textbook of epilepsy* eds Laidlaw J, Richens AN and Oxley J (London: Churchill Livingstone)

Porter R, Adey WR and Kado RT 1964 Measurement of electrical impedance in the human brain *Neurol.* **14** 1002-12

Press WH, Teukolsky SA, Vettering WT and Flannery BP 1992 *Numerical recipes* (New York: Cambridge University Press)

Prudnikova IF 1959 The effects of eserine on the action potential and impedance spike in frog nerve *Biofizikia* **4** 666-76

Rabbani KS and Kabir AMBH 1991 Studies of the effect of the third dimension on a two-dimensional electrical impedance tomography system *Clin. Phys. Physiol. Meas.* **12** 393-402

Ranck JBJ 1963 Analysis of specific impedance of rabbit cerebral cortex *Exp. Neurol.* **7** 153-74

Ranck JBJ 1964 Specific impedance of cerebral cortex during spreading depression, and an analysis of neuronal, neuroglial and interstital contributions *Exp. Neurol.* **9** 1-16

Ranck JBJ 1975 Which elements are excited in electrical stimulation of the mamalian central nervous system: a review *Brain. Res.* **98** 417-40

Record PM 1994 Single-plane multifrequency electrical impedance instrumentation *Clin. Phys. Physiol. Meas.* **15** (Suppl. 2A) 29-36

Record PM, Gadd R and Rolfe P 1990 A signal-conditioning electrode for electrical impedance tomography *Proceedings of the Copenhagen Meeting on Electrical Impedance Tomography (Copenhagen 1990)* ed Hames TJ (Sheffield: Sheffield University)

Record PM and Hargreaves RW 1994 Frequency-independent common-mode voltage compensation for EIT applications *Innov. Tech. Biol. Med.* **15** (Suppl. 1) 9-15

Rigaud B, Anah J, Givelin P, Grazoitin P and Morucci JP 1990 A multi-function electrode module for electrical impedance tompgrahy *Proceedings of the Copenhagen Meeting on Electrical Impedance Tomogrpahy* ed Hames TJ (Sheffield: University of Sheffield)

Rigaud B, Shi Y, Anah J, Martinez E and Morucci JP 1990 Acquisition problems of the electrical bioimpedance signal *Proc. Copnhagen meeting on electrical impedance tomography (Copenhagen, 1990)* ed Hames TJ (Sheffield: Sheffield Unviersity Press)

Riu P, Lozano A and Rosell J 1990 Errors in tomography systems caused by reactive electrode impedance *Proceedings of the Copenhagen Meeting on Electrical Impedance Tompgraphy (Copenhagen, 1990)* ed Hames TJ (Sheffield: Sheffield University)

Riu P, Rosell J and Pallas-Areny R 1992 Multifrequency electrical impedance imaging as an alternative to absolute imaging *Proceedings of the 1st European concerted action on process tomography*

Riu P, Rossel J, Lozano A and Pallas-Arény R 1992 A broadband system for multifrequency static imaging in electrical impedance tompgraphy *Clin. Phys. Physiol. Meas.* **13** (Suppl. A) 61-6

Rosell J, Colominas J, Riu P, Pallas-Areny R and Webster JG 1988 Skin impedance from 1 Hz to 1 Mhz *IEEE. Trans. Biomed. Eng.* **35** 649-51

Rosell J, Murphy P, Pallas R and Rolfe P 1988 Analysis and assessment of errors in a parallel data acqusition system for electrical impedance tomography *Clin. Phys. Physiol. Meas.* **9** (Suppl. A) 93-9

Rosell J and Riu P 1992 Common-mode feedback in electrical impedance tomography *Clin. Phys. Physiol. Meas.* **13** (Suppl. A) 11-4

Rosell J, Riu P and Pallas-Areny R 1989 A parallel data acquisition system for electrical impedance tomography *Proc. IEEE. EBMS.* **11** 459-60

Roth BJ 1989 Interpretation of skeletal muscle four-electrode impedance measurements using spatial and temporal frequency-dependent conductivities *Med. Biol. Eng. Comp.* **27** 491-5

Ruch TC and Patton HD 1965 *Physiology and Biophysics* (Philadelphia: WB Saunders)

Rush S, Abildskov JA and McFee R 1963 Resitivities of body tissues at low frequency *Circ. Res.* **12** 40-9

Sahalos JN, Kyriacou GA and Vafiadis E 1994 An efficient finite-element algorithm for 3D layered complex structure modelling *Physiol. Meas.* **15** (Suppl. 2a) 65-8

Sakamoto K, Yorkey TJ and Webster JG 1987 Some physical results from an impedance camera *Clin. Phys. Physiol. Meas.* **8** (Suppl. A) 71-6

Sansen W, Geeraerts B, Van Petegem W and Stetaert M 1992 Eelctrical impedance tomography systems based on voltage drive *Clin. Phys. Physiol. Meas.* **13** (Suppl. A) 35-42

Schoonhoven R, Stegman DF and De Weerd JPC 1986 The forward problem in electroneurography I: a generalized volume conductor method *IEEE. Trans. Biomed. Eng.* **33** 327-33

Schoonhoven R, Stegman DF and Van Oosterom A 1986 The forward problem in electroneurography II: comparison of models *IEEE. Trans. Biomed. Eng.* **33** 335-41

Schwan HP 1959 Alternating current spectrosopy of biological substances *Proc. IRE.* **11** 1841-55

Schwan HP, Schwan J, Maczuk J and Pauly H 1962 On the low-frequency dispersion of colloidal particles in electrolyte solution *J. Phys. Chem.* **66** 2626-35

Seagar AD, Barber DC and Brown BH 1987 Theoretical limits to sensitivity and resolution in impedance imaging *Clin. Phys. Physiol. Meas.* **8** (Suppl. A) 13-31

Selvín-Testa A and Urbina-Vidal C 1975 Axon-glia relationships in crab nerves *J. Neurocytol.* **4** 23-31

Shevelov IA, Kuznetsova GD, Gulyacov YY, Godik ÉÉ, Petrov AV and Taratorin AM 1986 Dynamic mapping of rat brain during sensory stimulation and spreading depression *Neurofiziologiya* **18** 26-35

Shi Y, Rigaud B, Marsili PM and Morucci JP 1990 An electrical impedance tomograph: hardware, software and static images *Proc. Copenhagen meeting on electrical impedance tomography (Copenhagen, 1990)* ed Hames TJ (Sheffield: Sheffield University Press)

Sinton AM, Brown BH, Barber DC, McArdle FJ and Leathad AD 1992 Noise and spatial resolution of a real-time EIT *Clin. Phys. Physiol. Meas.* **13** (Suppl. A) 125-30

Smith RWM, Brown BH, Freeston IL and McArdle FJ 1990 Real-time electrical impedance tomography *Proc. Copenhagen meeting on electrical impedance tomography* ed Hames TJ (Sheffield: Sheffield University Press)

Spencer SS, Williamson PD and Bridgers SL 1982 The localising value of depth EEG in 32 patients with refractory epilepsy *Ann. Neurol.* **12** 248-53

Taheri BA, Knight RT and Smith RL 1994 A dry electrode of EEG recording *Electroenc. Clin. Neurophysiol.* **90** 376-83

Ter-Pogossian MM 1977 Basic principles of computed axial tomography *Sem. Nucl. Med.* **7** 109-27

Thomas DC, McArdle FJ, Rogers VE, Beard RW and Brown BH 1991 Local blood volume changes in women with pelvic congestion measured by applied potential tomography *Clin. Sci.* **81** 401-4

Tobias JM and Bryant SH 1955 An isolated giant axon preparation from the lobster nerve cord *J. Comp. Physiol.* **46** 163-83

Toumazou C and Lidgey FJ 1989 Novel current-mode instrumentation amplifier *Electron. Lett.* **25** 228-30

Trillaud C and Jossinet J 1992 An improved design of voltmeter for semi-parallel data acquisition *Clin. Phys. Physiol. Meas.* **13** (Suppl. A) 5-10

Van Buren JM 1987 Complications of surgical procedures in the diagnosis and treatment of epilepsy *Surgical Treatment of the Epilepsies* ed Engel J (New York: Raven Press)

Van Harreveld A, Hooper NK and Cuisick JT 1961 Brain electrolytes and cortical impedance *Am. J. Physiol.* **201** 139-43

Van Harreveld A and Schadé JP 1962 Changes in the electrical conductivity of cerebral cortex during seizure activity *Exp. Neurol.* **5** 383-400

Van Osterom A 1991 History and evolution of methods for solving the inverse problem *J. Clin. Neurophysiol.* **8** 371-80

Wang M, Dicken FJ and Beck MS 1992 Improved electrical impedance tomography system and data collection protocols *Proceedings of the first european concerted action on process tomography* 40-53

Wilson B 1981 A low-distortion bipolar feedback current amplifier technique *IEEE Proc.* **69** 1514-5

Wilson B 1991 Current mirrors, amplifiers and dumpers *Elect. Wire. World* **87** 47-50

Winkler S, Sackett J and Holden J 1977 Xenon inhalation as an adjunct to computerised tomography of the brain, preliminary study *Invest. Radiol.* **12** 15

Woo EJ 1990 *Ph.D. Thesis* University of Wisconsin-Madison

Woo EJ, Hua P, Webster JG and Tomkins WJ 1993 A robust image reconstruction algorithm and ites parallel implementation in electrical impedance tomography *IEEE. Trans. Med. Imag.* **12** 137-46

Yorkey TJ, Webster JG and Tomkins WJ 1986 An optimal impedance tomographic reconstruction algorithm *Proc. 8th Ann. Conf. IEEE. EBMS.* **8** 339-42

Zadehkoochak M, Blott BH, Hames TK and George RF 1991 Spectral expansion in electrical impedance tomography *J. Phys. D: Appl. Phys.* **24** 1911-6

Zadehkoochak M, Blott BH, Hames TK and George RF 1992 Pulmonary perfusion and ventricular ejection imaging by frequency domain filtering of EIT images *Clin. Phys. Physiol. Meas.* **13** (Suppl. A) 191-6

Zhu QS, Lidgey FJ and Vere-Hunt MA 1992 Improved wideband instrumentation amplifier *Clin. Phys. Physiol. Meas.* **13** (Suppl. A) 51-5

Appendices

Appendix A: mathematical details

This appendix provides derivations of the equations used in §5.2.1-§5.2.3.

A1. Impedance of a uniform nerve in the steady state

We represent the nerve axon as a uniform cylinder which consists of axoplasm (resistivity ρ_i Ω.cm) surrounded by a membrane of specific resistance ρ_m Ω.cm^2 and capacitance C_m μF/cm^2 (figure A1). The membrane passes a current i_m and developes voltage V_m. The axon is 'closed-ended' since in practice no current can enter the axon except through the membrane. The axons are surrounded by interstitial fluid of resistivity ρ_e Ω.cm which occupies a fraction α of the overall tissue volume. Measuring electrodes are placed some distance 2L apart along the length of the nerve, so that the electric field in the interstitial space is parallel to the fibre. The extracellular and intracellular current densities and voltages are represented by i_e, V_e, i_i and V_i respectively. The origin of the x-axis is half-way along the fibre, at which point V_e, V_i and V_m are zero.

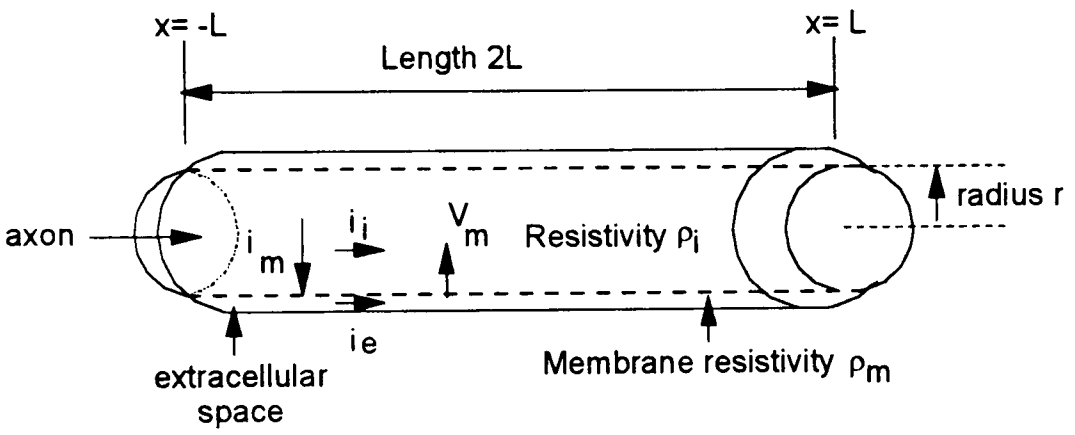

Figure A1: the geometry of the nerve fibre model. See text for explanation of symbols

The steps in the derivation of the effective impedance of the nerve are as follows:

Step1. Derive relationships between membrane current i_m, axoplasm current i_a, *etc.*

Step2. Write down a differential equation in V_m which combines these relationships.

Step3. Solve for the membrane voltage V_m.

Step4. Calculate the axoplasm current density as a function of V_m, and integrate it over the range x = -L to L to determine the mean current carried by the fibre.

Step5. Divide the mean current by the applied voltage to obtain the effective admittance of this length of fibre; from this derive the effective admittivity of a sample of tissue containing only nerve fibres

Step6. Calculate the overall admittivity of the tissue, allowing for the extracellular component.

Step7. Evaluate the tissue impedance with the neurons polarised and depolarised; derive the proportional impedance decrease from these figures.

Step 1: Relationships between membrane current, *etc.*

Standard cable theory assumes that the current (I_m) crossing a small region of membrane is equal to the difference between axoplasm currents (I_i) at the ends of the region. When this region is small, the current difference reduces to a differential:

$$i_m = -\frac{r}{2}\frac{\partial i_i}{\partial x} \qquad \text{[A1a]}$$

where i_m is the membrane current density (amps.cm^{-2}), r is the fibres radius (cm) and i_i is the axoplasm current *density* (amps.cm^{-2}). All currents and voltages are functions of time *t* and length *x*. Cable models often assume that the axon is suspended in a large volume of conductive fluid, so the extracellular current density is uniform. This will not be the case when the extracellular space is small. In this case, we must take account of the current density in the extracellular compartment i_e. The current entering the extracellular compartment in a given region is equal to the current leaving the intracellular compartment, and therefore to the membrane current (with an appropriate sign reversal):

$$i_m = \frac{r\alpha}{2(1-\alpha)}\frac{\partial i_e}{\partial x} \qquad \text{[A1b]}$$

where α is the fraction of the tissue that is regarded as extracellular. The term $\alpha/(1-\alpha)$ derives from consideration of the geometry of the nerve; it relates the extracellular area to the intracellular. The membrane current consists of two components: an 'in phase' component due to the cell membrane resistance, and a 'quadrature' component due to membrane capacitance:

$$i_m = \frac{V_m}{\rho_m} + C_m\frac{\partial V_m}{\partial t} \qquad \text{[A2]}$$

The currents along the axoplasm and extracellular compartments develop voltages V_i and V_e given by

$$i_i = -\frac{1}{\rho_i}\frac{dV_i}{dx} \qquad \text{[A3a]}$$

$$i_e = -\frac{1}{\rho_e}\frac{dV_e}{dx} \qquad \text{[A3b]}$$

where ρ_i and ρ_e are the resistivities of the axoplasm and extracellular fluid (in ohm.cm).

Step 2: The differential equation

From [A1b] and [A2],

$$\frac{\alpha r}{2(1-\alpha)}\frac{\partial \mathbf{i_e}}{\partial \mathbf{x}} = \frac{\mathbf{V_m}}{\rho_m} + \mathbf{C_m}\frac{\partial \mathbf{Vm}}{\partial t} \qquad [A4]$$

Substituting [A3a] and [A3b], and noting that the membrane voltage is the difference of the intracellular and extracellular voltages gives (after straightforward but lengthy algebraic manipulation):

$$V_m + C_m\rho_m\frac{\partial V_m}{\partial t} = \frac{r\rho_m}{2(\rho_i + \rho_e(1-\alpha)/\alpha)}\frac{\partial^2 V_m}{\partial x^2}$$

This can be expressed more concisely:

$$\lambda^2\frac{\partial^2 V_m}{\partial x^2} = V_m + \tau\frac{\partial V_m}{\partial t} \qquad [A5]$$

where

$$\tau = \rho_m C_m$$

and

$$\lambda^2 = \frac{r\rho_m}{2(\rho_i + \rho_e(1-\alpha)/\alpha)} \qquad [A6]$$

Since λ has dimensions of length, and will be seen to dictate the variation of voltage and current with length, it is normally referred to as the *length constant*. The predicted value of λ for crab nerve in the resting state, based on the values in table 5.1, is 0.6 mm. The term 'space constant' is also used. τ has dimensions of time, and is referred to as the *time constant*. Note that if the extracellular space is large ($\alpha \rightarrow 1$), or the extracellular resistivity is low, the effect of extracellular resistivity on λ disappears. If the resistivities ρ_m and ρ_i are expressed as resistances per unit length of fibre R_m and R_i, the length constant reduces to the more familiar form

$$\lambda^2 = R_m / R_i$$

Step 3: Solution

To determine the membrane voltage we need a solution of [A5] which also satisfies the boundary conditions

i. $V_m = 0$ at $x = 0$ (from symmetry), and

ii. $i_i = 0$ at $x = \pm L$ (because the ends of the fibre are 'closed', current has to cross the membrane to reach the axoplasm)

iii. $V_e = V$, the applied voltage, at $x \pm L$.

The analysis is restricted to a steady-state condition with sinusoidal excitation. The solution will be derived in terms of the (time-domain) Fourier transform of V_m, represented by V_m'. Taking the Fourier transform of [A5] gives:

$$\lambda^2 \frac{\partial^2 V_m'}{\partial x^2} = V_m' + j\tau\omega\, V_m \qquad [A7]$$

Where ω is the angular frequency of the membrane voltage (which is, of course, the same as that of the excitation current). j is the $\sqrt{-1}$ operator. Inspection suggests a general solution:

$$V_m' = E\sinh(Fx) \qquad [A8]$$

where E and F are constants to be determined. Differentiation of V_m twice with respect to x gives:

$$EF^2 \sinh(Fx) = E\sinh(Fx) + j\omega\,\tau\, E\sinh(Fx)$$

and therefore $F = \sqrt{(1+j\omega\tau/\lambda^2)} = \sqrt{(1+j\omega\tau)}/\lambda$. To determine E we apply the boundary condition $I_a(L) = 0$, and given that

$$V_i = V_e + V_m \qquad [A9]$$

we obtain

$$\left.\frac{\partial V_m'}{\partial x}\right|_{x=L} = \left.\frac{\partial V_e'}{\partial x}\right|_{x=L} \qquad [A10]$$

where V_e' is the Fourier transform of the extracellular voltage. It is common at this point to make the approximation that the external electric field dV_e'/dx is a constant equal to V'/L, where V' is the Fourier transform of the applied voltage. Differentiating [A7] would allow us to determine E, and therefore derive a simple and concise particular solution:

$$V_m' = -\frac{V'\sinh(Fx)}{LF\cosh(FL)} \qquad [A11]$$

This equation is essentially the same as that derived by Ranck (1963). Since we expect the extracellular space to be small, and to have a resistivity not very different from the axoplasm, this approximation may produce a substantial error. We therefore proceed without making any assumptions about the distribution of field in the extracellular space. From [A8] and [A9]:

$$E\sinh(FL) = V_i'(L) + V \qquad [A12]$$

The arguments in brackets, '(L)', signify evaluation at the end of the fibre. Since $V_i(0) = 0$,

$$V_i'(L) = \int_0^L \frac{\partial V_i'}{\partial x} dx = -\rho_i \int_0^L i_i'\, ds \qquad [A13]$$

We now express i_i in terms of i_m:

$$i_i = -\int_0^x \frac{2}{r} i'_m \, dx - -\int_0^L \frac{2}{r} i'_m \, dx$$

By substituting the Fourier transform of [A2] and [A8] we obtain, after further lengthy manipulation:

$$i'_i = \frac{2E(1 + j\omega\tau)(\cosh(Fx) - \cosh(FL))}{Fr\rho_m} \qquad [A14]$$

Substituting [A14] in [A13] and evaluating the integral eventually yields an expression for E in terms of known parameters. Substituting this in [A8] gives the particular solution

$$Vm' = \frac{V' \sinh(Fx)}{(1 - K_s)\sinh(FL) + K_s FL \cosh FL} \qquad [A15]$$

where the constant K_s is given by:

$$K_s = \frac{1}{1 + \frac{\rho_e \alpha}{\rho_i (1 - \alpha)}}$$

K_s is a dimensionless constant that describes the effect of the extracellular space on the membrane potential. When the extracellular space becomes large, or its resistivity small, K_s tends to unity. In these cases, equation [A15] reduces to the simpler form [A11]. For brevity, the whole of the denominator of equation [A15] will be represented below by the symbol 'D'.

Step 4: Calculate the mean current carried by the fibre

The Fourier transform of the mean membrane current density is calculated by integrating i'_i between x = 0 and L, and dividing by L. From [A3]:

$$i_i' = -\frac{1}{\rho_i}\frac{\partial V_m'}{\partial x} - \frac{1}{\rho_i}\frac{\partial V_e'}{\partial x} \qquad [A16]$$

Substituting [A15]:

$$i_i' = -\frac{1}{\rho_i}\frac{\partial}{\partial x}\left(\frac{V' \sinh(Fx)}{D}\right) - \frac{1}{\rho_i}\frac{\partial V_e}{\partial x} \qquad [A17]$$

The mean current density is therefore:

$$\overline{i_i'} = \frac{V'}{L\rho_i}\left(1 - \frac{1}{D}\sinh(FL)\right) \qquad [A18]$$

Step 5: Effective admittance of the fibre

The effective admittance of the single fibre is obtained by dividing [A18] by V', and the admittance for unit volume (y_n) by further dividing by half the length of the sample, L. Thus:

$$y_n = \frac{1}{\rho_i}\left(1 - \frac{1}{D}\sinh(FL)\right) \qquad [A19]$$

Step 6: Overall conductance of the nerve bundle

The total admittivity of the longitudinal nerve tissue, y_{total}, is the weighted sum of the admittivities of the neuronal and interstitial components:

$$y_{total} = p_n y_n + p_e y_e + p_g y_g \qquad [A20]$$

where p_n, p_g and p_e are the proportions of neurons, glia and interstitium, and y_n, y_g and y_e are their admittivities.

A2. Expression of the neuronal impedance in terms of membrane voltage

Equation [A20] allows us to estimate the steady-state impedance of uniform nerve tissue. Of greater interest, however, is the change in resistivity during depolarisation. The neuronal membrane is capacitive, so it will tend to maintain the membrane voltage in the presence of a rapidly changing membrane conductance. At low measuring frequencies, the tissue may depolarise at faster rate than that at which the membrane voltage approaches a steady state. The measured impedance change, if determined from a change in voltage at the measuring electrodes, will underestimate the true change. This effect will be analysed for the worst case, that of direct current excitation.

As described above, the neuronal resistivity is determined from the mean axoplasm current. From equation [A16] we express the mean axoplasm current i'_i in terms of the membrane voltage by integrating between 0 and L but without substituting [A15]:

$$i'_i = \frac{V' - V'_m(L)}{\rho_i}$$

where '(L)' refers to evaluation at the end of the fibre. At constant frequency, the division of two Fourier transforms is equivalent to division of the time-domain values, so the proportional change in DC conductivity is then

$$\frac{\delta Y_n}{Y_n} = \frac{\delta i_i}{i_i} = \frac{i'_{i,depol} - i'_{i,rest}}{i'_{i,rest}} = \frac{V_{m,rest}(L) - V_{m,depol}}{V - V_{m,rest}(L)} \qquad [A21]$$

where the subscripts 'rest' and 'depol' represent evaluations in the resting and depolarised states. Since the denominator of the right-hand-side of [A21] is constant during depolarisation, we obtain the surprisingly satisfying relationship

$$\frac{\delta\rho_n}{\rho_n} = -\frac{\delta Y_n}{Y_n} \propto \delta V_m(L)$$

i.e., the fractional change in neuronal resistivity is proportional to the change in the membrane voltage measured at the end of the fibre.

The membrane voltage $V_m(L)$ will depend in some complicated way on the distribution of current along the axon and on the membrane resistance. However, we already have an expression [A19] by which to evaluate the resistance change if a steady state were reached. We therefore need only to evaluate the ratio k_τ of the resistance change with, and without, an appreciable membrane time constant:

$$k_\tau = \frac{\delta V_m(L)_\tau}{\delta V_m(L)_0}$$

where $\delta V_m(L)_\tau$ is the change in membrane voltage during depolarisation with the non-zero time constant and $\delta V_m(L)_\tau$ is the corresponding value with the time constant set to zero, *i.e.*, with no membrane capacitance.

Appendix B: design and evaluation of a system for measuring small evoked changes in the DC resistance of nerve

1 Introduction

The model of neuronal resistivity described in chapter 4 predicted that resistivity changes during depolarisation will be much greater at DC than at higher frequencies, although still small (~3%). Despite the theoretical advantage of DC excitation, its use leads to significant technical difficulties. This chapter describes the development and evaluation of an instrument for measuring small transient changes in the DC resistance of biological tissue. It was subsequently used (chapters 7 and 8) to investigate the DC resistance changes in unmyelinated nerve and in the cortex. The specific problems which the design had to address were as follows.

i. *High electrode impedance.* The contact impedance of bare-metal electrodes can be Megohms at DC. To avoid electrode polarisation and possible damage to the tissue under study, the measuring system reversed the excitation polarity between each measurement cycle. Since the biological response from peripheral nerve (2 msec - 10 msec) is very much shorter than the measurement cycle (about 100 msec), this can be considered equivalent to DC. This 'polarity reversal' technique also allowed the system to 'subtract out' intrinsic action potential voltages (see section 2.5), which inevitably added to the resistance signal. Even with this 'square-wave' excitation, measured electrode impedances were 2 kΩ-10 kΩ. To avoid the generation of common-mode voltages by the flow of the excitation current through these electrode impedances, (see chapter 2), the current excitation circuit was fully isolated from the recording system.

ii. *Electrode 'polarisation'.* The electrodes used in the experiments of chapter 7 developed an unpredictable half-cell potential between 10 mV and 100 mV. Since the gain of the recording amplifier was normally 100, the system could not amplify these DC offsets along with the true signal. I experimented with correction of DC offsets between measurements, but the half-cell potentials were too irregular over time. It was decided to limit the low-frequency bandwidth, but to the smallest extent compatible with stable recording. A 1 Hz high-pass filter was used; this should not have removed any significant biological information from the recording.

iii. *Low allowable current.* It is undesirable that the current excitation itself cause stimulation of the nervous tissue under study; furthermore, excitation current for measurement in the human brain will limited by safety considerations. The allowable excitation current will therefore be much lower than the current normally used for APT, which is typically 1-5 mA. In the experiments of chapter 7, the threshold for nerve stimulation was typically 24 μA - 40 μA, so an excitation of 6 μA - 10 μA was employed. This low current produces a small voltage response, necessitating a low-noise design.

iv. *Noise.* The voltage amplifiers will detect a higher level of extraneous noise than is the case at higher frequencies. 50 Hz mains interference will lie within the recording bandwidth, as will intrinsic EEG activity in the brain (up to about 100 μV with scalp electrodes). We can largely eliminate both of

these effects by cancellation, if an appropriate recording strategy is used (see §B2.5). A bigger problem is electrode noise. The intrinsic noise generated by electrodes is greatest at low frequencies. For stainless steel skin electrodes, Godin *et al* (1991) found that the power spectral density of noise approximated a '1/f' distribution. The noise generated by a 1 cm diameter stainless steel electrode on clean skin was 1.7 μV to 4.4 μV (n = 8 subjects) over a measuring bandwidth 8 Hz to 10 kHz. Recording with a bandwidth of 0.15 Hz to 10 kHz, Flasterstein (1966a,b) found noise levels of tens of microvolts to millivolts with plain silver and stainless steel disks (8 mm diameter) in saline. Superimposed on the electrode noise will be a DC potential varying from a few tens of microvolts to hundreds of millivolts.

Although the system to be described was specifically designed for use on nerve tissue, some of the principles discussed are relevant to DC resistance measurement in any biological material.

2 Design overview

The DC resistance measurement system (figure B1) consisted of a personal computer with a digital interface board (PDMA-16, ComputerBoards Inc.), an isolated current generator, a differential amplifier with gains 10, 100 or 1000, a commercial 16-bit analogue-to-digital converter module (CS5501, Crystal Semiconductors Inc.) and an isolated nerve stimulator ('Mark IV', Devices Ltd.). Resistivity measurements were made in the usual way, by applying a known constant current and measuring the resulting voltage.

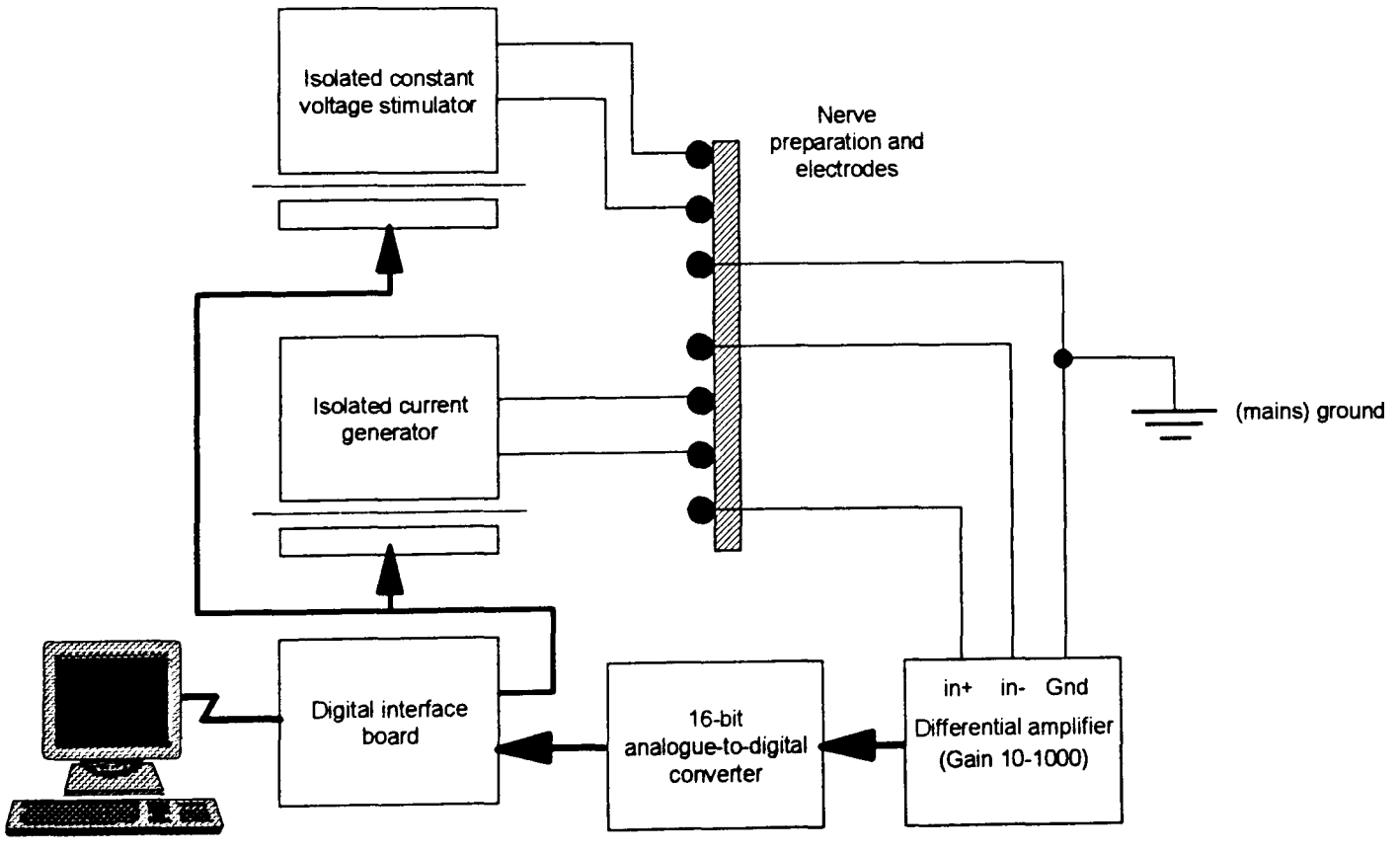

Figure B1: Diagram of the resistance measuring system. See text for details

2.3 Current generator

The isolated current generator (figure B2) provided a current whose polarity was selected by the computer (via the digital interface board) by signaling on 'current strobe A' or 'current strobe B'. The current generator was required to have an output impedance at least ten times as high as the expected

load (2 kΩ - 10 kΩ), and have a high (> 1 MΩ) isolation resistance between the control (current strobe) inputs and the current outputs. This isolation was necessary for two reasons:

i. A generator which is 'floating' with respect the amplifier 'ground' prevents common-mode voltages being developed across the electrode impedances.

ii. To prevent the excitation current affecting the measurement of the compound action potential (see section 6.4.3) it was important that current was confined to the region between the two excitation electrodes. If the generator and the amplifier shared a ground, there might be a tendency for common-mode currents to flow between the generator electrodes and the ground. This would cause an unpredictable effect on the compound action potential.

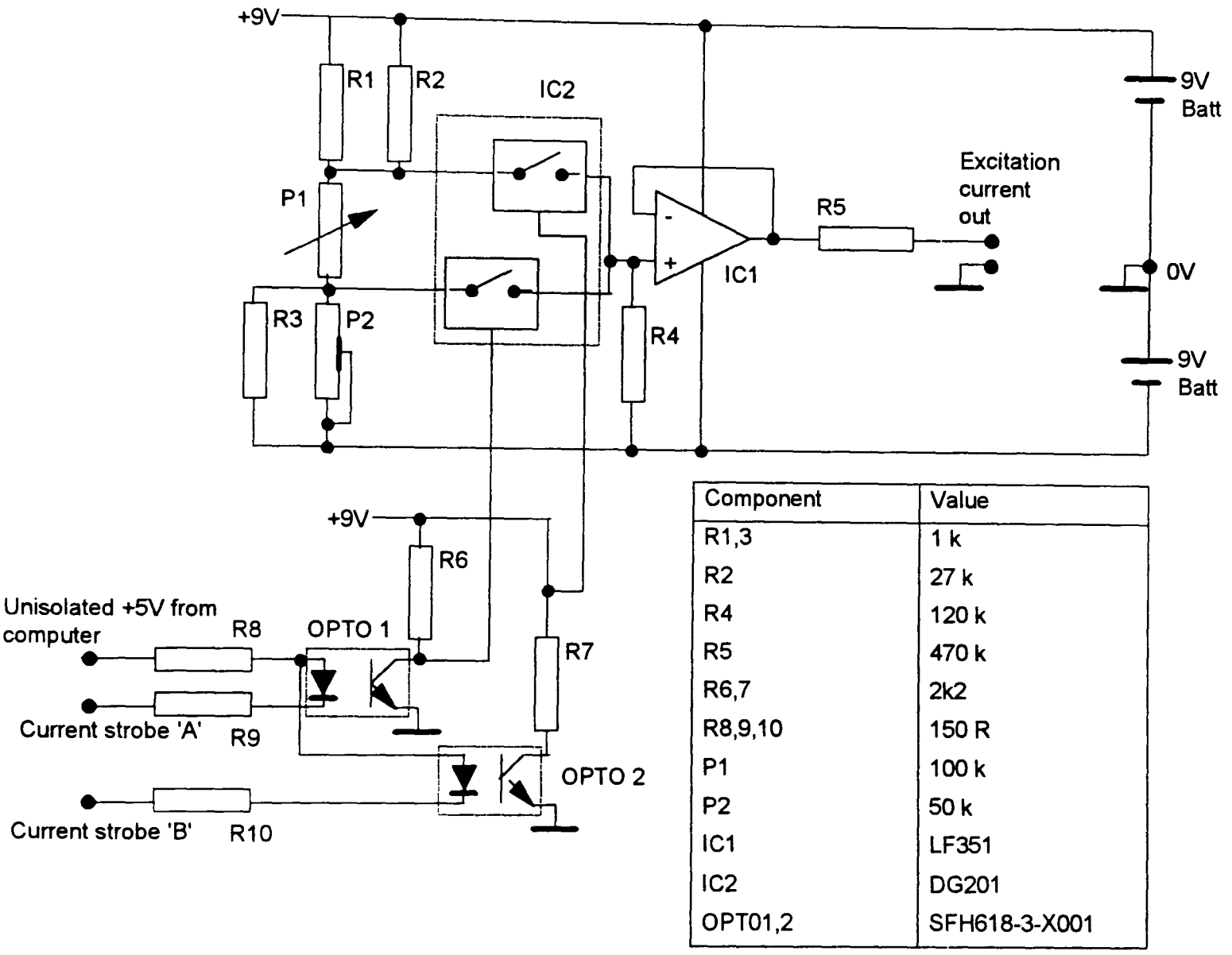

Component	Value
R1,3	1 k
R2	27 k
R4	120 k
R5	470 k
R6,7	2k2
R8,9,10	150 R
P1	100 k
P2	50 k
IC1	LF351
IC2	DG201
OPT01,2	SFH618-3-X001

Figure B2: circuit diagram of the isolated current generator

A constant current was provided by applying a constant voltage (from IC1 output) to the nerve sample via a large (470 kΩ) resistor. This output resistance was large compared to the resistance between the current terminals on nerve samples (2 kΩ - 10 kΩ). The voltage output from IC1 was determined by switching equal and opposite control voltages onto the non-inverting terminal of IC1 using the analogue switches in IC2. The control voltages were derived from the resistor network consisting of R1-3 and P1,2. P1 set the magnitude of the output current from 0 μA to 12 μA as follows. With P1 at its maximum value, the control voltage at IC1 input approached the positive or negative supply voltage,

depending on the settings of the current strobes. With P1 at its minimum (~ 50 Ω) value, the control voltage was close to zero.

For the control voltages to be equal and opposite, the resistances of parallel combinations[1] R1|R2 and R3|P2 must be equal, as must the two battery voltages. In practice the batteries did not generate exactly equal voltages, and P2 was adjusted to 'balance' the positive and negative output currents with reference to a Hewlett-Packard 34401A 6-digit digital multimeter. Because the resistance of P2 (1 kΩ) was much higher than that of R3 (1 kΩ), P2 provided a very fine adjustment of the parallel resistance R3|P2. Current 'balancing' was carried out with the output current magnitude set to about 5 μA; the magnitudes of the positive and negative currents then remained within 5% of each other over an output current range 0 μA - 10 μA. Re-balancing was necessary whenever the batteries were replaced.

OPT1 and OPT2 provided optical isolation (5 kV) between the computer, whose control outputs are referenced to (mains) ground and to the measurement circuit. The minimum impedance between the current output terminals and the current strobe inputs was found to be 8.6 pF in parallel with 4.5 MΩ (measured at 10 kHz with Hewlett-Packard 4284A, 2V excitation).

2.4 Differential amplifier

This was based on a 'current sensing' design reported by Zhu *et al.*, (1992). This circuit requires two different split supply rails; the best common-mode rejection was achieved when these were ±14 and ±6 Volts. The 3 dB bandwidth of 1 Hz - 3 kHz was set by passive first-order circuits[2] to prevent any possible time-domain ripple that might manifest itself as a biological signal. To prevent saturation of the amplifier by the large electrode potentials, the high-pass filter was positioned between two gain stages, the first of which had unity gain. Common-mode rejection was assessed as follows. The inputs were connected to electrodes (surface area 1 mm^2) in a saline bath of diameter 2 cm. The common-mode voltage was applied to a third electrode. This electrode was driven by a signal generator ('LFM2', Farnell Instruments Ltd) with respect to amplifier ground. The input voltage was 1.0 V p-p; this was the largest common-mode signal that the amplifier could tolerate. Common-mode voltages greater than this were not rejected, since they saturated one of the current mirrors. The common-mode output voltage was measured at frequencies between 10 Hz and 100 kHz using a Hewlett-Packard 34401A integrating meter.

---

[1] The symbol '|' denotes two components connected in parallel

[2] For measurements on the cortex, the passive low-pass filter did not give adequate noise rejection. It was therefore replaced by a 6^{th}-order Butterworth design that was designed and constructed by Mr Y Hanquan. The time taken for the output of the filter to settle to 0.1% was about 10 msec.

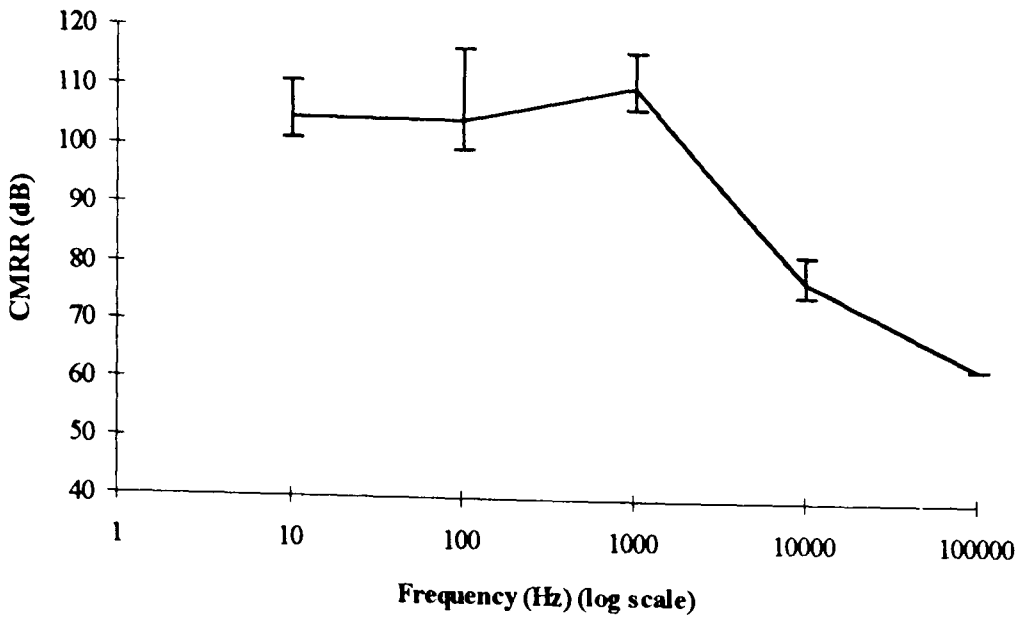

Figure B3: the common-mode rejection ratio (CMRR) of the differential amplifier. The error bars indicate maximum and minimum values, based on the range of the voltmeter reading; the line is the mean of the maximum and minimum values. The normal-mode gain was set at 100

Common-mode rejection was optimised by adjustment of the transconductance of one of the current mirrors in the differential amplifier circuit. Normally the common-mode rejection was optimum for only one frequency. However, after optimisation at 1 kHz, the common-mode rejection was always greater than 100 dB at frequencies of interest (figure B3).

2.5 Data acquisition cycle

Although normal neuronal resistivity changes are expected to be much smaller than those associated with pathology, they have the advantage that they can be evoked with a stimulus and averaged. It is normal practice in EEG studies to average several hundred responses to a visual, auditory or sensory stimulus; a complete response may last 100 msec. In principle, therefore, we can obtain 10 measurements per second, or 36000 per hour. The data acquisition cycle was controlled by a program written in C++ for the Microsoft Windows environment on a Pentium™-based PC. Overheads of the Windows operating system effectively limited the maximum sampling rate to 6000 samples per second. This rate was used for all the measurements described in this thesis. The data acquisition process produced two sets of data. First, a record of resistance was obtained by subtracting alternate measurement cycles. This would be expected to cancel the action-potential recording and reveal the voltage change due to resistivity change. This record will be referred to below as the 'resistance' record. Second, to reveal the action potential, the software also added the alternate cycles. This should cancel any effect due to impedance change. This record will be referred to as the 'action potential' record. The operation of the system is as follows (the bracketed number refer to the numbered points in figure B4).

1. Switch the current generator on; polarity set to positive by setting 'current strobe A' high (1).
2. Wait 20 msec for any transient effects to settle.
3. Begin acquiring data (2) at 6000 samples per second.
4. Trigger the nerve stimulator one or more times during the data acquisition period (3).

5. Switch off current by setting both current strobes low (4).
6. Add data to both 'action potential' and 'resistance' records.
7. Switch the current generator on; polarity set to negative by setting 'current strobe B' high (5).
8. - 1 As 2-5 above

16. Add data to the 'action potential' record, *subtract* from the 'resistance' record.

Subsequent pairs of cycles were identical. The first of each pair of cycles will be referred to below as the 'odd' cycle, and the second as the 'even'.

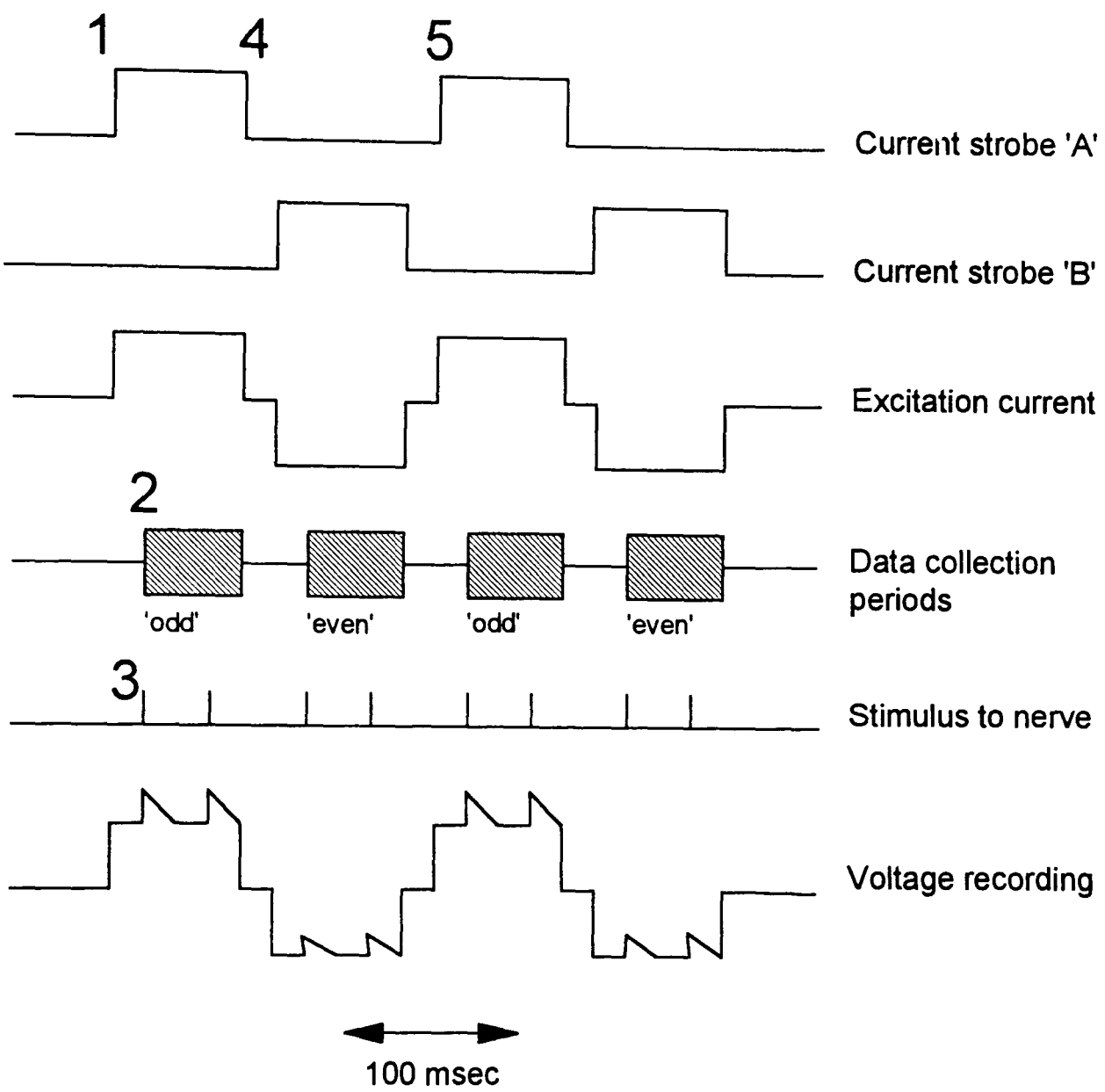

Figure B4: overview of the data acquisition process; see text for details.

2.6 Correction for the effect of the high-pass filter

The low frequency limit of the measuring amplifier was set to 1 Hz. A side-effect of this filter was that a square-wave input signal produced an output whose amplitude was subject to an exponential decline during the measurement period. Since the voltage change due to resistance variation was normally less than about 1%, it was somewhat difficult to see. I therefore adopted a procedure of correction for the exponential decay. A first-order high pass filter with time constant τ_f subject to a DC input of V_i has an output voltage V_o given by

$$V_o = V_i e^{-t/\tau_f}$$

where t is the time from the start of measurement. Taking logarithms:

$$\ln(V_o) = \ln(V_i) - t / \tau_f$$

Rearrangement of this expression reveals that the input voltage can be recovered from the output if the time constant τ_f is known:

$$V_i = V_o - e^{t/\tau_f}$$

τ_f was determined by performing a linear regression with '$\ln(V_i)$' and '$\ln(V_o)$' as the abscissa and ordinate respectively. This yields $1/\tau_f$ as the gradient.

3 Test for artefact due to acquisition timing errors

The resistance measuring system attempts to remove the intrinsic action potential signal from the resistance signal by subtraction. It is therefore vital that the action potentials were recorded identically on every measurement cycle. If this were not the case, the differences would appear as an artefactual resistance change. Although the PC sampled the output of the ADC at a constant rate, and was synchronised to the nerve stimulator, the ADC itself took a variable time (0 μsec - 12 μsec) to update its output. This variability could potentially produce a difference between the action potentials recorded on subsequent cycles. This effect was tested in the worst possible condition: the input signal was a rectangular pulse. Since a real action potential will not have rise or fall times as sharp as this pulse, the difference between time-shifted recordings will not be as great.

3.1 Method

A 1 mV, 2 msec pulse was supplied to the input of the differential amplifier 40 msec after the start of each data acquisition cycle. Since this pulse would be the same in both the 'odd' and 'even' cycles, it should be subtracted out, leaving only noise. Acquisition was repeated over 200 cycles and the subtracted records examined. This process was repeated to give a total of 10 recordings.

3.2 Results.

After subtracting alternate measurement cycles, artefacts were between 1 μV and 8 μV, with mean 3 μV.

3.3 Discussion

The smallest voltage encountered in the biological measurements was about 5 mV. In this case the worst error due to ADC timing (8 μV) could imitate a resistance change of 0.2%. In practice the action potential will not have rising or falling edges as sharp as a square pulse. It seemed unlikely that this source of error would be significant in practice.

4 Measurement of sensitivity and accuracy

4.1 Method

To assess the accuracy and sensitivity of the measurement system, I made measurements of small changes in resistivity in a resistance network (figure B5). The 4.7 kΩ resistances represented electrode contact resistance, while the 1.5 kΩ resistance approximated to the resistance of a nerve sample. To generate a small resistance decrease, a reed relay momentarily switched a large resistance 'R_{cal}' (10 kΩ to 390 kΩ) in parallel with the 1.5 kΩ load. The relay contacts were closed for 1.5 msec, approximating to the expected duration of resistivity decrease in nerve.

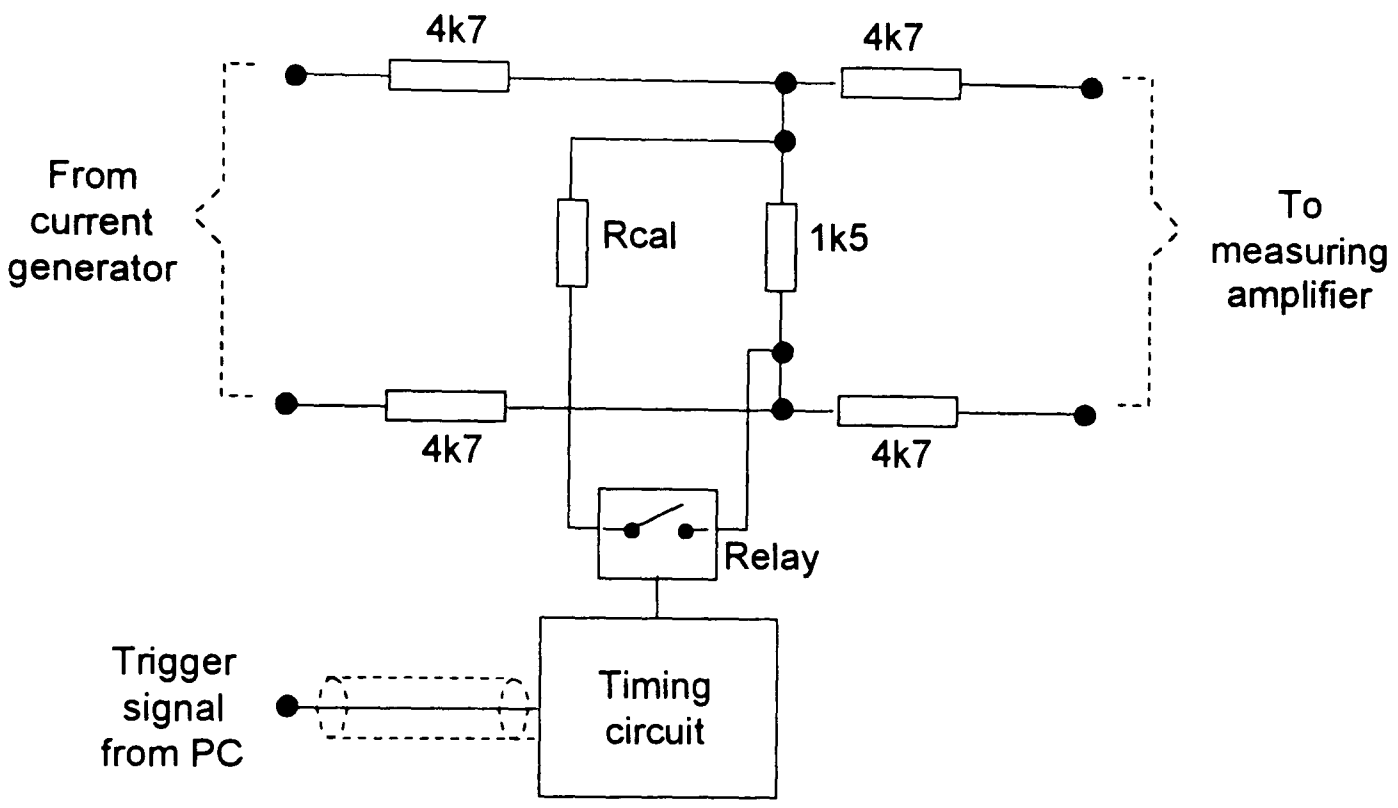

Figure B5: the calibration circuit. The relay, whose contacts were closed for about 1.5 msec per measurement cycle, connected a large resistor in series with 1.5kΩ. This had the effect of producing a small (< 2%) resistivity decrease.

The use of the relay, as opposed, for example, to an analogue switch circuit, effectively isolated the timing circuit from the simulation network. This reduced any tendency there might have been for interaction between these circuits to cause artefacts. Two hundred acquisition cycles were recorded and averaged in each trial. The excitation current was fixed at 10 μA, and the gain of the measuring amplifier at 100. The true resistivity decrease was determined by measuring the values of the resistance R_{cal} and the nominal 1.5 kΩ load resistor using a Hewlett-Packard 4294A impedance bridge.

4.2 Results.

The system could detect resistance decreases as small as 0.1%, although systematic artefacts, rather than noise, tended to distort these smaller changes. Decreases of over 0.4% could be clearly seen, and measured. Over the range of resistivity decrease 0.4% - 2.0%, the error of measurement was between -15% and -4%, *i.e.*, the system always underestimated the true resistance decrease. A typical recording is shown in figure B6; this corresponds to a true resistivity decrease of -0.78%.

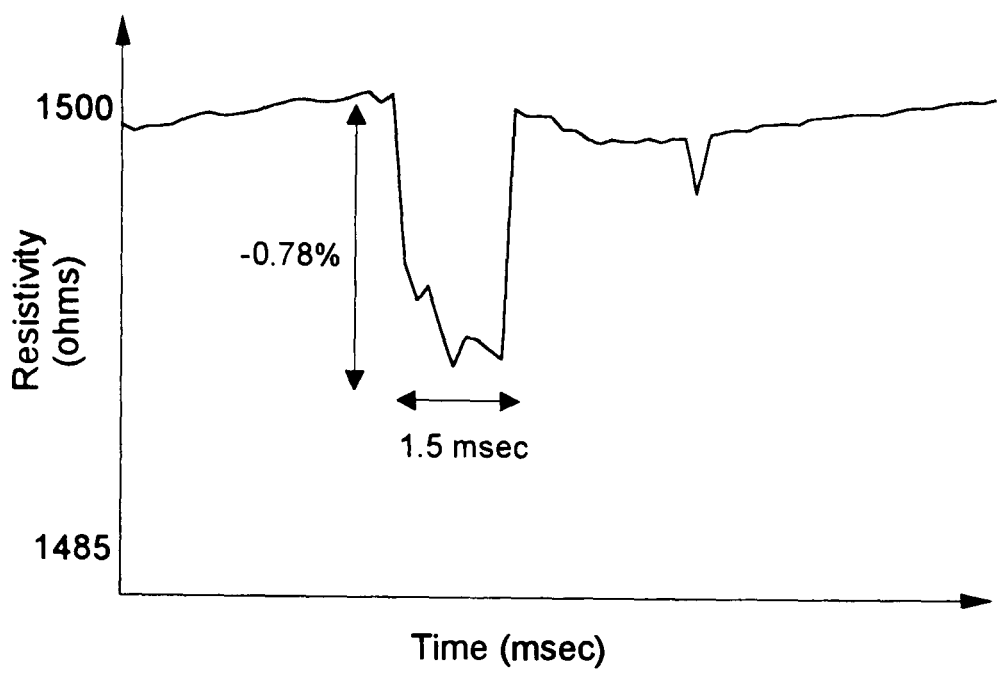

Figure B6: an example of a measurement of resistance during a small resistance decrease. The horizontal arrow shows the time during which the relay contacts were closed. The vertical arrow shows to scale the true resistance decrease of -0.78%. The apparent resistance decrease in this example is -0.73%; the error is about -6%.

5 Discussion

The original design intention was to produce a system which could measure resistivity changes as small as 0.1%. Although the system described could record such changes, they may be distorted by the presence of systematic errors. Changes of over 0.4% could be detected with confidence; measurement of the size of the change was subject to an uncertainty of about 4%-15%. It should be possible to measure, with reasonable accuracy, changes in nerve resistivity whose magnitude are up to one order of magnitude smaller than those predicted in chapter 5.

Appendix C: a prototype 'direct-current' applied potential tomograph

1 Introduction

Chapter 5 described the considerable theoretical advantages that direct current excitation would offer, for imaging electrical resistivity changes in the brain. Despite these advantages, substantial technical difficulties (see §B1) are associated with such a technique. Appendix B described a single-channel system for measuring DC resistance changes; this was subsequently used for measurements on nerve tissue. The design of a complete imaging system is complicated by the need to multiplex the current sources, and the need to handle measurements with a wide dynamic range. This chapter describes the construction of a simple prototype 'direct current tomography' (DCT) system and its performance in imaging resistivity changes in a saline-filled tank. The objective of this work was to determine whether the technical problems associated with DC excitation could be overcome in a complete imaging system. Considerations of time and expense meant that it was not possible to construct a system of equivalent complexity to the single-channel design. Despite its simplicity, the tomograph was able to produce images of 'test objects' in a saline phantom with a resistivity contrast at least as small as 13%, at a rate of 4000 frames per second. This suggests that the construction of an accurate DC tomograph is possible.

2 Method

2.1 Choice of current amplitude.

There are no published guidelines on the safe limits for current applied to the head. There are, however, guidelines, defined by British standards and the International Electrotechnical Commision, for preventing an electrical current inadvertently stimulating the heart. These guidelines recognise that it is sometimes desirable to apply a continuous ('auxiliary') current to the patient's body. It is also recognised that the 'safe' current is frequency-dependent, down to 1 kHz. At this frequency, and below, the 'auxiliary' current limit is 100 μA rms. This corresponds to a square wave of 90 μA peak, based on considerations of equal charge transfer. Agnew and McCreery (1987) concluded from animal experiments that recognisable neuronal damage occurred if charge densities under cortical electrodes were greater than 30-50 $\mu C.cm^{-2}$ per phase. They found also that the effect of the skull and scalp was to attenuate the applied current by up to a factor of 30. On this basis, the allowable excitation current on the scalp at 5 Hz would be about 9 mA: far greater than the 100 μA limit. In contrast, Nathan *et al.*, (1992) found that cortical current density was as much as half the scalp current density when the electrodes were 13 cm apart. This would suggest a maximum current of about 600 μA (=30 $\mu C.cm^{-2}$ / 100 msec * 2). Furthermore, electrical stimulation studies of the fingertip showed (Korniewicz, 1993) that, at 1 kHz, the threshold of stimulation was about 500 μA rms. It is likely, therefore, that

recognisable electrical stimulation of the skin will occur well before damage to the brain. Excitation currents of the order of 50 μA (at 5 Hz) seem appropriate, being ten times smaller this threshold.

2.2 Data Collection

As for the single-channel resistance measurement apparatus, data collection in the prototype tomograph takes the form of averaging following a repeated stimulus. Each data collection cycle consists of acquisition of 400-1000 samples in 100 msec.

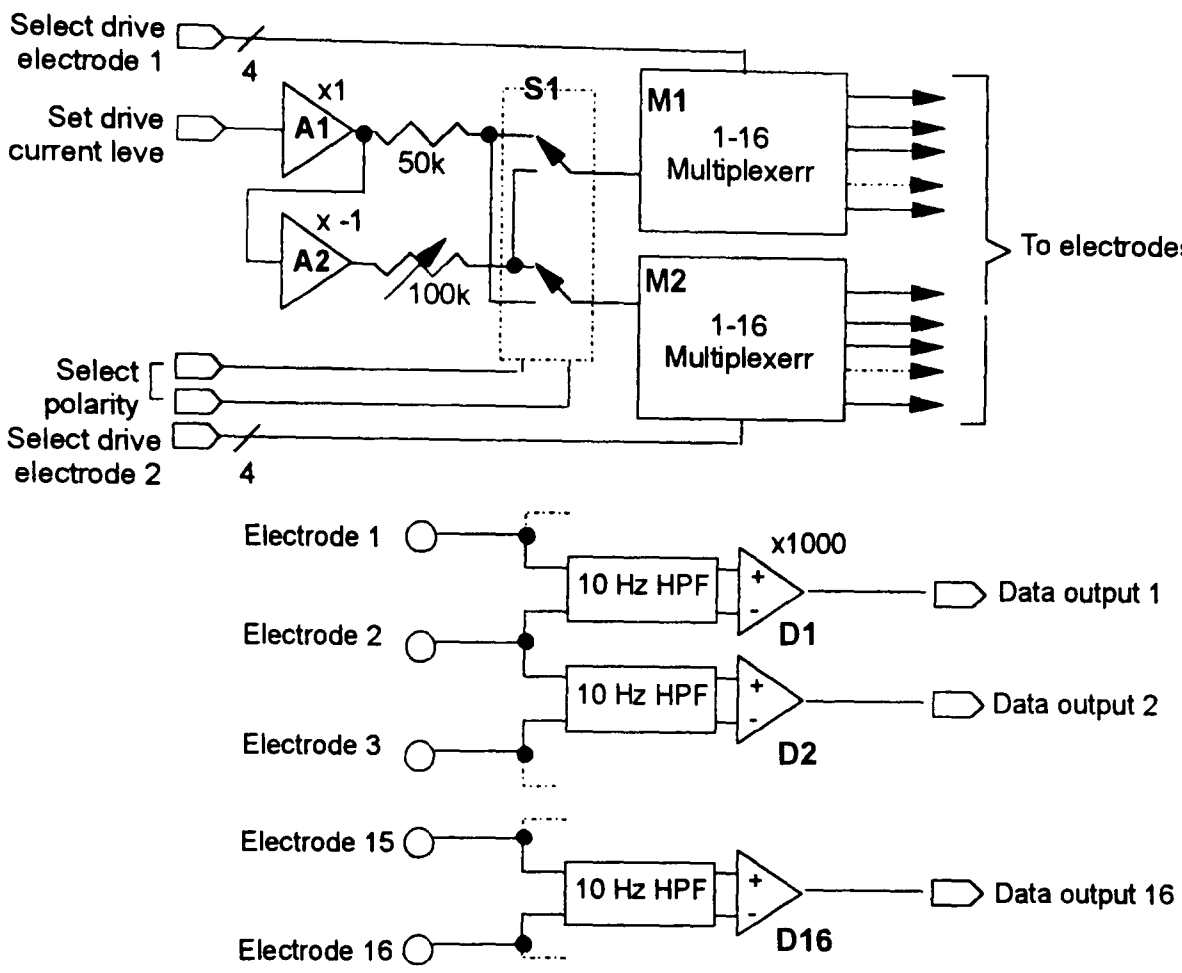

Figure C1: A block diagram of the prototype DCT system. 'HPF'=high pass filter.

2.3 Current sources

One pair of current sources is multiplexed between 16 electrodes, while each pair of electrodes has its own differential amplifier for voltage measurement (figure C1).

Amplifiers A1 and A2 are unity gain non-inverting and inverting buffers respectively. The input voltage to A1 sets the overall output amplitude of the source. This signal is derived from a computer via a digital-to-analogue converter (DAC). The outputs of A1 and A2 are therefore a complementary pair of voltages; these are applied to the current multiplexer by a 50 kΩ fixed and 100 kΩ preset resistor. For the purposes of this prototype, it was assumed that these resistances alone would provide adequate current regulation. The use of a resistor as a constant current source is, of course, only viable when the applied current is small. The adjustment of the null points of A1 and A2, together with the 100 kΩ preset resistance, allowed the common-mode current and voltage generated by the source to be set to an unmeasurable level. In practice the resistances of the presets drifted slightly,

presumably due to temperature change, which introduced a small common-mode component (up to about 5% of the differential current).

S1 is an analogue switch network that selects the polarity of the current; this is controlled by the computer, as are multiplexers M1 and M2 that select the drive currents onto the 16 electrodes. The computer can therefore select any bipolar current pattern.

2.4 Voltage sensing

Considerations of noise and DC electrode potential preclude an amplifier whose low-frequency response extends to DC. When setting a low frequency cut-off point, there has to be a compromise between noise rejection and distortion of the signal. The present design has a low-frequency cut-off of about 10 Hz. To improve data collection speed, and thereby increase signal-to-noise ratio, voltage sensing was carried out 'in parallel' using 16 instrumentation amplifiers, each connected between an adjacent pair of electrodes. For simplicity, the high pass filters were simple RC circuits on both inputs to each amplifier. However, owing to the difficulty in matching the time constants in the inverting and non-inverting inputs, these filters place a limit on the common-mode rejection of the amplifiers.

2.5 Evaluation of performance

The prototype tomograph was connected either to a 'Cardiff' resistor phantom (Griffiths, 1988), or to a saline-filled tank (88 mm diameter; 30 mm depth of 0.09% saline; stainless steel electrodes of 8 mm diameter). The applied current was 50 μA. Data acquisition was in 100 msec bursts at a rate of 4000 samples per second, so each experiment produced 400 sets of boundary voltages at 0.25 msec intervals. 100 such sets were averaged to form each 'frame'. In the saline phantom, acquisition runs were performed both with and without a resistivity change at one of five positions between the centre and the edge of the tank.. The resistivity change was produced by inserting a cylinder of either perspex or polyacrylamide gel (Holder and Kahn, 1994) into the tank. The images presented below are of data acquired 1 msec after the start of excitation. This reduced the effect of error due to the mismatch in input capacitances (see section C4.1). All reciprocity errors (104 in total) were measured. Reciprocity error was defined as

$$(1 - V_1/V_2) * 100\%$$

where V_1 and V_2 are the lower and higher values of a pair of reciprocal measurements. Adjacent electrode excitation was used, even though this would probably not be satisfactory for imaging of the brain. It did, however, allow comparison of the results with those which are obtained from the 'Sheffield Mark 1' (Brown and Seagar, 1987) system, whose characteristics are well known.

3 Results

3.1 Images

A feature whose outline was approximately circular was visible in all images (figure C2); its position corresponded approximately to the position of the resistivity disturbance. This feature was visible even for the smallest resistivity disturbance (13%), although accompanied in this case by clear artefacts. These artefacts appeared to be consistent in successive images made under the same conditions.

3.2 Reciprocity errors

With the resistor phantom, all reciprocity errors were less than 10%. Only about 10% of errors were above 5%. With the saline phantom, reciprocity errors were normally over 10%; about 50% of values were above 20%. Occasional errors of over 100% were observed. Selective abrasion of the surfaces of the electrodes taking part in such measurements improved the reciprocity errors *these* measurements, but correspondingly increased reciprocity errors in voltages acquired from *other* electrode combinations.

3.3 Signal-to-noise ratio

The normalised voltage noise (n) was defined as :

$$n = \frac{SD(V) * \sqrt{2} * 100\%}{E(V)}$$

where SD(V) and E(V) are the standard deviation and mean of the sequential voltage measurements respectively. Figure C3 shows the variation of this noise figure around the phantom boundary. Its worst value was just under 1%: a signal-to-noise ratio of 40 dB.

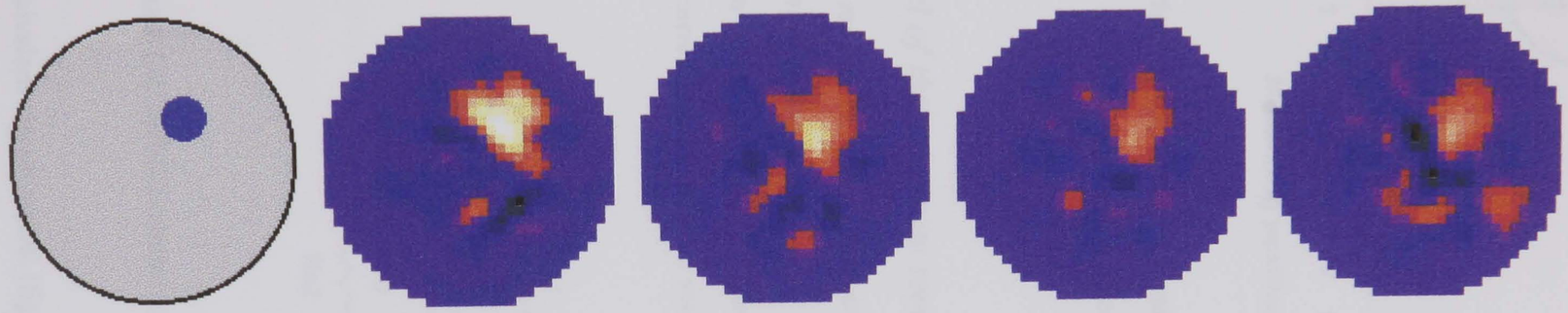

True size and position	Insulator	260% resistivity increase	61% resistivity increase	13% resistivity increase

Figure C2: images of resitivity changes of various size in a saline phantrom, produced by the prototype direct current tomograph

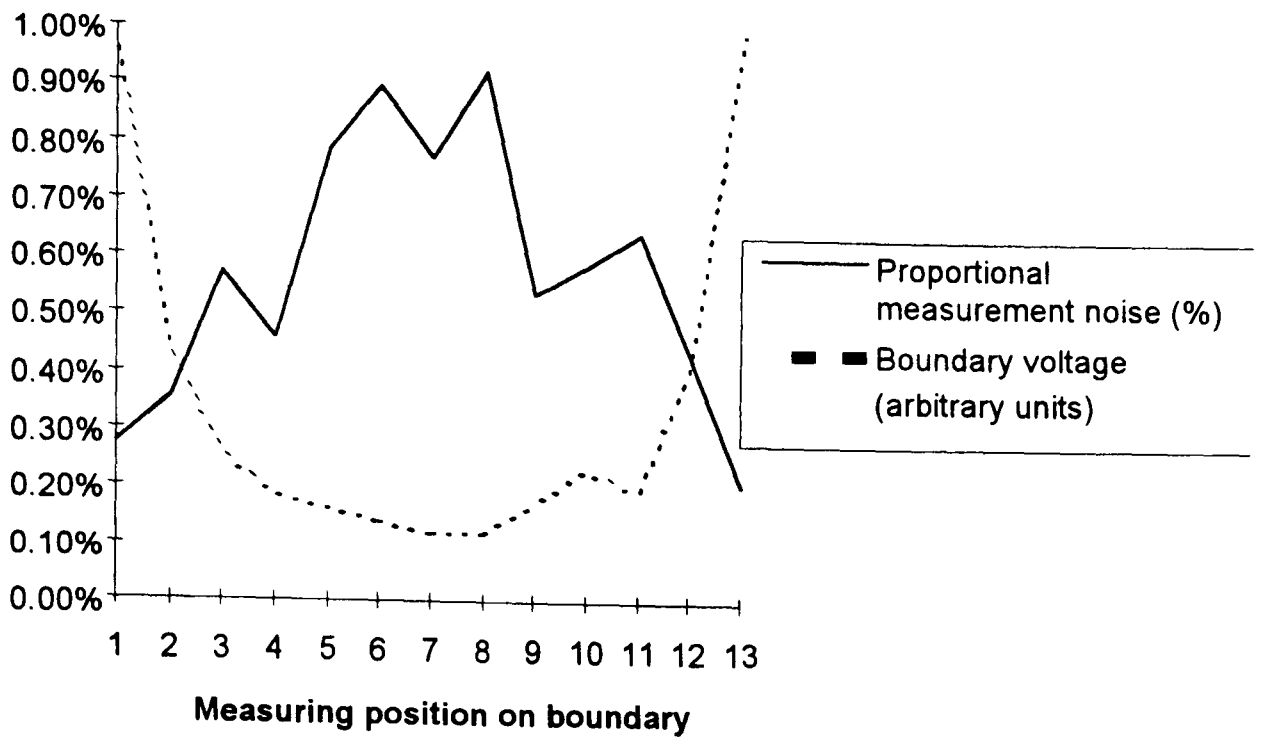

Figure C3: Boundary voltage and normalised noise in the saline phantom measurements. The noise figure is expressed as a percentage of reading

4 Discussion

4.1 SPICE model of the prototype tomograph

Examination of the measuring system suggested three likely significant error sources:

i. variation in electrode resistance,

ii. reduced common-mode rejection of the amplifiers caused by wide component tolerance, and

iii. common-mode currents due to current source imbalance.

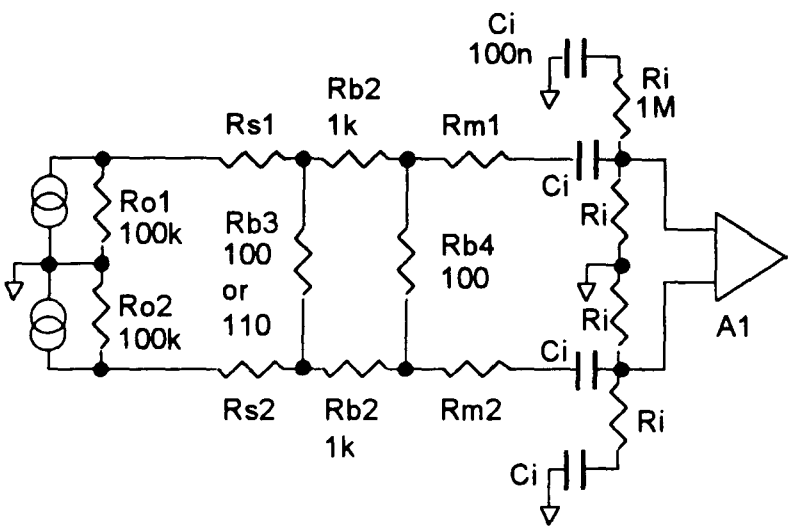

Figure C4: SPICE model of a channel of the prototype DCT system

I used A SPICE equivalent circuit model (figure C4) to investigate these error sources, and to determine whether they were sufficiently large to account for the observed measurement error. The current imbalance in the push-pull current drive was to 5%, a 'worst case' value.

The model parameters are as follows: R_o was the output resistance of the current source, 100 kΩ. Resistances R_s represent the electrode resistances for the source electrodes, while R_m were those for the measuring electrodes. R_{b1} to R_{b4} represented the resistance of the saline phantom. R_i and C_i were the

input resistances and capacitances of the measuring circuit. The duplication of these components reflects the 'parallel' arrangement of the amplifiers. The values of R_i and C_i were chosen to give a time constant of about 50 msec. Simulations were performed with R_{b1} set first to 100 Ω, then to 110 Ω, *i.e.*, a 10% resistivity change.

To simulate the effect of electrode resistance, four electrode configurations were simulated: (i) All electrode resistances were 100 Ω. (ii) All were 100 Ω, except for one of the 'source' electrode resistances which was 200 Ω. (iii) All were 100 Ω, except for one of the 'sense' electrode resistances which was 200 Ω. (iv) All electrode resistances were 10 kΩ.

A simulation was also performed with one of the input capacitances increased by 10%.

Table C2 summarises the simulated proportional and absolute errors.

Simulation condition	Electrode resistances	Absolute error	Proportional error
'Perfect' circuit	All 100 Ω	Negligible	Negligible
	All 100 Ω, except $R_s2=200\Omega$	<1%	<1%
	All 100 Ω, except $R_m2=200\Omega$	<1%	<1%
	All 10 kΩ	10%	4%
5% source imbalance	All 100 Ω	3%	3%
	All 100 Ω, except $R_s2=200\Omega$	3%	3%
	All 100 Ω, except $R_m2=200\Omega$	11%	8%
	All 10 kΩ	8%	7%
One C_i increased to 110 nF	All zero	*77%	*37%

*Table C2: summary of measurement errors for various conditions. *These values were measured 50 msec after the start of the current pulse; all others were measured 1 msec after. The error due to the source capacitance was negligible at the start of the current pulse, and increased very rapidly. Other errors varied little over time.*

These simulation results have a number of implications: (i) errors of less than 1% were obtained with perfectly balanced sources and small electrode resistances; (ii) if a source imbalance was present, then *equal, large* electrode resistances gave rise to smaller errors than *unequal, small* ones; (iii) unequal time constants in the limbs of the sense amplifier will produce the largest errors.

4.2 Comparison of measured errors with the SPICE model

The resistor phantom had no electrodes, and therefore no errors due to electrode impedance mismatch. The measurements were made 1 msec after the start of excitation, so it is unlikely that source capacitance mismatch was a significant source of error. Therefore imbalance in the current source appears to be the only important error source; the measured reciprocity errors were, in fact, comparable with the predicted absolute error figures, for a 5% current imbalance and equal electrode resistances.

When mismatched electrodes were present, the predicted absolute errors were 3%-11%. In practice, the actual electrode resistances in the saline phantom could not reliably be reduced to the figures used in the model (most were greater than 500 Ω) so we might expect larger errors than shown in table C2. This also was found to be the case.

The effect of input capacitance mismatch was expected to increase dramatically with time after the start of the current excitation. Indeed, it was impossible to construct an image of any resistance change with voltage measurements more than about 50 msec from the start of the excitation. It was concluded therefore that the error sources (i) - (iii) above could largely account for the observed measurement errors.

4.3 Necessary improvements

To obtain better accuracy, a 'Mark II' system must overcome the problems of electrode resistance and current source imbalance; the problem of input component mismatch is a straightforward instrumentation issue. The following improvements should increase the accuracy.

i. A 'floating' (isolated) current source, as used in the single-channel instrument. A 'true' floating source can, by definition, introduce no common-mode current. The amount of common-mode voltage introduced will depend on how well the source is isolated from the measuring circuit.
ii. Equalisation of electrode resistances. In the simplest case this could be carried out by manual adjustment of a series resistance.
iii. A two-stage amplifier design, as used in the single-channel instrument. A high-pass filter would be positioned between low-gain and high-gain stages. This would remove the problem of input component mismatch, and thus allow a better CMRR (at least 100 dB) to be achieved

5. Conclusion

The construction of a prototype 'direct current' tomograph has shown that the practical problems associated with DC excitation can be overcome. Further development would be needed to produce a system suitable for clinical use.

Appendix D: The effect of skin impedance on measurement error and image quality

1. Introduction

1.1 The problem of the electrode-skin interface

In applied potential tomography (APT) we use skin electrodes to apply current and measure voltage. The skin, particularly the outer *stratum corneum*, has a large, variable impedance (Rosell *et al.,* 1988) compared to other body tissues. In principle, the subject's skin is part of his body, and part of the imaging field. In practice the *stratum corneum* is very thin compared to the volume of tissue enclosed by the electrodes, and cannot be imaged, for reasons that will be described. Most APT systems apply current and measure voltage on different electrodes: we refer to this as a 'four-terminal' measurement. The effect of skin impedance will be the same on a system that uses more than two current electrodes, provided that it does not attempt to measure the voltage between current electrodes. The distribution of current in a four-terminal measurement is such that we cannot *usefully* measure changes in skin impedance on any measuring electrode, however close to the current electrodes. The skin is simply too thin in comparison to the electrode spacing. We may consider skin resistance to be 'in series' with electrode-electrolyte impedance, which is also outside the imaging field. An 'ideal' measuring circuit would therefore be insensitive to variations in skin impedance, a fact that is unfortunately not true of any practical instrument. Since skin impedance is subject to 'noise' and 'drift' artefacts (Boone and Holder, 1994) it will cause a reduction in image quality.

1.2 Purpose and scope of this study

This study was carried out to estimate the size and distribution of measurement errors caused by realistic skin impedances and the effect these errors might have on image quality. For imaging of the brain, it is particularly important we identify and control potential sources of artefact, since the signal sizes are so small (see chapters 5 and 8). This study was mostly concerned with APT systems like the 'Sheffield Mark 1' (Brown and Seagar, 1987) which apply current and measure the in-phase component of voltage between adjacent pairs of electrodes. It assumes also that the system will use linear backprojection to reconstruct images of resistivity difference. To the best of my knowledge, this description applies to all but one of APT system (Newell *et al.*, 1993) for which biomedical images are available.

Other workers have studied the effect of individual electrode impedance variation on measurement error using SPICE (Record *et al.,* 1990; Riu *et al.*, 1990). This study confirms their results using a similar model, and extends it to include:

i. the effect of a statistical distribution of electrode impedances on the measurement errors in complete sets of boundary voltage measurements, and
ii. the effect of such a distribution on image quality.

A practical APT measurement 'frame' (*i.e.*, a complete set of boundary voltage data) consists of at least one hundred measurements. The measurement errors will be distributed in a complicated way depending on the statistical distribution of electrode impedances and the magnitude of the boundary voltage for a given applied current. I used random number generation to provide sets of electrode impedance with a known distribution. These impedances were then used to 'corrupt' the boundary voltage measurements from a finite-element-model. By repeating this process a large number of times, statistical information was obtained about the measurement errors. Three types of skin impedance variation were considered:

i. The skin impedances were initially random, and remained constant during the APT study.
ii. The skin impedance were initially random, and 'drifted' linearly between measurements.
iii. The skin impedances varied randomly between measurements.

It will be shown that 'difference' imaging is tolerant of skin impedances that remain constant between measurements, but is very sensitive to a variable skin impedance.

2. Skin impedance with different electrode materials

2.1 Introduction

Impedance measurements were made with different electrode materials on the skin of a volunteer, to provide the models described below with realistic values of the distribution of electrode impedance.

2.2 Method

Four each of three types of electrodes were placed on an area 8 cm by 4 cm on each forearm of a volunteer. These electrodes were 'Biotab' pregelled silver/silver chloride (MLB Ltd, Wales), brass disks and steel disks. The skin under alternate electrodes was prepared by cleaning and abrasion. Although the abrasion was vigorous, we did not measure skin impedance during the preparation. The electrode areas were 100 mm^2, 63 mm^2 and 50 mm^2 respectively (the pregelled electrodes were cut in half to save space). The electrodes were placed within 15 mm of one another, and their impedance measured with respect to a large (200 cm^2), distant, silver reference electrode on the subject's back. In this configuration:

i. the contribution to the overall impedance made by the body tissue would be small (compared to the skin impedance) and the same for all electrodes;
ii. the impedance of the reference electrode would be negligible.

A Hewlett-Packard 4284A LCR bridge, set at 2 cycles integration time, measured the electrode impedance from 1 kHz to 1 MHz. The measurement sets were repeated six times, and corresponding measurements averaged.

2.3 Results

At 50 kHz, measured resistances varied between 30 Ω and 250 Ω (figure D1) and reactances between 0 Ω and 1200 Ω. The resistance comprised components for skin and for tissue. Two resistances were measured as 30 Ω to within 1%, and showed complete semicircles on 'Cole-Cole' plot. We therefore assumed that these were measurements of tissue impedance alone, and that abrasion or electrode manipulation had eleiminated the resistance of the skin. Even if the tissue component were smaller than this, it is such a small fraction of the overall impedance that the effect on the model results would be negligible. Accordingly, I subtracted this putative tissue resistance from the measured impedances to give the skin impedance. The mean reactive component was similar, but with a greater range. Clearly, there is considerable variation of skin impedances, even between electrodes of the same type. One-way analysis of variation shows a significant ($p < 0.001$) variation between materials, but all the variation could be accounted for by the difference between the pregelled electrodes and either of the metal types. There was no significant difference between the two metal electrode materials ($p > 0.1$ on unpaired t-test). Pooling the steel and brass values, there was no significant difference between the unprepared and abraded skin ($p > 0.2$ by unpaired t-test). At 1 kHz however, there were large (170 % in resistance and 5800 % in reactance) and significant ($p < 0.05$) differences between abraded and unabraded skin with all electrode types.

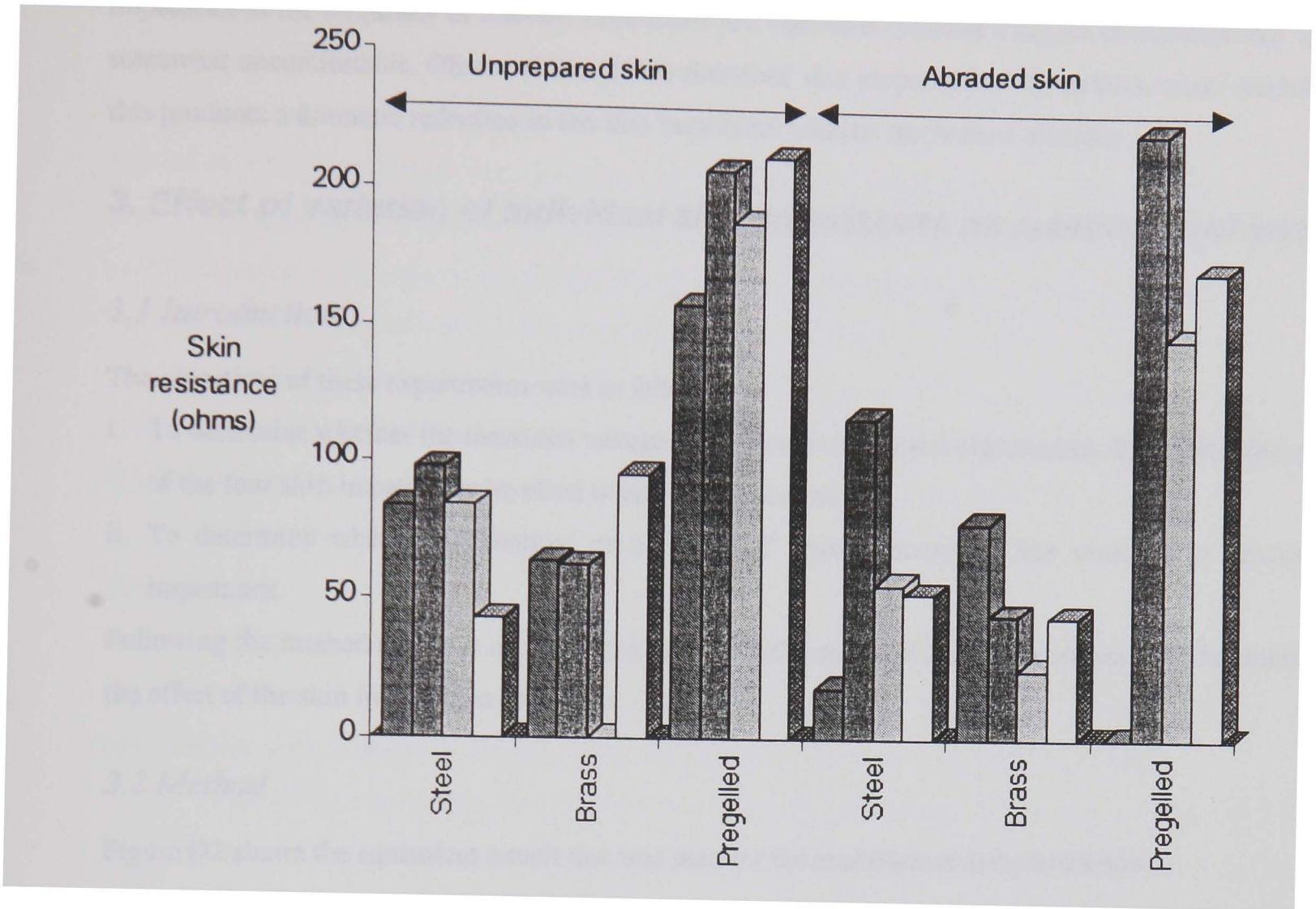

Figure D1: The skin resistance at 50 kHz with different electrode types on unprepared and abraded skin. Each group of bars shows the resistance of four electrodes of the same material.

2.4 Discussion

The figures obtained for skin resistance and its variation were similar to other reports: for example Lu *et al.*, (1994) obtained electrode-skin resistances of about 80 Ω at 50 kHz, with a variation of about 20% between 6 subjects. At 50 kHz, the variations in skin impedance due to positioning of electrodes of the same type are as large as the variation between abraded and unprepared skin. Abrasion became relatively more effective with decreasing frequency. The distribution of resistance and reactances at all frequencies appears to have more a 'uniform' than a 'Gaussian' form. A uniform distribution was therefore used in the statistical studies.

Surprisingly, the pregelled electrodes gave a skin impedance about twice that of bare metal. Later experience revealed that this particular type of electrode has to be applied for about fifteen minutes to reach a steady value. After this time its resistance is comparable to that of metal electrodes. This suggests that it is the skin itself, and not the electrode material, which is dictating the skin resistance. Another unexpected result was that skin preparation did not significantly change the skin impedance at 50 kHz. Later experiments revealed that skin impedance could *always* be reduced to a very low value (less than about 20 Ω, measured as above) if the skin abrasion were carried out while measuring the

impedance at the frequency of interest. Sometimes this operation required a degree of abrasion that was somewhat uncomfortable. Ollmar *et al.*, (1994) described skin preparation with sodium lauryl sulphate; this produces a dramatic reduction in the skin impedance without mechanical abrasion.

3. Effect of variation of individual skin impedances on measurement error

3.1 Introduction

The objectives of these experiments were as follows.

i. To determine whether the measured voltage was affected much more significantly by a particular one of the four skin impedances involved in each measurement.
ii. To determine whether a 'floating' or a 'balanced' current source is less sensitive to electrode impedance.

Following the method of Riu *et al.*, (1990), I used a SPICE model of the APT measurement to simulate the effect of the skin impedances at 50 kHz.

3.2 Method

Figure D2 shows the equivalent circuit that was used for the experiments described below.

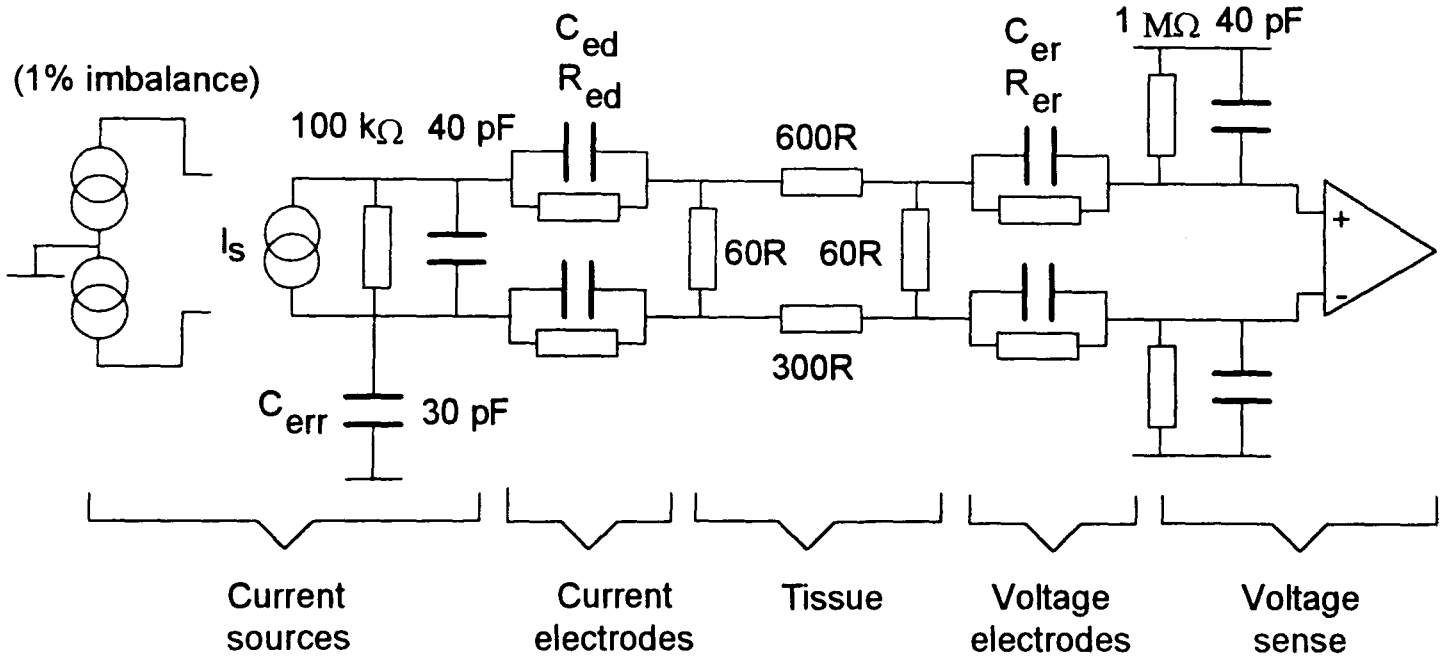

Figure D2: An equivalent circuit model of an APT measurement. See text for details

The model component values were chosen to be typical of APT systems such as the Sheffield Mark 1.

Current source: The output impedance of the current source was set to 100 k Ω in parallel with 40 pF. The latter figure included cable and multiplexer capacitance. Two current source configurations were studied: a 'floating' source (shown connected), and a 'balanced' source (shown to the left of figure D1). When the floating source was connected, we assumed that the most significant source of common-

mode voltage at the amplifier inputs resulted from imperfect isolation of the current source from the measuring circuit (see chapter 2). This was simulated by the 'error capacitance' C_{err}. I felt that this was a more realistic method of generating a common-mode error voltage than to apply a voltage source to one limb of the current generator (*e.g.*, Riu *et al.*, 1990). With our configuration, the common-mode voltage seen by the amplifier is dependent on the impedance of the current electrodes, as expected. The balanced source was assumed to generate an error due to imbalance between the two sources. With this source, C_{err} was removed. In both cases, the current amplitude was 1 mA rms at 50 kHz.

Electrode-skin impedances: These are denoted by R_{ed}, C_{ed}, R_{er} and C_{er} in figure D1. The initial values were taken as the highest of those in figure D1. When electrode-skin impedance was perturbed, the resistive and reactive components were always increased or decreased in the same proportion.

Tissue: the 300 Ω and 600 Ω resistances shown in figure D2 represent the transconductance of the tissue.

Voltage sense: The input resistance of the voltage amplifier was set to 1MΩ in parallel with 40 pF; its CMRR was 60 dB. Only the in-phase component of the measured voltage was determined. We assumed that the errors due to demodulation and waveform generation were not significant.

Neither C_{err} nor the amount of current source imbalance correspond to actual parameters that could be measured on a practical APT system. They were determined as follows. In measurements on saline-filled tanks, electrode contact impedance is negligible: a few ohms (Boone and Holder, 1994). On such a tank the Sheffield Mark 1 System can produce a set of measurements whose worst-case reciprocity error is as low as 5%. Following the 'Mark 1' convention, the worst-case 'reciprocity ratio' will be referred to as 'Check 1'. In an error-free measurement, 'Check 1' would be 100%. The electrode resistances were first short-circuited to determine the output voltage in the 'ideal' case (which was approximately 3.5 mV). The size of the error component (error capacitance or current source imbalance) was increased until the absolute error was 5%. This corresponded to an error capacitance of 30 pF, or a current source imbalance of 1%. The 'starting' voltage was calculated for the condition where all skin impedances were equal. Each of the electrode impedances was then perturbed by -60%, -40%, -20%, 20%, 40% and 60%. After each perturbation the SPICE program recalculated the in-phase component of the output voltage. These voltages were compared with the 'ideal' voltage to derive a measure of voltage change due to skin impedance change.

3.3 Results

With both single and balanced current sources, changes in the skin impedance in the voltage sense circuit (R_{er}, C_{er}) caused the largest variation in the measured voltage. The effect of variation of current electrode skin impedance was negligible (< 0.1%) for the balanced source. For a single source the impedances produced an effect whose magnitude was one quarter to one half that obtained by a variation of the skin impedance in the voltage circuit. The effects of perturbing the electrode impedances in the

'inverting' and 'non-inverting' limbs of the circuit were opposite and almost equal (within 10%). The errors obtained with the balanced sources were considerably larger than with a single source despite configuring for equal errors with the same initial electrode impedances (figure D3).

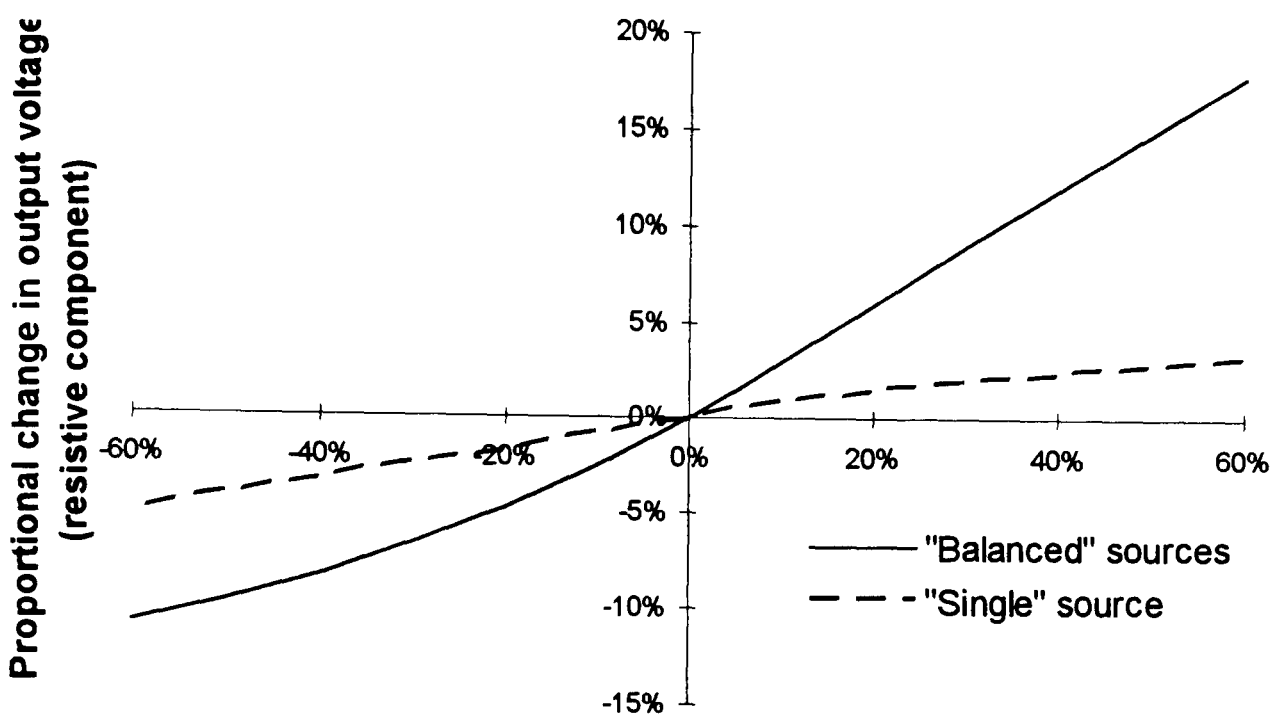

Figure D3: The effect on output voltage of a skin impedance disturbance under the voltage sense electrodes (50 kHz)

3.4 Discussion

Unless the two limbs of a balanced current source can be perfectly matched, the single floating source leads to smaller overall errors as a result of skin impedance variation. For the statistical model described below, it is assumed that only the skin impedance under the voltage electrodes is significant.

4. Measurement error and image quality as a function of a distribution of electrode impedance

4.1 Introduction

In a practical APT experiment, each electrode will have its own skin impedance. A given measurement will be subject to an error that depends on the impedances under the voltage and current electrodes from which that measurement is made. The distribution of errors in a complete measurement frame, and therefore the image quality, will depend in a complicated way on the skin impedance distribution and

the variation of absolute voltage around the body. In this section we describe a model of the effects of these factors.

Rather than attempt to derive an analytical expression for the statistical properties of the measurement error, the method to be described is pragmatic: repeated simulation, with statistical analysis of the results.

4.2 Method

The results of section 2 suggested that a uniform distribution of skin impedance might be more appropriate than a Gaussian (figure D4). The skin impedances described below therefore refer to a uniform distribution for which the quoted value is the maximum. For simplicity, skin impedance was assumed to consist of equal resistive and reactive components. The 'Mark 1' system makes 104 independent measurements per data frame. To determine all the meaurement errors for this set of data using the SPICE model of section 3 would be extremely time-consuming. Since most of the error is due to the skin impedance under the voltage electrodes, only these electrodes were taken into account. Figure D5 shows the model circuit, the output voltage of which may be readily determined from the input by circuit theory. The input voltages themselves were derived from the finite element model described in chapter 6. The finite element model had a 50% resistance increase of about one twentieth the diameter of the image, placed midway between the centre and the '9 o'clock' position. These voltages were 'corrupted' by errors due to skin impedance before statistical analysis and reconstruction into images. Images were generated for constant and variable skin impedance. In all cases, 60 image frames were processed. The fixed common-mode voltage V_{cm} provided the basis for a measurement error. V_{cm} was adjusted until we obtained a 'Check 1' value of 95% with the electrode impedances short-circuited. For analysis at frequencies other than 50 kHz, we assumed that the amplifier CMRR varied linearly between 80 dB at 10 Hz and 60 dB at 50 kHz, while the skin resistance varied as $1/\sqrt{(\text{frequency})}$.

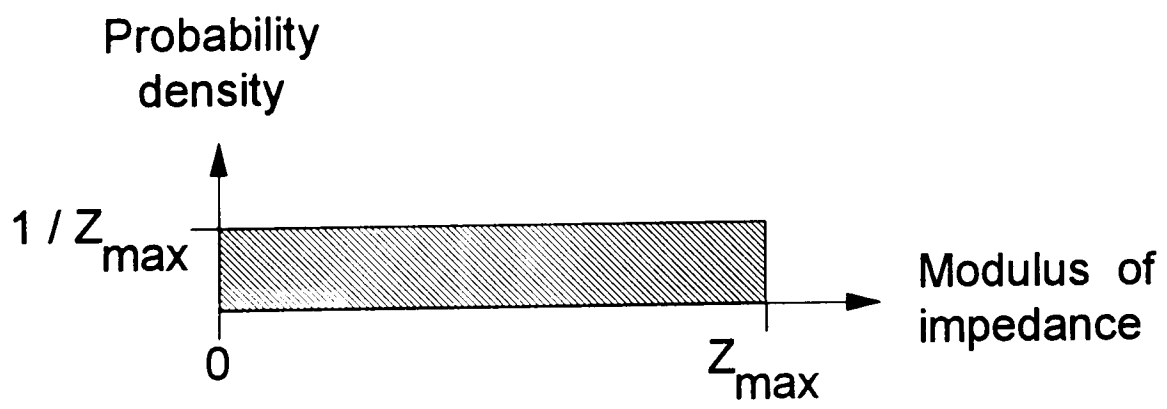

Figure D4: a uniform distribution of the modulus of impedance, between 0 and Z_{max}

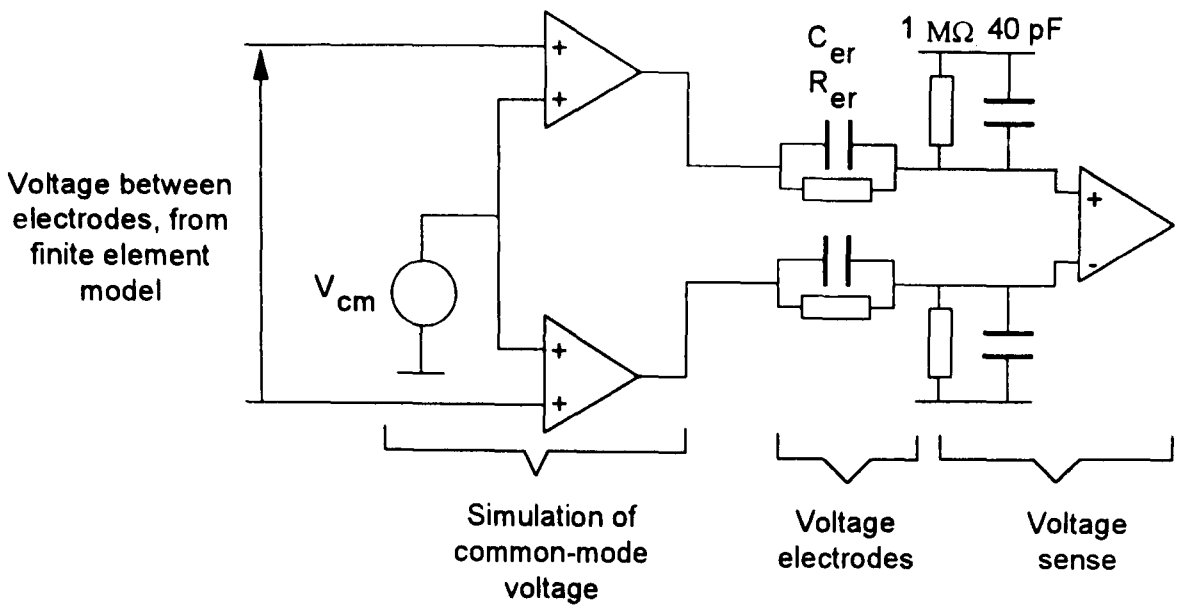

Figure D5: a model of the voltage measurement circuit only, with a fixed common-mode voltage

4.3 Results

4.3.1 Measurement error

Not surprisingly, root-mean-square (rms) measurement error at constant frequency (50 kHz) increases with maximum electrode impedance (figure D6), while 'Check 1' decreases. The *mean* measurement error does not vary with skin impedance, since the skin impedance associated with the amplifiers 'non-inerting' input is equally likely to be higher or lower than that of its 'inverting' input.

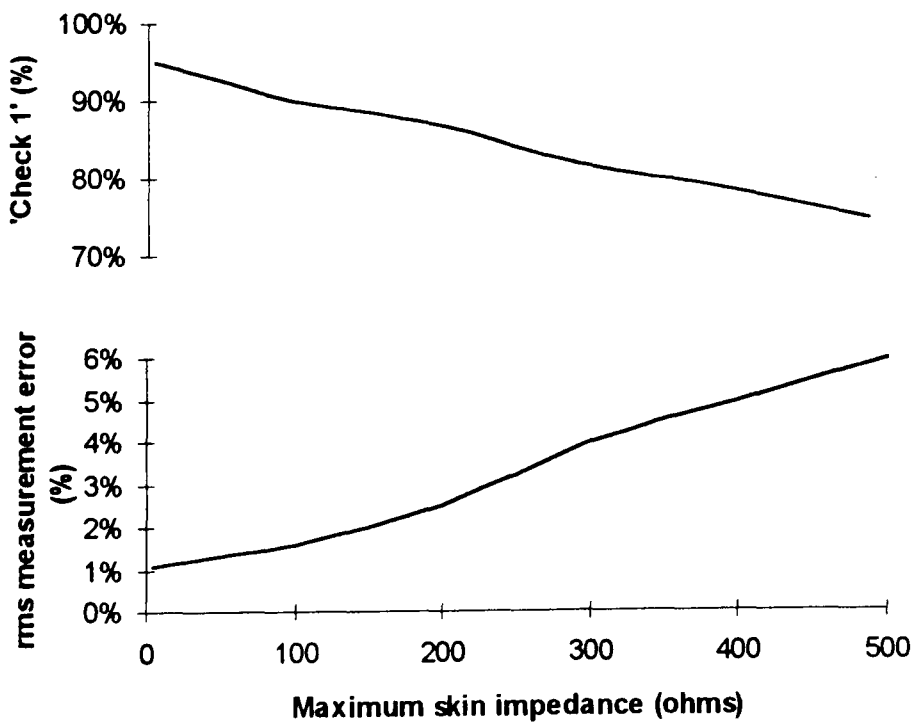

Figure D6: 'Check 1' and rms measurement error against skin impedance. Impedances were uniformly distributed between zero and the x-axis value.

For a skin impedance of 100 Ω at 50 kHz which varied over frequency as 1/√(frequency), the measurement error and 'Check 1' were reasonably constant over a frequency range 1 kHz - 100 kHz. Nevertheless, a 'best' frequency could be determined: it was about 10 kHz with the circuit parameters studied.

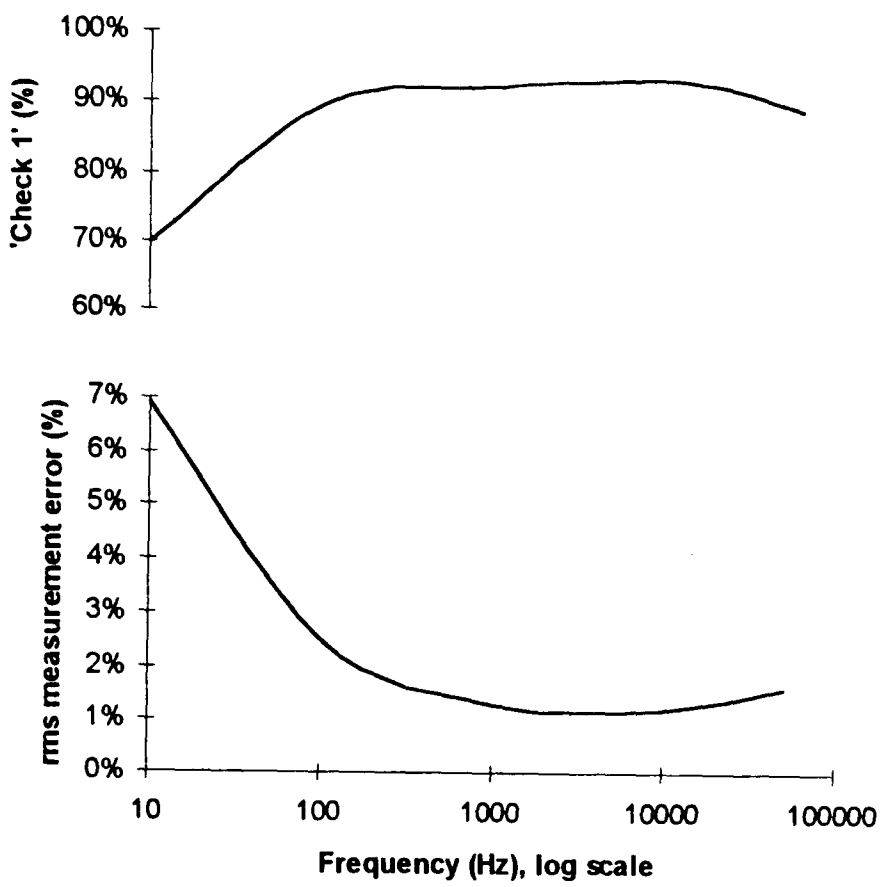

Figure D7: The rms measurement error and 'Check 1' figure against frequency for a distribution of electrode resistances whose values lie between 0 and 100 Ω at 50 kHz

4.3.2 Image quality

The image artefacts were random in nature and therefore different from one image to another. The images presented below were chosen at random from the set of sixty available.

i. *Electrode impedance was initially variable, and remained constant between measurements.* In this case, a skin impedance of up to about 2 kΩ was tolerable, (figure D8, top row), before obvious distortion was seen in the image.

ii. *Electrode impedance was initially variable, and drifted linearly at 1% per frame.* When the initial maximum skin impedance was 100 Ω, a linear drift of 2% was sufficient to cause noticeable distortion (figure D8, middle row). At 5% the original feature was almost lost. After 10% drift, 'false' features were found in the image. A linear drift with constant (*i.e.*, all 100 Ω) skin impedances caused a noticeable change in the overall intensity of the image, but features were not distorted (not shown in figure D8).

iii. *Electrode impedance varied randomly between frames* When the skin impedance varied randomly between frames, a maximum value of 10 Ω was sufficient to cause a noticeable distortion. 20 Ω rendered the image almost meaningless (figure D8, bottom row).

4.4 Discussion

Comparison of the top row of figure 8 with the middle and bottom demonstrates the effectiveness of difference imaging. Provided that measurement errors remain constant between frames, the errors can be large before they cause a significant distortion. The worst errors occur when the skin impedances vary at random between frames. This might be the case where, for example, the patient is fitted with an ill-fitting rigid electrode array that moves with breathing. In this case one would need to ensure skin impedances of less than about 10 Ω to image a 50% change in resistivity. A more likely source of error with self-adhesive electrodes, for example, is the gradual drift in electrode impedance during the study. Drift is most rapid immediately after application of the electrodes (McAdams and Jossinet, 1990). In the author's experience, initial drifts of 10% per minute are not unusual. The differences between the images of figure 8 (middle row) at 1% and 5% drift are considerable. If measurements were made of a resistivity change (50%, 1/20 diameter) during this period, it is likely that distortions will result. If the area of resistivity change were larger, for example during studies of gastric emptying, the apparent resistivity change will be larger. In this case worse drifts may be tolerated, perhaps as much as 20%.

5. Conclusion

Electrode-skin impedance artefacts of the sizes encountered in practice readily produced artefacts in difference images, particularly if the skin impedance changes between measurement frames. In a practical measurement, skin impedance drift over time is probably the most important factor. If the skin resistance remains constant, APT could probably tolerate skin impedances greater than those normally encountered. Boone and Holder (1994) showed that skin preparation reduced the variation in impedance over time, except during an initial 'settling' period of about ten minutes. This period is the worst time to begin a study, regardless of how the skin is prepared. If the skin is to be abraded, one needs to measure its impedance during abrasion, to ensure that the process has been successful.

Random initial resistances, constant between frames

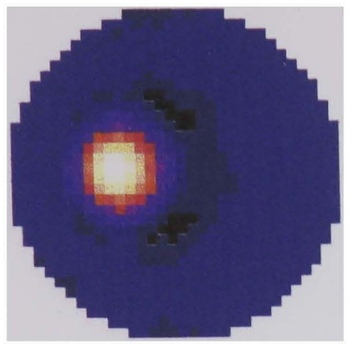

100 Ω

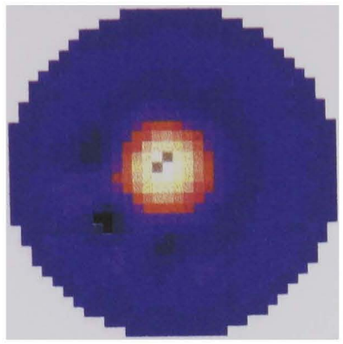

1000 Ω

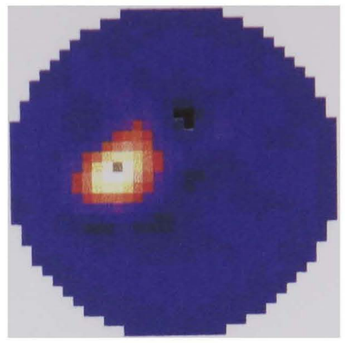

2000 Ω

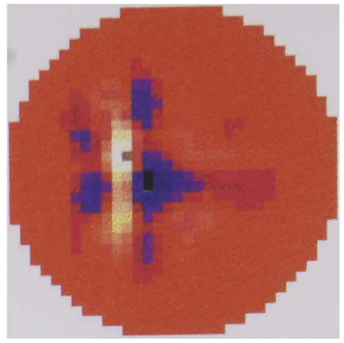

5000 Ω

Random initial resistances of 0-100Ω, linear drift between frames

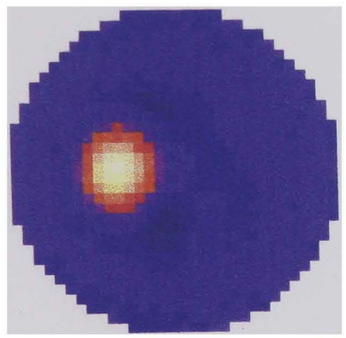

1%

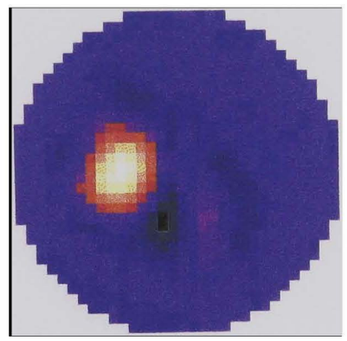

2%

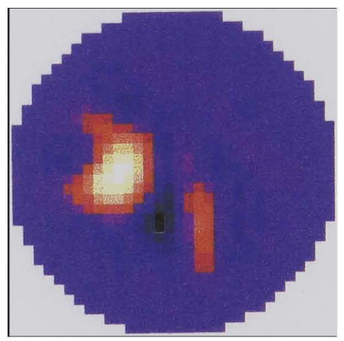

3%

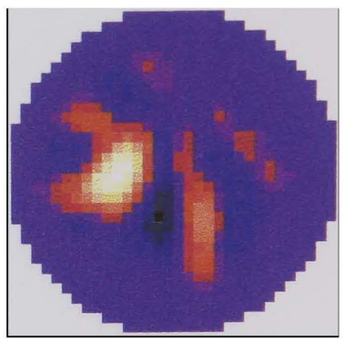

4%

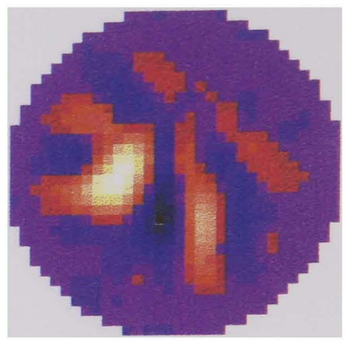

5%

Random resistances at each frame

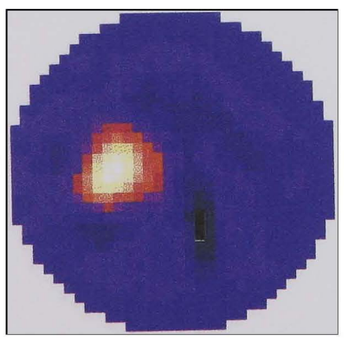

5 Ω

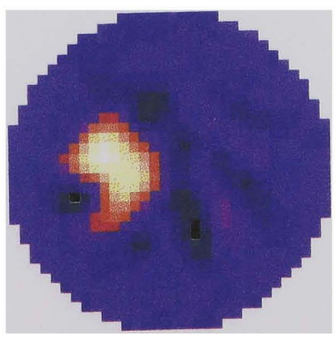

10 Ω

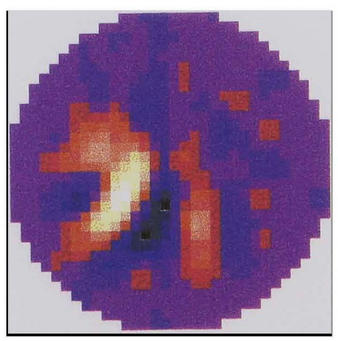

15 Ω

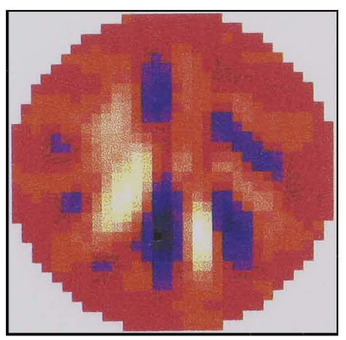

20 Ω

Figure D8: see text for details